

AFM studies of the Metallicity of Single-walled Carbon Nanotubes and Corrosion
Inhibitor Adsorption

A dissertation presented to
the faculty of
the College of Arts and Sciences of Ohio University

In partial fulfillment
of the requirements for the degree
Doctor of Philosophy

Yao Xiong

August 2011

© 2011 Yao Xiong. All Rights Reserved.

This dissertation titled
AFM Studies of the Metallicity of Single-walled Carbon Nanotubes and Corrosion
Inhibitor Adsorption

by

YAO XIONG

has been approved for
the Department of Chemistry and Biochemistry
and the College of Arts and Sciences by

Liwei Chen

Assistant Professor of Chemistry and Biochemistry

Benjamin M. Ogles

Dean, College of Arts and Sciences

ABSTRACT

XIONG, YAO, Ph.D., August 2011, Chemistry

AFM Studies of the Metallicity of Single-walled Carbon Nanotubes and Corrosion Inhibitor Adsorption

Director of Dissertation: Liwei Chen

Two families of novel materials, carbon nanotubes and corrosion inhibitors, were studied in this dissertation research. Their unique structures and properties were analyzed using atomic force microscopy in conjunction with other optical spectroscopies. Applications of atomic force microscopy were developed to measure the dielectric responses of nanomaterials, operate in aqueous environments and for removal of adsorbed molecules.

The heterogeneity of carbon nanotube samples has hindered their application and further development. A scanning probe microscopy assay has been established to differentiate between metallic and semiconducting nanotubes as well as to quantitatively determine metallicity; this was based on the different dielectric responses of metallic and semiconducting nanotubes. The metallic contents of multiple nanotube samples with various metallic-to-semiconducting ratios were determined using this method, the results being further confirmed by UV-Vis and Raman spectroscopy. This assay can provide a rapid method for evaluation of the effectiveness of selective nanotube synthesis and separation methods. The technique can be extended for the study of the dielectric properties of other nanomaterials.

Based on the different electronic properties between metallic and semiconducting nanotubes, a microwave irradiation effect directed towards the preferential etching of metallic nanotubes was further studied. Irradiation was found to cause the fracturing of a nanotube-film coated glass substrate, indicating nanotubes can absorb microwave energy and convert it to heat. THz transmission and Raman spectra show that the metallic content decreased after irradiation as particular spectral features decreased in intensity. UV-Vis absorption spectra indicated that the decreased metallicity was not solely due to the complete decomposition of the nanotube structure, but was affected by preferential oxidation or defect induction in metallic nanotubes.

The adsorption structure, film thickness, penetration force and removal force of adsorbed corrosion inhibitors were studied in aqueous solution. The structure and thickness of inhibitor films was found to depend on their concentration, bulk pH, solution ionic strength and surface properties. The measured force for penetration of an inhibitor film and removal of inhibitor molecules was of the order of 1~10 MPa, indicating inhibitor molecules cannot be removed by fluid flow alone. This is the first time that the adsorption structures of inhibitors on metal surfaces were directly visualized and the mechanical properties of adsorbed inhibitor films quantitatively measured.

Approved: _____

Liwei Chen

Assistant Professor of Chemistry and Biochemistry

DEDICATION

To

My Parents, Ping Xiong and Yining Huang

and

My wife, Yi Liu, and My Soon-to-be-born Baby, Audrey

ACKNOWLEDGMENTS

The author would like to express his great appreciation to Prof. Srdjan Nesic for supporting and supervising his research work in Institute for Corrosion and Multiphase Technology, Ohio University.

The author would like to express his great appreciation to Prof. Liwei Chen for supporting and supervising his research work in Department of Chemistry and Biochemistry, Ohio University.

The author would like to thank Prof. Brian Kinsella for advising his research work in Institute for Corrosion and Multiphase Technology, Ohio University, and Prof Alain Pailleret for advising his research work in Laboratoire Interfaces et Systèmes Electrochimiques (LISE), Université Pierre et Marie CURIE (PARIS VI), Paris, France.

The author would like to thank his committee members Prof. Hugh Richardson and Prof. Marcia Kielizewski for supervising his proposal and dissertation, and Prof. P. Gregory Van Patten and Prof. Ido Braslavsky for supervising his proposal.

The author would like to thank his collaborators Prof. Hao Xin for providing transmission spectra, Prof. Hugh Richardson for using Raman spectrometer, Prof. Jeffery Rack for using UV-vis absorption spectrometer, Dr. Ming Zheng for providing DNA-nanotube samples, and Dr. Abdou Hassanien for providing laser ablation nanotube samples.

The author would like to thank Dr. David Young for deeply reviewing his dissertation and providing research suggestion, Bruce Brown for reviewing his dissertation and providing research support, and Cody Shafer for technical support.

The author would like to thank his former group member Dr. Wei Lu for teaching AFM techniques, Dr. Dan Wang for teaching nanotube dispersing and filming techniques, Dr. Yunxiang Gao for spin-coating and plasma techniques, Dr. Christian Canto for teaching LPR and EQCM techniques and inhibitor knowledge, and all other labmates and co-workers for discussion.

The author would like to express sincere gratitude to Prof. Srdjan Nestic, Prof. Brian Kinsella, Prof. Huet Francois, Prof. Alain Pailleret and Bruce Brown for providing and supporting the great opportunity to study in Paris, France.

TABLE OF CONTENTS

	Page
Abstract.....	3
Dedication.....	5
Acknowledgments.....	6
List of Tables	12
List of Figures.....	13
List of Abbreviations.....	26
Chapter 1. Introduction.....	28
1.1 Atomic force microscopy.....	28
1.1.1 History.....	28
1.1.2 Basic principles of AFM.....	30
1.1.3 AFM image modes.....	32
1.1.3.1 Contact mode	32
1.1.3.2 Non-contact mode.....	32
1.1.3.3 Tapping mode	33
1.1.3.4 Chemical force microscopy (CFM)	34
1.1.3.5 Electrostatic force microscopy (EFM).....	34
1.1.3.6 Magnetic force microscopy (MFM).....	35
1.1.3.8 Nanolithography and manipulation.....	36
1.1.4 AFM probes	37

	9
1.1.4.1 Cantilevers	37
1.1.4.2 Tips	38
1.2 Carbon nanotubes	40
1.2.1 History.....	40
1.2.2 Structure and synthesis of nanotubes	40
1.2.3 Electrical properties of nanotubes.....	44
1.2.4 Dispersion and separation of nanotubes	45
1.2.5 Characterization of nanotubes.....	52
1.2.5.1 Atomic force microscopy.....	52
1.2.5.2 Raman spectroscopy	53
1.2.5.3 Absorption spectroscopy.....	57
1.2.5.4 Fluorescence spectroscopy.....	58
1.3 Corrosion inhibitor.....	60
1.3.1 Background	60
1.3.1 Driving forces for inhibitor adsorption	62
1.3.2 Adsorption isotherm.....	64
1.3.3 Adsorption structure.....	66
1.3.4 Environmental effects	68
1.3.4.1 pH effect.....	68
1.3.4.2 Temperature effect.....	69
1.3.4.3 Surface potential	71
1.3.5 Adsorption kinetics	71

	10
1.4 Overview of dissertation.....	72
Chapter 2. An Electric Force Microscopy Assay for Single-Walled Carbon Nanotube	
Metallicity.....	74
2.2 Experimental.....	78
2.2.1 Materials	78
2.2.2 Methods.....	79
2.3 Results and discussion	80
2.3.1 Dielectric response and metallic content of DNA coated nanotubes.....	80
2.3.2 Length effect on dielectric response	90
2.3.3 Dielectric response and metallic content of commercial nanotube samples....	92
2.3.4 Verification of EFM assay via absorption and Raman spectra.....	99
2.4 Conclusions.....	110
Chapter 3. Microwave Irradiation of Single Walled Carbon Nanotubes.....	111
3.1 Introduction.....	111
3.2 Experimental.....	112
3.2.1 Materials	112
3.2.2 Methods.....	114
3.3 Results and discussion	116
3.3.1 Microwave irradiation on individual nanotubes	116
3.3.2 Microwave irradiation on nanotube thin films.....	117
3.3.3 Characterization of nanotube thin films before and after irradiation.....	118
3.4 Conclusions.....	130

	11
Chapter 4. AFM Investigation of Corrosion Inhibitors	131
4.1 Introduction.....	131
4.2 Experimental.....	133
4.2.1 Materials	133
4.2.2 Methods.....	136
4.3 Results and discussion	139
4.3.1 Surface morphology of corrosion inhibitors on mica	139
4.3.2 Film thickness measurement.....	150
4.3.3 Penetration force and force distance curves.....	159
4.3.4 Lateral removal force.....	169
4.3.5 Environmental effects	173
4.3.5.1 Effect of [NaCl] on inhibitor adsorption.....	173
4.3.5.2 Effect of pH on inhibitor adsorption.....	176
4.3.5.3 Effect of ethanol on inhibitor adsorption.....	178
4.3.6 Desorption of inhibitor molecules	179
4.3.7 Re-adsorption of inhibitor molecules.....	181
4.3.8 Adsorption of corrosion inhibitors on metal surfaces.....	183
4.4 Conclusions.....	200
Chapter 5. Future work	202
References.....	204

LIST OF TABLES

	Page
Table 2.1 Information of two target nanotubes from Raman and EFM measurements..	109
Table 3.1 Metallic-to-semiconducting ratios before and after irradiations from Raman spectra at both 514 nm and 532 nm excitation wavelengths.	123
Table 4.1. Corrosion inhibitors and CMC values.	134

LIST OF FIGURES

	Page
Figure 1.1 Photographs of (a) Asylum research MFP 3D AFM and (b) Pico scan 2000 AFM.....	29
Figure 1.2 Basic principles of AFM.	30
Figure 1.3 Schematic drawings of contact mode, non-contact mode and tapping mode..	34
Figure 1.4 Schematic drawings of (a) a CFM setup containing a functionalized tip and surface; (b) an EFM setup containing a biased tip and a sample with different charge distributions; (c) a MFM setup containing a magnetic coated tip and a flat magnetic sample.	36
Figure 1.5 AFM image of a generated pattern by nanolithography. (Figure reproduced with permission from reference 37).....	37
Figure 1.6 SEM images of AFM probes with (a) rectangular cantilever, (b) V-shaped cantilever.....	38
Figure 1.7 SEM image of a sharp tip with a diameter of ~60nm on its “head” part.....	39
Figure 1.8 Schematic of a graphene sheet. A nanotube can be constructed by rolling of a graphene sheet.....	41
Figure 1.9 Schematic of (A) a zigzag (10, 0) nanotube; (B) an armchair (9, 9) nanotube; (C) a chiral (8, 5) nanotube.	42
Figure 1.10 Schematic drawings of electronic structures of (A) a semiconducting (12, 8) nanotube and (B) a metallic (10, 10) nanotube.....	45

Figure 1.11 TEM image of nanotube bundle consisting of approximately 100 nanotubes. (Figure reproduced with permission from reference 45).	46
Figure 1.12 Schematics of (A) a covalent functionalization of nanotubes and (B) a noncovalent functionalization of nanotubes.	47
Figure 1.13 Schematics of selective chemical reaction of nanotubes.....	48
Figure 1.14 Microelectrode device for ac-dielectrophoresis (DEP).	49
Figure 1.15 Absorption spectra of separated fractions in ion-exchange chromatography (IEX). Each fraction showed enrichment of different species of nanotubes.	50
Figure 1.16 Colored band and corresponding absorption spectra of enriched nanotubes in density gradient ultracentrifugation (DGU).	51
Figure 1.17 An AFM image of individual single-walled nanotubes dispersed on a SiO ₂ substrate.	53
Figure 1.18 A typical Raman spectrum for a nanotube. (Figure reproduced with permission from reference 92).	54
Figure 1.19 G bands for (a) semiconducting nanotubes and (b) metallic nanotubes.....	55
Figure 1.20 RBM bands for different nanotube species.	57
Figure 1.21 Adsorption spectrum for a HiPco nanotube samples after microwave irradiation.	58
Figure 1.22 Fluorescence spectrum of a nanotube sample (A) from 658 excitation and (B) from 785 nm excitation.....	59
Figure 1.23 Molecular structure of an organic corrosion inhibitor (a quaternary ammonium salt).	61

Figure 1.24 Molecular structures of organic corrosion inhibitors: (a) cationic; (b) anionic; (c) zwitterionic; (d) nonionic surfactants.	62
Figure 1.25 Schematic drawings of (A) the Electrostatic interaction between a cationic quaternary ammonium salt surfactant and a negatively charged surface; (B) the Dipole-dipole interaction between a non-ionic surfactant and a positively charged surface; (C) the Dispersion interaction between the hydrophobic tail of a quaternary ammonium salt surfactant and non-polar surface.	63
Figure 1.26 Schematic of adsorption isotherm for an ionic surfactant on an oppositely charged substrate.	65
Figure 1.27 Schematic drawings of adsorption structures in four regions: (A) Initial stage, no adsorption. (B) In region 1, only a few surfactant molecules adsorb onto the surface. (C) In region 2, surfactants gradually form a compact monolayer with the hydrophobic tails stand up. (D) At the end of region 3, a bi-layer structure is formed and the adsorption reaches its maximum.	67
Figure 1.28 Different aggregation structures of cationic surfactant tetradecyltrimethylammonium bromide (C14TAB) in the (A) absence and (B) presence of Br ⁻ ions	68
Figure 1.29 (a) Adsorption isotherms of anionic surfactants on a positively charged surface at different pH values; (b) Adsorption isotherms of cationic surfactants on negatively charged surfaces at different pH values.	70
Figure 1.30 Adsorption isotherms of anionic surfactant SDS at different temperature, pH, ionic strength.	70

Figure 1.31 Adsorption kinetics for CTAB at the following bulk surfactant concentrations: (a) 0.50mM (0.55 CMC); (b) 0.80mM (0.89 CMC); (c) 10mM (11 CMC).	72
Figure 2.1 Schematics of the double pass mode of EFM scanning. (a) On the first-pass, the cantilever vibrates over the sample and produce (c) a topographic image. (b) On the second-pass, a bias voltage is applied to the tip. The induced dipole on nanotube surface in turn interacts with the charged tip, leading to (d) a dielectric image.....	77
Figure 2.2 Influence of the longitudinal polarizability on the interaction forces between tip and nanotubes. The different Potential distributions around (a) a metallic nanotube and (b) a semiconducting nanotube result in stronger interaction forces of metallic nanotubes than semiconducting nanotubes.....	78
Figure 2.3 Dielectric response <i>versus</i> D^2 plot from numerical modeling. The dielectric signal of metallic nanotubes (M) and semiconducting nanotubes (S) locate in different zones in the plot as they have significantly different dielectric responses.	79
Figure 2.4 Topographic images (A,B) and corresponding dielectric images (C,D) for DNA coated HiPco nanotubes in different zones.	81
Figure 2.5 Dielectric signal <i>versus</i> D^2 plot for DNA coated HiPco nanotubes.	83
Figure 2.6 Topographic images (A,B) and corresponding dielectric images (C,D) for DNA coated CoMoCAT nanotubes in different zones.	84
Figure 2.7 Dielectric signal <i>versus</i> D^2 plot for DNA coated CoMoCAT nanotubes.	85
Figure 2.8 (A) absorption spectrum, (B) Topography image, (C) dielectric image, and (d) dielectric signal <i>versus</i> D^2 plot of the metallic enriched DNA nanotube sample.	86

Figure 2.9 (A) absorption spectrum, (B) Topography image, (C) dielectric image, and (D) dielectric signal <i>versus</i> D^2 plot of the semiconducting enriched DNA nanotube sample.	88
Figure 2.10 Dielectric signal <i>versus</i> D^2 plot for both metallic enriched sample and semiconducting enriched sample.	89
Figure 2.11 Dielectric signal versus D^2 plot for five mixed nanotube solutions from metallic enriched samples and semiconducting enriched samples.	90
Figure 2.12 Dielectric signals <i>versus</i> diameter square in different length ranges.	92
Figure 2.13 Topographic images (A, B) and dielectric images (C, D) for laser ablation nanotubes dispersed with 1,2-dichloroethane in a bath sonicator.	93
Figure 2.14 Dielectric signal <i>versus</i> D^2 plot for laser ablation nanotubes. The percentage of metallic nanotubes in this sample is 49%.	94
Figure 2.15 Topographic images (A, B) and dielectric images (C, D) for HiPco nanotubes dispersed though 1,2-dichloroethane in a bath sonicator.	95
Figure 2.16 Dielectric signal <i>versus</i> D^2 plot for HIPco nanotubes. The percentage of metallic nanotubes in this sample is 28%.	96
Figure 2.17 Topographic images (A, B) for and dielectric images (C, D) CoMoCAT65 nanotubes dispersed though 1,2-dichloroethane in a bath sonicator.	97
Figure 2.18 Dielectric signal <i>versus</i> D^2 plot for CoMoCAT65 nanotubes. The percentage of metallic nanotubes in this sample is 14%.	98

Figure 2.19 Dielectric signal <i>versus</i> D^2 plot for (A) HiPco and (C) CoMoCAT65 nanotube samples, and absorption spectra for (B) HiPco and (D) CoMoCAT65 nanotube samples.....	100
Figure 2.20 AFM images of marker substrate (A, B).....	101
Figure 2.21 Schematic depiction of NOSM instrument which enables Raman spectroscopy in CCD mode and confocal Raman images in APD mode.	102
Figure 2.22 (A) AFM images, (B) confocal Raman images and (C) EFM images captured on the same areas.	103
Figure 2.23 Kataura plot shows that the excitation energy for nanotubes at different diameters.	104
Figure 2.24 (A) topographic image; (B) dielectric image; (D) dielectric <i>versus</i> D^2 plot from experimental data; (D) dielectric <i>versus</i> D^2 plot from numerical modeling.	105
Figure 2.25 (A) confocal Raman image; (B) G band and RBM band features.	106
Figure 2.26 (A) topographic image; (B) dielectric image; (D) dielectric <i>versus</i> D^2 plot from experimental data; (D) dielectric <i>versus</i> D^2 plot from numerical modeling.	107
Figure 2.27 (A) confocal Raman image; (B) G band and RBM band features.	108
Figure 3.1 Individual nanotubes dispersed on Si substrate <i>via</i> sonication in 1,2-dichloroethane.....	113
Figure 3.2 (a) AFM image of a HiPCO nanotube thin film; (b) SEM image of a HiPCO nanotube thin film.	114
Figure 3.3 AFM images and profiles of the edges of (A) HiPco nanotube film and (B) CoMoCAT nanotube film.	115

Figure 3.4 AFM images of dispersed individual nanotubes on Si (A, B) before microwave irradiation, and (C, D) after microwave irradiation.	117
Figure 3.5 Photographs of glass substrates with nanotube thin films (a) before and (b) after microwave irradiation.	118
Figure 3.6 THz transmission spectra of a HiPco nanotube thin film sample before and after various irradiation time periods.	120
Figure 3.7 Raman spectra of a HiPco nanotube thin film, deposited on a glass substrate, before (solid curves) and after (dashed curves) microwave irradiations. (a) RBM band spectra, 514 nm laser excitation; (b) G and D bands spectra, 514 nm laser excitation; (c) RBM band spectra, 532 nm laser excitation; (d) G and D bands spectra, 532 nm laser excitation.	122
Figure 3.8 Raman spectra of a CoMoCAT nanotube thin film, deposited on a glass substrate, before (solid curves) and after (dashed curves) microwave irradiations. (a) RBM band spectra, 514 nm laser excitation; (b) G and D bands spectra, 514 nm laser excitation; (c) RBM band spectra, 532 nm laser excitation; (d) G and D bands spectra, 532 nm laser excitation.	124
Figure 3.9 Absorption spectra for a HiPco nanotube thin film on a glass substrate before and after multiple irradiations.	127
Figure 3.10 Absorption spectra for a CoMoCAT nanotube thin film on a glass substrate before and after multiple irradiations. T.	128
Figure 3.11. Schematic drawing of induced defects on a metallic nanotube in the microwave irradiation.	129

Figure 4.1 Molecular structures of (A) TOFA/DETA imidazolium and (B) C ₁₆ coco quaternary ammonium salts.	135
Figure 4.2 Critical micelle concentration (CMC) of corrosion inhibitor K1 TOFA imidazolium, 8 mM, determined by drop weight surface tension measurements.	135
Figure 4.3 (a) The diameter of the “head” of the tip was determined to be ~30 nm. (b) Schematic drawing of AFM analysis with the tip fully immersed inside inhibitor solution.	137
Figure 4.4 Set-up of AFM system in an anaerobic environment. By pre-purging N ₂ or CO ₂ into this box, O ₂ is eliminated.	138
Figure 4.5 Schematic diagrams of (a) penetration force measurements and (b) lateral removal force measurements.	139
Figure 4.6 AFM image of blank mica substrate in deionized water. Mica provides an atomically flat surface with a roughness of 0.1 nm.	140
Figure 4.7 AFM images and corresponding profiles of inhibitor K1 at (a) 0.5 CMC and (b) 2 CMC on mica.	141
Figure 4.8. AFM image of 2 CMC inhibitor K1 on mica. Two types of artifacts, Periodic curves and horizontal lines, are shown in this image.....	143
Figure 4.9. AFM images of inhibitor K1 on mica. Massive artifacts, including periodic curves, horizontal lines and random structures, were shown in images..	144
Figure 4.10. AFM images of inhibitor K1 at (a) 0.5 CMC and (b) 2 CMC on mica.....	145
Figure 4.11 AFM images and corresponding profiles of inhibitor K2 coco quaternary alkyl ammonium salt (quat) at (a) 0.5 CMC and (b) 2 CMC on mica.	146

Figure 4.12 AFM images on mica surface in the presence of 24% sodium thiosulfate solution.....	147
Figure 4.13 AFM images and corresponding profiles of inhibitor K4, a mixture of 20% TOFA imidazolium and 4% sodium thiosulfate at 0.5 CMC (a) and 2 CMC (b) on mica.	149
Figure 4.14 AFM images and corresponding profiles of inhibitor K5, a mixture of 20% coco quaternary amine salts (Quats) and 4% sodium thiosulfate at 0.5 CMC (a) and 2 CMC (b) on mica.	150
Figure 4.15 Inhibitor films formed at $2 \times$ CMC and scratched using different normal forces applied to the cantilever.	152
Figure 4.16 Film thickness measurement of TOFA imidazolium inhibitor K1 after scratching away an area ($\sim 1 \times 1 \mu\text{m}$) of the inhibitor film with a normal load of 60 nN applied to the cantilever, (a) film formed at 0.5 CMC and (b) at 2 CMC.	153
Figure 4.17 Schematic drawings of the monolayer and the bi-layer structures for inhibitor K1 TOFA imidazolium at 0.5 CMC (a) and 2 CMC (b).....	153
Figure 4.18 Film thickness measurement of TOFA imidazolium inhibitor K1 at (a) 0.5 CMC and (b) 2 CMC, using Picoscan AFM and DP-19 probes.....	154
Figure 4.19 Film thickness measurement of $C_{12} \sim C_{16}$ coco quaternary alkylammonium (inhibitor K2) after scratching away an area ($\sim 1 \times 1 \mu\text{m}$) of the inhibitor film with a normal load of 60 nN applied to the cantilever tip, (a) film formed at $0.5 \times$ CMC and (b) at $2 \times$ CMC.....	156

Figure 4.20 Schematic drawings of the monolayer and the hemi-micelle structures for inhibitor K2 ~ C ₁₆ coco quaternary alkylammonium at (a) 0.5 CMC and (b) 2 CMC...	156
Figure 4.21 Film thickness measurement of corrosion inhibitor K4 and K5 after scratching away an area (~1 x 1 μm) of the inhibitor film with a normal load of 60 nN applied to the cantilever, (a) film formed by inhibitor K4 and (b) film formed by inhibitor K5.....	158
Figure 4.22 Summary of the film thickness for different inhibitors at 0.5 CMC and 2 CMC conditions.....	159
Figure 4.23 Force curve on blank mica on deionized water, used as the blank curve...	160
Figure 4.24 Force distance curves for inhibitor films on mica and a bare mica surface.	162
Figure 4.25 Force distance curves for 0.5 CMC and 2 CMC inhibitor films on mica and a bare mica surface. Results obtained from Picoscan 2000 AFM using DP-19 probes. ...	163
Figure 4.26 Force distance curves for inhibitor films on mica and a bare mica surface.	164
Figure 4.27 Force distance curves on mica in the presence of 24% K3 solution. The curve is the same as the curve on bare mica in water.	165
Figure 4.28 Force distance curves on mica in the presence of K1, 2 CMC (dotted line) and K4, 2 CMC (solid line), respectively.	166
Figure 4.29 Force distance curves on mica in the presence of K2, 2 CMC (dotted line) and K5, 2 CMC (solid line), respectively.	167
Figure 4.30 Lateral force curves performed under a normal load of 60 nN.	171

Figure 4.31 Lateral force curves performed under a normal load of 60 nN, solid lines, TOFA imidazolium at 2 CMC and dotted lines in pure water.....	172
Figure 4.32 Measured lateral removal forces for different corrosion inhibitors.....	173
Figure 4.33 AFM images on mica surface in the presence of inhibitor K1 (2 CMC) solution with (a) 3 wt.%, (b) 5 wt.%, (c) 10 wt.% NaCl, respectively, and corresponding film thickness measurements at (d) 3 wt.%, (e) 5 wt.%, (f) 10 wt.% NaCl conditions, respectively.	174
Figure 4.34 (a) Penetration force measurements for inhibitor K1 (2 CMC) at different NaCl concentrations; (b) Lateral force measurements for inhibitor K1 (2 CMC) at different NaCl concentrations.	176
Figure 4.35 (a.) Film thickness measurement for inhibitor K1 at pH 2; (b.) Film thickness measurement for inhibitor K1 at pH 5; (c.) Film thickness measurement for inhibitor K1 at pH 8.....	177
Figure 4.36 (a) Penetration forces for inhibitor K1 at different pH values; (b) Lateral forces for inhibitor K1 at different pH values.....	178
Figure 4.37 (a) Surface morphology of inhibitor K1 in water-ethanol mixture; (b) film thickness measurement for inhibitor K1 in water-ethanol mixture; (c) penetration force for inhibitor K1 in water-ethanol mixture.....	179
Figure 4.38 (a) Multiple force curves on the same position showing the penetration process did not destroy the inhibitor film; (b) inhibitor molecules were removed away under different scan rates of the tip.....	180
Figure 4.39 The re-adsorption of inhibitor molecules <i>versus</i> time.	182

Figure 4.40 (a) Surface morphology of blank Au in DI water and (b) Au in the presence of 2 CMC inhibitor K1 solution.....	184
Figure 4.41 Penetration force measurement on blank Au in deionized water (blank) and on Au in the presence of 2 CMC inhibitor K1.....	185
Figure 4.42 AFM image of Au surface with the center area where inhibitor molecules were removed and the surface profile across the image.	187
Figure 4.43 Lateral force curves measured on blank Au in DI water (black curve) and on Au in the presence of 2 CMC inhibitor K1 (red curve).	187
Figure 4.44 (a) The surface morphology and surface profile of blank Fe in DI water and (b) Fe in the presence of 2 CMC inhibitor K1, both in N ₂ saturated environment.	189
Figure 4.45 Force curve of blank Fe in deionized water and Fe in the presence of inhibitor K1, 2 CMC. A 0.2 nN penetration force was measured from the inhibitor film.	190
Figure 4.46 AFM images with the center area where inhibitor molecules were removed and the surface profile across the image.	191
Figure 4.47 Lateral force curves measured on blank Fe in deionized water (black curve) and on Fe in the presence of 2 CMC inhibitor K1 (red curve).	192
Figure 4.48 (a) surface morphology, (b) film thickness, (c) penetration force, and (d) lateral removal force on Fe in the presence of 2 CMC inhibitor K4 solution.	194
Figure 4.49 AFM images of polished X65 steel surface, (a) 3 × 3 μm area and (b) 1 × 1 μm area, in deionized water, in N ₂ saturated environment. The surface roughness after polishing was less than 15 nm.	195

Figure 4.50 AFM images of X65 steel in the presence of 0.5 CMC (a) and 2 CMC (b) inhibitor K1 solutions in N ₂ saturated condition.....	196
Figure 4.51 AFM images of X65 steel surface with the center area where inhibitor K1 molecules were removed and the surface profile across the image. The depth in the scratched area is ~2 nm for 0.5 CMC condition (a) and ~4nm for 2 CMC (b).	197
Figure 4.52 Force distance curves for inhibitor films on X65 surface in the presence and absence of inhibitor films.....	198
Figure 4.53 Lateral removal force measured on X65 steel in the presence of 0.5 CMC (a) and 2 CMC (b) inhibitor K1 solutions.	199

LIST OF ABBREVIATIONS

SPM	Scanning probe microscopy
STM	Scanning tunneling microscopy
AFM	Atomic force microscopy
APD	Avalanche photodiode
CCD	Charge coupled detector
CMC	Critical micelle concentration
CoMoCAT	Co-Mo catalyst formulation
CTAB	Cetyl tetradecyltrimethylammonium bromide
CVD	Chemical vapor deposition
D^2	Square of diameter
DEP	Dielectrophoresis
DGU	Density gradient ultracentrifugation
DI water	Deionized water
DOS	Density of states
EFM	Electrostatic force microscopy
FET	Field effect transistor
HiPco	High pressure CO disproportionate
IEX	Ion-exchange chromatography
k_n	Normal spring constant

M/S	Metallic-to-semiconducting ratio
MWNT	Multi-walled carbon nanotube
Quats	Quaternary ammonium salts
RBM	Radial breathing mode
SDS	Sodium dodecylsulfate
SWNT	Single-walled carbon nanotube
TDS	Time Domain Spectroscopy
THz	Terahertz
TOFA/DETA	Tall oil fatty acid/ diethylenetriamine
VHS	Van Hove singularities

Chapter 1. Introduction

1.1 Atomic force microscopy

1.1.1 History

Scanning probe microscopy (SPM) is an advanced technique that uses a physical probe to scan the surface of a specimen. Images and curves are measured by recording the interaction between the scanning probe and the surface, as a function of position. The foundation of SPM was the invention of Scanning Tunneling Microscopy (STM) by Binnig and Rohrer at IBM¹⁻³. STM was the first microscopic method to generate real-space images at atomic-level resolution. In STM analysis, a conducting probe applied with a bias is brought within ~10 nm of the conductive surface, resulting in a tunneling current occurring between the tip and the sample surface. By recording the tunneling current which is related to the tip-to-sample distance, surface morphology and electronic structure of the sample are revealed⁴⁻⁶. However, the use of STM requires conductive probes and samples, and thus this technique has limitations on insulating materials.

In 1986, Atomic force microscopy (AFM) was developed by Binnig, Gerber and Quate, and expanded the SPM technique to non-conductive surfaces⁷⁻⁹. AFM probes themselves, however, are not necessarily conductive. AFM can measure three-dimensional topography and does not require particular specimen treatment¹⁰⁻¹⁴. The first commercial AFM was available from Park Scientific, and more than 10 major AFM manufacturers are now established worldwide. Figure 1 shows available AFM equipment from two leading manufacturers. Both instruments were used in this research.

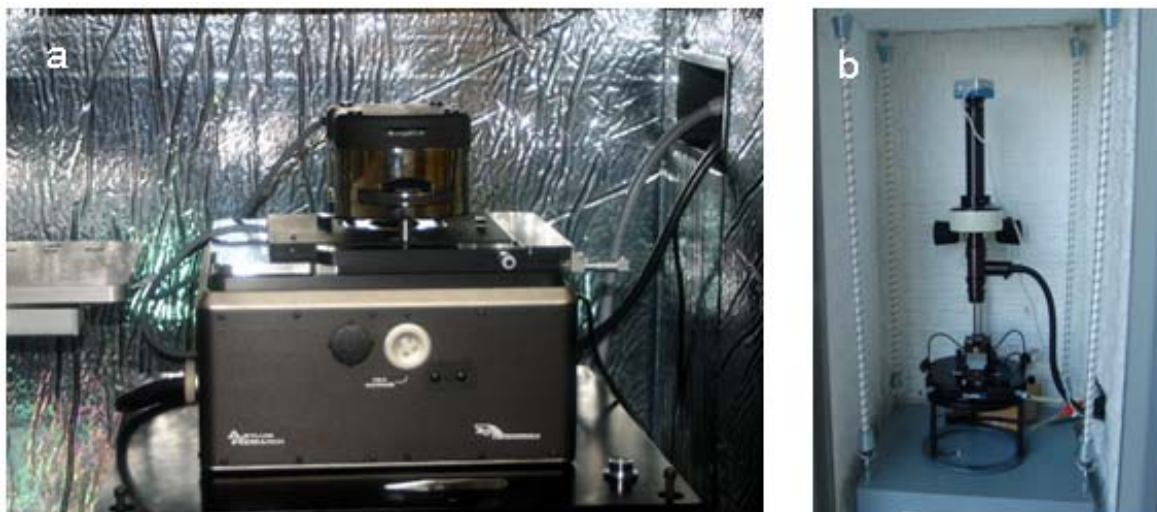


Figure 1.1 Photographs of (a) Asylum research MFP 3D AFM and (b) Pico scan 2000 AFM.

Another advantage of AFM, over the STM, is that it does not require a vacuum environment. It can operate in both gas and liquid environments. To serve various research purposes, AFM provides different scanning modes and can measure multiple types of interactions, such as van der Waals forces, electrostatic forces, magnetic forces, capillary forces, chemical bonding¹⁵⁻¹⁹. AFM is not only a technique for imaging surface morphology and structures at the nanometer scale, but also provides precise force measurements and material manipulation at designated conditions²⁰⁻²². After 20 years of development, AFM has become a powerful tool for exploration of the “nano world”.

1.1.2 Basic Principles of AFM

Even though the instruments have different designs, an AFM system usually contains similar components: an AFM probe, an optical lever, a piezoelectric scanner, a feedback loop, and a conversion system (Figure 1.2)

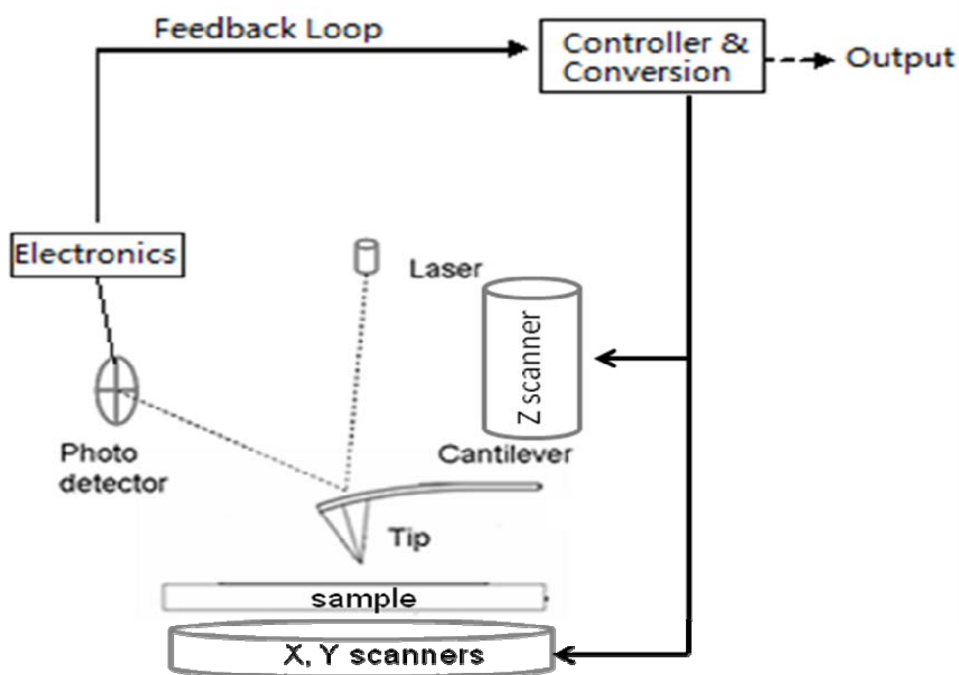


Figure 1.2 Basic principles of AFM.

In a typical AFM scan, an AFM probe, which consists of a sharp tip mounted on the cantilever, is first assembled within the system. A laser beam is adjusted to focus onto the back of the cantilever and reflected onto a photodiode detector. In order to image the surface morphology, the tip must be brought within 5 nm of the surface, either manually or remotely. At this point, the tip scans over a selected area, in a range from 100 nm by 100 nm to 100 μm by 100 μm , based on the scanning protocols. As the laser beam is

focusing on the cantilever during the scanning, any cantilever deflection created by the tip-sample interaction can instantaneously induce the reflection change of the laser beam in the photodiode. This deflection or reflection is the raw signal for AFM images. However, in most AFM systems, the cantilever deflection is at a constant value in the scanning, and thus the AFM probe is correspondingly moving up and down in the z-direction to keep the tip-sample interaction constant. The voltage created to move the AFM tip up and down in the z-direction is recorded as information for topography. Finally, a three-dimensional image is produced through the feedback loop and conversion system, and displayed on a monitor²⁰.

As AFM measures the interaction between the tip and the sample surface, the resolution of the image is defined by the size and symmetry of the tip, the spring constant of the cantilever, the sample preparation, and the scanning conditions. Artifacts may be created due to a variety of conditions, including a worn tip, a rough sample surface, scanning at a high velocity, and outside noise²¹⁻²³. Therefore, obtaining a perfect AFM image requires the understanding of the AFM principle, the selection of suitable tips, and samples as well as the setting of appropriate scanning parameters.

In order to measure interactions for various analysis purposes, AFM has been developed to work in different modes. Most AFM instruments include three basic scanning modes: contact mode⁹, non-contact mode²⁴, and tapping mode²⁵. Based on these basic modes, more advanced modes have also been established such as chemical force microscopy^{17,26}, electrostatic force microscopy²⁷, conductive AFM²⁸, magnetic force microscopy²⁹⁻³⁰, Kelvin probe force microscopy³¹ and lateral force microscopy³².

1.1.3 AFM image modes

1.1.3.1 Contact mode

The earliest mode created is the contact mode⁹. In this mode, the tip is physically in contact with the sample surface, and the overall interaction between the tip and the surface is repulsive. Contact mode is also referred as static mode because the surface morphology is measured directly from the deflection of the cantilever. This mode is the basic mode for every AFM, and it can work in vacuum, air and liquid environments and further serve as a basis for other advanced modes.

1.1.3.2 Non-contact mode

In contact mode, due to the direct contact, the scanning tip may alter the sample position or even change the sample morphology. In order to conquer problems associated with this configuration, a non-contact image mode was developed³³⁻³⁴. In this technique, the tip is usually 5 to 15 nm above the sample surface, avoiding direct contact. At this distance, the attractive van der Waals interaction is acting between the tip and the surface. This attractive force is usually much weaker than the repulsive force in the contact mode. Therefore, an oscillation must be applied to the tip, and the AC detection method can help to measure the small attractive force by measuring the change in amplitude, phase, or frequency of the oscillating cantilever.

1.1.3.3 Tapping mode

In tapping mode, an oscillation is applied to the cantilever near its resonant frequency using a piezoelectric crystal. During the scanning, the cantilever oscillates in a pre-set amplitude, and the sharp tip correspondingly “taps” on the surface²⁵. The oscillating tip is moving towards the surface until it slightly or softly touches the surface itself. Interaction, such as van der Waals forces, dipole-dipole interactions and electrostatic forces, can decrease the amplitude of tip oscillation. However, in most AFM instrumentation, the amplitude of the tip oscillation is set to a constant value by adjusting the height of the tip using the z scanner. Therefore, the voltage change for adjusting the tip during the scanning is used as the signal for producing a tapping mode image. The major difference between tapping mode and non-contact mode is the amplitude in the tapping mode is much higher than that in the non-contact mode (Figure 1.3).

Usually tapping mode can provide higher resolution images than contact and non-contact modes. This is because the tapping avoids dragging the tip across the surface, which could happen in the other two modes³⁵. The gentle tapping also helps to image soft materials, such as DNA and lipids, as the tapping avoids continuous contact between the probe tip and the sample features.

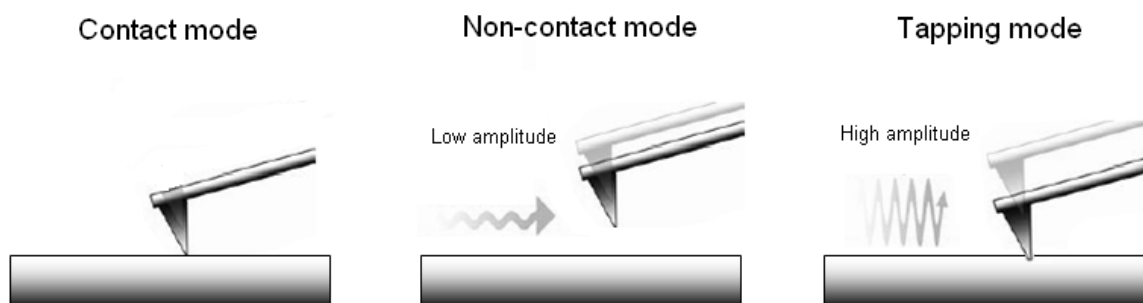


Figure 1.3 Schematic drawings of contact mode, non-contact mode and tapping mode.

Based on the three basic modes, advanced imaging modes have been developed to measure electrostatic forces, forces between specific molecules, magnetic forces, etc. In these advanced modes, AFM is usually called as electrostatic force microscopy (EFM)¹⁷, chemical force microscopy (CFM)²⁶ and magnetic force microscopy (MFM)³⁰.

1.1.3.4 Chemical force microscopy (CFM)

CFM is used to detect interactions between designated molecules, instead of between the AFM tip, usually Si or Si₃N₄, and the sample. If the interaction between molecule A and molecule B is interested, the sharp tip can be modified by molecule A or similar functional groups, while the substrate can be coated with molecule B or similar functional groups²⁶ (Figure 1.4a). Therefore, the specific interaction between A and B can be measured.

1.1.3.5 Electrostatic force microscopy (EFM)

EFM measures the electrostatic force between the charged tip and the surface. In this mode, a bias is applied on the scanning tip and the electrostatic force can be

measured based on the charge density on the sample surface¹⁷. Figure 1.4b shows the measurement between a biased tip and a sample surface in EFM. EFM usually applies to map charged domains and polarizations on the sample surface. However, if the charged scanning tip is within 5nm above the surface, the obtained image is a combination of topographic signal and electrostatic force signal. To separate electrostatic force from surface morphology, a double-pass mode was developed for EFM measurements³⁶. In a double-pass mode scanning, the first pass is a standard tapping mode scanning on a normal topographic line. On the second pass, the conductive tip is lifted a set amount of height and scan the same line with an applied bias. This double-pass scanning mode can help to avoid the interference from topography. This double-pass method has been also applied to magnetic force microscopy (MFM) and other advanced modes.

1.1.3.6 Magnetic force microscopy (MFM)

The mechanism of MFM is similar to EFM. Instead of applying a bias to the conductive tip, the tip in MFM is coated with a layer of magnetic film and scans a magnetic sample in the non-contact mode (Figure 1.4c). Different magnetic domains and their strengths can be detected during the scanning, based on measured magnetic forces³⁰.

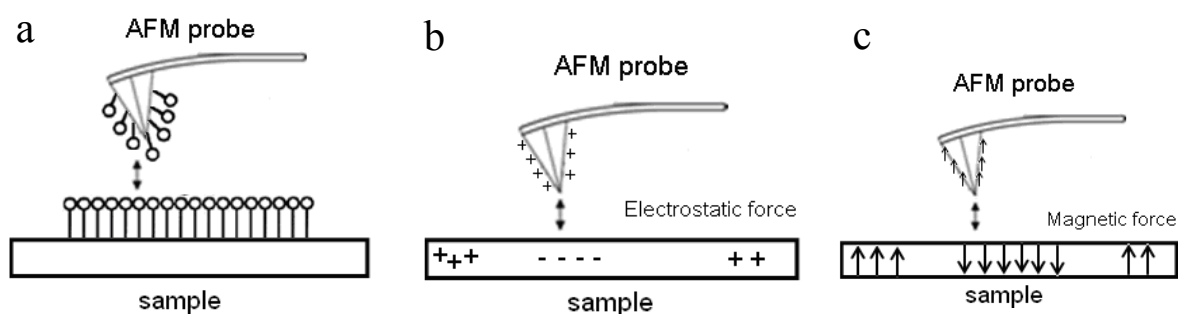


Figure 1.4 Schematic drawings of (a) a CFM setup containing a functionalized tip and surface; (b) an EFM setup containing a biased tip and a sample with different charge distributions; (c) a MFM setup containing a magnetic coated tip and a flat magnetic sample.

1.1.3.8 Nanolithography and manipulation

Normally AFM is used to image the surface without further changing or damaging its morphology. By applying excessive force on the cantilever or using specific tips, however, AFM can change the surface by “writing” down new features or moving a feature to a new position. This function is referred as nanolithography or nano-manipulation. Figure 1.5 shows a pattern generated by AFM nanolithography on a photoresist material³⁷.

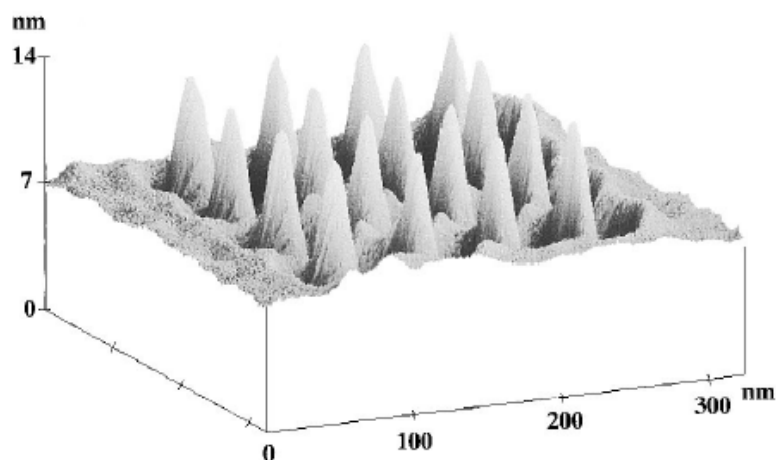


Figure 1.5 AFM image of a generated pattern by nanolithography. (Figure reproduced with permission from reference 37)

1.1.4 AFM probes

Hundred types of AFM probes are available for various samples and scanning conditions. But no matter how different they are, AFM probes are a combination of tips and cantilevers³⁸. For general imaging of surface topography, AFM probes are usually made of Si or Si₃N₄, which can work in contact, non-contact and tapping modes. By functionalizing the probes with extra layers/coatings, AFM can be sensitive for the designated interactions. For example, By coating a probe with a conductive Pt/Ti layer, the AFM instrument can measure electrostatic interactions³⁹.

1.1.4.1 Cantilevers

As discussed above, the cantilever deflects the interaction, which is sensed by the sharp tip, based on Hooker's law⁴⁰. Therefore, the cantilever material is crucial to the

sensitivity of the instrument. The spring constant of a cantilever defines the smallest force that can be measured by AFM. The selection of inappropriate cantilever may even cause the difficulty in imaging or damage on sample features. For example, biological samples, such as DNA and protein, can be damaged by hard AFM probes with large spring constants (>10 N/m). Soft AFM probes with small spring constants (<1 N/m) are used for biological samples and in aqueous environments²⁵.

Based on the number of cantilevers in a probe, AFM probes can be classified as 1-lever probes and multiple-probes. For a multiple-lever probe, it usually consists of cantilevers with different lengths and spring constants. The shape of a cantilever can also be rectangular (Figure 1.6a) or V-shaped (Figure 1.6b).

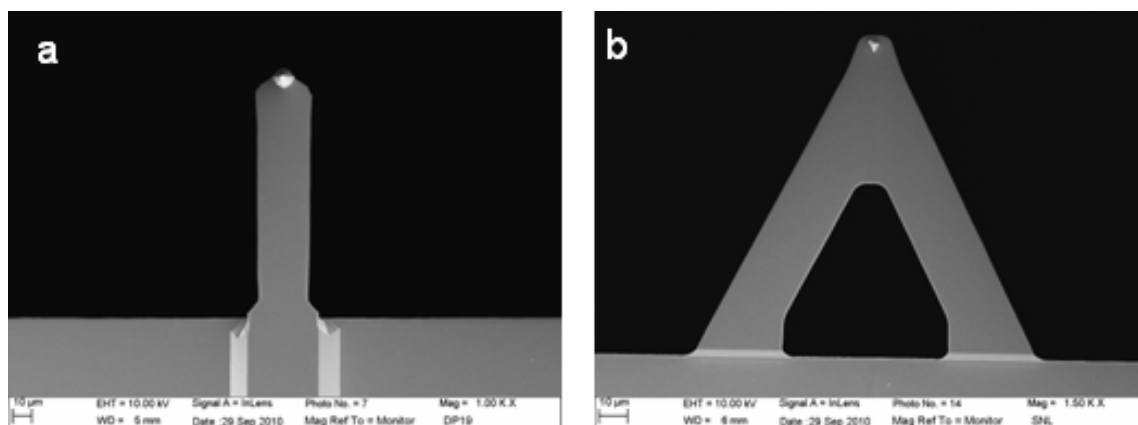


Figure 1.6 SEM images of AFM probes with (a) rectangular cantilever, (b) V-shaped cantilever.

1.1.4.2 Tips

The resolution of an AFM image is highly dependent on the size, shape and symmetry of the tip⁴¹⁻⁴². Small and sharp tips can provide higher resolution images than large and

blunt tips. Figure 1.7 shows a sharp tip with a diameter of $\sim 60\text{nm}$ on its “head” part. The diameter of the tip can change during the scanning because of the wear of the tip. Possible reasons for tip wear can be due to the scanning at a high velocity, excessive applied force, contamination, and long-term usage. The continuous use of a worn tip may cause enormous artifacts in an image, or generate “fake” images. For conductive tips and magnetic tips, their diameters are usually increased by the extra layers, and thus the resolution of images provided by these functionalized tips may not be as high as images provided tips for regular topographic scanning.

For nanolithography and nano-manipulation, a diamond tip may be applied to change the features of the sample as diamond is one of the hardest materials.

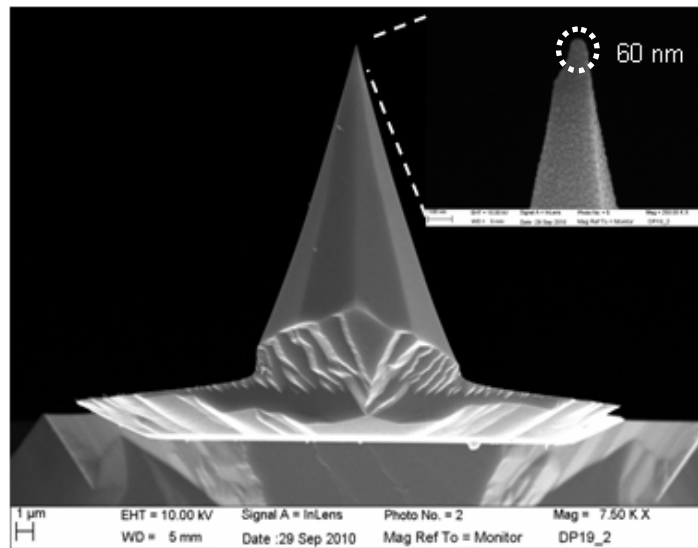


Figure 1.7 SEM image of a sharp tip with a diameter of $\sim 60\text{nm}$ on its “head” part.

1.2 Carbon nanotubes

1.2.1 History

Carbon nanotubes were first synthesized by Sumio Iijima in 1991⁴³. Since their discovery, carbon nanotubes have attracted continuous academic and industrial interest because of their unique structures and special properties⁴⁴⁻⁴⁹. The one-dimensional structure and sp^2 C-C bonding confer nanotubes useful properties of high strength, high thermal conductivity and metallic or semiconducting properties. All these physicochemical properties make carbon nanotubes good candidates for applications, such as electronic devices⁵⁰⁻⁵¹, drug delivery⁵²⁻⁵⁴, energy storage⁵⁵⁻⁵⁶, etc.

1.2.2 Structure and synthesis of nanotubes

Based on the number of sidewalls, nanotubes are categorized as multi-walled carbon nanotubes (MWNTs) and single-walled carbon nanotubes (SWNTs). In this dissertation, we only focus on SWNTs and all nanotubes refer to single-walled carbon nanotubes. An individual nanotube has a small diameter of about 1~2 nm, but a length on the micrometer scale⁵⁷⁻⁵⁸. It can be conceptualized by rolling of a graphene sheet into a cylindrical tube. The diameter and chirality of a nanotube are characterized by chiral vector $C_h = na_1 + ma_2 \equiv (n, m)$, where a_1 and a_2 are unit vectors and n and m are integers⁵⁹. (Figure 1.8, generated from Nanotube Modeler © JCrystalSoft). Based on different chiral vectors, the nanotubes can be refer to as ‘zigzag’ if $m = 0$, or ‘armchair’ if $n = m$. All other nanotubes are of the ‘chiral’ types. Figure 1.9 shows the structures of (10, 0), (9, 9), (8, 5) nanotubes. The electronic type of nanotubes is dependent on the chiral vectors (n ,

m). When $(n - m) = 3q$, where the q is an integer, nanotubes are metallic, otherwise they are semiconducting⁵⁷. An as-synthesized nanotube sample is always a mixture of many species, thus containing both metallic and semiconducting types.

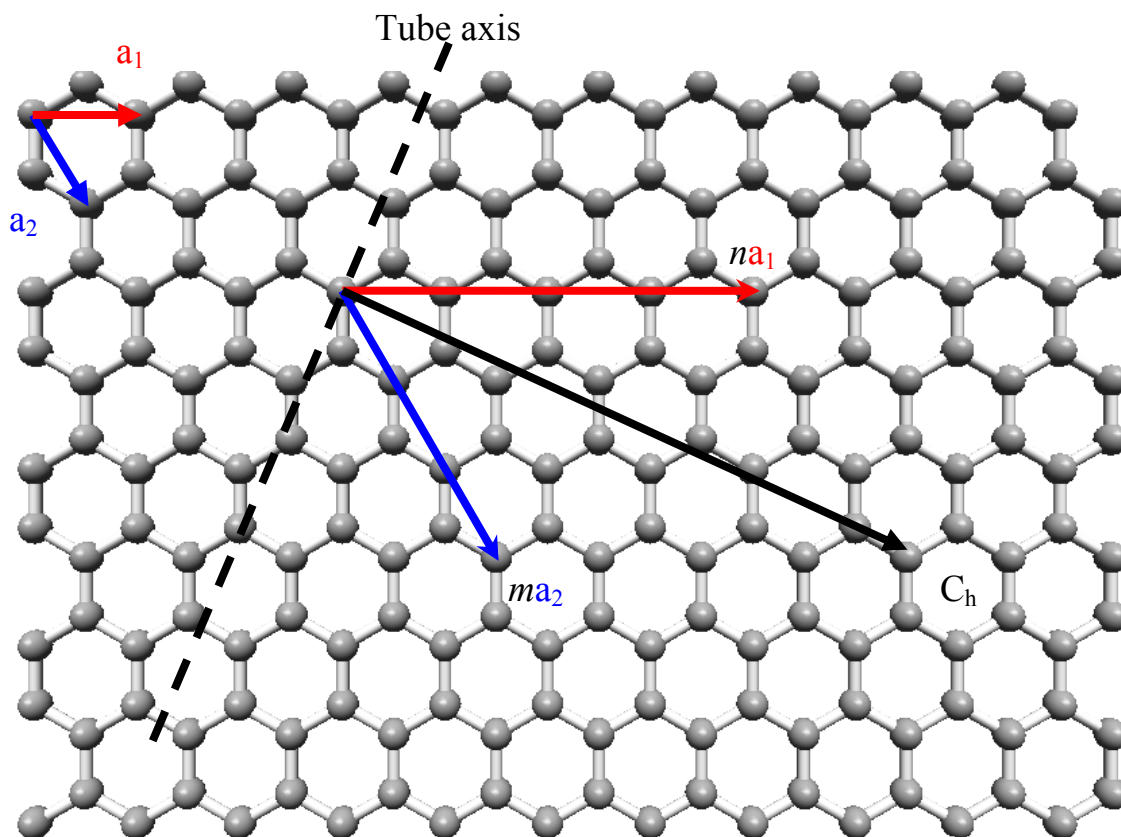


Figure 1.8 Schematic of a graphene sheet. A nanotube can be constructed by rolling of a graphene sheet. The diameter and chirality are characterized by chiral vector $C_h = na_1 + ma_2 \equiv (n, m)$, where a_1 and a_2 are unit vectors and n and m are integers.

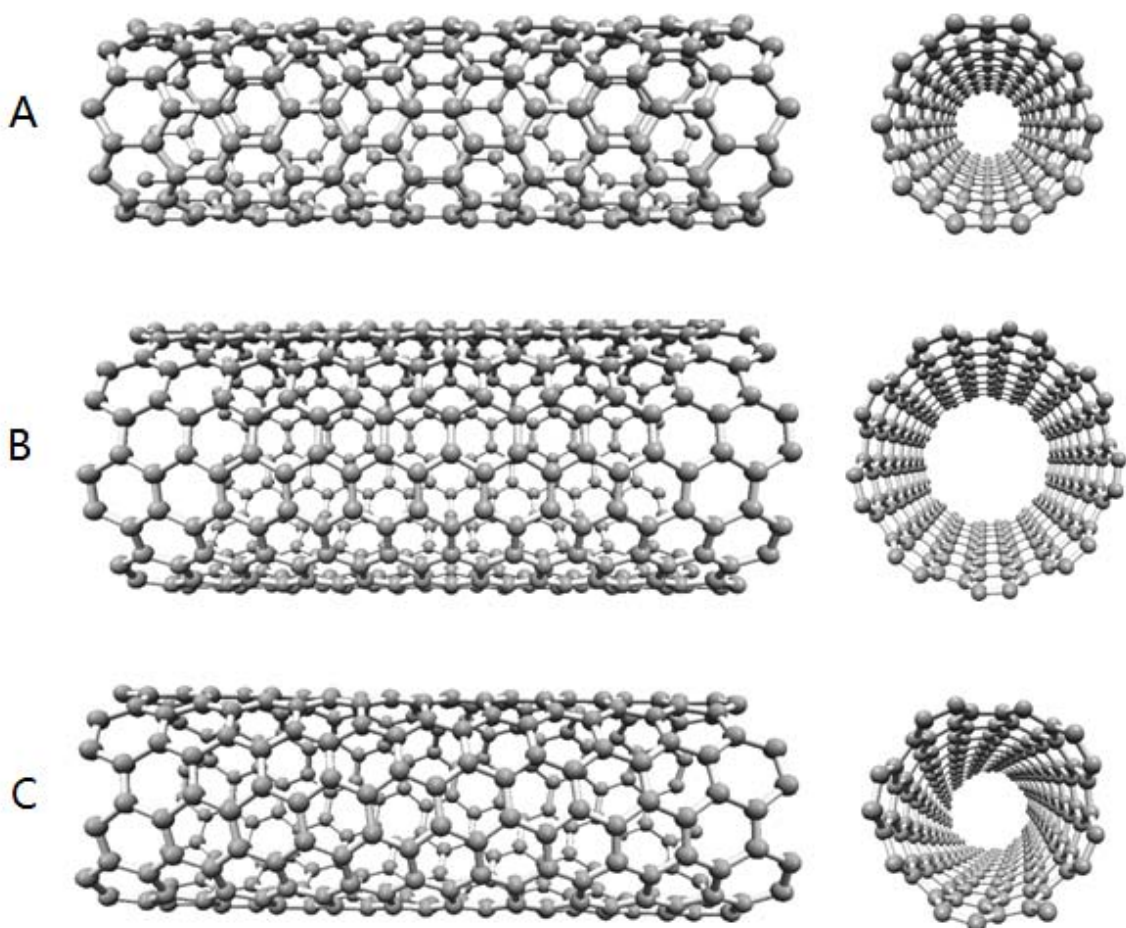


Figure 1.9 schematic of (A) a zigzag (10, 0) nanotube; (B) an armchair (9, 9) nanotube; (C) a chiral (8, 5) nanotube.

Multiple techniques have been developed to synthesize nanotubes over the past two decades including arc discharge, laser ablation and chemical vapor deposition (CVD)^{57,60-62}. In the arc discharge method, nanotubes are synthesized between two graphite electrodes where an arc is generated in a helium atmosphere. The yield for this method is up to 30%, producing both multi-walled nanotubes and single-walled nanotubes⁶².

In the laser ablation process, graphite is vaporized by a pulsed laser in a 1200°C reactor in flowing argon. The vaporized carbon source then condenses on the cooler side of the reactor and carbon nanotubes are produced. One benefit of this method is the high yield of ~70%, but it is very expensive to create the high temperature⁶².

In chemical vapor deposition (CVD), nanotubes are synthesized from gaseous carbon onto the substrate with catalyst particles. The catalyst particles behave as “seed” for nanotube growth and nanotubes are directly produced on the substrate at several hundred degrees⁶⁰. Large scale production of nanotubes can be achieved in industry *via* the CVD method, and the selection of gaseous carbon source and catalyst particles can help to control the diameter and chirality of synthesized nanotubes. For example, in the high pressure CO disproportionate (HIPco) process, a continuous CO flow is used as the carbon source and Fe(CO)₅ is used as the catalyst precursor⁶³⁻⁶⁴. The diameter or chirality distribution of produced nanotubes can be adjusted by varying the partial pressure of CO⁶³. In the CoMoCAT process, a unique Co-Mo catalyst formulation is selected with the CO source. The Co-Mo catalyst can help to inhibit the formation of undesirable forms of carbon, and selectively synthesize nanotubes with a certain diameter range by controlling the temperature⁶⁵. Nanotubes produced from these two CVD methods are usually called HIPco nanotubes and CoMoCAT nanotubes. The HIPco and CoMoCAT processes provide high quality nanotubes and do not change the structure and property of nanotubes.

However, multiple synthesis methods have been developed during the past twenty years to control the diameter and properties of the nanotube samples, but the synthesized nanotube samples are still a mixture of metallic and semiconducting types.

1.2.3 Electrical properties of nanotubes

As discussed above, nanotube types can be expressed by chiral vectors (n, m) . Nanotubes are metallic when $n-m$ can be evenly divided by 3. Otherwise, they exhibit semiconducting properties. All nanotubes species have different (n, m) chiral vectors and unique electronic structures⁶⁶.

Figure 1.10 shows the density of states (DOS) diagrams of a metallic nanotube and a semiconducting nanotube. A nanotube is metallic when the DOS is continuous between the first pair of van Hove singularities (VHS), or the DOS is non-zero at Fermi-level, while a semiconducting nanotube has a clear gap between the first pair of van Hove singularities^{57,67}. This gap is called band gap. Electronic transitions from valence bands to corresponding conducting bands are called E_{ii} transitions ($i = 1, 2, 3, 4\dots$). For example, the E_{11} transition corresponds to the electron transition from the first valence band V1 to the first conduction band C1. M_{ii} and S_{ii} are used to express the E_{ii} transitions in metallic nanotubes and semiconducting nanotubes, respectively⁶⁸⁻⁶⁹. The band gap between each pair of van Hove singularities is inversely proportional to the diameter of the nanotube, and thus nanotubes in larger diameters have smaller band gaps⁷⁰.

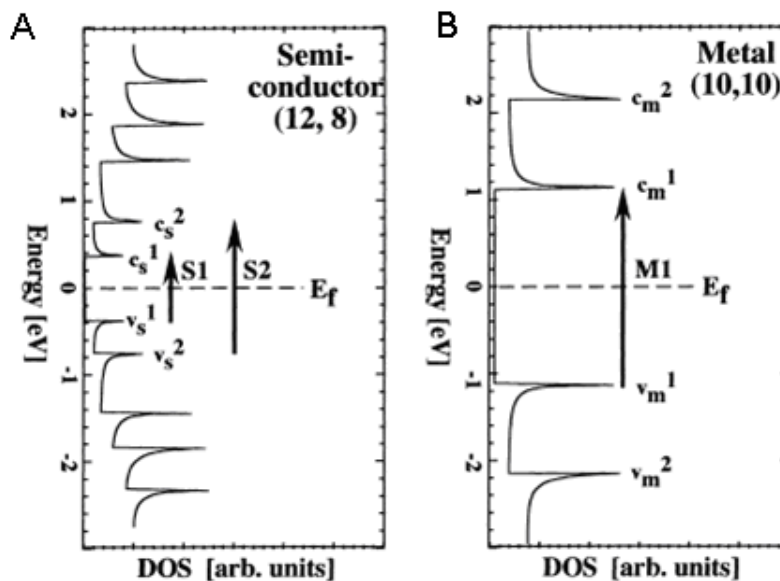


Figure 1.10 Schematic drawings of electronic structures of (A) a semiconducting (12, 8) nanotube and (B) a metallic (10, 10) nanotube. (Figure reproduced with permission from reference 68).

1.2.4 Dispersion and separation of nanotubes

Although nanotubes have many potential applications due to their unique properties, their insolubility and heterogeneity have hindered their development. As-synthesized nanotubes are agglomerated bundles of various species due to the strong van der Waals interactions and inherent hydrophobicity (Figure 1.11)⁴⁵. Therefore, the first step prior to nanotube analysis and application is usually the dispersion of individual nanotubes in solution. To overcome the strong inter-tube interactions, covalent functionalization⁷¹⁻⁷⁵ or non-covalent dispersion methods have been developed⁷⁵⁻⁷⁸. Covalent functionalization to modify the sidewall structure of nanotubes can be performed *via* various chemical reactions, such as nitrene addition, arylation, alkylation, fluorination^{73,79}, etc. Nanotubes become soluble because the original sp^2 hybridization is

changed to sp^3 in the functionalization and the π -conjugation system becomes disrupted (Figure 1.12A). However, the structure and properties of nanotubes are also changed in this process. Noncovalent methods have become more appealing as the properties and structures of nanotubes are preserved after dispersion⁷⁹. Multiple noncovalent methods have been published such as DNA-assisted dispersion⁷⁸, surfactant assisted dispersion⁷⁰, polymer assisted dispersion⁸⁰ and organic solvent dispersion⁸¹. With the help of assisting molecules, nanotube bundles can be dispersed to individual ones in solution without changing any of their inherent properties (Figure 1.12B).

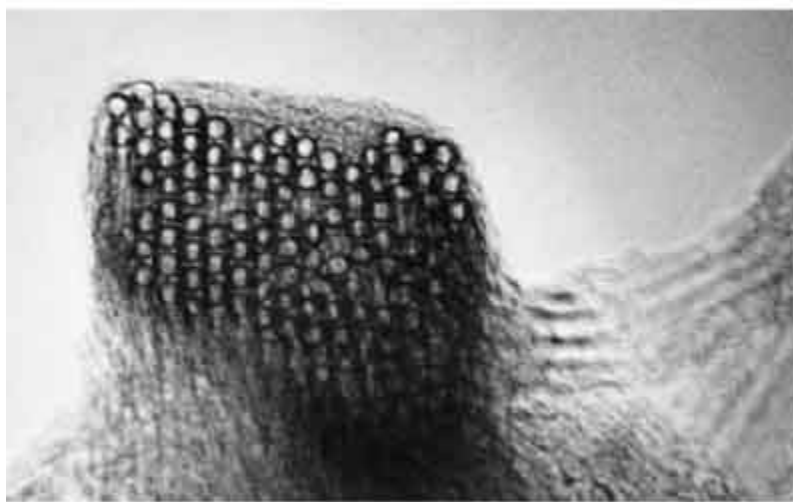


Figure 1.11 TEM image of nanotube bundle consisting of approximately 100 nanotubes. (Figure reproduced with permission from reference 45).

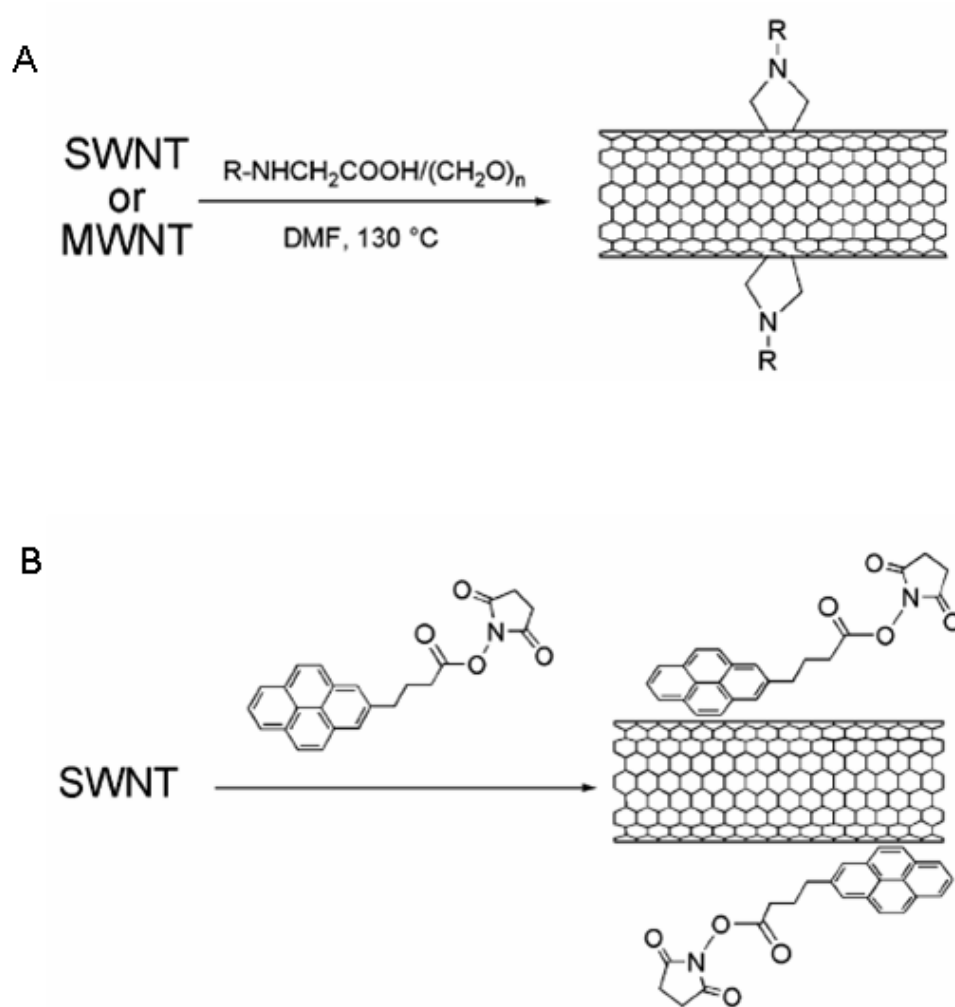


Figure 1.12 Schematics of (A) a covalent functionalization of nanotubes and (B) a noncovalent functionalization of nanotubes. (Figure reproduced with permission from reference 79).

Even if the bundled nanotubes can be dispersed to individual tubes, the nanotube sample is still a mixture of a variety of species, including metallic and semiconducting types. Applications in electronic devices and biomedicine usually require high purity of the materials. Therefore, the separation of nanotubes based on their diameter, chirality and electronic structure has become an important topic in nanotube research. Strano and

co-workers designed a selective chemical reaction to eliminating metallic nanotube contents using diazonium reagents⁸². The diazonium reagents can react with metallic nanotubes and form covalent bonds on the sidewalls of the nanotubes (Figure 1.13). However, this chemical reaction can only react with metallic nanotubes faster than semiconducting ones, but cannot eliminate all the metallic content.

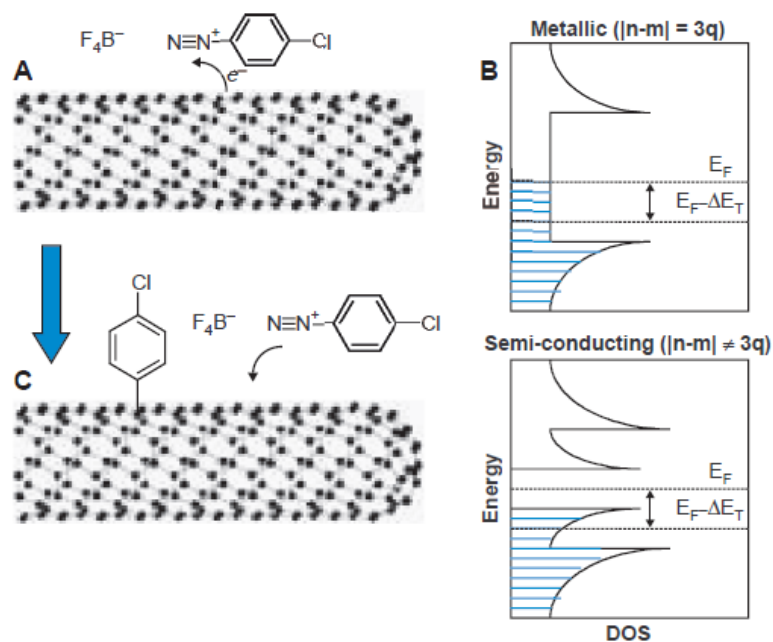


Figure 1.13 Schematics of selective chemical reaction of nanotubes. The diazonium reagents selectively reacted with metallic nanotubes, leaving semiconducting nanotubes unreacted. (Figure reproduced with permission from reference 82).

Other methods are based on the physical properties of nanotubes. Krupke, *et al.*, fabricated a dielectrophoresis (DEP) device that took advantage of differences in dielectric properties of metallic and semiconducting nanotubes⁸³. Once the nanotube

suspension was dropped onto this device and a 10V AC voltage was applied, metallic nanotubes were attracted toward a microelectrode array, leaving a semiconducting suspension in the solvent (Figure 1.14). One drawback of this ac-dielectrophoresis method is that the amount of separated nanotubes is only about 100pg metallic nanotubes per recovery.

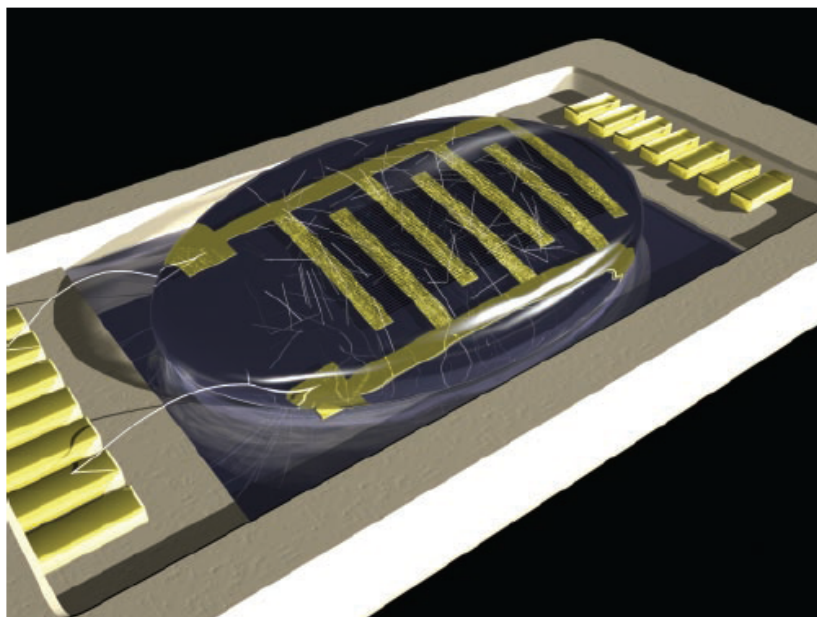


Figure 1.14 Microelectrode device for ac-dielectrophoresis (DEP). With an applied voltage, metallic nanotubes are attracted toward a microelectrode array, leaving semiconducting nanotubes in the solvent. (Figure reproduced with permission from reference 83).

To achieve the dispersion and separation of nanotube, Zheng and co-workers designed DNA-coated nanotubes which helps to disperse individual nanotubes⁷⁸. Further investigation of DNA-nanotubes has found that the DNA coating on the nanotube surface

can also assist the separation of nanotubes by ion-exchange chromatography (IEX)⁸⁴⁻⁸⁶. In a typical IEX experiment, a nanotubes suspension was injected into a column in which the resin was functionalized with quarterized polyethyleneimine and then eluted with a linear salt gradient. DNA coated nanotubes which weakly interacted with the resin flowed out of the column earlier and nanotubes can be separated based on their type. Figure 1.15 shows the absorption spectra of separated fractions in ion-exchange chromatography with enrichments of different nanotube species.

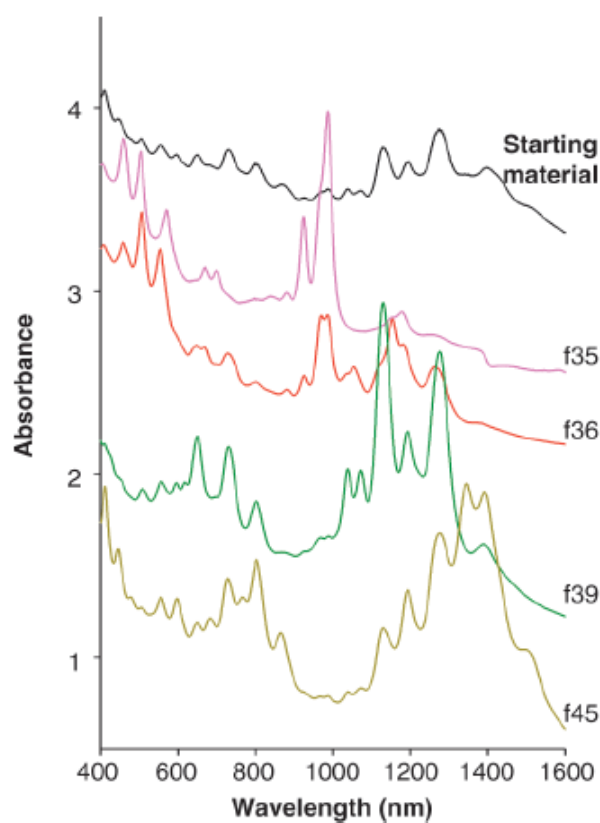


Figure 1.15 Absorption spectra of separated fractions in ion-exchange chromatography (IEX). Each fraction showed enrichment of different species of nanotubes. (Figure reproduced with permission from reference 78).

Hersam group developed the separation of surfactant-nanotubes by using density gradient ultracentrifugation(DGU)⁸⁷. Density gradients were formed from a non-ionic density gradient medium, and centrifugation was carried out at 40,000~60,000 rpm for 9~24 hours. Due to the different densities of surfactant-nanotubes, the nanotube suspension in the centrifuge tube forms several colored bands with different contents. For example, the pink colored band in Figure 1.16 only contains metallic nanotubes as only one peak in the M11 region, while the bottom contents are still mixtures. By varying the surfactants, which means the control of the density of surfactant-nanotubes, nanotubes become separated by diameter, band gap or electronic structure, using this technique.

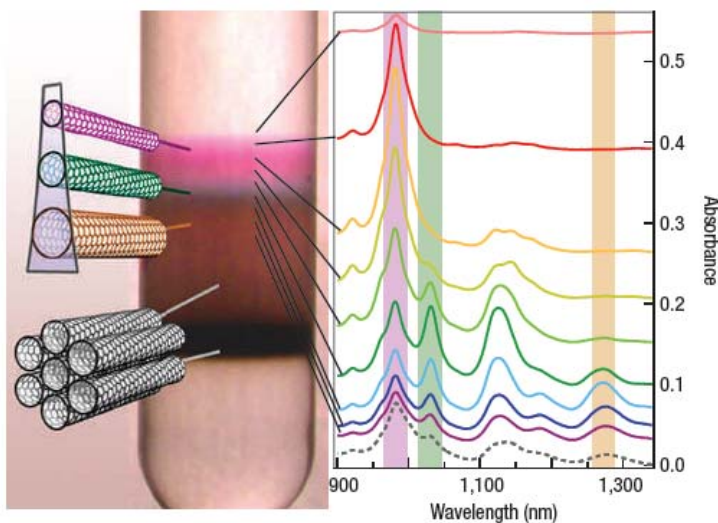


Figure 1.16 Colored band and corresponding absorption spectra of enriched nanotubes in density gradient ultracentrifugation (DGU). The pink colored band contains only metallic nanotubes as only one peak in M11 region, while the bottom contents are still mixtures. (Figure reproduced with permission from reference 87).

The mechanisms of all these methods are still not fully understood. Comparing with selective chemical reactions, the physical separation methods are more attractive because they do not change the unique properties of nanotubes⁸⁷. As the dielectric polarization directly affects the intermolecular interaction, the dielectric properties of nanotubes become the key in the understanding of separation mechanism in DEP, IEX and DGU methods. In chapter two, we studied the dielectric polarization of nanotubes and developed an assay for determining the metallicity of nanotubes using electrostatic force microscopy (EFM). In chapter three, we further investigate the microwave irradiation effect on nanotubes, as well as the selective etching of metallic nanotubes using the irradiation.

1.2.5 Characterization of nanotubes

The most common characterization techniques for nanotubes are transmission electron microscopy (TEM), scanning electron microscopy (SEM), atomic force microscopy (AFM) and optical spectroscopy. In this research, Raman and absorption spectroscopy, as well as AFM, have been used to characterize nanotubes.

1.2.5.1 Atomic force microscopy

As discussed above, AFM is able to provide high resolution image in nanometer scale. Figure 1.17 shows an AFM image of individual nanotubes. The direct measurement of the tube diameter is very helpful for determining whether the nanotubes are in the forms of bundles or individuals⁸⁵, as well as whether they are multi-walled⁸⁸ or

single-walled⁸⁹ nanotubes. An individual single-walled carbon nanotubes has a diameter of 0.6 nm to 2 nm. Therefore, AFM is often used for evaluating the dispersion and separation methods of nanotubes, as well as the sample quality.

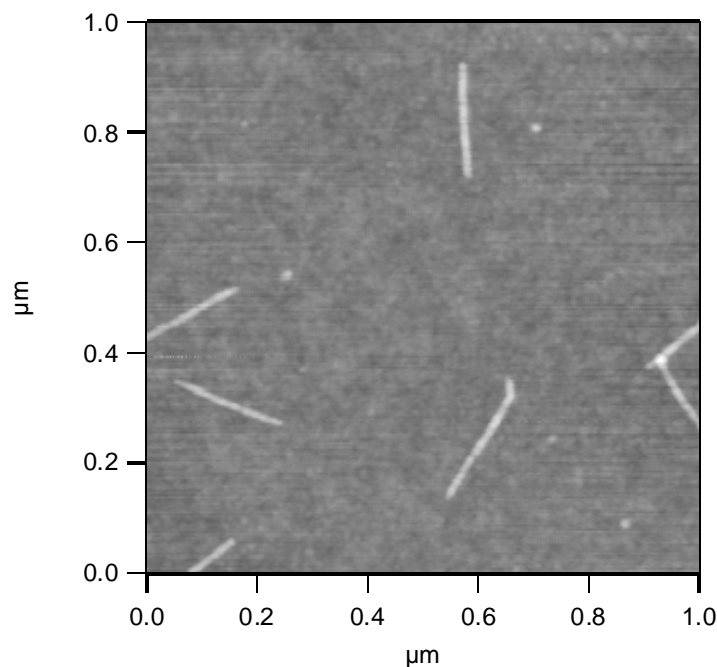


Figure 1.17 An AFM image of individual single-walled nanotubes dispersed on a SiO₂ substrate.

1.2.5.2 Raman spectroscopy

Raman spectroscopy is very important for studying the physical and electronic properties of nanotubes. Figure 1.18 shows four major bands in a Raman spectrum of an individual nanotube, including the radial breathing mode (RBM), the tangential G band, the disorder-induced D band and its second-order harmonic G' band⁹⁰⁻⁹³. Among these four

bands, the G band and RBM band are the most important features to determine the electronic properties of nanotubes.

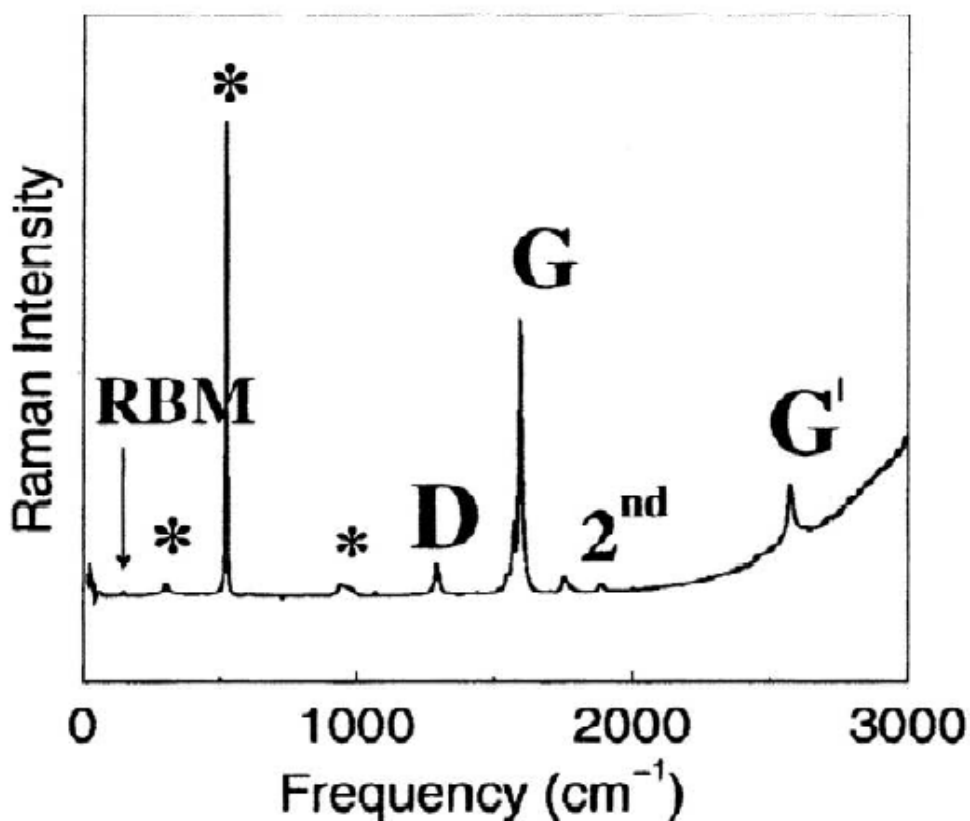


Figure 1.18 A typical Raman spectrum for a nanotube. (Figure reproduced with permission from reference 92).

Figure 1.19 shows the G band features from (a) semiconducting nanotubes and (b) metallic nanotubes⁹¹. Each possesses two G band features, one at 1590 cm^{-1} (G^+) and the other at about 1570 cm^{-1} (G^-). The G^+ and G^- feature are associated with the vibrations of carbon atoms along the axis direction and the circumferential direction of the tube, respectively⁹². It has been found that the lineshape of the G^- feature is sensitive to

whether the nanotube is metallic or semiconducting. For semiconducting nanotubes, two dominant Lorentzian features are shown with 6-15 cm^{-1} linewidth. For metallic nanotubes, G^+ bands are still dominant Lorentzian features but G^- features are broad Breit-Wigner-Fano lines⁹².

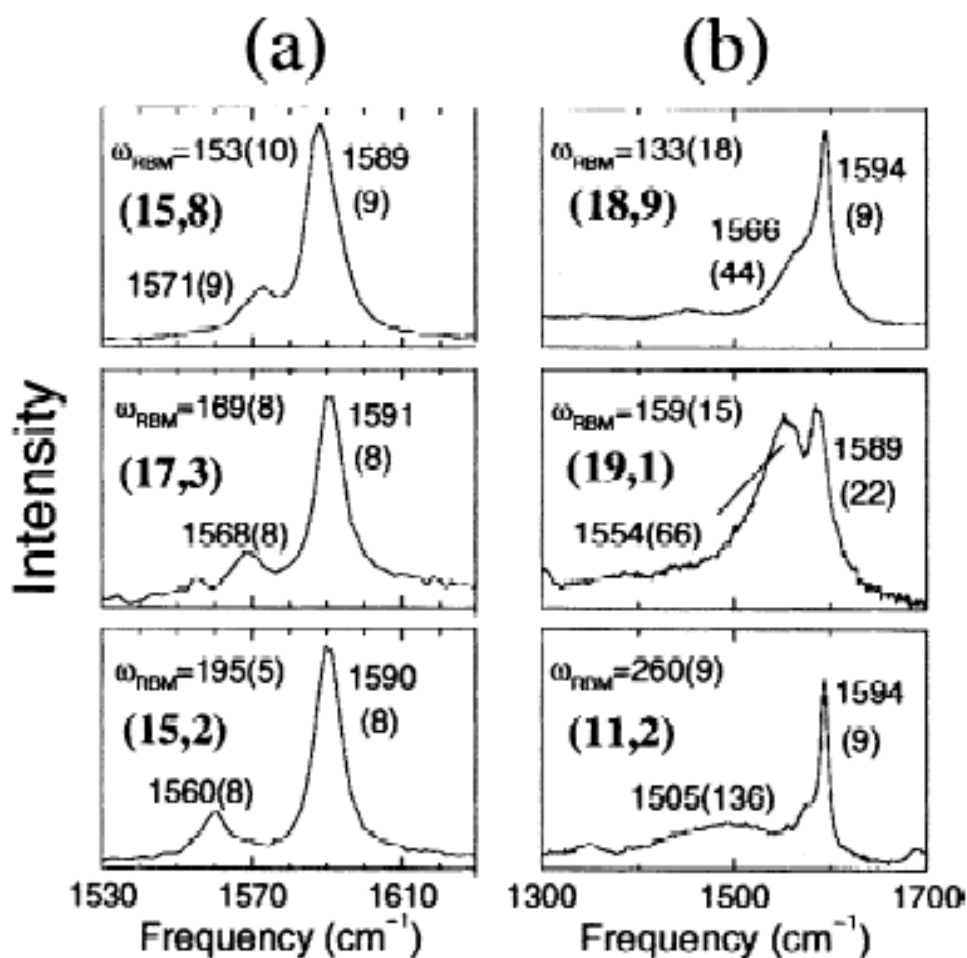


Figure 1.19 G bands for (a) semiconducting nanotubes and (b) metallic nanotubes. (Figure reproduced with permission reference 92).

The Radial breathing mode (RBM) features are generated from the coherent vibration of the carbon atoms in the radial direction, and usually occur at between 120 cm^{-1} and 350 cm^{-1} (Figure 1.20)⁹¹⁻⁹². These RBM features are very useful for identifying the diameters of nanotubes, through the use of the Equation 1.1 $\omega_{\text{RBM}} = A/d_t + B$.

$$\omega_{\text{RBM}} = A/d_t + B \quad \text{Equation 1.1}$$

In Equation 1.1, ω_{RBM} is the frequency of Raman shift, d_t is the tube diameter, and A and B are constants. Figure 1.20 shows the RBM spectra for three different nanotube species. Dresselhaus has reported $A = 248 \text{ cm}^{-1}\text{nm}$ and $B = 0$ for individual tubes⁹¹, and thus the diameter of nanotubes can be calculated from the measured RBM features. After knowing the diameter of the tubes, their chiral vector (n, m), as well as their species, can be further solved through the following Equation 1.2 and 1.3, where $a = 2.46 \text{ \AA}$, and n and m are all integers:

$$d_t = L/\pi \quad \text{Equation 1.2}$$

$$L = |\mathbf{C}_h| = a\sqrt{n^2 + m^2 + nm} \quad \text{Equation 1.3}$$

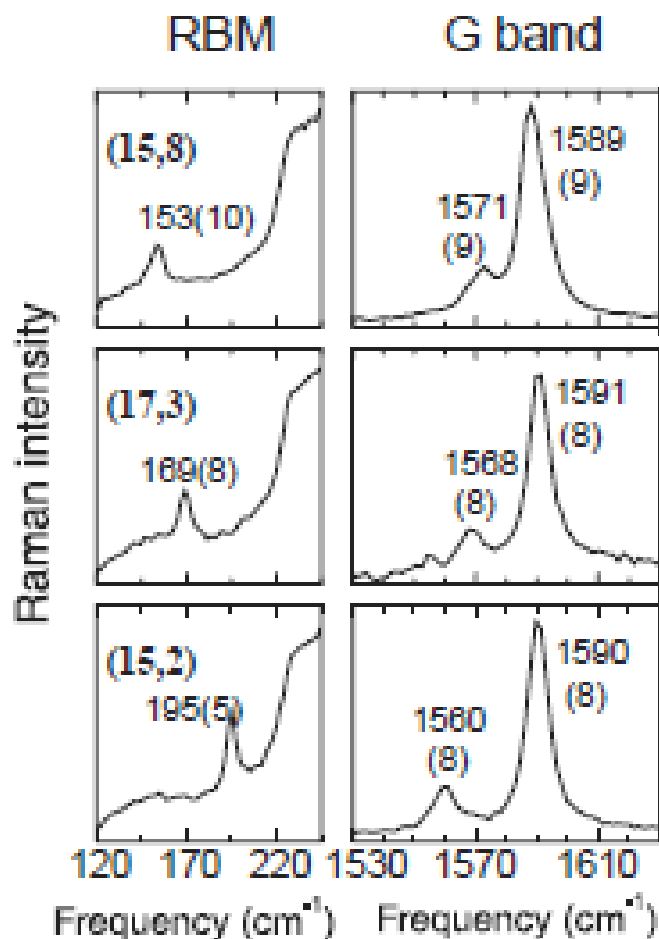


Figure 1.20 RBM bands for different nanotube species. (Figure reproduced with permission from reference 93)

1.2.5.3 Absorption spectroscopy

UV-vis-NIR absorption spectroscopy has been widely used to study the electronic structure of nanotubes^{68-70,94}. The absorption peaks originate from E_{ij} electronic transitions, such as from a valence band v_1 to a conduction band c_1 , or from valence band v_2 to conduction band c_2 . E_{ij} transition ($i \neq j$) transitions are not allowed. A typical absorption spectrum ranges from 400 nm to 1400 nm in wavelength. The M11 transitions

from metallic nanotubes are from 400 nm to 650 nm. The S11 and S22 transition from semiconducting nanotubes range from 900nm to 1600 nm and 550 nm to 900 nm, respectively⁹⁵⁻⁹⁷. Absorption spectra are useful for charactering the composition of nanotube sample and for qualitative determination of the metallic-to-semiconducting ratio⁹⁷. Figure 1.21 shows absorption spectra for a HiPco nanotube thin film after microwave irradiation.

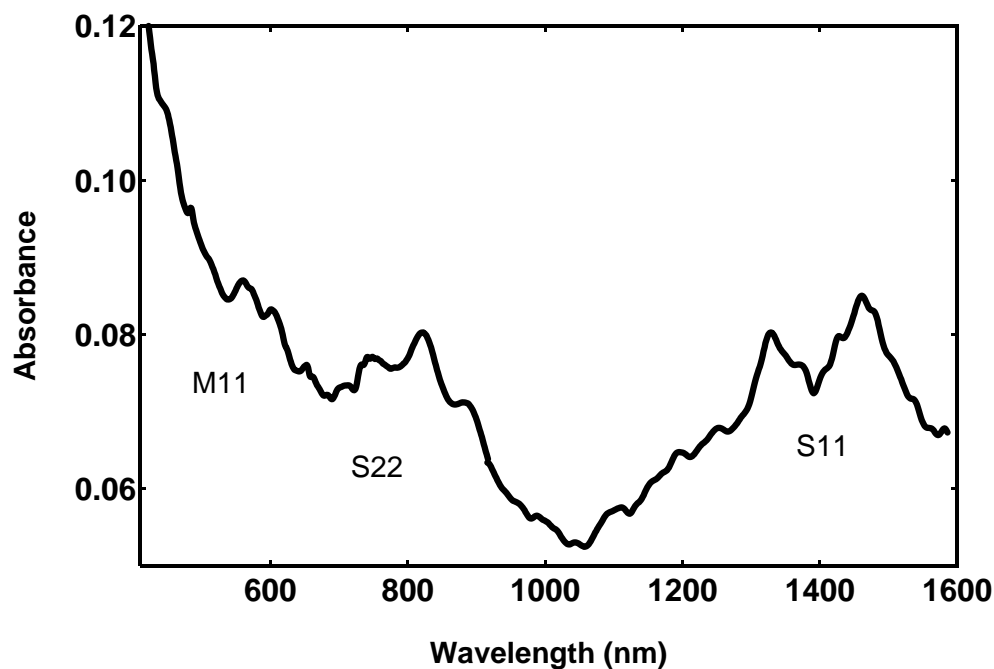


Figure 1.21 Adsorption spectrum for a HiPco nanotube samples after microwave irradiation.

1.2.5.4 Fluorescence spectroscopy

Fluorescence, also call photoluminescence, is an important technique for charactering the species in semiconducting nanotube components^{70,98-99}. Fluorescence

occurs when excited electrons decay through radioactive emission. For semiconducting nanotubes, the decay of electrons from the excited valance band v_1 to the ground state conduction band c_1 is associated with S11 transition⁷⁰. Therefore, fluorescence spectra can reveal the electronic band gap structures of nanotubes. However, no fluorescence of metallic nanotubes can be obtained because the excited electrons decay non-radioactively, and no photon emission is generated⁹⁸. Figure 1.22 shows the fluorescence spectra for semiconducting nanotubes from 658 nm and 785 nm excitations. The wavelengths of fluorescence features show the S11 transition energies of excited semiconducting nanotubes. The relative contents of these semiconducting tubes can be further calculated based on the intensity of these features.

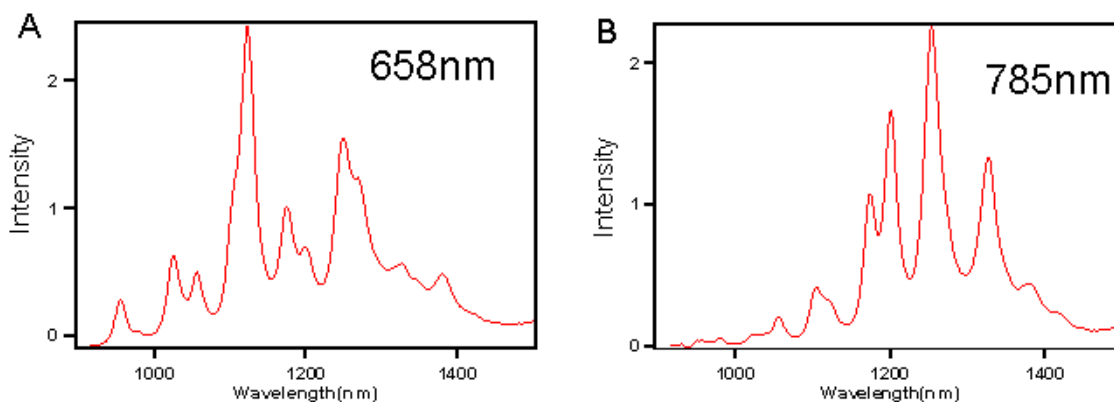


Figure 1.22 Fluorescence spectrum of a nanotube sample (A) from 658 excitation and (B) from 785 nm excitation.

1.3 Corrosion inhibitor

1.3.1 Background

Corrosion inhibitors are materials which retard corrosion when added to an environment in small concentrations (defined by the National Association of Corrosion Engineers). Over the last twenty years, protection mechanisms for corrosion inhibitors have been widely studied¹⁰⁰⁻¹⁰⁵; it is commonly accepted that the protection conferred by inhibitors is usually provided by the formation of protective layers on the metal surface¹⁰⁶⁻¹⁰⁸. After the formation of the protective layers, the contact between the metal and its corrosive environment is reduced. Different kinds of protective layers can be formed according to the properties of the inhibitor molecules. For example, the inorganic corrosion inhibitor chromate forms a passive layer and prevents the oxidation of a metal surface¹⁰⁹. Silicates and phosphates as corrosion inhibitors act by precipitation on the metal surface, blocking both anodic and cathodic sites¹¹⁰.

Organic corrosion inhibitors are surface active agents which form protective films by adsorbing on the metal surface. They are usually referred to as surfactants, amphiphilic molecules composed of hydrophilic polar heads and hydrophobic non-polar tails¹¹¹⁻¹¹². Figure 1.23 shows the molecular structure of a quaternary ammonium salt which is an organic corrosion inhibitor. The hydrophobic tail group is a long-chain alkyl group and the hydrophilic head group has either an ionic or highly polar functionality. Based on the property of the hydrophilic group, surfactants (organic corrosion inhibitors) are classified as ionic and non-ionic types. Ionic surfactants can be further categorized as anionic, cationic and zwitterionic types (Figure 1.24). One of the most important

properties of surfactant-type corrosion inhibitors is their ability to significantly retard corrosion on metal surface by forming adsorption layers¹¹³⁻¹¹⁵. Understanding the adsorption mechanism of surfactants is a significant step in selecting an appropriate inhibitor for a realistic scenario, to evaluate inhibitor performance, and to develop a predictive model for corrosion in the presence of inhibitors.

The adsorption of surfactants at the solid-liquid interface is strongly influenced by a number of factors, in particular the nature of the structural groups terminating the solid surface, the adsorption structures of the surfactants themselves and the nature of the aqueous environment¹¹⁶⁻¹¹⁷. Therefore, in this chapter, the adsorption mechanism will be described in three sections:

- (1) The driving force for the adsorption of surfactants from bulk solution to the interface.
- (2) Adsorption isotherms and aggregation structures of surfactants.
- (3) Environmental effects on the adsorption process.

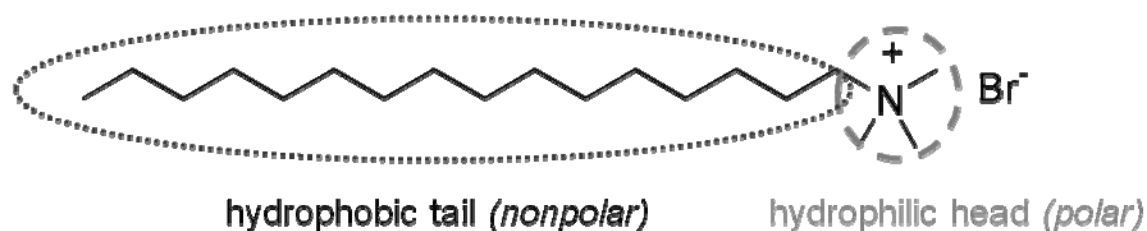


Figure 1.23 Molecular structure of an organic corrosion inhibitor (a quaternary ammonium salt).

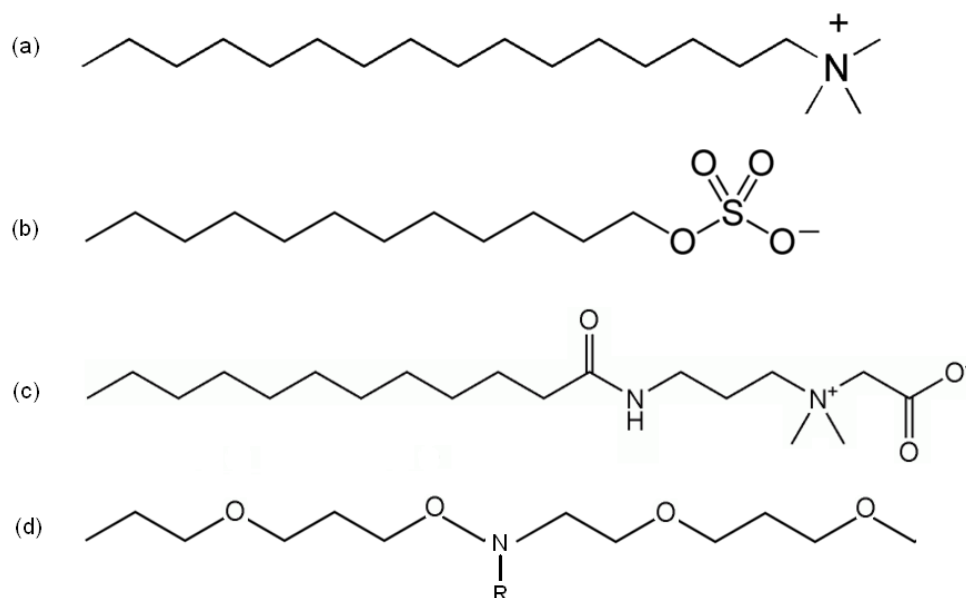


Figure 1.24 Molecular structures of organic corrosion inhibitors: (a) cationic; (b) anionic; (c) zwitterionic; (d) nonionic surfactants.

1.3.1 Driving forces for inhibitor adsorption

Adsorption of surfactants is driven by intermolecular interactions¹¹⁸⁻¹²¹. These interactions are related to the molecular structures of surfactants – particularly whether they are ionic or non-ionic and whether the hydrophobic groups are long or short, aliphatic or aromatic¹¹⁹. For example, one driving force for cationic surfactants adsorbing on negatively charged surfaces is the electrostatic force between positively charged surfactant molecules and the negatively charged surface. Figures 1.25 list the most common intermolecular interactions between surfactants and substrates: electrostatic interactions between ionic surfactants and oppositely charged surfaces; dipole-dipole interactions between polar hydrophilic groups of non-ionic surfactants and substrates; dispersion interactions between non-polar hydrophobic groups of surfactants and non-

polar surfaces¹¹⁶⁻¹¹⁷. In corrosion science, most of the corrosion inhibitors are ionic surfactants, with either positive charges or negative charges on their hydrophilic heads. Therefore, the most important driving force for corrosion inhibitors is electrostatic interaction, as the metal surfaces are often positively or negatively charged¹²²⁻¹²⁴. Other intermolecular forces such as dipole-dipole interactions and dispersion interactions are usually supplementary driving forces for the corrosion inhibitors, even though they are not as strong as electrostatic interactions.

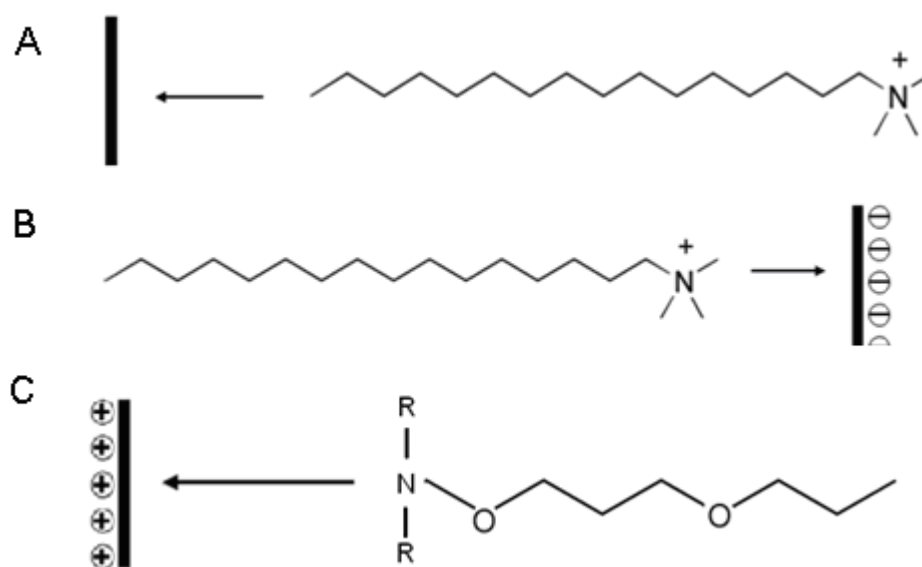


Figure 1.25 Schematic drawings of (A) the Electrostatic interaction between a cationic quaternary ammonium salt surfactant and a negatively charged surface; (B) the Dipole-dipole interaction between a non-ionic surfactant and a positively charged surface; (C) the Dispersion interaction between the hydrophobic tail of a quaternary ammonium salt surfactant and non-polar surface.

Another important intermolecular interaction existing in every surfactant is called the hydrophobic effect or hydrophobic interaction¹¹⁶. This interaction comes from the

hydrophobicity, which means fear of water, of the hydrophobic groups in surfactants. In aqueous solution, surfactant molecules would move away from water molecules because of this hydrophobicity, resulting in the adsorption at the solid/liquid interface. After the concentration of surfactant exceeds the critical micelle concentration in the bulk solution, the hydrophobic groups of surfactants can aggregate together and form compact micelles^{116-117,119}. This compact micelle structure also increases the adsorption of surfactants on the solid surface. Therefore, after the electrostatic interaction drives the corrosion inhibitors from bulk solution to the interface, this hydrophobic effect further increases the adsorption and aggregation of corrosion inhibitors, and a high surface coverage is achieved.

1.3.2 Adsorption isotherm

An adsorption isotherm describes the amount of surfactants on the surface as a function of its concentration at constant temperature¹²⁵⁻¹²⁶. The isotherm usually depends on the type of surfactants and the nature of surfaces. Many isotherms have been reported indicating different adsorption processes and mechanisms¹²⁶⁻¹²⁸. Here, we mainly focus on the adsorption isotherm of ionic corrosion inhibitors adsorbing on oppositely charged metal surfaces. Figure 1.26 shows a typical isotherm of a cationic surfactant adsorbing on a negatively charged surface. Four regions were shown in this graph^{120,129-134}. In region 1, at very low bulk concentration, the surfactant adsorbs mainly by electrostatic interactions, possibly with the hydrophobic group more or less prone on the substrate. In region 2, a remarkable increase in adsorption isotherm is shown. This increase is due to the

hydrophobic interaction between previously adsorbed molecules and the oncoming surfactant ions. Both electrostatic interaction and hydrophobic interaction drive the surfactants from bulk solution onto the surface. A monolayer is usually formed at the end of region 2. For further adsorption, the slope of the isotherm is reduced in region 3, because of the repulsive interaction between the oncoming surfactants and the similarly charged solid. A bi-layer film may be formed through tail-to-tail hydrophobic interactions, and adsorption at the end of region 3 usually reaches the maximum value. Therefore, in region 4, the adsorption keeps a constant value. No more molecules or layers can adsorb onto the surface at this stage.

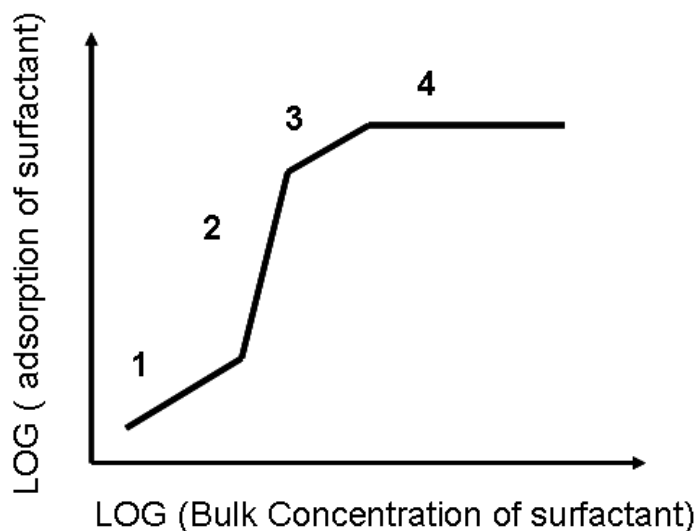


Figure 1.26 Schematic of adsorption isotherm for an ionic surfactant on an oppositely charged substrate.

1.3.3 Adsorption structure

Figure 1.27 shows the aggregation structures of surfactants on the surface in the four regions shown in figure 1.26. At low concentration (region 1), only a few surfactant molecules adsorb onto the surface with the hydrophobic groups more or less prone on the substrate. As the concentration increases (region 2), more surfactants coming from the bulk solution adsorb onto the surface. In this region, surfactants form a compact layer with the hydrophobic tails stand up, allowing more molecules adsorb on the water/solid interface. At the end of this region, the original charge of the surface is neutralized by the oppositely charged surfactants, and the surface is fully covered with a monolayer. After a fully covered monolayer is formed on the surface, more adsorption of surfactant molecules can only aggregate on top of the monolayer through tail-to-tail hydrophobic interactions. This tail-to-tail hydrophobic interaction is induced by the hydrophobicity of non-polar hydrocarbon tails. Non-polar tails repel water molecules and aggregate together. At region 3, an aggregated bi-layer structure is formed and the adsorption remains it a maximum at the end of this region. Therefore, the adsorption in region 4 remains at a constant value as no more surfactant molecules can absorb onto the surface.

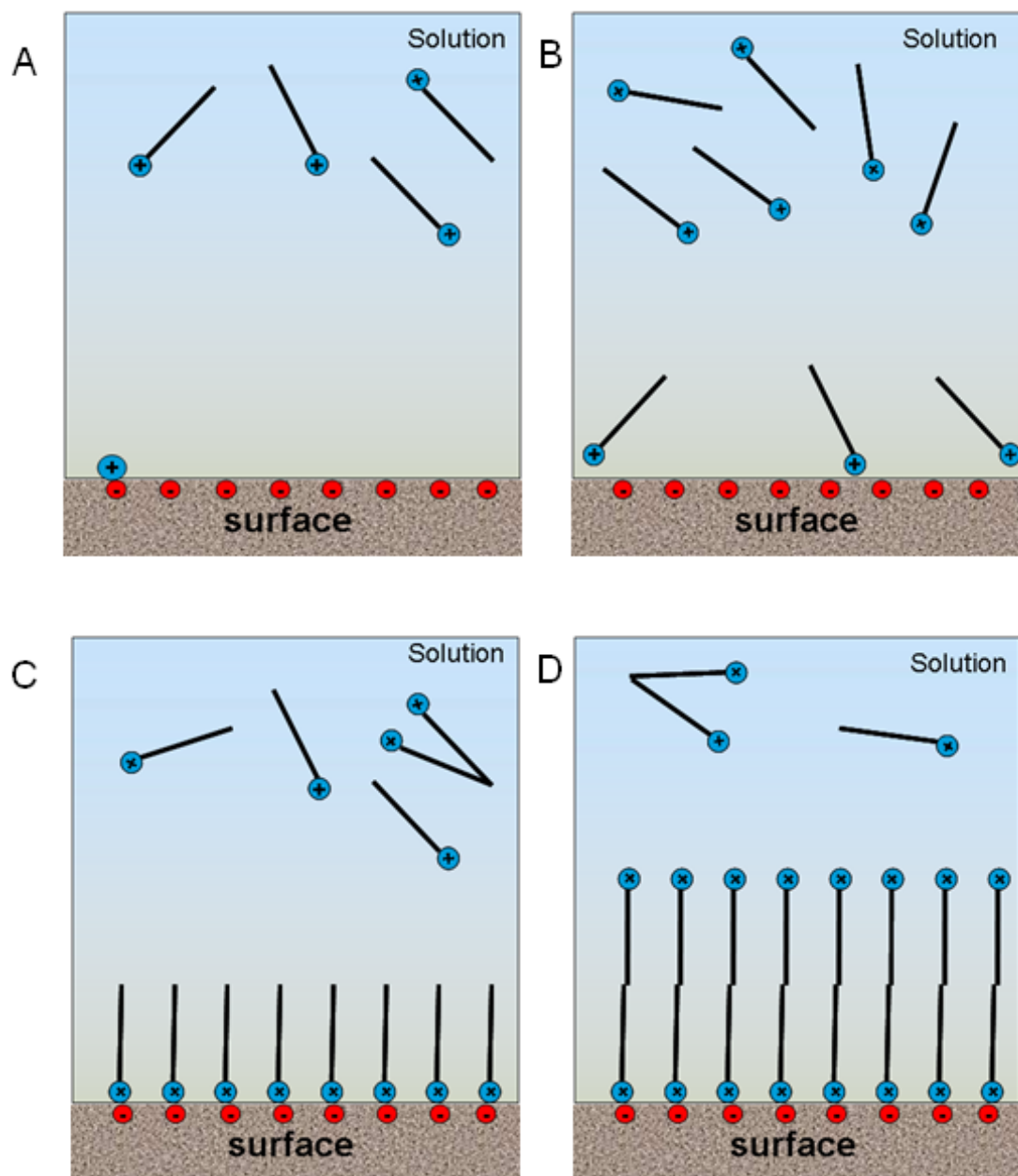


Figure 1.27 Schematic drawings of adsorption structures in four regions: (A) Initial stage, no adsorption. (B) In region 1, only a few surfactant molecules adsorb onto the surface. (C) In region 2, surfactants gradually form a compact monolayer with the hydrophobic tails stand up. (D) At the end of region 3, a bi-layer structure is formed and the adsorption reaches its maximum.

However, at the maximum adsorption, the aggregation structures of surfactants are not always bi-layer structures. Multiple micelle structures have been reported and it is believed that different aggregation structures are formed for various surfactants at different environmental conditions^{130,135-138}. It has been reported that the structure of surfactant can be transformed by controlling the water chemistry¹³⁹. Figure 1.28 shows two possible aggregation structures for tetradecyltrimethylammonium bromide in the absence and presence of Br^- ions¹⁴⁰. No matter what kind of aggregation structure is formed, corrosion inhibitors reach their maximum adsorption at certain concentrations and their protection efficiencies also reach the maximum.

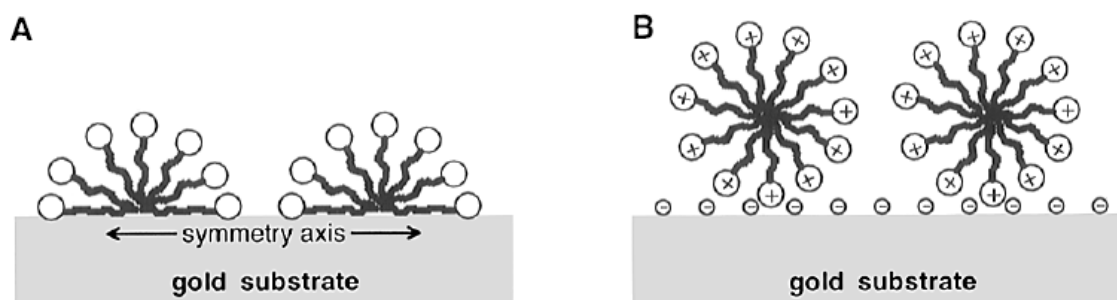


Figure 1.28 Different aggregation structures of cationic surfactant tetradecyltrimethylammonium bromide (C14TAB) in the (A) absence and (B) presence of Br^- ions . (Figures reproduced with permission from reference 141).

1.3.4 Environmental effects

1.3.4.1 pH effect

Because more hydrogen ions adsorb from the solution onto the surface, the surface becomes more positive, or less negative, at lower pH. Consequently, the

adsorption of anionic surfactants will increase and the adsorption of cationic surfactants will decrease. Figure 1.29 shows the isotherms of cationic and anionic surfactants adsorbing on oppositely charged substrates at multiple pH values¹⁴¹. As the pH decreases, the adsorption of sodium p-3-nonylbenzene sulfonate increases while the adsorption of dodecyl pyridinium chloride decreases. Therefore, to better achieve protection at a certain pH, the selection of inhibitor type is very important.

Changes in the pH may also affect the structure and property of surfactant molecules. For example, zwitterionic surfactants can be either positively or negatively charged at different pH values. Positively or negatively charged functional groups may also be induced on nonionic surfactants at certain pH, because nonionic surfactants can act as hydrogen ion donors or acceptors. For example, an amine can protonate to form an alkyl ammonium salt at acidic condition. Therefore, the selection of corrosion inhibitors highly depends on the pH value of the environment.

1.3.4.2 Temperature effect

A temperature increase generally causes a decrease in the adsorption of ionic surfactants, the change being relatively small compared to that caused by pH changes. Figure 1.30 shows the adsorption isotherms of anionic surfactant sodium dodecylsulfate (SDS) at different temperatures¹⁴². From 293 K to 313 K, the adsorption of SDS only decreases less than 10%, while the change from 7.0 to 9.0 at 298 K causes a significant change in the adsorption process.

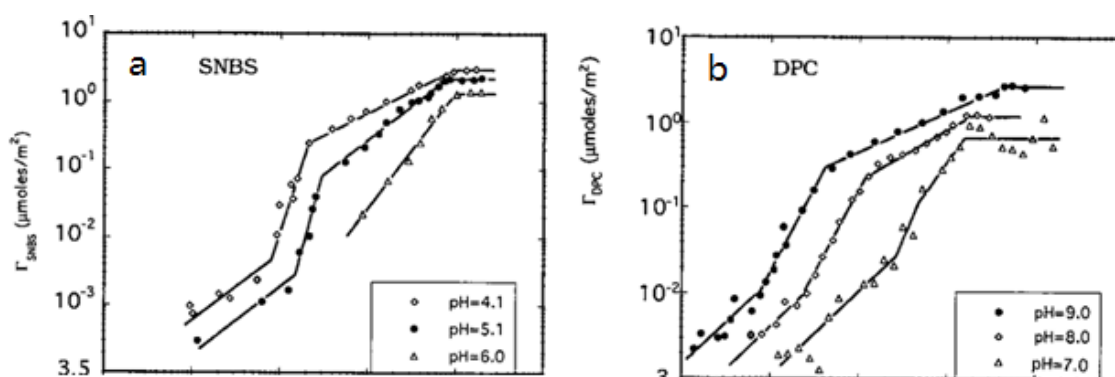


Figure 1.29 (a) Adsorption isotherms of anionic surfactants on a positively charged surface at different pH values; (b) Adsorption isotherms of cationic surfactants on negatively charged surfaces at different pH values. (Figures reproduced with permission from reference 142).

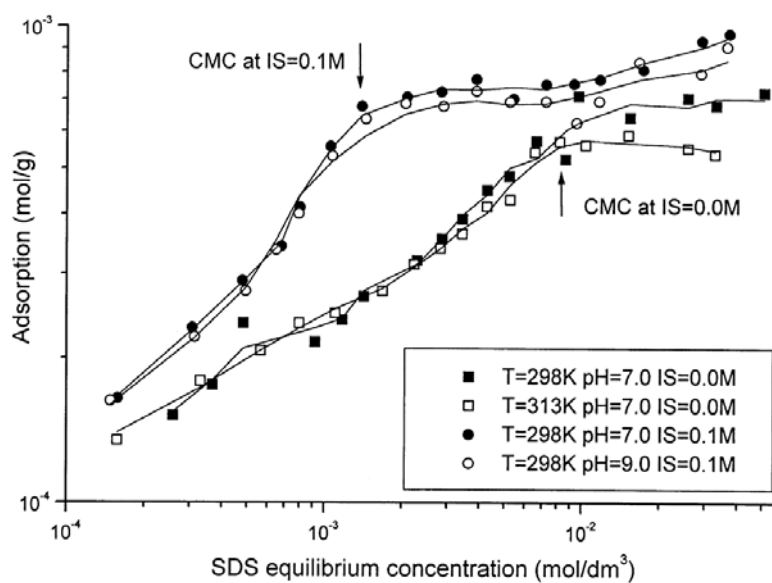


Figure 1.30 Adsorption isotherms of anionic surfactant SDS at different temperature, pH, ionic strength. Temperature increase causes a decrease in the adsorption of ionic surfactants. (Figure adopted from reference 143).

1.3.4.3 Surface potential

Surface potential can be adjusted by varying the pH in the bulk solution or by applying an extra potential directly on the substrate. Most metal oxides can behave either positively charged or negatively charged based on the pH of the bulk solution. If at a specific pH the metal oxide is neutral then this pH value is called “point of zero charge” (PZC)¹⁴³⁻¹⁴⁴. When the pH is lower than the point of zero charge value, the acidic water donates more hydrogen ions than hydroxide groups, and so the adsorbent surface is positively charged. A point of zero charge of CuO at 9.5 indicates that the CuO surface is positively charged when the pH is below 9.5¹⁴⁵.

Applying an external potential onto the surface directly changes the charge density, or even reverses the charge. Lowering potential can induce more negative charges on a surface, and the adsorption of cationic inhibitors will be consequently increased.

1.3.5 Adsorption kinetics

Although the adsorption happens immediately after adding surfactants into the solution, adsorption kinetics are quite different between various surfactants and substrates. Even for the same type of surfactants, the adsorption kinetics can be significantly varied by the concentration, pH and ionic strength. Figure 1.31 shows the adsorption isotherms of cetyl tetradecyltrimethylammonium bromide (CTAB) at various concentrations¹⁴⁶. At 0.5 mM, it takes 800 minutes for surfactant molecules to reach the adsorption maximum, while at 10 mM only 5 minutes are needed to reach the maximum.

Therefore, in the use of corrosion inhibitors, even through inhibition may happen immediately after adding inhibitor dose, enough time needs to be given to achieve the full adsorption of inhibitor molecules.

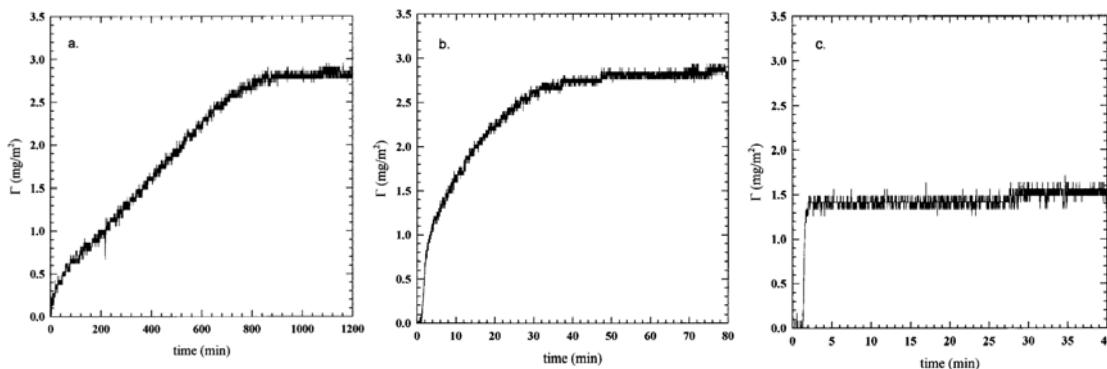


Figure 1.31 Adsorption kinetics for CTAB at the following bulk surfactant concentrations: (a) 0.50mM (0.55 CMC); (b) 0.80mM (0.89 CMC); (c) 10mM (11 CMC). (Figures reproduced with permission from reference 147).

1.4 Overview of dissertation

This dissertation mostly describes the study of carbon nanotubes and corrosion inhibitors using atomic force microscopy, as well as the application and development of AFM in an electric field and an aqueous solution.

In Chapter 2 a scanning probe assay, based on electrostatic force microscopy (EFM) will be described for the study of the metallicity of nanotube samples. In an electric field, nanotubes are polarized and induced dipoles are created on their sidewalls. EFM is able to measure significant different dielectric signals from metallic nanotubes and semiconducting nanotubes, as they have different polarizabilities. This assay can be used to recognize the electronic type of a nanotube, differentiate metallic and

semiconducting nanotubes, and evaluate the effectiveness of nanotube separation methods.

After furthering the basic knowledge to distinguish metallic from semiconducting nanotubes, a study of microwave irradiation on nanotubes, towards the selectively etching of metallic nanotubes, is described in Chapter 3. Due to the high thermal and electric conductivities of metallic nanotubes, microwave irradiation may induce strong currents and produce excessive heat on metallic nanotubes, and selectively decreasing the metallic content in nanotube samples. However, AFM images and optical spectra indicate that metallic nanotubes were not completely destroyed by irradiation in a commercial microwave oven, but only preferentially oxidized or defected. In future, this potential method can be further developed by increasing the power of microwave device and changing the frequency of irradiation.

In Chapter 4, the study of the adsorption of corrosion inhibitors in aqueous solutions is described. The measured surface morphology and film thickness can help to determine the internal adsorption structures of flat inhibitor films. The further force measurements in vertical and lateral directions on inhibitor films provide the first quantitative studies of the mechanical properties of corrosion inhibitors. The measured penetration force and lateral force values can be converted to 1~10 MPa stresses based on the diameter of the AFM tip. These MPa order stresses indicate that inhibitor molecules cannot be removed by fluid flow alone.

Chapter 2. An Electric Force Microscopy Assay for Single-Walled Carbon

Nanotube Metallicity

(Part of the work in this chapter has been published in *Nano Letters* (2009), 9 (4), 1668-1672, and *J. Phys. Chem. C* (2009), 113 (24), 10337–10340)

2.1 Introduction

Their unique one-dimensional structures make single-walled carbon nanotubes (nanotubes) potential candidates for future applications in many fields, such as energy storage⁵⁵⁻⁵⁶, drug delivery⁵²⁻⁵⁴ and electronic devices⁵⁰⁻⁵¹. Depending on their chiralities and diameters, nanotubes can be either metallic or semiconducting, and each electronic-type nanotube exhibits unique properties for various applications. Metallic nanotubes are excellent conductors in nano-circuits and nano-connectors¹⁴⁷⁻¹⁴⁸, while semiconducting nanotubes can be applied in logic, memory and sensor nano-devices¹⁴⁹⁻¹⁵¹.

However, metallic and semiconducting nanotubes are produced together in as-synthesized samples. Due to the strong intermolecular interactions between nanotubes and their insolubility in aqueous solution, the dispersion and separation of nanotubes has become important research topics in the last two decades^{79,84,152-154}. Special methods and techniques have been applied to separate nanotubes based on their electronic properties and diameters. Ralph Krupke, *et al.*, reported an AC dielectrophoresis method to separate metallic nanotubes from semiconducting nanotubes in a microelectrode device⁸³. Zheng and co-workers designed a DNA-assisted nanotubes dispersion method to separate nanotubes through ion-exchange chromatography (IEX)^{78,84}. Recently, The Hersam group

has developed a density gradient ultracentrifugation (DGU) method to separate nanotubes by utilizing their density variations in different species⁸⁷. Besides physical separation methods, a chemical separation method by selective etching metallic nanotube has been reported by Strano and co-workers⁸². Other preferential synthesis processes, including plasma-enhanced chemical vapor deposition¹⁵⁵ and cobalt-molybdenum catalyst-based processes⁶⁵ have been invented to control the distribution of nanotube species in the synthesis system.

As multiple separation methods and techniques have been developed to achieve the separation of nanotubes based on their electronic structures, it is also very important to establish a method to characterize their metallic percentage, hence metallic-to-semiconducting ratio, in nanotube samples. This method cannot only determine the quality of nanotube samples, but also verify the effectiveness of the nanotube separation methods. The current method to detect the electronic type of individual nanotubes is to measure their electronic transport in field effect transistors (FETs). By making 100 field effect transistors with individual nanotubes, the electronic type of each tube, as well as the metallic-to-semiconducting ratio can be determined¹⁵⁶. This method is impractical as fabricating 100 FETs is time consuming and expensive. Optical techniques such as Raman and absorption spectroscopy are valuable tools for characterization of nanotube samples. However, Raman spectroscopy is limited by the resonance condition and absorption spectra usually show very broad and overlapping peaks. Therefore, a key goal in this research is to establish a reliable and fast-response assay to differentiate metallic

and semiconducting nanotubes based on their different dielectric responses in an electric field.

The Chen group has studied the dielectric response of nanotubes using electrostatic force microscopy (EFM) and reported the first experimental measurement of transverse dielectric constants of individual nanotubes^{36,157}. This has demonstrated that the non-uniform electric field around the conductive tip results in a weak but discernible influence from the longitudinal polarization of nanotubes, which could be used to distinguish metallic nanotubes from semiconducting ones.

EFM^{36,158-161}, working in the non-contact double-pass mode and probing the electrostatic force, is an advanced mode of AFM. In an EFM experiment (Figure 2.1), the first pass corresponds to a standard tapping mode scan on a normal topographic line. On the second pass, the conductive tip is lifted a set amount of height and scans the same line with an applied bias. The electric field, created by the bias, induces the polarization on the surface of nanotubes. The induced dipoles on the tubes in turn interact with the charged tip, leading to an attractive electrostatic force. Dielectric images are generated based on the measured electrostatic forces.

Based on the continuum model¹⁵⁷ for nanotubes, the high dielectric constant of metallic nanotubes effectively screens the external field and forms equal potential surfaces parallel to their central axes (Figure 2.2a). On the semiconducting nanotubes, the screening of external field is less effective and localized bound charges accumulate mostly below the tip (Figure 2.2b). Therefore, the potential difference between the tip and the nanotube is larger in metallic nanotubes, which results in stronger signals in dielectric

images. Previous work reported in the Chen group, using numerical modeling, has predicted that the difference in the dielectric signals between metallic nanotubes and semiconducting nanotubes are large enough to show two distinct zones in the plot¹⁵⁷.

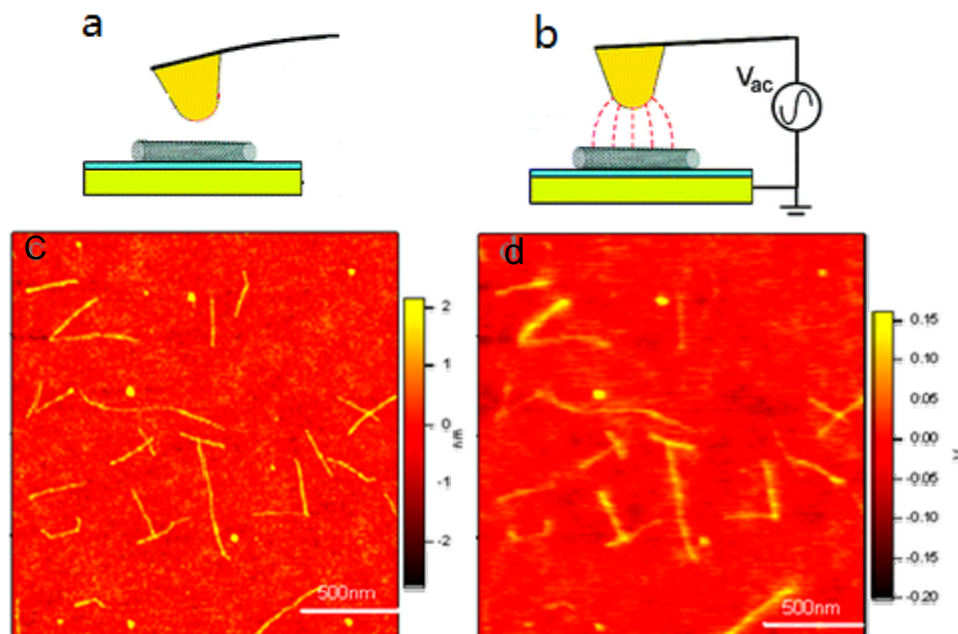


Figure 2.1 Schematics of the double pass mode of EFM scanning. (a) On the first-pass, the cantilever vibrates over the sample and produce (c) a topographic image. (b) On the second-pass, a bias voltage is applied to the tip. The induced dipole on nanotube surface in turn interacts with the charged tip, leading to (d) a dielectric image.

Figure 2.3 shows the dielectric response *versus* D^2 (square of the nanotube diameter) plot from numerical modeling. In this modeled plot, metallic nanotubes show larger dielectric signals in the upper zone while semiconducting nanotubes show lower signals in the bottom zone. This work has led to an EFM assay to differentiate metallic and semiconducting nanotubes in dielectric images. Another goal of this project is to

experimentally determine the metallic and semiconducting contents in commercial nanotube samples.

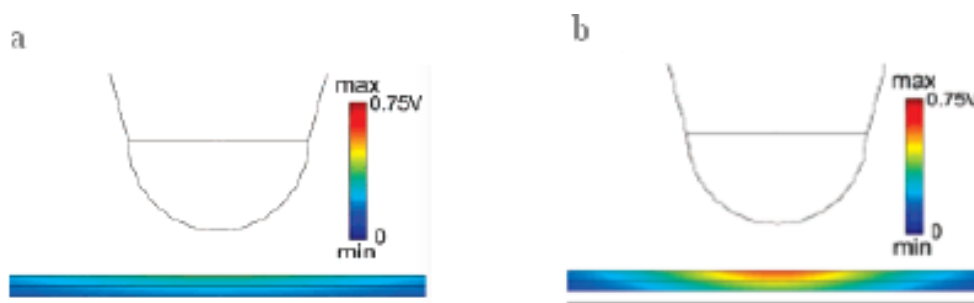


Figure 2.2 Influence of the longitudinal polarizability on the interaction forces between tip and nanotubes. The different Potential distributions around (a) a metallic nanotube and (b) a semiconducting nanotube result in stronger interaction forces of metallic nanotubes than semiconducting nanotubes. (Figure reproduced with permission from reference 157).

2.2 Experimental

2.2.1 Materials

DNA-assisted nanotube suspensions, metallic enriched DNA-nanotube suspensions, and semiconducting enriched DNA-nanotube suspensions were provided by Dr. Ming Zheng at DuPont Central Research and Development, Wilmington, Delaware. Preparation routines for DNA-assisted nanotubes have been published in the literature^{78,84-85}.

Other individual nanotubes were prepared from commercial laser ablation, HiPco and CoMoCAT nanotube samples, respectively. Raw nanotubes bundles were sonicated in 1,2-dichloroethane for 15 minutes, and the resultant suspension was spin-coated onto a

Si wafer. No surfactant or polymer additives were added to assist the dispersion. The sample was then assembled into a closed environmental cell and purged with dry nitrogen for 1 hour to eliminate the moisture and oxygen. Low nitrogen flow was maintained during the scanning.

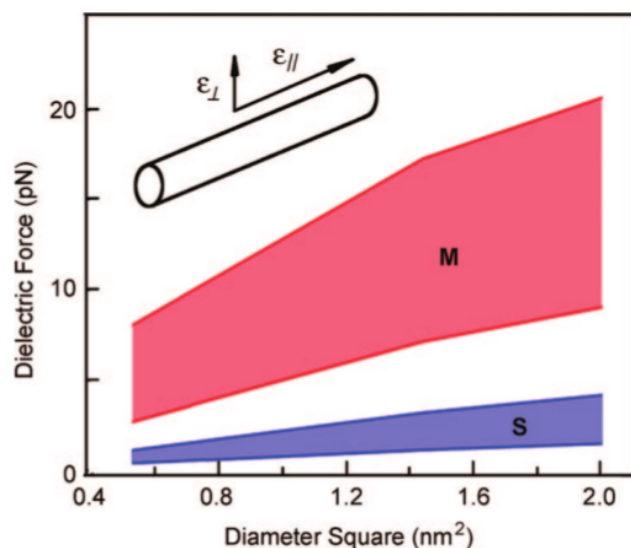


Figure 2.3 Dielectric response *versus* D^2 plot from numerical modeling. The dielectric signal of metallic nanotubes (M) and semiconducting nanotubes (S) locate in different zones in the plot as they have significantly different dielectric responses. (Figure reproduced with permission from reference 157).

2.2.2 Methods

The nanotube samples were studied using an Asylum research MFP3D AFM in a double-pass mode. The first pass is a standard tapping mode scan on a normal topographic line and provides topographic information. On the second pass, the conductive tip is lifted a set height and scans the same line with an applied bias of 5 V,

and generate dielectric signals. Pt and Ti coated tips, purchased from Mikromasch Co., were used in the double-pass scanning. The averaged diameters and averaged dielectric signals of imaged nanotubes were measured along the longitudinal axis of the tubes from topographic images and dielectric images, respectively.

UV-vis adsorption spectra were collected from surfactant-assisted nanotube dispersions using an Agilent 8453 spectrophotometer. Raw nanotube bundles were dispersed in aqueous solution containing 1 wt. % of surfactant sodium dodecyl sulfate (SDS) *via* ultrasonication treatment, and centrifuged at 25000 G for 2 hours to remove the catalyst particles. Raman spectra were collected from individual nanotubes on a Si wafer with 81 markers, using a WiTec Raman/near-field scanning optical microscope (532 nm excitation laser). The avalanche photodiode (APD) mode in this Raman microscope enabled the location of the target nanotubes which had been analyzed in EFM. G band and RBM band features of the target nanotubes were further collected *via* the charge coupled detector (CCD) mode.

2.3 Results and Discussion

2.3.1 Dielectric response and metallic content of DNA coated nanotubes

Figure 2.4 shows the topographic images and corresponding dielectric images of DNA coated HiPco nanotubes. The lengths of nanotubes shown in the AFM images were mostly less than 1000 nm, and the diameters of the nanotubes were less than 2 nm. Four nanotubes with similar lengths and diameters were selected for comparison. For nanotubes circled by dotted lines, they exhibit very weak dielectric signal in the images

indicating their surface were hardly polarized and they are probably semiconducting types. The other two nanotubes circled by solid lines show much stronger signal along the tube axis, indicating they have high polarizabilities and thus they are metallic ones.

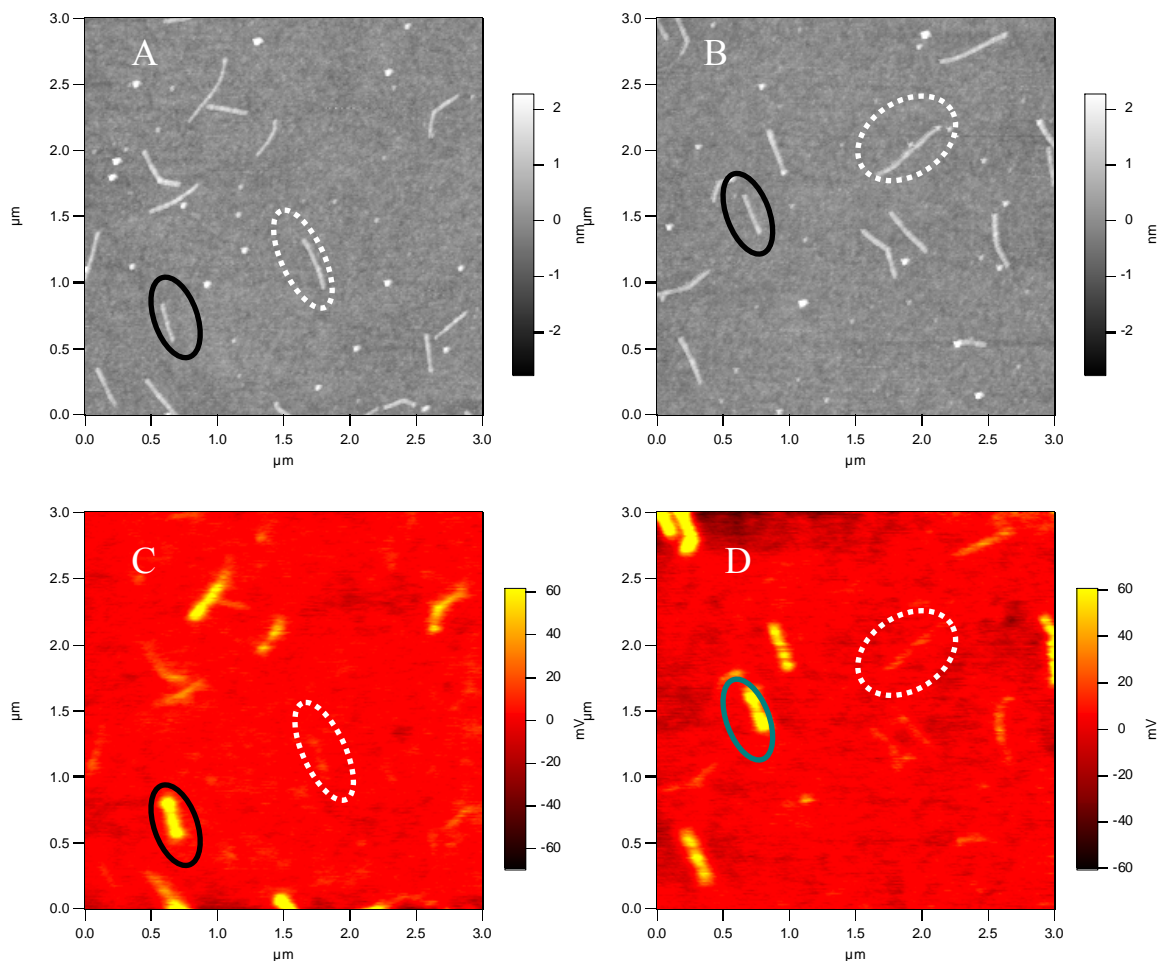


Figure 2.4 Topographic images (A,B) and corresponding dielectric images (C,D) for DNA coated HiPco nanotubes in different zones. By comparing these images, nanotubes with similar lengths and diameters were found to exhibit different dielectric signal.

As the dielectric response is related to the square of the nanotube diameter (D^2) but independent of tube chirality¹⁶²⁻¹⁶³, the measured dielectric signals and diameters were

plotted together. Figure 2.5 shows a dielectric signal *versus* D^2 plot for the above DNA coated HiPco nanotubes. Each data represents a nanotube measured in the EFM experiments. Two separated zones, which correspond to metallic and semiconducting nanotubes are clearly identified in this plot. Because metallic nanotubes have higher polarizabilities and exhibit stronger dielectric signals, the upper zone represents the metallic nanotubes while the lower zone corresponds to those with semiconducting properties. By counting the number of data points in each zone the metallic-to-semiconducting ratio, hence the percentage of metallic nanotubes present in the sample, can be determined. Based on our measurements, the percentage of metallic nanotubes in this sample is 37%, very close to the theoretical 33% value¹⁴⁷.

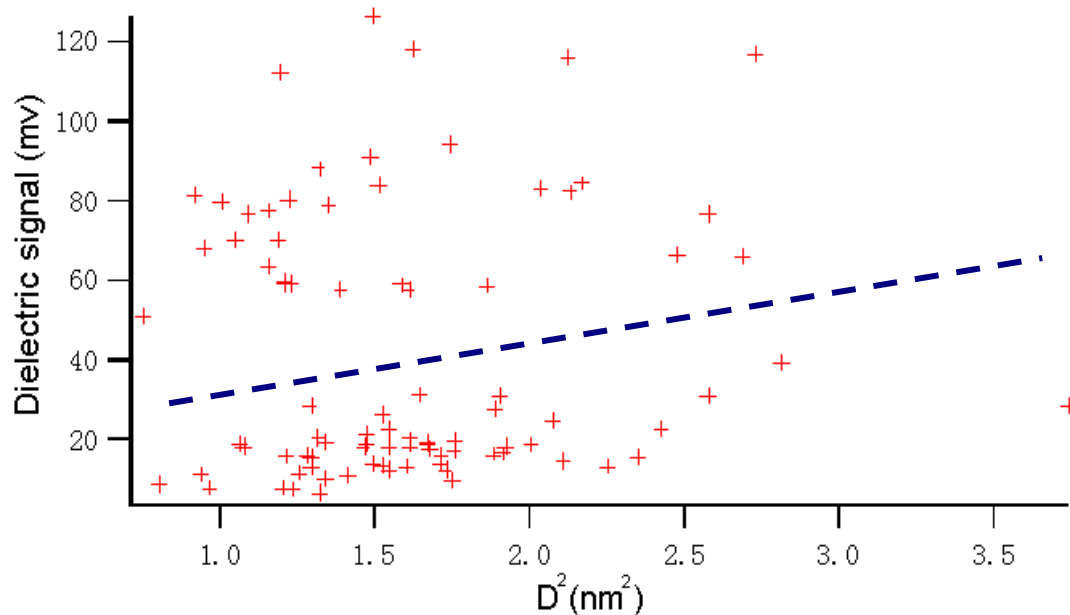


Figure 2.5 Dielectric signal *versus* D^2 plot for DNA coated HiPco nanotubes. Two zones are shown in the plot, upper zone for metallic nanotubes and bottom zone for semiconducting types.

Since the previous nanotube sample was synthesized *via* the HiPco (High pressure CO conversion) method, this assay was then applied to study whether other nanotube samples, *i.e.*, CoMoCAT nanotubes, have the same response in EFM. Figure 2.6 shows the topographic and dielectric images of DNA-coated nanotubes synthesized by the CoMoCAT method. CoMoCAT nanotube samples usually have different metallic-to-semiconducting ratios compared with HiPco nanotubes. From the selected nanotubes, circled by solid and dotted lines, the same phenomenon was observed: nanotubes with similar lengths and diameters show quite different dielectric signals. Since the signal variation is unrelated to the lengths and diameters of nanotubes, it must be related to their electric properties.

After plotting the measured diameter and signal values, the metallic-to-semiconducting ratio of the nanotube sample is determined. Figure 2.7 shows the dielectric signal *versus* D^2 plot for CoMoCAT DNA-nanotubes. Two separated zones for metallic and semiconducting nanotubes are again shown in this plot. By counting the number of data points in the upper metallic zone and bottom semiconducting zone, respectively, the percentage of metallic nanotubes in this sample was determined to be 55%.

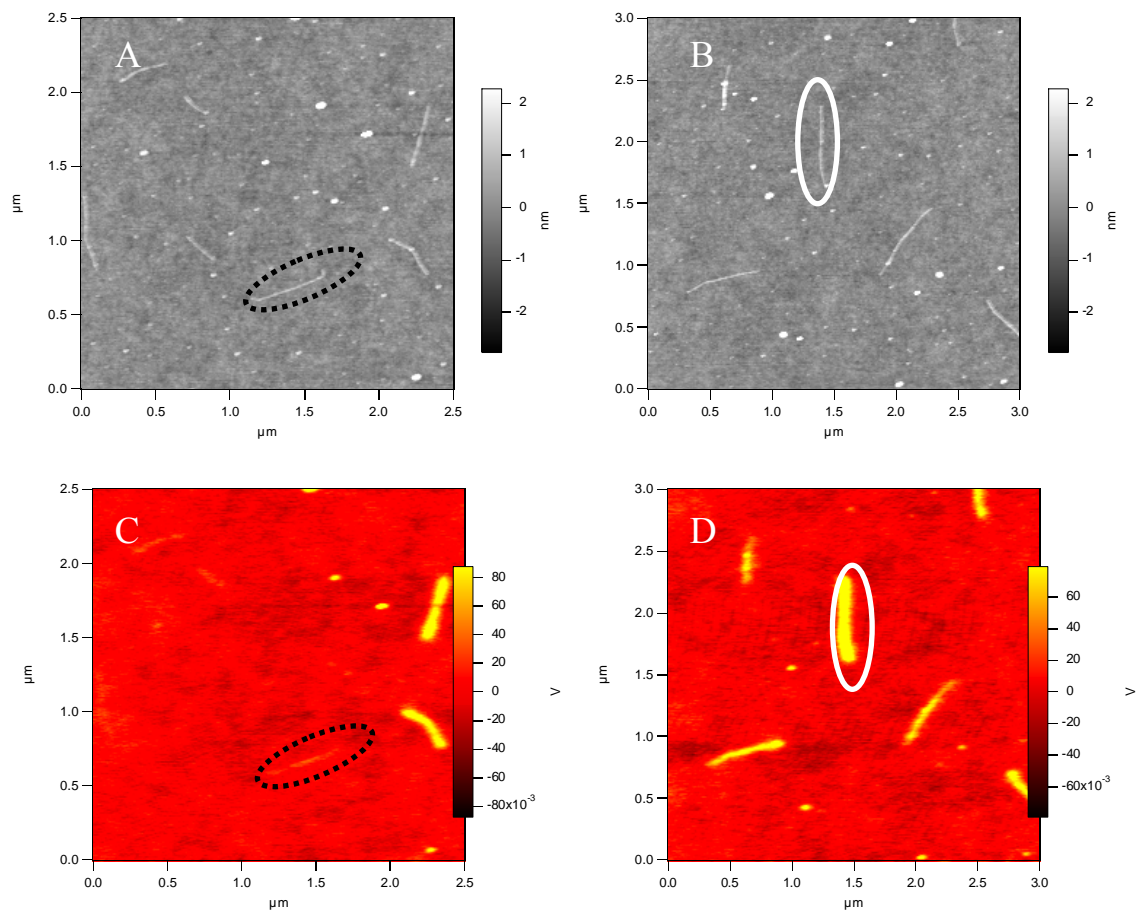


Figure 2.6 Topographic images (A,B) and corresponding dielectric images (C,D) for DNA coated CoMoCAT nanotubes in different zones. By comparing these images, nanotubes with similar lengths and diameters were found to exhibit different dielectric signals. Nanotubes circled by the blue solid line exhibit much weaker signal than nanotubes circled by the green dotted line, even though they have similar physical properties.

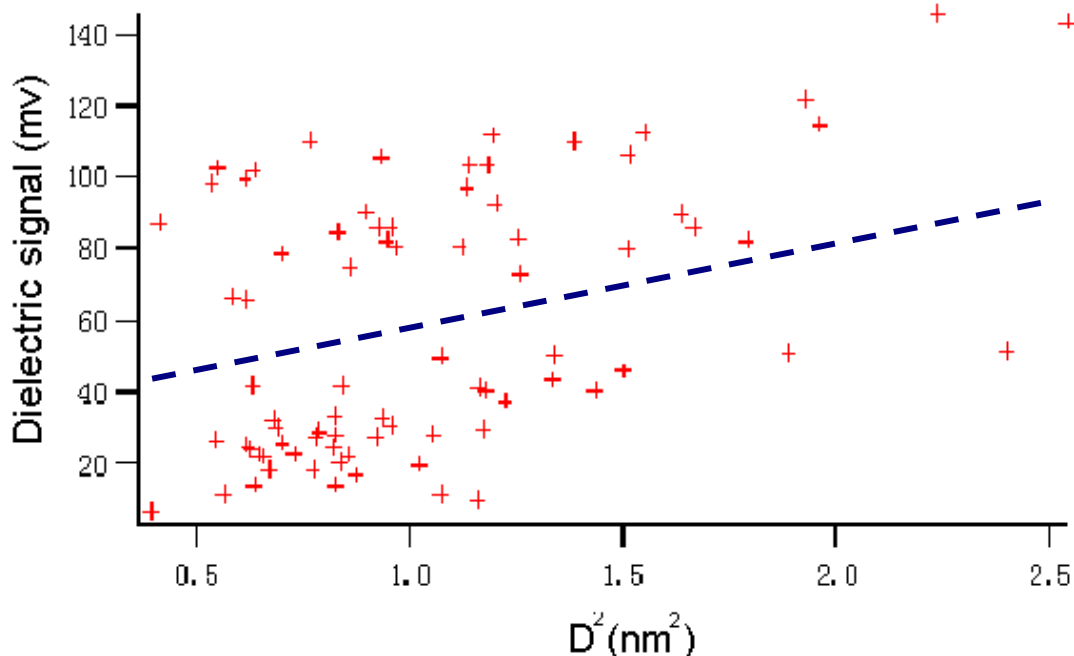


Figure 2.7 Dielectric signal *versus* D^2 plot for DNA coated CoMoCAT nanotubes. Two zones are shown in the plot, an upper zone for metallic nanotubes and a bottom zone for semiconducting types. The percentage of metallic nanotubes in this sample is 55%.

To verify our assay, a metallic enriched DNA coated nanotube sample and a semiconducting enriched DNA coated nanotube sample were similarly characterized using this assay. Both samples were prepared by the ion exchange chromatography (IEX) method described in Chapter 1 and provided by our collaborator Ming Zheng. Absorption spectra confirm the enrichment of metallic nanotubes in the first sample, and then enrichment of semiconducting nanotubes in the second sample. Figure 2.8 shows the absorption spectrum, topographic image, dielectric image, and signal *versus* D^2 plot for the metallic nanotube enriched sample. As the absorption spectrum (Figure 2.8A) indicates that most of the nanotubes are metallic, the signal *versus* D^2 plot also shows that

90% of the measured data from EFM are located in the upper metallic zone. Therefore, the results from absorption spectra and EFM assay are consistent, and EFM assay can further provide an accurate value for metallic nanotube content.

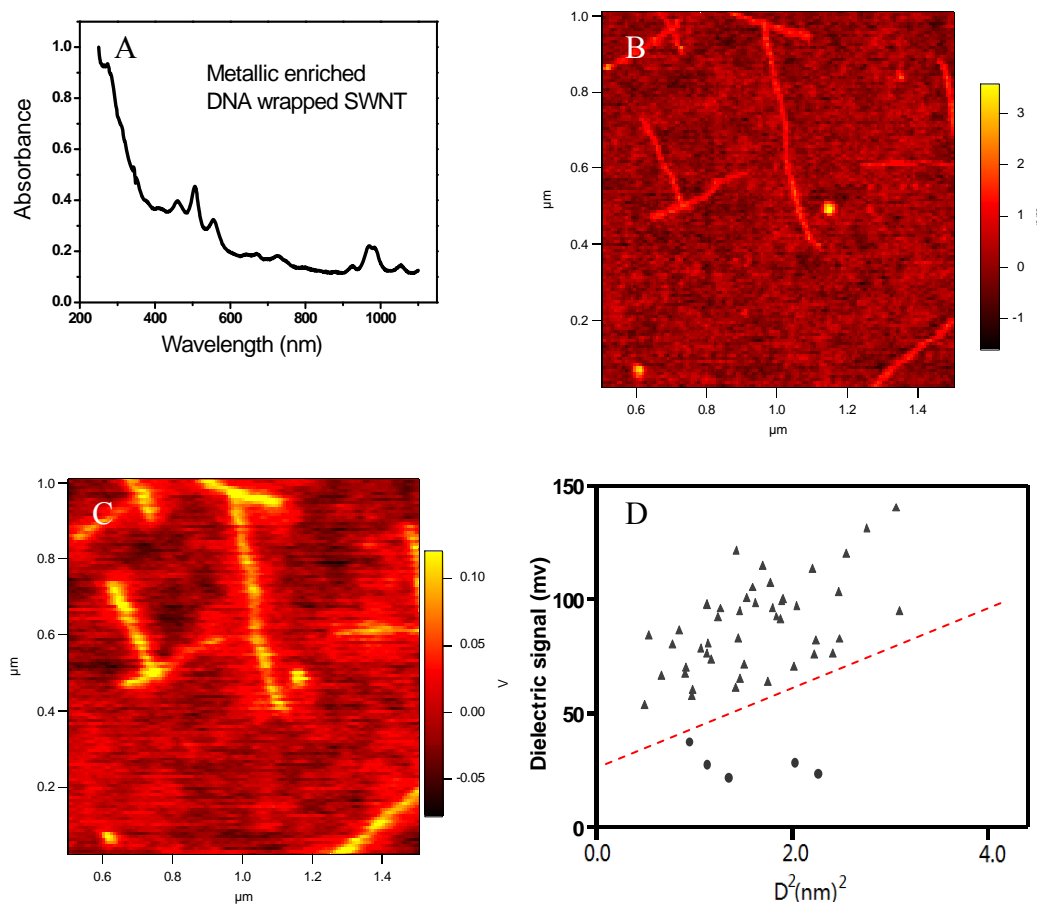


Figure 2.8 (A) absorption spectrum, (B) Topography image, (C) dielectric image, and (d) dielectric signal *versus* D^2 plot of the metallic enriched DNA nanotube sample. As the absorption spectrum indicates most nanotubes in this sample are metallic, the signal *versus* D^2 plot quantitatively shows a 90% metallic content in this sample.

The other semiconducting enriched sample was analyzed using the EFM assay. Figure 2.9 shows the absorption spectrum, topographic image, dielectric image and dielectric signal *versus* D^2 plot of the semiconducting enriched nanotube sample. From the absorption spectrum, most of the nanotubes in this sample were semiconducting, as the major absorption peaks are in the S11 and S22 regions. The signal *versus* D^2 graph also shows that 85% of the data are located in the bottom of the graph, the semiconducting zone, while only 15% data are in the upper metallic zone.

Figure 2.10 corresponds to plotted combined data from the metallic enriched sample and the semiconducting enriched sample together in the signal *versus* D^2 graph. All data from these two samples remain in two discrete zones after their combination. As discussed above, nanotubes in the top zone correspond to metallic types and those in the bottom zone correspond to semiconducting types. Therefore, metallic nanotubes and semiconducting nanotubes have been differentiated and the metallic-to-semiconducting ratio can be determined from the plot.

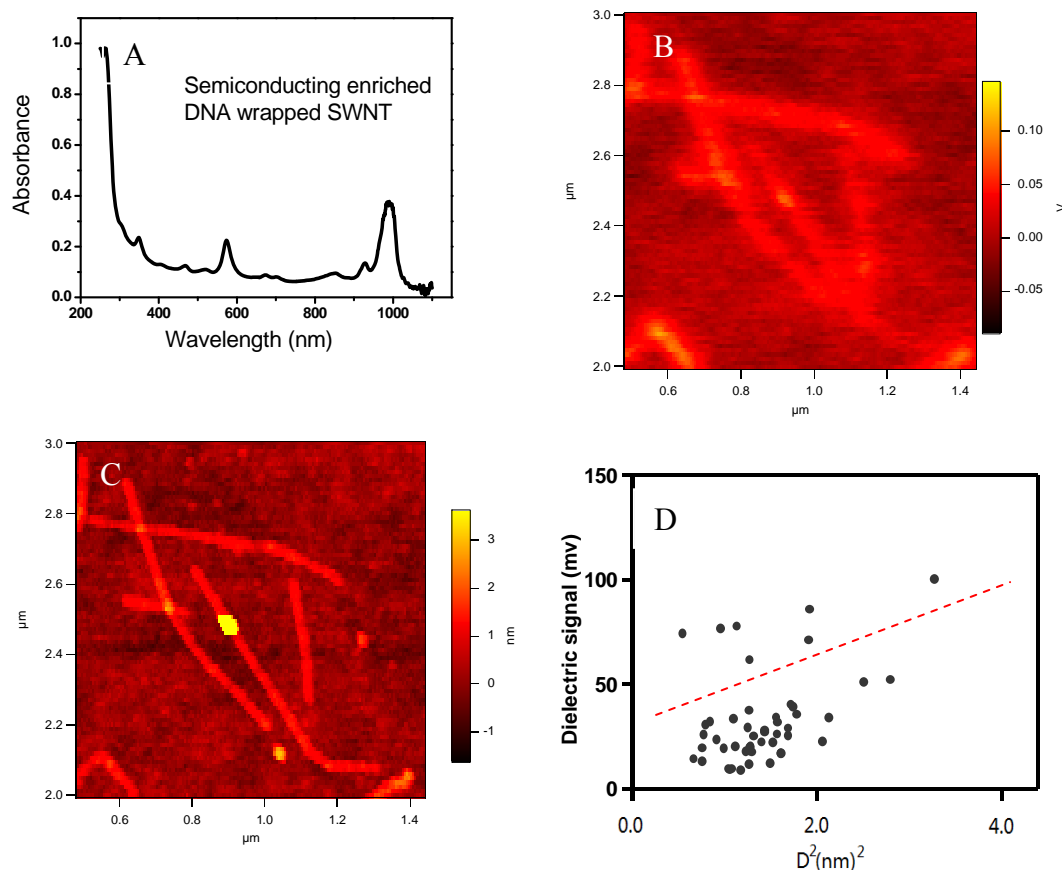


Figure 2.9 (A) absorption spectrum, (B) Topography image, (C) dielectric image, and (D) dielectric signal *versus* D^2 plot of the semiconducting enriched DNA nanotube sample. As the absorption spectrum indicates most nanotubes in this sample are semiconducting, the signal *versus* D^2 plot quantitatively shows an 85% semiconducting content in this sample.

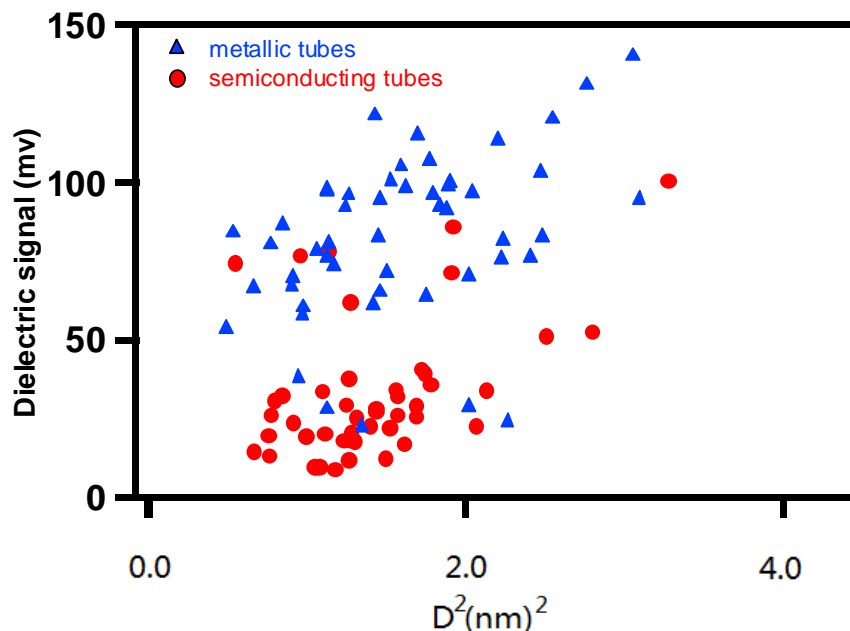


Figure 2.10 Dielectric signal *versus* D^2 plot for both metallic enriched sample and semiconducting enriched sample. (Triangle dots from metallic enriched sample and diamond dots from semiconducting enriched sample)

The EFM assay was further studied by mixing semiconducting enriched nanotube samples with metallic enriched samples in five different volume ratios ($\text{Vol}_B/\text{Vol}_A+\text{Vol}_B$). Figure 2.11 shows topographic images, dielectric images and dielectric signal *versus* D^2 plots for mixture solutions at 0%, 33%, 50%, 67% and 100% volume of the metallic enriched sample, respectively. Those volume ratios (0%, 33%, 50%, 67% and 100%) do not represent the real metallic contents in nanotube mixtures because not 100% tubes in the metallic enriched sample were metallic ones and not 100% tubes in the semiconducting enriched sample were semiconducting types. From the signal *versus* D^2 plots, the determined metallic contents from EFM for five mixed solutions are gradually increased as the volume ratio of metallic enriched sample increased in the

mixed solutions. These two increasing trends are also consistent quantitatively, indicating our EFM assay is sensitive to the change of sample composition.

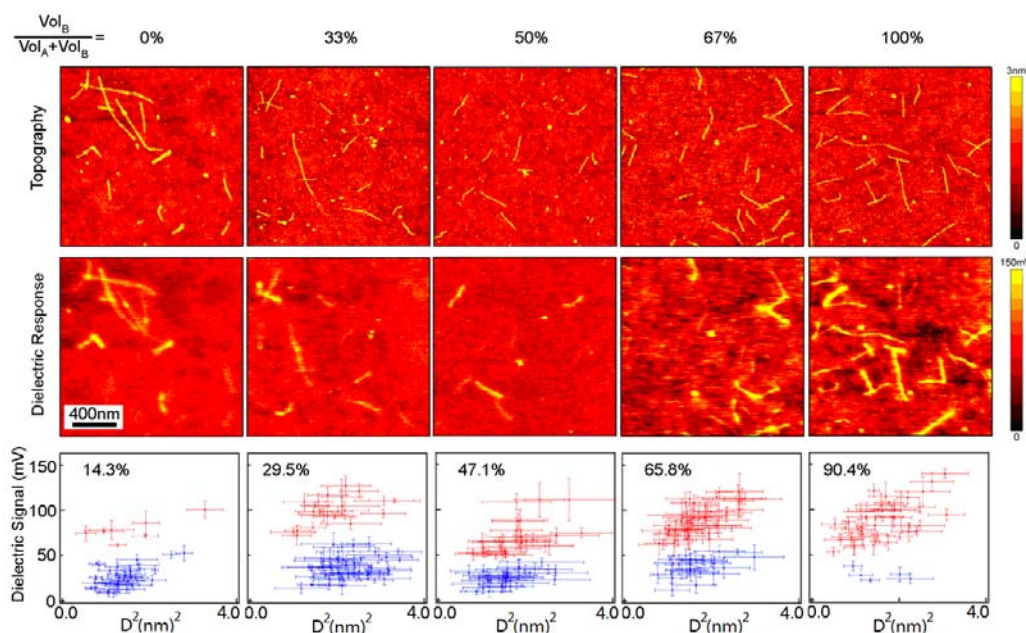


Figure 2.11 Dielectric signal versus D² plot for five mixed nanotube solutions from metallic enriched samples and semiconducting enriched samples. The determined metallic contents from EFM consistently increased as the volume ratio of metallic enriched sample increased in the mixed solutions. (Figure reproduced with permission from reference 27)

2.3.2 Length effect on dielectric response

The data discussed above are all derived from DNA coated nanotubes. DNA can help to disperse nanotube bundles to individual ones, without changing their properties⁸⁴. However, it is impractical to treat all nanotube samples with DNA. Therefore, the EFM assay was further developed on pristine individual nanotubes without any additives. At the same time, it was determined that nanotubes shorter than 200 nm only exhibited low

dielectric signal (<20mV), indicating all short nanotubes were semiconducting types. However, the electric properties of nanotubes should not be length sensitive, both long and short nanotubes should have similar relative metallicity to semiconductivity ratios (M/S). The possible reason for this length effect is due to the defects concentrated at the ends of nanotubes¹⁶⁴. According to the Drude model, the dielectric response of metals can be expressed in the equations 2.1¹⁶⁵, where is $\tilde{\epsilon}$ the dielectric constants, σ is the conductivity, and ω is the angular frequency:

$$\tilde{\epsilon} \approx \epsilon_0(1 + i(\sigma/\omega)) \approx i(\sigma/\omega) \quad \text{Equation 2.1}$$

and the conductivity σ is related to electron density N , electronic charge e , the average time between collisions τ , and the electron mass m , expressed in equation 2.2. The average time τ can be determined by the electron free mean path l and the electron Fermi velocity v_f , shown in equation 2.3.

$$\sigma = (Ne^2\tau/m) \quad \text{Equation 2.2}$$

$$\tau = (l/v_F) \quad \text{Equation 2.3}$$

A one-dimensional structure nanotube usually has an electron free mean path from several hundred nanometers to several micrometers. But for a metallic nanotube short than this length, the defects on the tube ends can significantly reduce the conductivity¹⁶⁶. Therefore, low dielectric signal was measured on short nanotubes.

Figure 2.12 shows the plot of dielectric signal *versus* length of nanotubes¹⁶⁴. For nanotubes which are longer than 200nm, metallic nanotubes and semiconducting nanotubes can be distinguished because two zones are present. Nanotubes short than 200

nm are undistinguishable, as no obvious two zones are shown. More details have been published in reference 166.

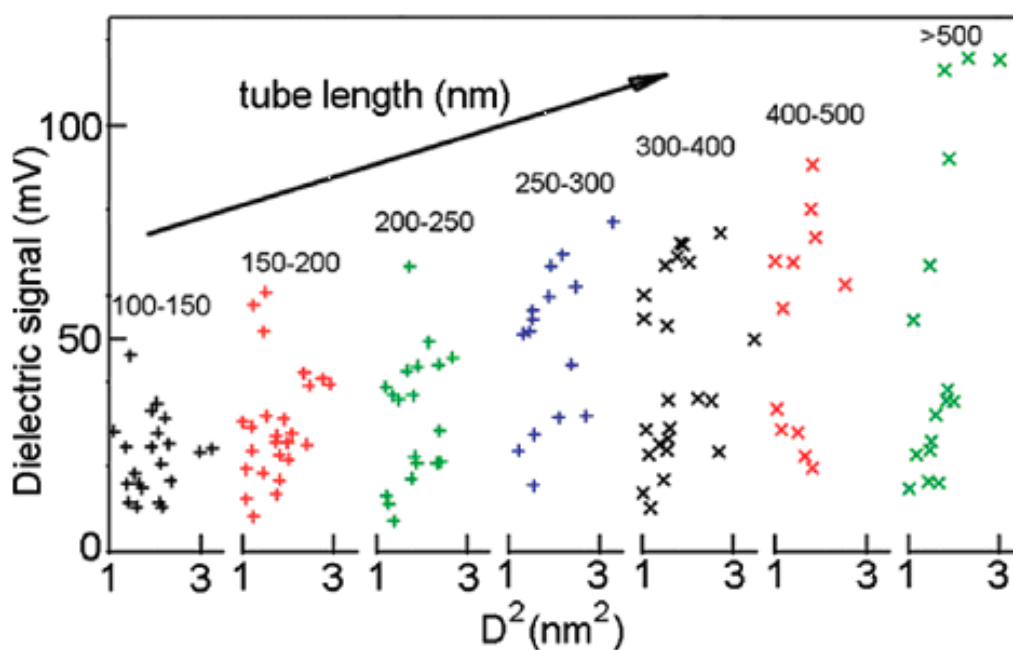


Figure 2.12 Dielectric signals *versus* diameter square in different length ranges. Metallic nanotubes and semiconducting nanotubes are distinguishable when their lengths are larger than 200 nm. (Figure reproduced with permission from 166).

2.3.3 Dielectric response and metallic content of commercial nanotube samples

Further development of this assay was focused on the long (>500nm), low-defect individual nanotubes. All following nanotube samples were prepared by sonicating raw nanotube bundles in 1,2 dichloroethane solvent for 15 minutes¹⁶⁷. The low power of the bath sonicator and short sonication time can help to decrease the induction of defects. Figure 2.13 shows topographic and dielectric images of laser ablation nanotubes. Most

of the nanotubes dispersed on the substrate are longer than 300 nm, and nanotubes shorter than 200 nm and tube bundles are not included in the statistical results.

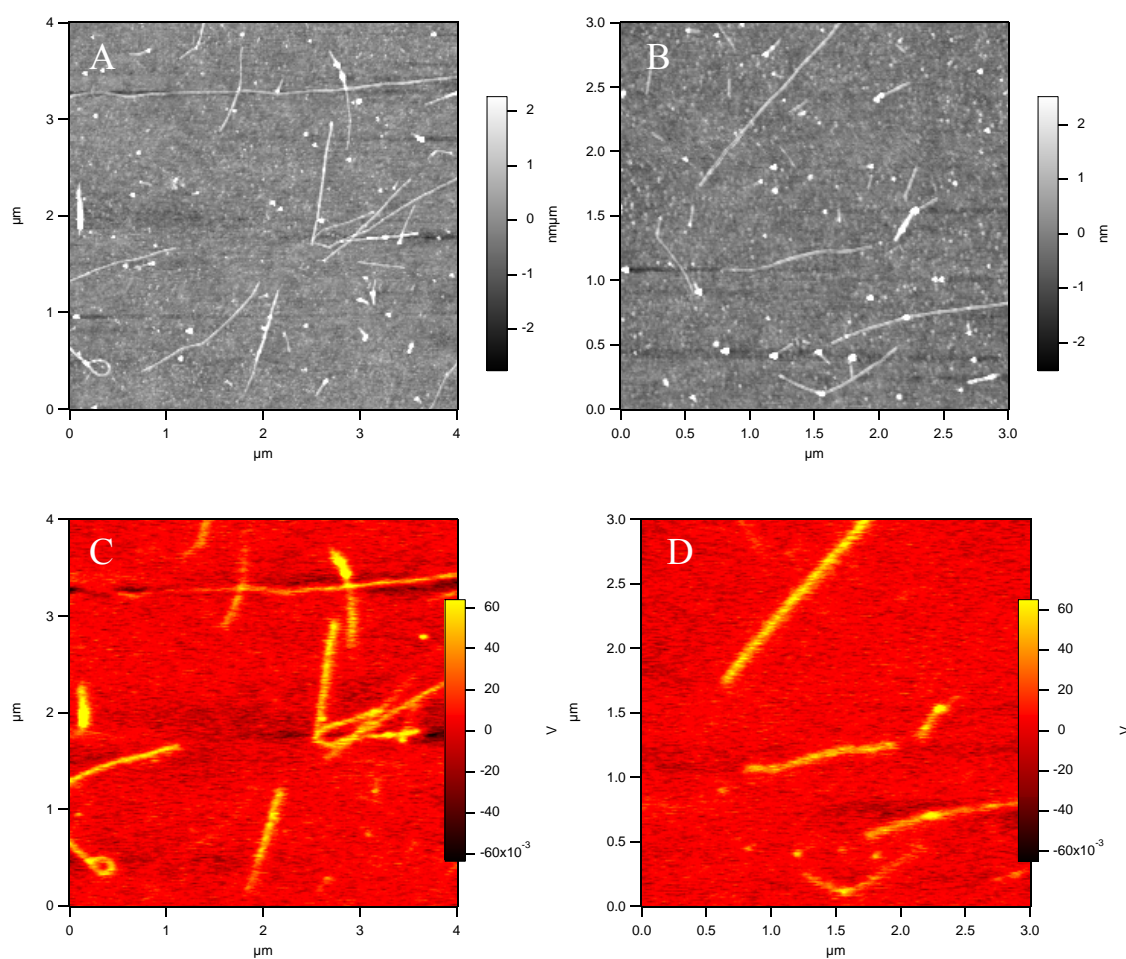


Figure 2.13 Topographic images (A, B) and dielectric images (C, D) for laser ablation nanotubes dispersed with 1,2-dichloroethane in a bath sonicator.

Figure 2.14 shows the dielectric signal *versus* D^2 plot for laser ablation nanotubes. The metallic zone and semiconducting zones are shown in the plot and 49% of nanotubes are metallic.

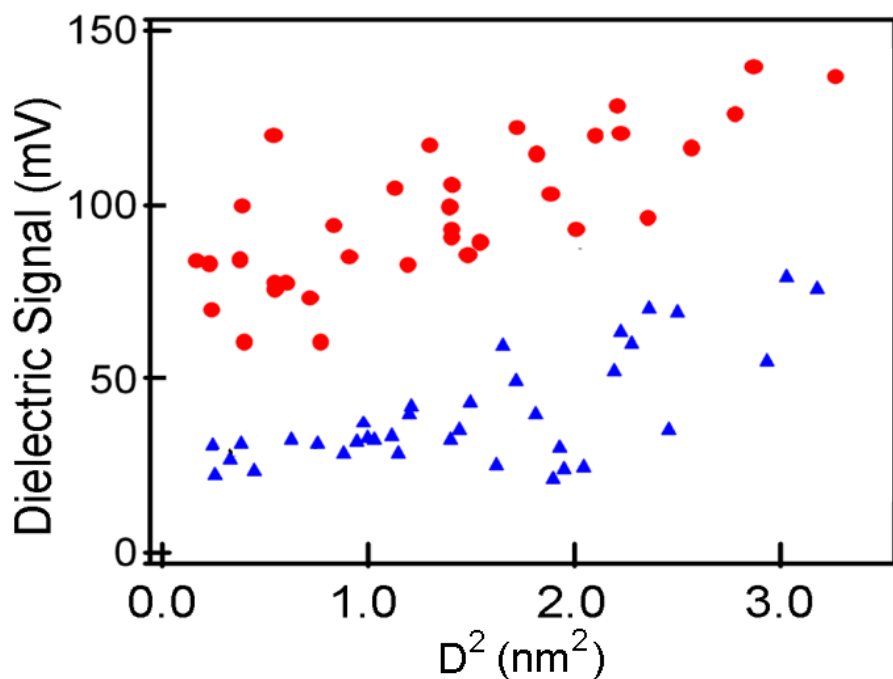


Figure 2.14 Dielectric signal *versus* D^2 plot for laser ablation nanotubes. The percentage of metallic nanotubes in this sample is 49%.

The same dispersion method was applied on commercial HiPco and CoMoCAT nanotube samples. Figure 2.15 shows the topographic images (A,B) and corresponding dielectric images (C,D) for HiPco nanotubes. The results from 170 nanotubes in the dielectric signal *versus* D^2 plot (Figure 2.16) indicates that 28% of the nanotubes in this sample are metallic. A metallic content of $28\% \pm 6\%$ for this HiPco sample was determined after three repeated EFM measurements.

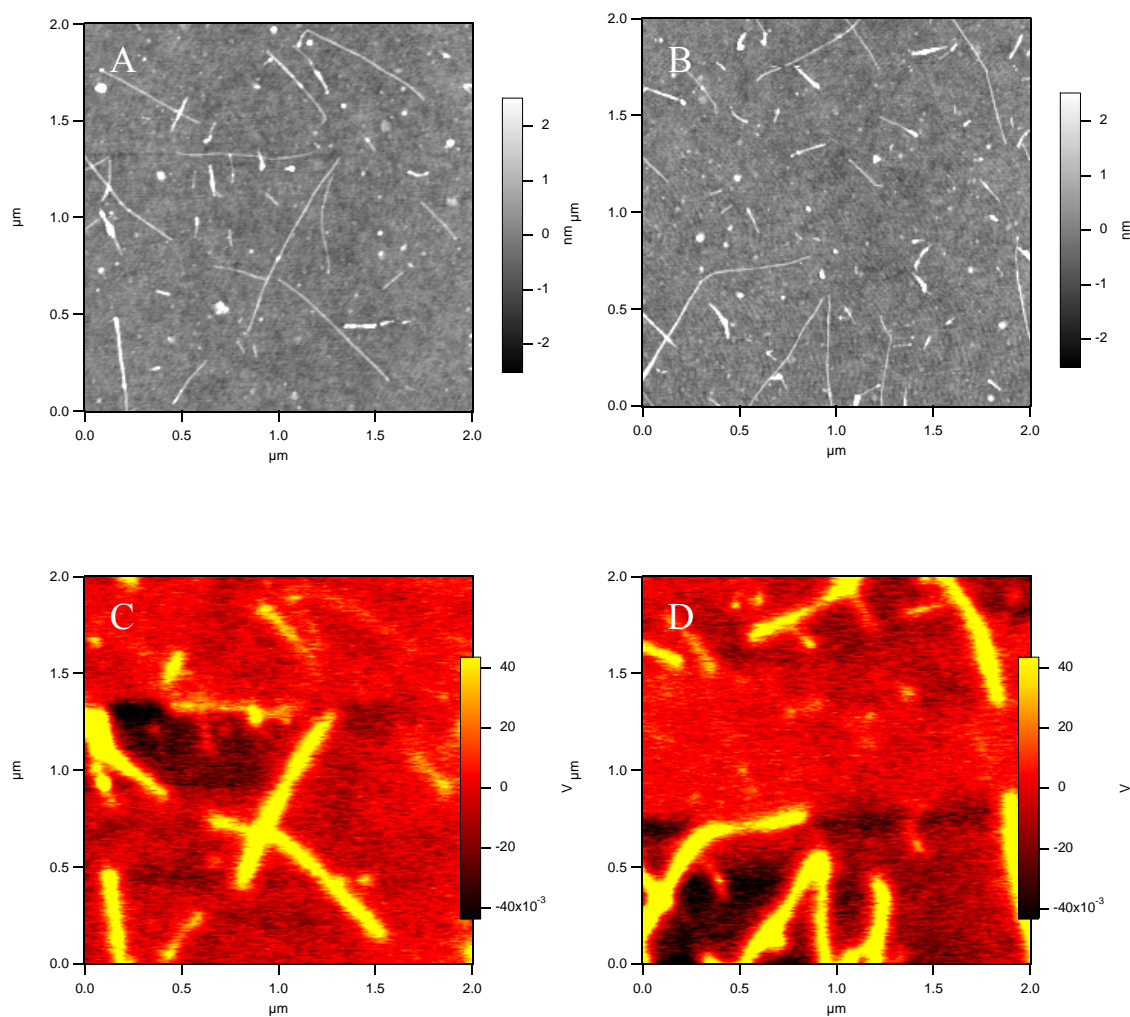


Figure 2.15 Topographic images (A, B) and dielectric images (C, D) for HiPco nanotubes dispersed through 1,2-dichloroethane in a bath sonicator.

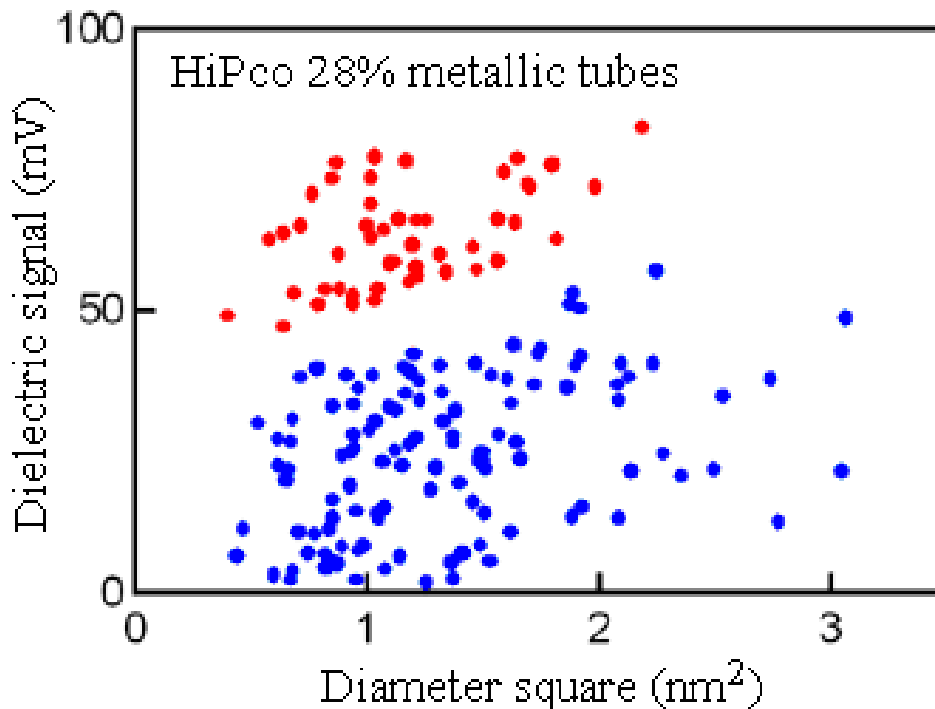


Figure 2.16 Dielectric signal *versus* D^2 plot for HiPco nanotubes. The percentage of metallic nanotubes in this sample is 28%.

Figure 2.17 shows the topographic images and dielectric images of CoMoCAT65 nanotubes. This commercial sample has been claimed to contain mostly semiconducting nanotubes, ideally (6, 5) species, by the manufacturer. The results shown in the dielectric signal *versus* D^2 plot (Figure 2.18) from more than 100 nanotubes show that the metallic content of this sample is 14%. A metallic content of $14\% \pm 5\%$ for this sample was determined after three repeated EFM measurements. However, the wide diameter distribution in this sample indicates the selective synthesis of (6, 5) species in the sample is not as good as been claimed by the manufacturer. Therefore, EFM assay can be applied to verify the quality of commercial samples.

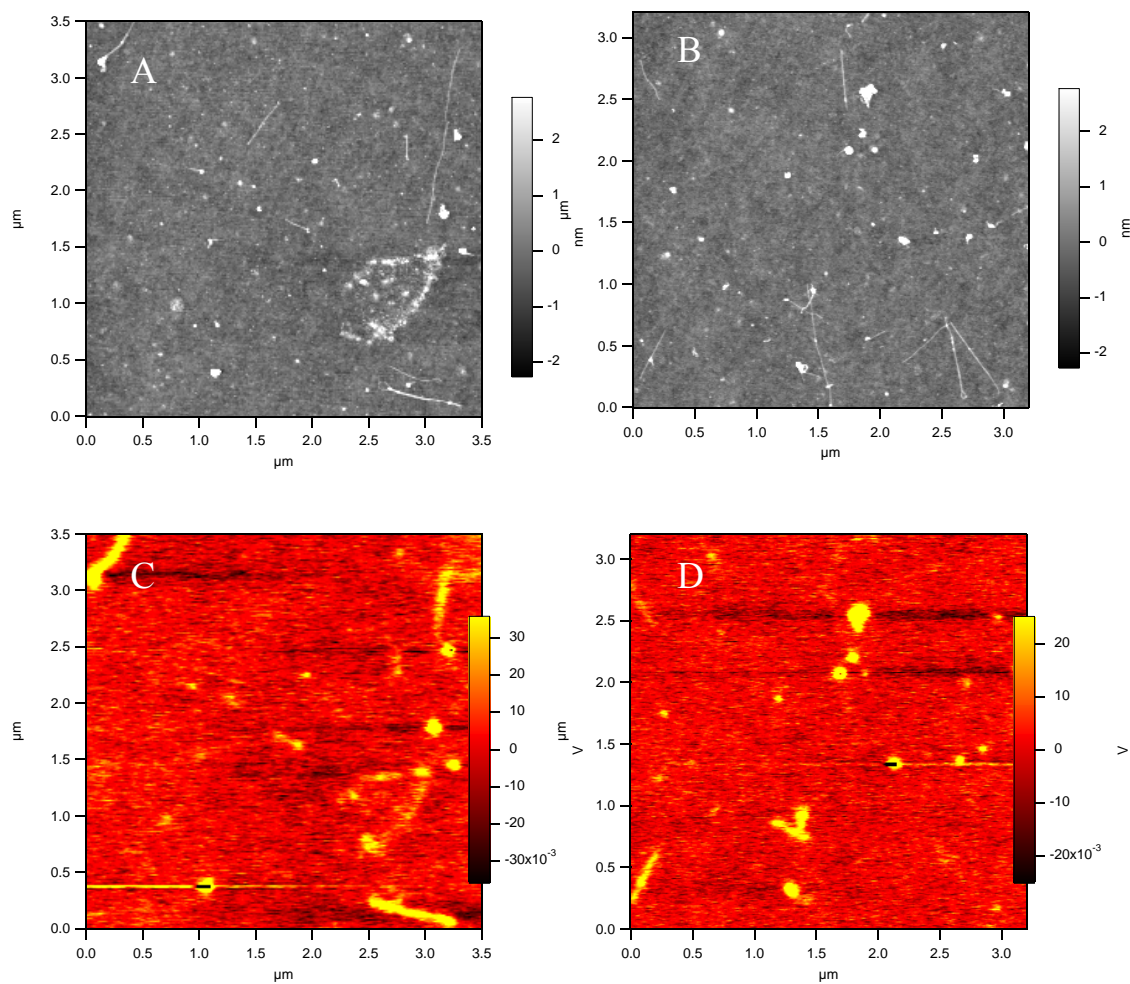


Figure 2.17 Topographic images (A, B) for and dielectric images (C, D) CoMoCAT65 nanotubes dispersed through 1,2-dichloroethane in a bath sonicator.

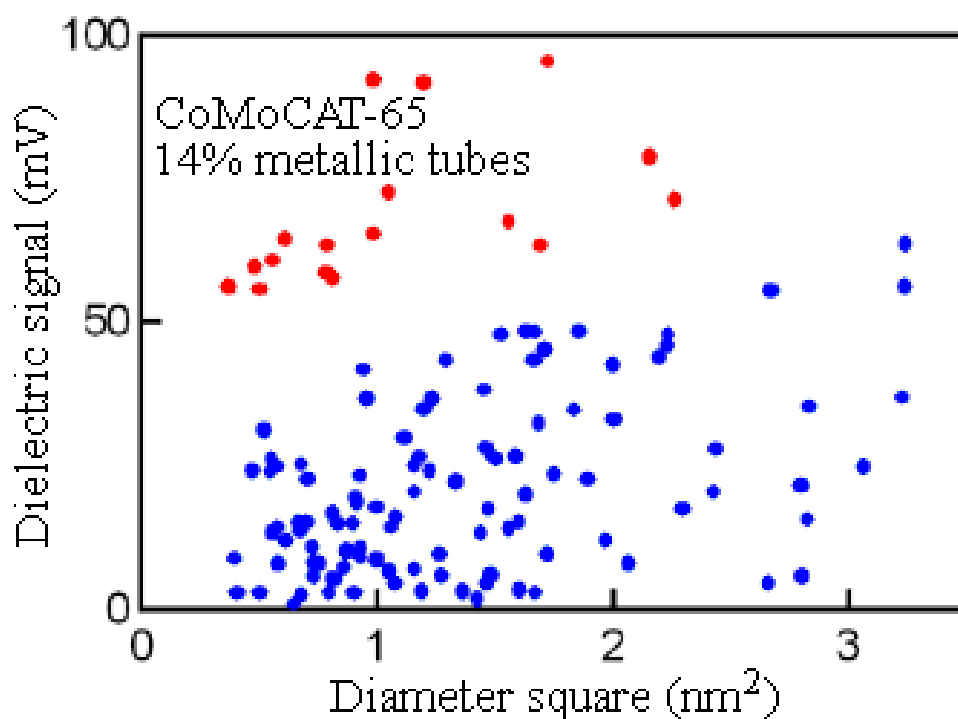


Figure 2.18 Dielectric signal *versus* D^2 plot for CoMoCAT65 nanotubes. The percentage of metallic nanotubes in this sample is 14%.

Although the theoretical metallic contents for as-synthesized nanotube samples are $\sim 33\%$ ¹⁴⁷, different metallicities have been determined using EFM measurements on DNA coated HiPco, DNA-coated CoMoCAT, commercial laser ablation, commercial HiPco, and commercial CoMoCAT65 nanotube samples. For DNA-coated HiPco nanotubes and commercial HiPco nanotubes, each exhibits different metallic contents even though they were synthesized using the high pressure CO conversion method. This indicates the metallic content in a sample actually depends on the specific synthesis condition and subsequent treatments relating to dispersion and separation.

2.3.4 Verification of EFM assay via absorption and Raman spectra

In order to further verify our EFM assay, optical techniques were applied to independently determine the electronic properties of nanotubes. Figure 2.19 shows the statistical results (dielectric signal *versus* D^2 plot) and absorption spectra for commercial HiPco (A, B) and CoMoCAT65 (C, D) nanotubes samples. As discussed above, it was determined that HiPco nanotubes contain ~30% metallic types and CoMoCAT65 contains ~10% metallic nanotubes from the EFM assay. Absorption spectra (Figure 19 B,D) also show similar trends, that the CoMoCAT65 sample contains a higher semiconducting content than the HiPco sample, as two strong peaks exist in S11 (900~1100 nm) and S22 (550~900 nm) regions of its absorption spectrum. However, the absorption spectrum only qualitatively shows the metallic percentage in those two samples, but does not provide quantitative values.

In the next step, Raman spectroscopy was applied to examine the EFM assay, because Raman spectroscopy is a well-established technique for determining the electronic type of individual nanotubes¹⁶⁸. Therefore, the strategy was to select a specific nanotube and measure its electronic property using both EFM and Raman spectroscopy, and then compare results from both techniques. A Si substrate with photolithography markers was used to help locate the same nanotube in both instruments. Figure 2.20 shows the topographic image of the marker substrate. In a 50 μm by 50 μm area, 81 markers with different shapes were made on the Si substrate through photolithography. Therefore, by observing the unique shapes of each marker, the same nanotubes can be found in both AFM and Raman spectrometer. For example, Figure 2.21 shows several

nanotubes inside a square area with four different markers in each corner. After locating every four markers in both EFM and Raman instruments, the dielectric signal and Raman activities can be repeatedly measured on the same tubes.

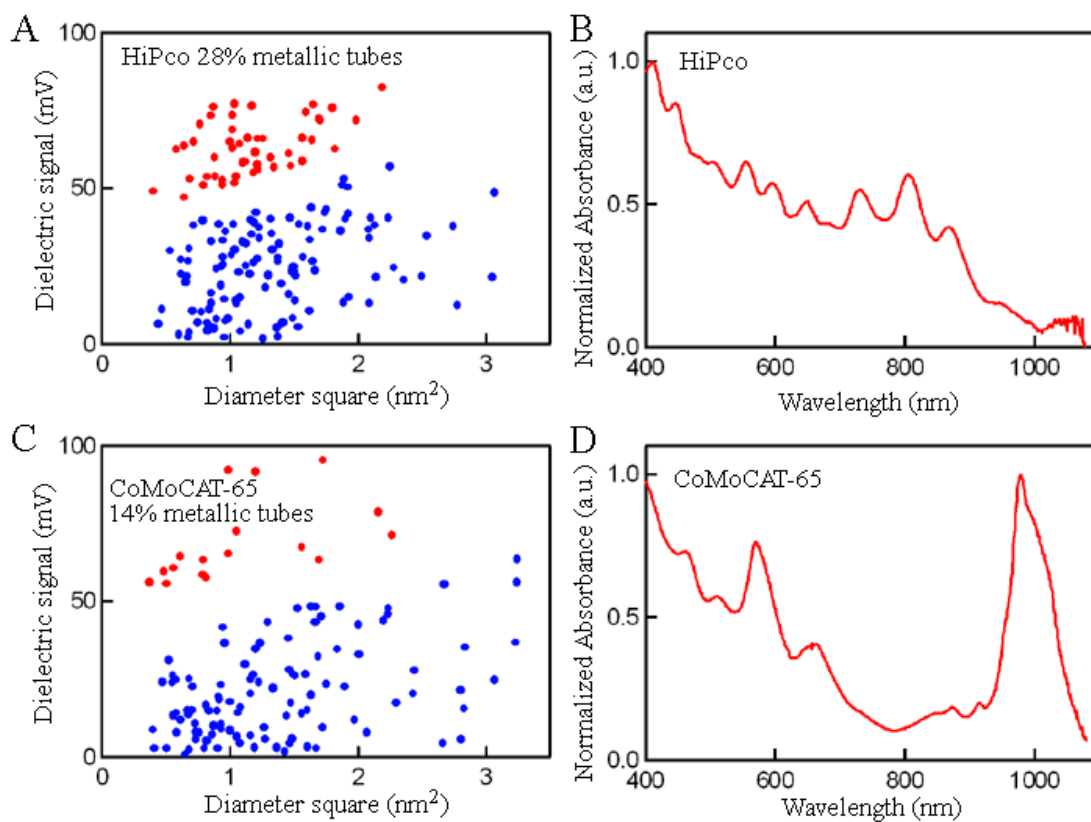


Figure 2.19 Dielectric signal *versus* D^2 plot for (A) HiPco and (C) CoMoCAT65 nanotube samples, and absorption spectra for (B) HiPco and (D) CoMoCAT65 nanotube samples. Both statistical plots and absorption spectra confirm that the HiPco sample has higher metallic content than the CoMoCAT65 sample.

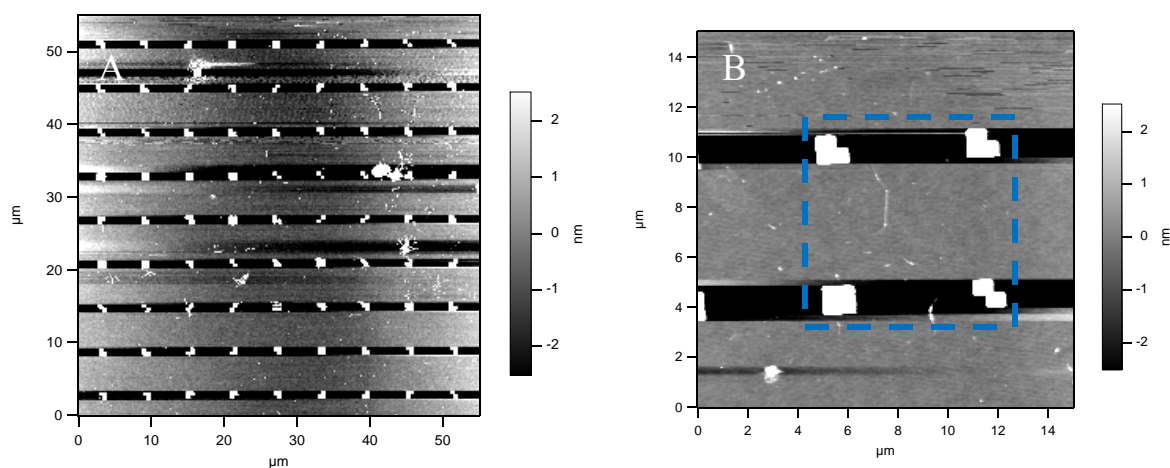


Figure 2.20 AFM images of marker substrate (A, B). By observing the unique shapes of four markers in a square area, nanotubes in this area can be found in both the AFM and Raman instruments.

Figure 2.21 shows the schematic of a WiTec Raman/near-field scanning optical microscope. A 532 nm laser beam was focused on the sample surface and a confocal Raman image was obtained through avalanche photodiode (APD) mode. After confirming the same nanotubes, which were measured in EFM, from the confocal image, the laser beam was moved onto these nanotubes and their Raman spectra were collected through charge coupled detector (CCD) mode.

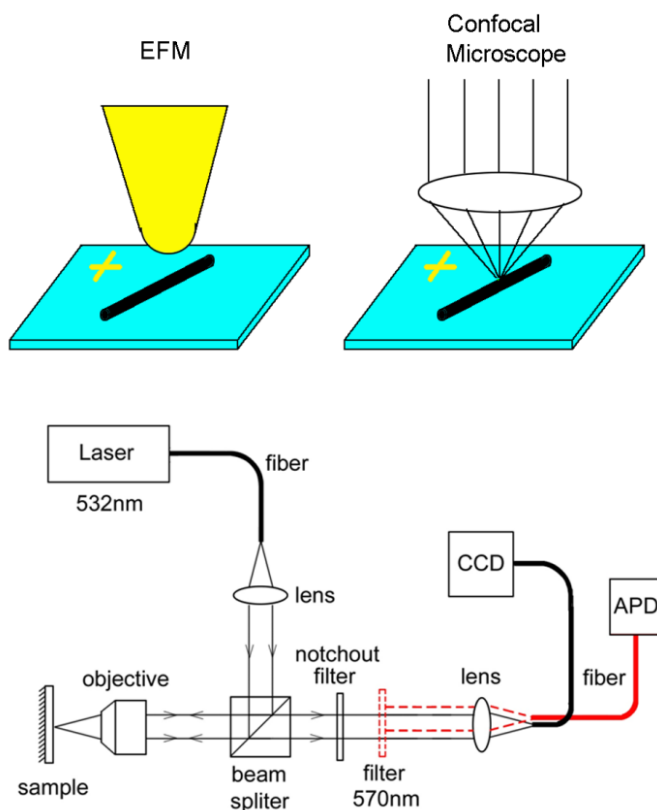


Figure 2.21 Schematic depiction of NOSM instrument which enables Raman spectroscopy in CCD mode and confocal Raman images in APD mode. The sample was first scanned in APF mode and selected nanotubes were located from the confocal images. The laser was focussed on these nanotubes and Raman spectra collected *via* the CCD mode. (Figure reproduced with permission from reference 27).

Figure 2.22 shows the (A) topographic images, (B) confocal Raman images, and (C) dielectric images on the same areas. Nanotubes are clearly shown in both topographic images and dielectric images. However, not every nanotube exhibits uniform signal in confocal Raman images. This is because the confocal Raman images and Raman spectra requires the excitation laser to be in resonance with a van Hove transition energy (E_{ii}) of the nanotube^{99,169}. Furthermore, the defects on the tube sidewall can also decrease the

Raman activities of nanotubes. The Kataura plot, shown in Figure 2.23, shows that only limited nanotubes species which are inside the blue and red circles may have Raman activities at the excitation of 532 nm laser. The blue circle corresponds to semiconducting nanotubes with diameter 0.7 nm – 0.9 nm and the red circle corresponds to metallic nanotubes with diameter 1.1 nm – 1.4 nm.

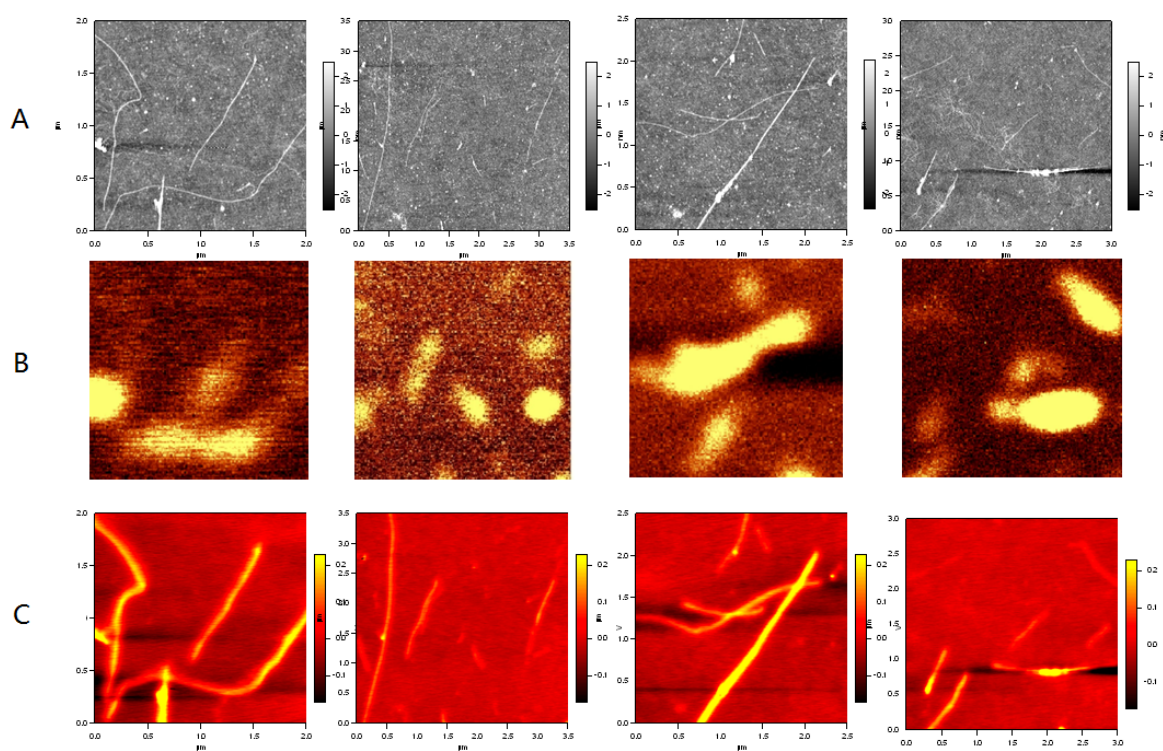


Figure 2.22 (A) AFM images, (B) confocal Raman images and (C) EFM images captured on the same areas.

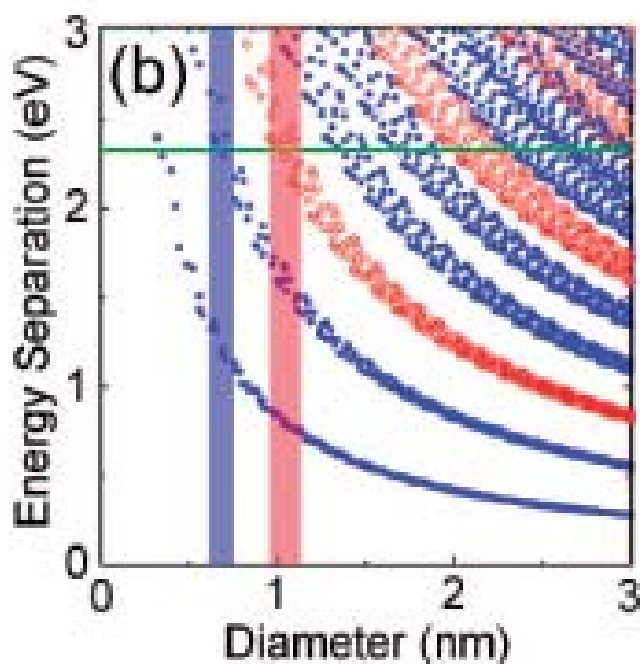


Figure 2.23 Kataura plot shows that the excitation energy for nanotubes at different diameters. The green solid line represents the energy of the 532 nm laser used in Raman spectroscopy. The blue and red circles correspond to the diameter of nanotubes which has Raman activities under the 532 nm laser. (Figures reproduced with permission from reference 27)

Eleven nanotubes, circled in Figure 2.24C, were selected for the collection of Raman spectra, because they exhibited identifiable signals in confocal images. These eleven nanotubes include both metallic types and semiconducting types, as their dielectric signals distribute in the upper metallic zone and the bottom semiconducting zone. However, only two of these eleven nanotubes provided strong and clear Raman features for determining their electronic types. We set these two tubes as target nanotubes for verifying EFM assay using Raman spectra. Figure 2.24 shows the topographic image,

dielectric image, dielectric *versus* D^2 plot for the first target nanotube and the theoretical numerical modeling. This nanotube was firstly determined to be a metallic one from EFM measurements, as its dielectric signal can be found in the upper metallic zone in the dielectric signal *versus* D^2 plot (Figure 2.24 C). The measured diameter of 1.2 ± 0.2 nm for this target nanotube confirmed it can have Raman activities at the excitation of 532 nm laser.

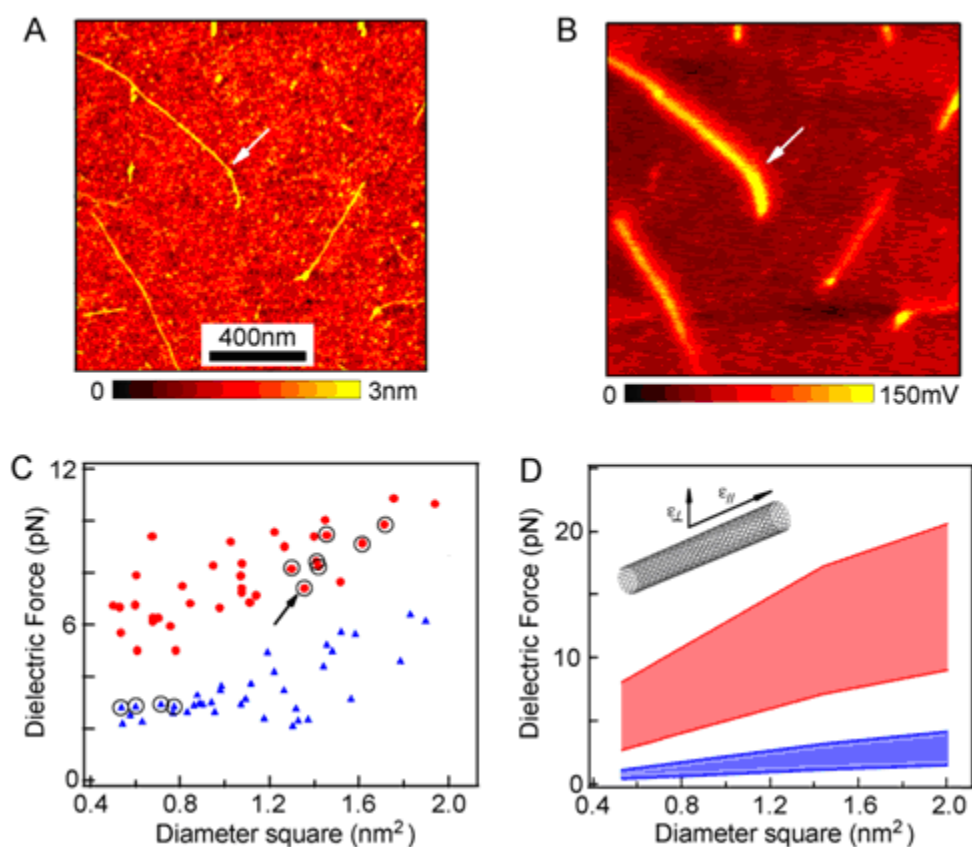


Figure 2.24 (A) topographic image; (B) dielectric image; (C) dielectric *versus* D^2 plot from experimental data; (D) dielectric *versus* D^2 plot from numerical modeling; From EFM measurements, the target nanotube pointed by the white arrow is a metallic nanotube because its dielectric signal is located in the upper metallic zone of the dielectric signal *versus* D^2 plot.

After the target nanotube was found again in the confocal Raman image (Figure 2.25 A) using the procedure discussed above, the instrument was switched to CCD mode to collect its Raman spectra. Figure 2.25B shows the G band and RBM band features from the target nanotube. Its G band shows a broad Breit-Wigner-Fano line, indicating it is a metallic nanotube. The RBM peak for this target nanotube, at 222 cm^{-1} , can be assigned to (11, 5) species which is also a metallic species. Therefore, both the G band and RBM band Raman spectra have confirmed that the target nanotube, which was assigned as metallic by EFM assay, is of metallic type. The capability of our EFM assay has also been verified by Raman technique.

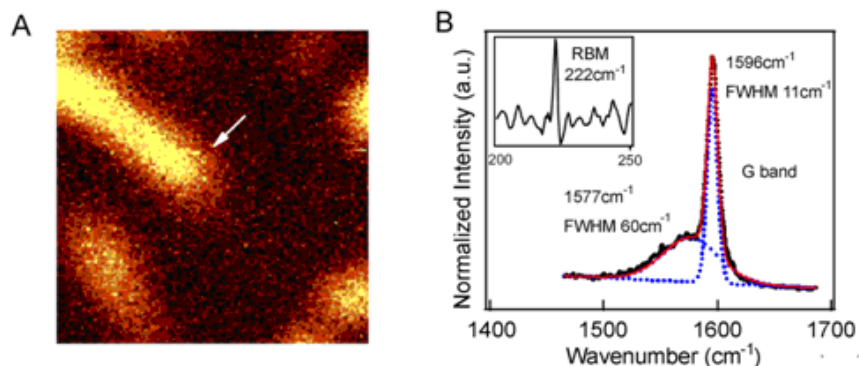


Figure 2.25 (A) confocal Raman image; (B) G band and RBM band features. Both the G band and RBM band Raman spectra have confirmed that the target nanotube is of metallic type.

Such verification of EFM using Raman technique was repeated on the other target nanotube. Figure 2.26 shows the topographic image, dielectric image, dielectric *versus* D^2 plot for the second target nanotube and the theoretical numerical modeling. This nanotube was also a metallic one determined by EFM assay, as it's dielectric signal can

be found in the upper metallic zone (Figure 2.26C), pointed by a black arrow. The measured diameter of 1.3 ± 0.2 nm for this target nanotube confirmed it can have Raman activities at the excitation of 532 nm laser.

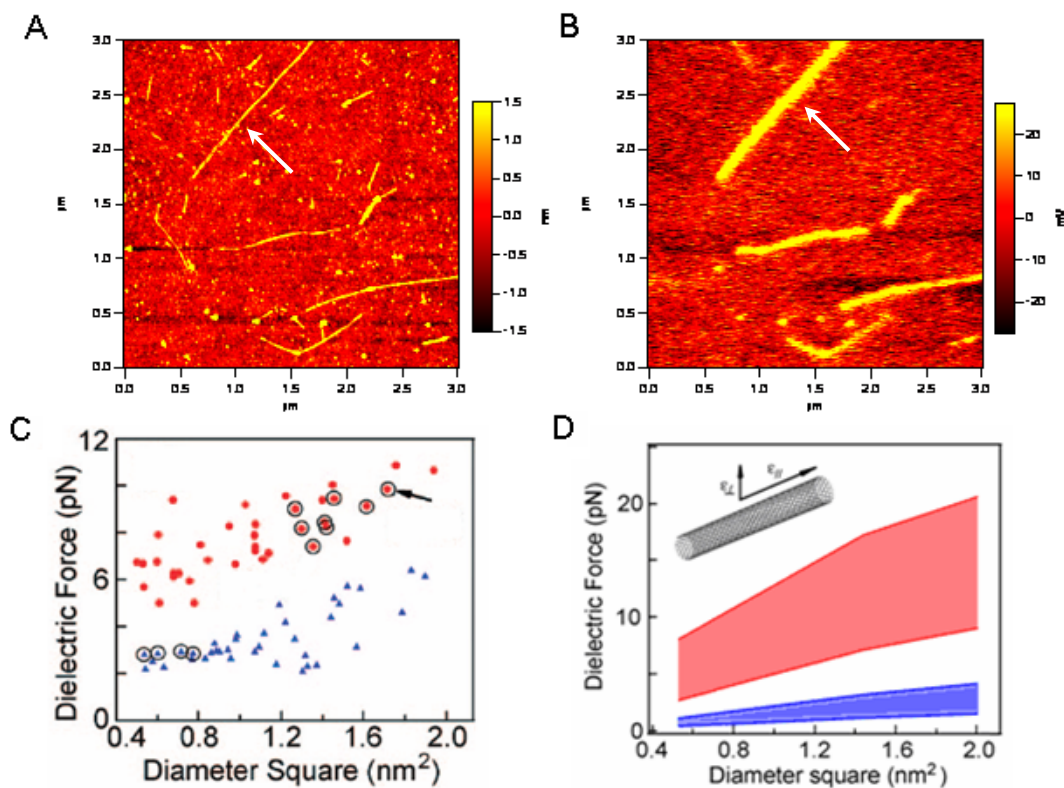


Figure 2.26 (A) topographic image; (B) dielectric image; (C) dielectric *versus* D^2 plot from experimental data; (D) dielectric *versus* D^2 plot from numerical modeling; From EFM measurements, the target nanotube pointed by the white arrow is a metallic nanotube because its dielectric signal is located in the upper metallic zone of the dielectric signal *versus* D^2 plot.

This target nanotube was found again in the confocal Raman image (Figure 2.27 A), although the signal is not as strong as the previous (11, 5) nanotube (Figure 2.25 A).

The relative lower signal of this nanotube could be due to the higher defect density on the tube sidewall. The Raman spectra of this nanotube were collected in CCD mode. Figure 2.27B shows the G band and RMB band from the target nanotube. Its G band shows a broad Breit-Wigner-Fano line, indicating it is a metallic nanotube. The RBM peak for this target nanotube, at 181 cm^{-1} , can be assigned to a metallic species of (13, 7).

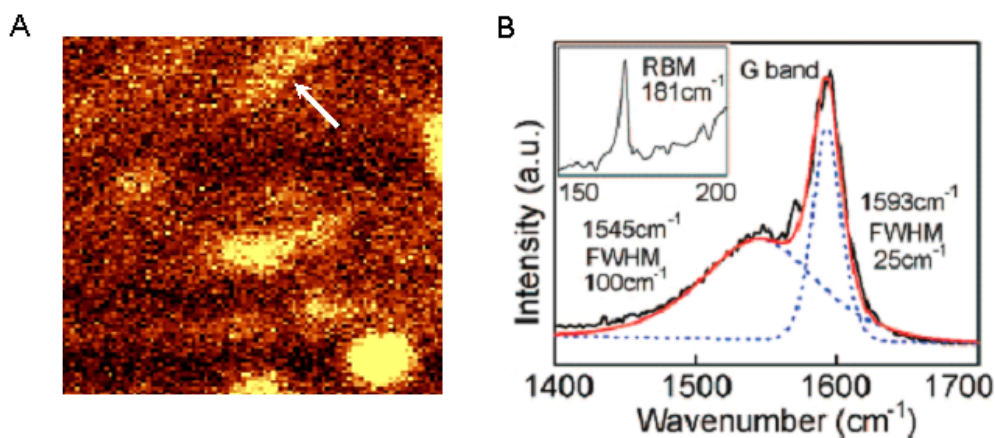


Figure 2.27 (A) confocal Raman image; (B) G band and RBM band features. Both the G band and RBM band Raman spectra have confirmed that the target nanotube is of metallic type.

Therefore, the Raman spectra have again confirmed the metallic assignment from EFM measurements for the second target nanotube. Table 2.1 lists the information of two target nanotubes from Raman spectra and EFM measurements. Although Raman spectra provide very detailed information for nanotubes, the quantitative metallic content of a nanotube sample is still unknown from Raman spectra. Comparing with Raman, EFM assay not only determines the electronic property of nanotubes, but also provides quantitative measurements for the metallicity of nanotube samples.

Table 2.1 Information of two target nanotubes from Raman and EFM measurements.

Nanotube:	Nanotube 1 (Figure 2.25, 2.26)	Nanotube 2 (Figure 2.27, 2.28)
RBM (cm^{-1})	222	181
$d_t = \alpha/\omega_{RBM}$ (nm) ($\alpha = 248 \text{ nm cm}^{-1}$)	1.12	1.37
d_{AFM} (nm)	1.2 ± 0.2	1.3 ± 0.2
$n^2 + m^2 + nm = (\pi dt/a)^2$ ($a = 2.46 \text{ \AA}$)	204	306
Possible (n, m)	(11,5)	(13,7)
$n^2 + m^2 + nm$	201	309
$\omega(G^-)$ (cm^{-1})	1577	1545
FWHM (G^-) (cm^{-1})	60	100
$\omega(G^+)$ (cm^{-1})	1596	1593
FWHM (G^+) (cm^{-1})	11	25
Metallic or semiconducting from Raman spectra	Metallic	Metallic
Metallic or semiconducting from EFM measurements	Metallic	Metallic

2.4 Conclusions

In this chapter, a probe assay for nanotube metallicity has been developed. After applying a bias on a conductive tip, nanotubes are polarized and induced dipoles are created on the tube sidewalls. Metallic nanotubes which have higher dielectric constants than semiconducting ones exhibit significant higher dielectric signal than semiconducting nanotubes. Therefore, the dielectric responses of nanotubes in the electric field are collected to differentiate nanotubes by electronic types. In a dielectric signal *versus* diameter square plot, data points usually distribute to two separated zones. The upper zone is for metallic nanotube with higher signal while the bottom zone is for semiconducting types. By counting the number of data points in each zone, the metallic-to-semiconducting ratio, as well as the metallic percentage, can be determined. This method has been applied for DNA-coated nanotube samples and commercial nanotube samples synthesized by different methods, and repeatable results were obtained. This assay was further verified by optical spectroscopy techniques. The percentage change of metallic nanotubes in different samples determined by EFM assay is consistent with the absorption spectra. The further Raman spectra of selected nanotubes also confirmed that the capability of EFM to determine the electronic type of nanotubes without any limitation on nanotube species.

Chapter 3. Microwave Irradiation of Single Walled Carbon Nanotubes

(Part of the work in this chapter has been published in *Appl Phys A* (2010), 102(2), 401-406.)

3.1 Introduction

Since dielectric properties of nanotubes can be utilized for differentiation of metallic and semiconducting nanotubes, in this chapter the microwave irradiation effect on nanotubes, towards the selective etching metallic nanotubes based on their high conductivity and high dielectric polarizability, is studied. Microwave irradiation has been reported to assist the covalent functionalization of nanotubes¹⁷⁰⁻¹⁷¹, and to remove catalyst particles in nanotubes by significantly raising the local temperature and oxidize the surface of catalyst particles¹⁷²⁻¹⁷³. However, the irradiation effects on pristine nanotubes without any additives have not yet been well studied. It has been reported previously that microwave energy can be absorbed by nanotubes and induced current is generated on their sidewalls¹⁷⁴. When the current is high enough, the sidewall of nanotubes can be destroyed by the excessive heat. Because the conductivity of metallic tubes is about 10^5 times higher than that of semi-conducting tubes¹⁷⁵, the breakdown of metallic nanotubes occurs more readily due to relative higher currents whereas semiconducting tubes may stay intact when exposed to the same microwave irradiation¹⁷⁶. This principle leads to a potential selective electrical breakdown scheme for nanotube differentiation.

In this project, a convenient method for characterization of nanotube films by measuring their THz transmissions was provided by research collaborators, the Xin group in the University of Arizona. This characterization method was then utilized to study the effects of microwave irradiation on nanotube thin films, which were readily fabricated from nanotube powder and preserved all the properties of the nanotubes while offering ready manipulation for experimentation. Detailed Raman and absorption spectroscopy studies were undertaken to further evaluate irradiation effects.

3.2 Experimental

3.2.1 Materials

The raw nanotube powder samples were purchased from Carbon Nanotechnologies, Inc., Houston, TX. Two types of nanotube samples with different metallic-to-semiconducting ratios were used for comparison (~30% metallic content in HiPco nanotubes and ~10% metallic content in CoMoCAT nanotubes). Nanotubes samples were prepared including individual nanotubes dispersed on Si substrates and nanotube films on glass substrates. To prepare individual nanotubes, raw nanotubes bundles were sonicated in 1,2-dichloroethane for 15 minutes, the resultant suspension was spin-coated onto a Si substrate with special markers. No surfactant or polymer additives were added to assist the dispersion. Due to the special markers on the Si substrate, nanotubes on a specific area can be relocated after irradiation, and thus the morphology of selected nanotubes before and after microwave irradiation can be

compared. Figure 3.1 shows the dispersed individual nanotubes on a Si substrate. Most of the nanotubes in the image were individual nanotubes, with diameters of 1~2 nm.

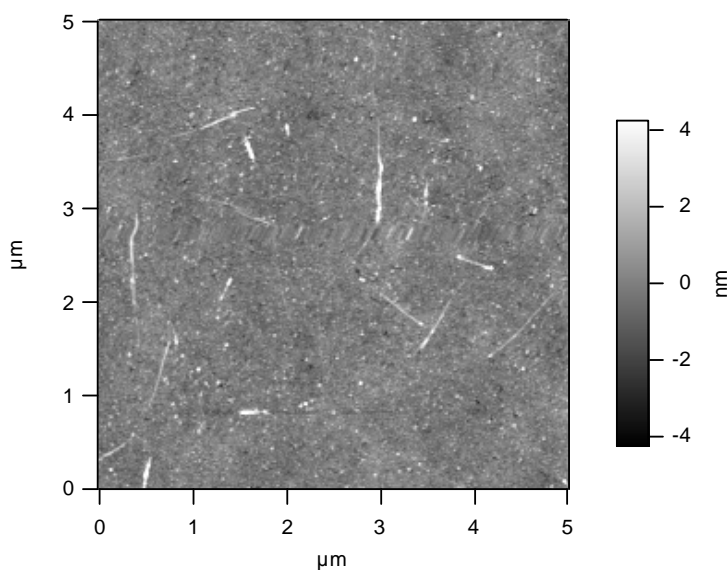


Figure 3.1 Individual nanotubes dispersed on Si substrate *via* sonication in 1,2-dichloroethane.

Nanotube thin films were prepared based on the vacuum-filtration method. Raw nanotube bundles were dispersed in aqueous solution containing 1 wt. % of sodium dodecyl sulfate (SDS) *via* ultrasonication treatment, and centrifuged at 25000 G for 2 hours to remove the catalyst particles. The nanotube suspension was then filtered through a 200nm Millipore polycarbonate membrane. A layer of nanotube thin film was formed on the membrane and SDS was washed away by excess deionized water. After the filtration, the membrane with attached nanotube thin film was quickly transferred onto a glass or quartz substrate, and then immersed in a chloroform bath for 6 hours, leaving the nanotube thin film on the substrate. Finally, thin film samples were dried at 75°C for 3

hours. Figure 3.2 shows the AFM and SEM images of a HiPco nanotube thin film deposited on a glass substrate. The thin film consisted of entangled nanotubes without any catalyst particles, and the thickness of the film was around 30nm (shown in Figure 3.3).

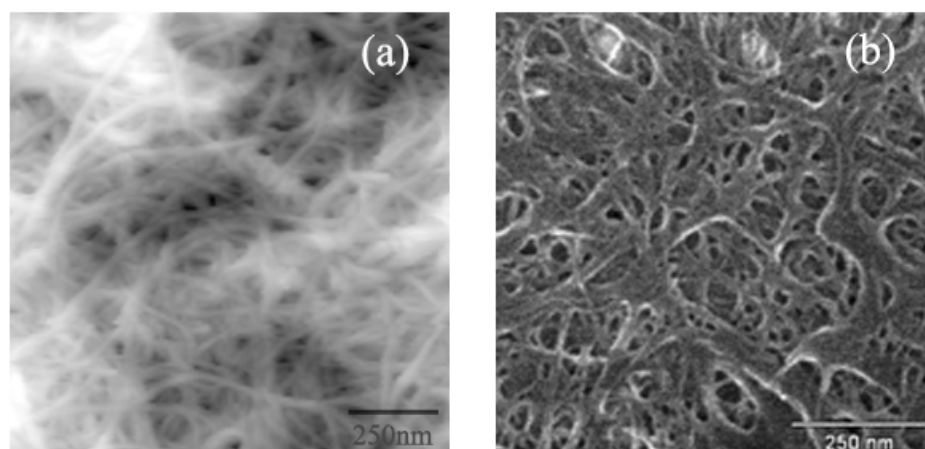


Figure 3.2 (a) AFM image of a HiPCO nanotube thin film; (b) SEM image of a HiPCO nanotube thin film.

3.2.2 Methods

Microwave irradiation was carried out by setting the nanotube samples close to the power-feeding waveguide in a commercial microwave oven (2.45 GHz, 1100 W), where the highest microwave field was located. The samples were fixed in the same position and the power level of the oven was preset to 100% each time. During the irradiation process, The Si substrate dispersed with individual nanotubes remained intact while the thin glass substrates coated with the nanotube thin films often broke from the film center. Bare glass substrates without any nanotubes did not break at all at the same irradiation

condition. Furthermore, the breaking of glass substrates covered with HiPco nanotube thin films (~30% metallic content) happened earlier than the glass substrates covered with CoMoCAT nanotube thin films (~10% metallic content) at the same irradiation. These observations indicate that nanotubes can absorb microwave energy and convert it to excessive heat, causing the breaking of the glass substrate. The increase of metallic content in nanotube samples can further accelerate this process.

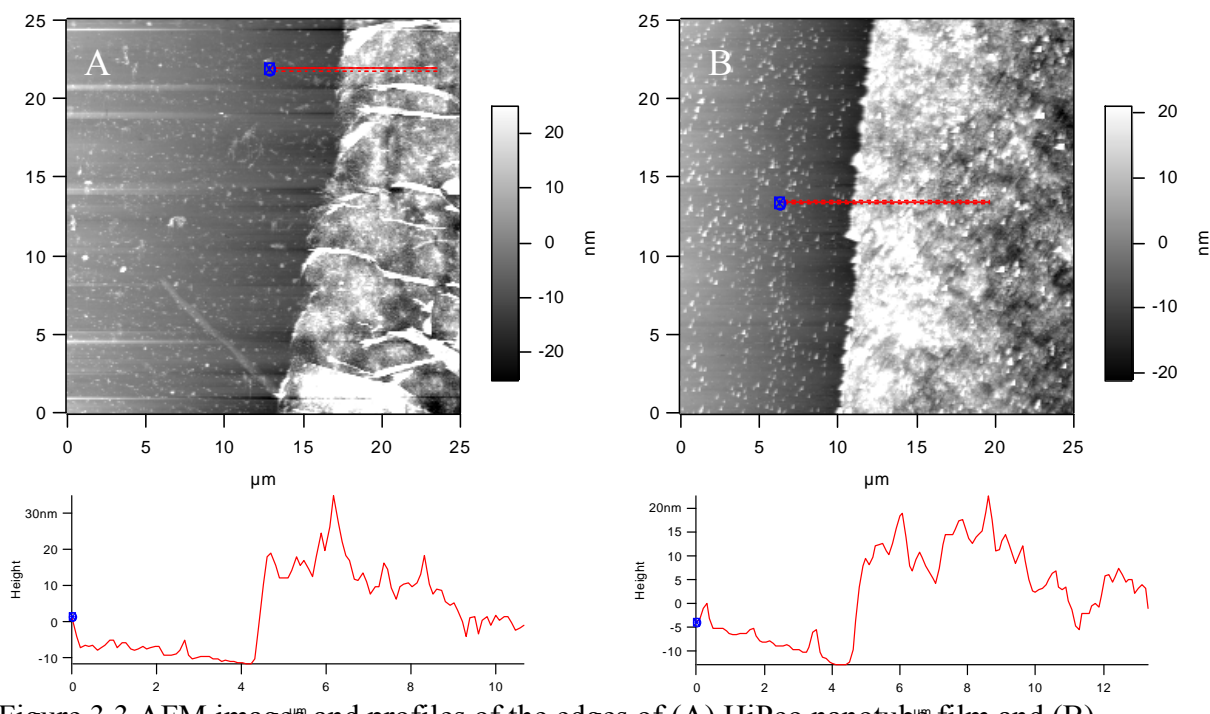


Figure 3.3 AFM images and profiles of the edges of (A) HiPco nanotube film and (B) CoMoCAT nanotube film.

To study the microwave effect on nanotubes, the individual nanotubes dispersed on Si substrates were examined by AFM before and after irradiation on the same areas. For nanotube thin films deposited on glass substrates, their property and composition

were studied using THz transmission, Raman (532 nm and 514 nm excitations) and UV-vis absorption spectroscopy. THz transmission analysis and 514 nm excitation Raman analysis were provided by our collaborator Dr. Xin Group, University of Arizona, Tucson, Arizona. All spectra were directly collected from nanotube thin films which were deposited on glass substrates.

3.3 Results and discussion

3.3.1 Microwave irradiation on individual nanotubes

Individual HiPco nanotubes dispersed on a Si substrate was irradiated in a microwave oven for 3 minutes. Based on our previous EFM study, the HiPco nanotube sample contains ~30% of metallic content. Figure 3.4 shows the AFM images of individual nanotubes before and after irradiation on multiple areas. By comparing the length and diameter of each nanotube before and after irradiation, it was determined that all nanotubes maintained the same dimensions, indicating nanotubes were undamaged. Further gradually increasing the radiation time to 10 minutes still did not cause any damage to the nanotubes. Irradiation times of greater than 10 minutes can cause overheating and shutdown of the microwave device. The reasons why the microwave irradiation had negligible effects on individual nanotubes can be due to the following:

- (1) The heat converted by individual nanotubes from microwave energy is insufficient to cause damage on the sidewalls of the nanotubes.
- (2) Either the heat created or the energy absorbed by the nanotubes was dissipated into the Si substrate

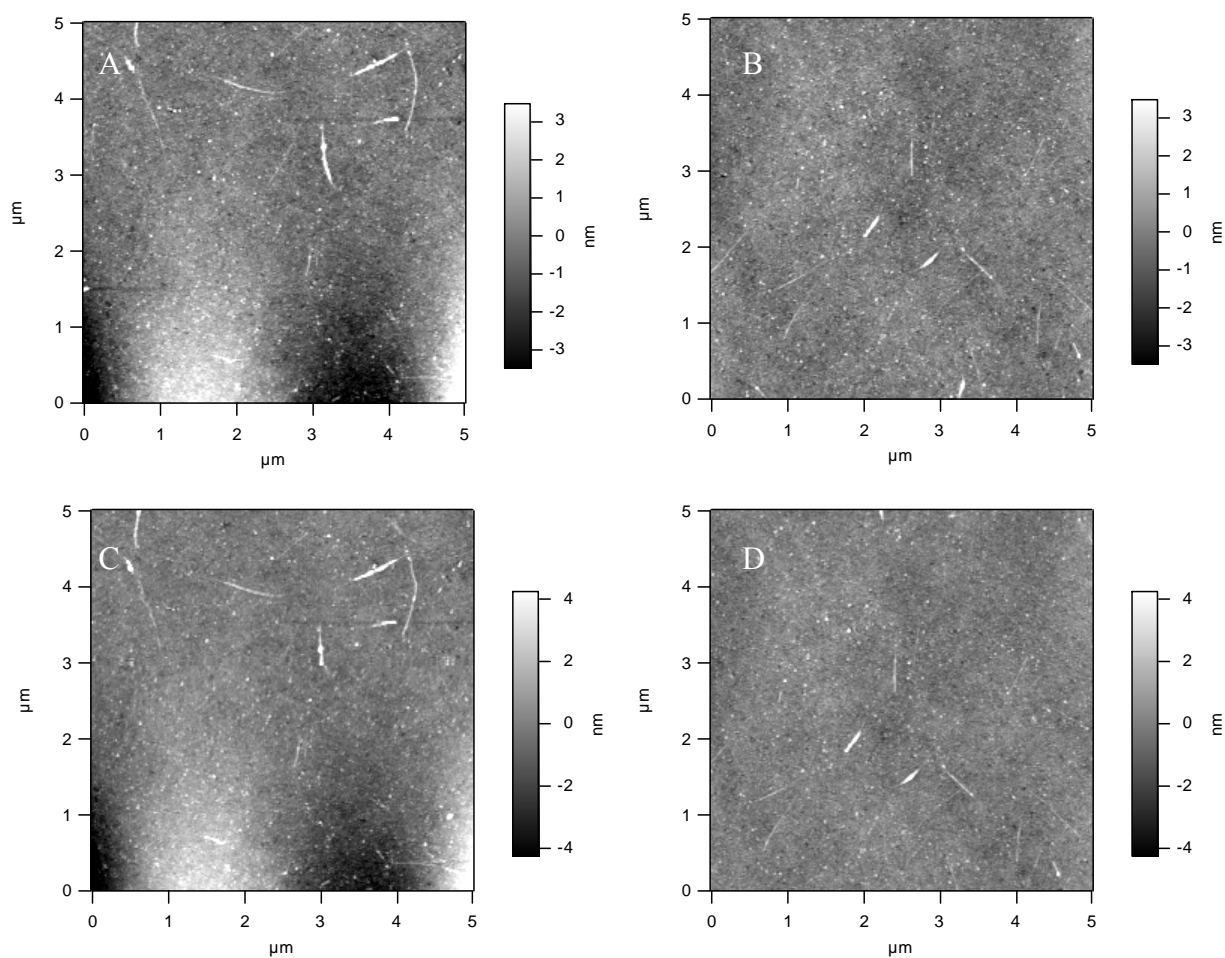


Figure 3.4 AFM images of dispersed individual nanotubes on Si (A, B) before microwave irradiation, and (C, D) after microwave irradiation. No nanotubes were destroyed during the irradiation.

3.3.2 Microwave irradiation on nanotube thin films

As an alternative to silicon substrates, glass substrates with nanotube thin films were irradiated in the microwave oven for 3 minutes. Figure 3.5 shows the photographs of thin film samples before and after irradiation. During the irradiation, the glass

substrates usually fractured from the center of the thin films, and the breaking mostly happened in the first 30 seconds of irradiation. Since the bare glass substrates do not break during the microwave irradiation, the fracturing of the glass substrate was due to the nanotube films. This result has confirmed that nanotubes can absorb microwave energy and convert it to excessive heat. Therefore, the next step was to analyze changes to the property and composition of thin films due to the microwave exposure.

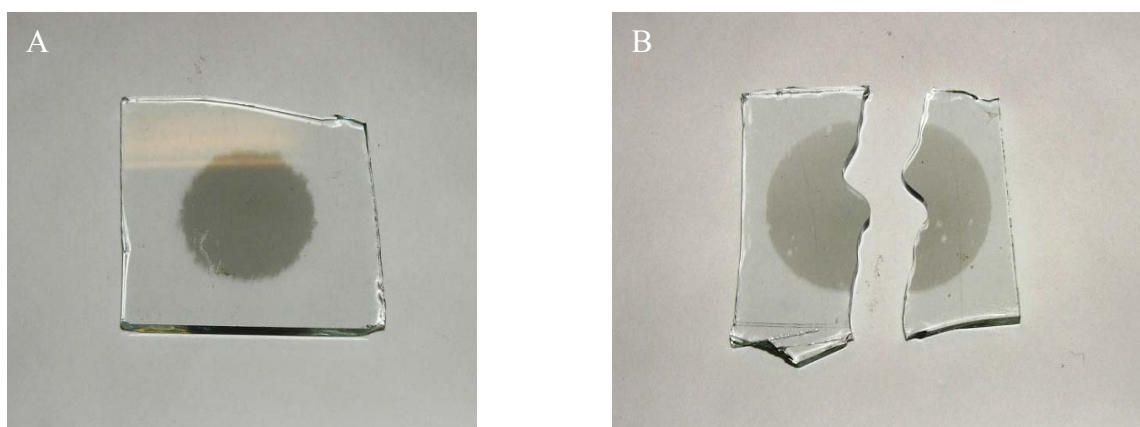


Figure 3.5 Photographs of glass substrates with nanotube thin films (a) before and (b) after microwave irradiation. The glass substrate fractured from the center of the thin film while bare glass substrate did not break under the same irradiation conditions.

3.3.3 Characterization of nanotube thin films before and after irradiation

To study the composition change in the irradiated samples, a HiPco nanotube thin film irradiated in different durations was studied by a photoconductive Terahertz (THz) Time Domain Spectroscopy (TDS) system operating from 50 GHz to 1.2 THz. The measured THz transmission reflects the composition of the sample. For example, if the sample is composed of pure metallic tubes, it behaves like a thin metal sheet, thus most of

the signal is reflected and the low transmission is obtained. On the contrary, if the sample contains pure semiconducting tubes, it behaves like a thin dielectric slab and a much higher transmission is obtained. Therefore, the measured transmission would indicate the change of metallic content in the sample. Figure 3.6 shows the THz transmission spectra of a nanotube thin film deposited on a glass substrate. After irradiation, the transmitted power increases dramatically by up to 10 dB, indicating a reduction of metallic content in the thin film. It is worth noting that the transmission signal rises more significantly during the first 30 seconds of irradiation. Afterwards, the change of transmission signal seems much slower, which is probably due to the limited metallic content in the film. This is consistent with our observation that glass substrates broke within 30 seconds of irradiation. Compared to the traditional four-point DC conductivity measurement, this characterization method does not require any contact with the samples, therefore it is more reliable. For CoMoCAT thin film samples, a similar but smaller THz transmission increase was observed after microwave irradiation, which is expected since CoMoCAT sample contains less metallic content.

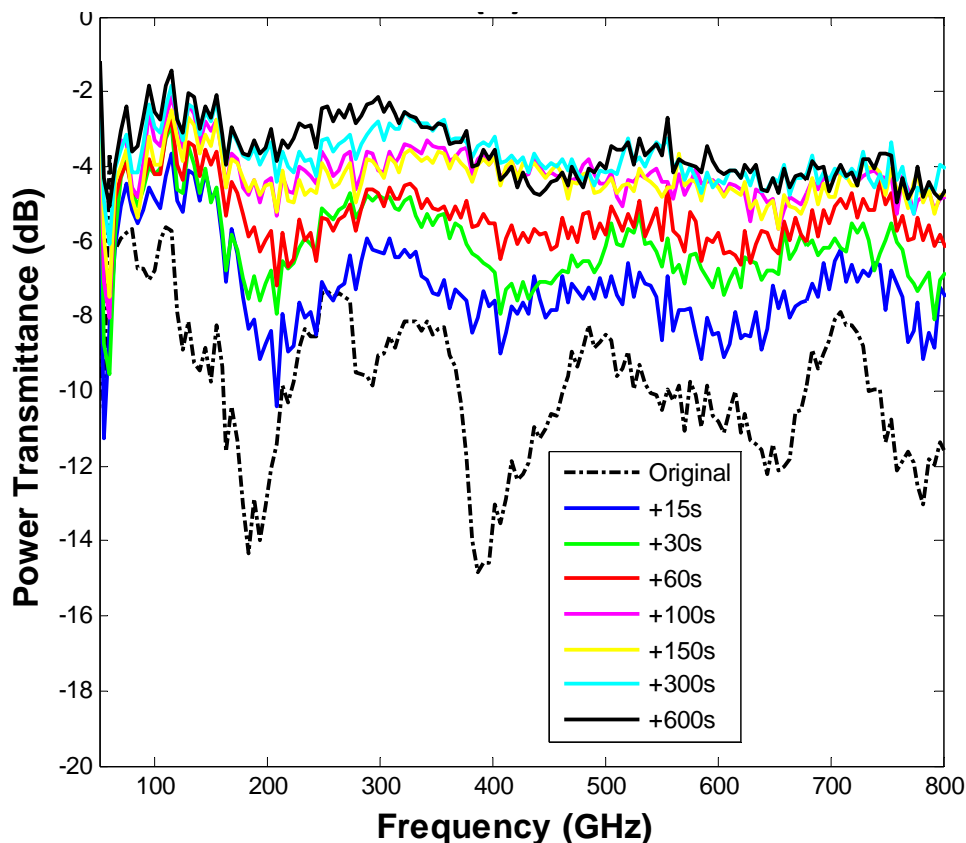


Figure 3.6 THz transmission spectra of a HiPco nanotube thin film sample before and after various irradiation time periods.

Since the THz transmission measurements imply that metallic content was significantly decreased after irradiation, HiPco nanotube thin films were further characterized using Raman spectroscopy to specify which nanotube species had decomposed after 180 seconds of irradiation. Figure 3.7 shows the RBM band and G band features obtained at two excitations wavelength (514 nm and 532 nm). Spectra were collected at multiple locations and averaged spectra are shown in the Figure 3.7. After 180 seconds of microwave irradiation, the metallic content in the irradiated sample was decreased, because the G band features ($1480\text{ cm}^{-1} \sim 1600\text{ cm}^{-1}$, Figure 3.7 b, d) obtained

at both excitations were narrowed¹⁶⁸. The RBM spectra shown in Figure 3.7(a) and 3.7(c) are discussed in two different regions, the M11 region ($215 \text{ cm}^{-1} \sim 290 \text{ cm}^{-1}$) for which the excitation laser is in resonance with the first van Hove singularities (vHs) of metallic tubes and the S33 region ($160 \text{ cm}^{-1} \sim 215 \text{ cm}^{-1}$) for which the excitation laser is in resonance with the third vHs of semiconducting tubes. A significant decrease of RBM features are shown in M11 region while no significant decrease or even a slight increase in the RBM features are shown in the S33 region. The slight increase of RBM features in semiconducting S33 region is still not fully understood. It is probably because the Laser was focusing on different locations of film in each measurement. There is no evidence to support that metallic nanotubes were converted to semiconducting ones during the microwave irradiation.

To quantitatively compare the changes of metallic tubes to the changes of semiconducting tubes, the M11 to S33 spectral ratios were then calculated by integrating the spectra under each region, followed by taking the ratio afterwards. As shown in Table 3.1, after irradiation, the M/S ratio was reduced by 18% for 514 nm excitation and 29 % for 532 nm excitation, respectively. However, it is worth noting that the decrease of metallic-to-semiconducting (M/S) spectral ratios calculated here is not representative of the decrease of the M/S ratio for the entire population in the sample, because Raman spectra only correspond to nanotubes which are in resonance with the excitation energies^{99,169}. Nevertheless, a clear trend of selective decreasing the metallic content in nanotube thin films has been observed from Raman spectra at both excitation

wavelengths. This is consistent with the observation from THz transmission measurements.

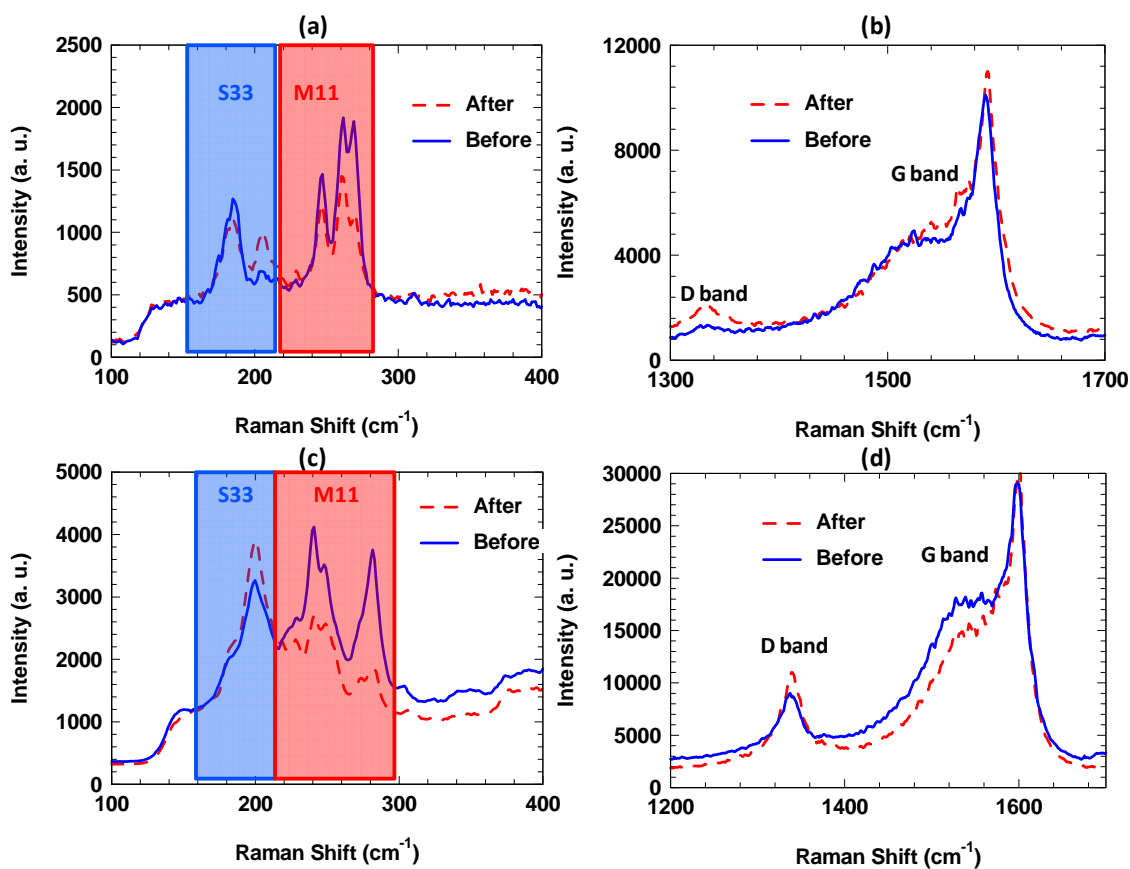


Figure 3.7 Raman spectra of a HiPco nanotube thin film, deposited on a glass substrate, before (solid curves) and after (dashed curves) microwave irradiations. Each spectrum was averaged from several spectra captured at different positions on the thin films. (a) RBM band spectra, 514 nm laser excitation; (b) G and D bands spectra, 514 nm laser excitation; (c) RBM band spectra, 532 nm laser excitation; (d) G and D bands spectra, 532 nm laser excitation.

Table 3.1 Metallic-to-semiconducting ratios before and after irradiations from Raman spectra at both 514 nm and 532 nm excitation wavelengths.

Laser excitation	514 nm	532 nm
M/S ratio (before)	2.38	1.46
M/S ratio (After)	1.96	1.04
M/S ratio decrease	17.6%	28.7%

CoMoCAT nanotube thin films were also characterized using Raman spectroscopy to specify which nanotube species had decomposed after 180 seconds of irradiation. Spectra were collected at two excitation wavelength, 514 nm and 532 nm, using the same procedure as on HiPco nanotube films. Figure 3.8 shows the RBM band and G band features obtained at 514 nm and 532 nm wavelengths. At 514 nm excitation, G band features ($1480\text{ cm}^{-1} \sim 1600\text{ cm}^{-1}$, Figure 3.8b) were narrowed after 180 seconds of microwave irradiation, indicating the metallic content of the sample was decreased in the irradiation¹⁶⁸. The RBM feature (Figure 3.8a) in the M11 region ($215\text{ cm}^{-1} \sim 290\text{ cm}^{-1}$) also decreased after irradiation while no significant decrease in the S33 region ($160\text{ cm}^{-1} \sim 215\text{ cm}^{-1}$). At 532 nm excitation, both G band and RBM band features (Figure 3.8c, d) only show slightly change after irradiation, probably because the nanotubes which were affected in microwave irradiation are not in resonance with the excitation energy^{99,169}. Nevertheless, a decreasing of the metallic content in CoMoCAT nanotube samples has also been observed from Raman spectra at both excitation wavelengths. This is consistent with the results of HiPco nanotube thin films.

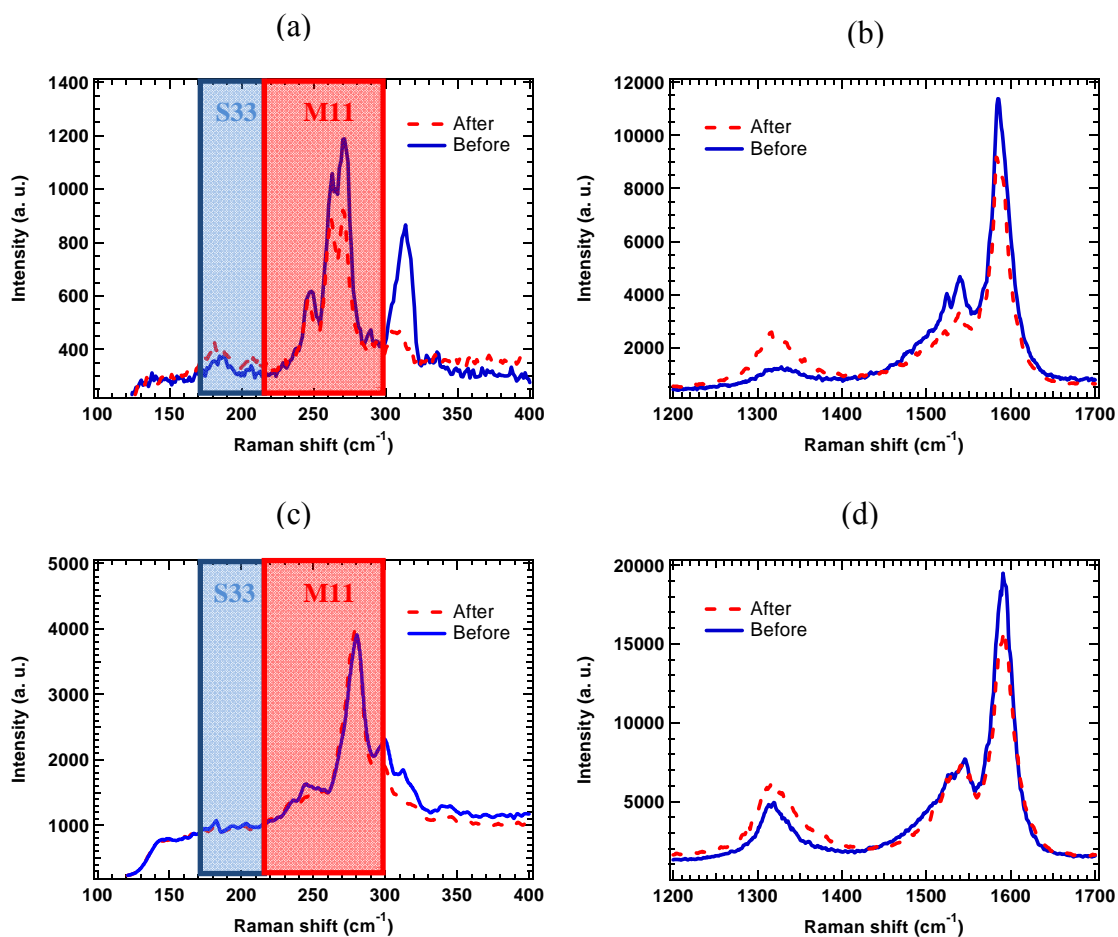


Figure 3.8 Raman spectra of a CoMoCAT nanotube thin film, deposited on a glass substrate, before (solid curves) and after (dashed curves) microwave irradiations. Each spectrum was averaged from several spectra captured at different positions on the thin films. (a) RBM band spectra, 514 nm laser excitation; (b) G and D bands spectra, 514 nm laser excitation; (c) RBM band spectra, 532 nm laser excitation; (d) G and D bands spectra, 532 nm laser excitation.

The observed metallic content decrease can be caused by two different mechanisms. In the first mechanism, microwave irradiation induces high localized temperature on metallic nanotubes, and causes the breakdown of the carbon shells. Therefore, the metallic content in the thin film is reduced. However, it is also possible

that the decrease of the metallic content is due to oxidation on the sidewall, instead of the destruction of the whole tubes. In the second mechanism, the heat produced by the metallic nanotubes was only enough to assist the partial oxidation on the sidewalls to create defects. Metallic nanotubes lost their conductivities or Raman activities due to the oxidation or created defects, but the main structures of those tubes still exist. In either mechanism, the electrical properties of metallic nanotubes were significantly altered so that they no longer respond to the THz or Raman analyses in the same way as before. From Raman spectra, the intensities of D band features ($1300\text{cm}^{-1} \sim 1360\text{cm}^{-1}$) from irradiated thin films were increased. This indicates more defects were induced on the sidewalls of nanotubes during the irradiation. Therefore, further analyses to confirm which mechanism is dominant were carried out using UV-vis absorption spectroscopy.

Figure 3.9 shows the absorption spectra of a HiPco nanotube thin film before and after multiple microwave irradiations. One benefit of UV-vis absorption spectroscopy is that it can show the features from all nanotube species in the sample, including both metallic content and semiconducting types⁹⁴. Differing from the significant changes in the previously discussed THz transmission and Raman spectra, the absorption spectra show same features of the thin film before and after microwave irradiations. This indicates the basic electronic structures of nanotubes remained the same after microwave exposure. The slight downshift of the absorption spectra for the irradiated thin film is probably due to the different orientations and positions of the glass substrate in the spectrometer. This shift also happens through the whole range of the spectra, and the spectral ratio between metallic content (M11 region, $400 \sim 550 \text{ nm}$) and semiconducting

content (S22 region, 600 ~ 900 nm) remained the same before and after irradiations. Further increasing of the irradiation time to more than 180 seconds, the same absorption features were shown in the whole range from 400 nm to 1100 nm. This evidence has confirmed that no complete breakdown of metallic nanotubes occurred during microwave irradiation. The main electronic structures of the nanotubes remained fundamentally the same, but a certain amount of nanotubes, especially metallic nanotubes, were oxidized or had induced defects due to the excessive heat generated from microwave energy.

Same Absorption analyses were carried out on a CoMoCAT thin film before and after multiple irradiations. Figure 3.10 shows the adsorption features after irradiation are the same as the features before irradiation in the whole wavelength range. Therefore, the same conclusions can be drawn that the electronic structure of nanotubes was not completely destroyed during the microwave irradiation. Comparison between the absorption spectra for both HiPco and CoMoCAT thin films reveals how the spectra reflect the different compositions of nanotube samples. As the HiPco thin film (~30% metallic content) has a higher percentage of metallic nanotubes than the CoMoCAT thin film (~10% metallic content), the spectra (Figure3.9) for the HiPco sample shows more absorption features in the M11 region (400~550nm) than the spectra for the CoMoCAT sample (Figure 3.10). Two dominant peaks in the S22 region (600 nm ~ 900 nm, Figure 3.10) for the CoMoCAT thin film indicate this sample is enriched with semiconducting nanotubes, while the HiPco sample does not have these two dominant peaks in the S22 region (Figure 3.9) because of the relative lower semiconducting content. However, none of the absorption spectra collected after microwave irradiations shows the change in

absorption features. Comparing with the conclusions published in our paper¹⁷⁷, this further absorption spectra provide strong evidence that metallic nanotubes were not completely decomposed in the microwave irradiation.

It is not surprising that results from THz transmission spectra, Raman spectra and absorption spectra have led to two different conclusions, because these three techniques measure different properties of nanotubes. For nanotubes, THz transmission spectra are associated with their conductivity, while Raman spectra are associated with the vibrations of C atoms and absorption spectra are associated with the transition energies from valance bands to conduction bands.

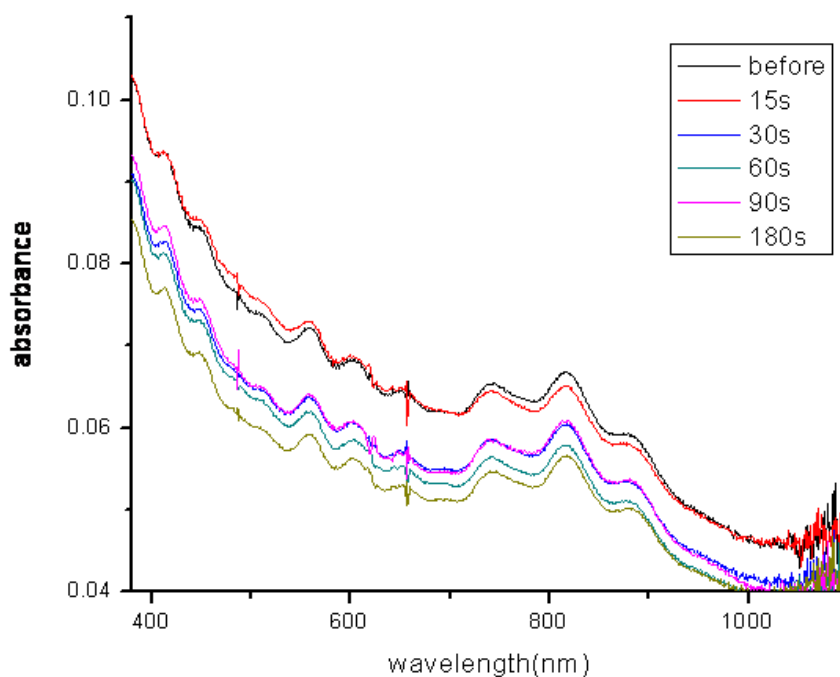


Figure 3.9 Absorption spectra for a HiPco nanotube thin film on a glass substrate before and after multiple irradiations. The absorption features for metallic and semiconducting nanotubes remain the same after irradiation.

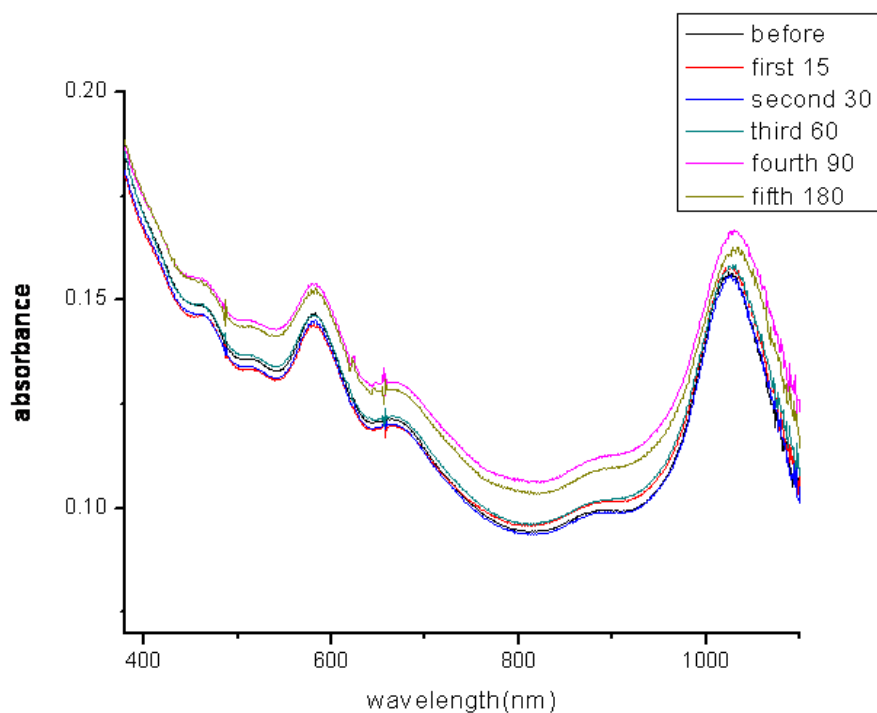


Figure 3.10 Absorption spectra for a CoMoCAT nanotube thin film on a glass substrate before and after multiple irradiations. The absorption features for metallic and semiconducting nanotubes remain the same after irradiation.

By converting the frequency in THz transmission spectra, the wavenumber in Raman spectra, and the wavelength in absorption spectra to electronic energy, we have found that the energy related to three techniques are significantly different. THz transmission spectra measured the signal from 4×10^{-4} eV to 3×10^{-3} eV; the Raman RBM spectra measured the shift from 1×10^{-2} eV to 5×10^{-2} eV; and the absorption spectra measured the transition from 1.2 eV to 3.1 eV. The energy required to change THz transmission spectra is the lowest while the energy required to change absorption spectra is the highest. The different energy distributions have confirmed that the spectra from these three techniques are actually related to different properties of nanotubes.

Defects created on the sidewall of a metallic tube, shown in Figure 3.11, can significantly decrease the conductivity of this tube, and correspondingly change the THz transmission spectra which only require the lowest energy. These defects can also change the vibrations of C atoms and thus change the Raman features of the tube. However, these defects, induced by the microwave, may not completely destroy the electronic structure of the nanotube, which requires the highest energy. The transition energies from valance bands to conduction bands remained the same after the irradiation and consequently no change was found in absorption spectra.

Therefore, it is believed that the second mechanism, which is the oxidation and defect induction of the nanotubes, dominate the whole microwave process. The measured decrease of the metallic content from THz transmission and Raman spectra is probably because of the preferential oxidation and defect induction metallic nanotubes, as metallic nanotubes having higher conductivities and producing more heat¹⁷⁵.

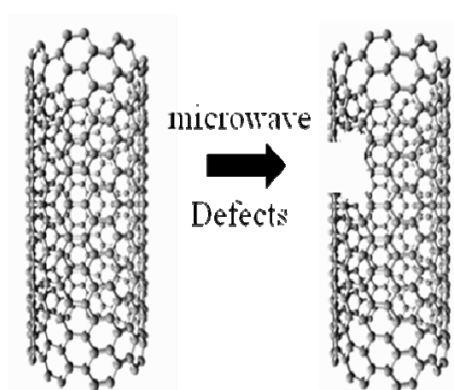


Figure 3.11. Schematic drawing of induced defects on a metallic nanotube in the microwave irradiation.

3.4 Conclusions

In summary, the effects of microwave irradiation on nanotube thin films without catalyst particles were studied. A convenient characterization method by measuring the THz transmission of the thin films was introduced to monitor the metallic content in the films. A significant transmission increase was observed after the microwave irradiation, which indicates possible reduction in metallicity of nanotube samples. The Raman spectra also confirm the M/S ratio decrease in the nanotube thin films after the irradiation. However, the absorption spectra provided strong evidence that metallic nanotubes were not destroyed by microwave irradiation, but only preferentially oxidized or otherwise had undergone defect induction. This microwave effect is believed to selectively change the properties of metallic nanotubes, because their high conductivities can help to generate more heat from microwave energy than semiconducting type. Further work to study whether microwaves with higher energies or different frequencies can completely destroy nanotubes is still under investigation.

Chapter 4. AFM Investigation of Corrosion Inhibitors

4.1 Introduction

Surfactant corrosion inhibitors can retard acid corrosion when added to an environment in small concentrations. Nitrogen-based organic molecules, such as imidazolines¹⁷⁸, imidazoline amido amines¹⁷⁹ and their salts¹⁸⁰⁻¹⁸³, have been widely used as corrosion inhibitors for protecting mild steel from CO₂ corrosion. Surfactant organic molecules consist of a polar hydrophilic head and a hydrophobic hydrocarbon tail¹¹⁶. One of the most important properties of surfactant-type corrosion inhibitors is their ability to significantly retard the corrosion on a metal surface, by forming adsorption layers^{113,126,130}. Understanding the adsorption mechanism of surfactants is a significant step in selecting an appropriate inhibitor for a realistic scenario, to evaluate inhibitor performance and to develop a predictive model for corrosion in the presence of inhibitors.

Over the last few decades, the adsorption characteristics of a wide variety of surfactants have been investigated, traditionally using adsorption isotherms^{120,126,184-185}, and more recently by fluorescence decay¹⁸⁶⁻¹⁸⁷, neutron reflection¹⁸⁸⁻¹⁸⁹ and surface force measurement instruments^{119,138}. One important property of a surfactant is its critical micelle concentration (CMC), which is the concentration that the surfactant molecules spontaneously agglomerate together to form micelles¹¹⁶. Micelles significantly affect the adsorption structure of surfactants and their performance¹⁹⁰. A previous study of surfactant adsorption¹¹⁸⁻¹²¹ reported that the formation of a first adsorbed layer was due to electrostatic interactions of positive ions on negative surfaces. The second layer, or “bi-

layer”, is formed with a further increase in surfactant concentration close to the CMC with hydrocarbon tails interacting with each other and the hydrophilic group pointing toward the solution. Other adsorption structures above the CMC, such as micelles, hemimicelles and admicelles, have also been reported for various surfactants^{130,135-138}. It has been found that the adsorption and aggregation structures of corrosion inhibitors may vary due to changes in the type of molecules, bulk concentration, bulk pH and surface property of the substrate^{137,191-194}.

Since the invention of atomic force microscopy (AFM) in 1986 by Binnig, Gerber and Quate⁹, this advanced technique enables images to be produced *in situ* with a magnification up to 10^7 times enabling, for the first time, resolution at the molecular level. The basic principle of AFM involves measurement of the interaction between a scanning probe and sample surface, as discussed in Chapter 1. A detailed description of the application of AFM in corrosion science has been published previously¹⁹⁵.

As the degree of protectiveness conferred by corrosion inhibitors strongly depends on the structure and properties of the adsorbed inhibitor film¹⁹⁶, this work focused on applying AFM to study the adsorption structure, film thickness and mechanical resistance of several cationic corrosion inhibitors. A main driver for the present work is the widespread reporting from industry that the inhibitor film can be removed from the metal surface at some critical fluid velocity¹⁹⁷⁻¹⁹⁹. This velocity apparently depends on the concentration and type of corrosion inhibitor and is manifested by a rapid increase in the corrosion rate when the molecules are removed from the surface. In fact, to evaluate the performance of corrosion inhibitors, most corrosion

engineers specify some shear stress test to evaluate inhibitor performance under high flow conditions²⁰⁰. This brings in another important property of AFM – the ability to measure the adhesive force of molecules on surfaces and the force to penetrate adsorbed organic films¹³⁸.

4.2 Experimental

4.2.1 Materials

Table 4.1 lists information for five corrosion inhibitor formulations studied in this chapter, labeled as K1, K2, K3, K4 and K5. Inhibitor K1 and K2 are generic inhibitors. The major component in K1 is TOFA/DETA imidazolium and the major component in K2 is C₁₂~C₁₆ coco quaternary ammonium salts (quats). The molecular structures of K1 and K2 are shown in Figure 4.1. They are organic surfactants, with positively charged hydrophilic head groups and non-polar hydrophobic tails. Their molecular lengths are ~ 2 nm. Inhibitor K2 actually contains three types of inhibitor molecules: C₁₂ coco quaternary ammonium salt, C₁₄ coco quaternary ammonium salt and C₁₆ coco quaternary ammonium salt. Their only difference is the number of C atoms in their hydrophobic tails. Inhibitor K3 is sodium thiosulfate (Na₂S₂O₃), an inhibitor additive that is often used to improve the efficiency of other surfactant-type inhibitors. By mixing 4% K3 with 20% K1 or K2 solution, inhibitor blends K4 or K5 are prepared. The critical micelle concentration (CMC) of each corrosion inhibitor was measured using the weight drop method²⁰¹. Figure 4.2 shows the measured CMC for inhibitor K1 TOFA imidazolium by measuring the surface tensions at different concentrations. After the CMC of each inhibitor was

determined, five corrosion inhibitors were prepared at 0.5 CMC and 2 CMC, respectively.

Table 4.1. Corrosion inhibitors and CMC values.

Product	Description	Components	CMC (DI water)	CMC (1wt.%NaCl)
K1	Generic Inhibitor	TOFA/DETA imidazolium	718 ppm	36 ppm
K2	Generic Inhibitor	C ₁₂ ~C ₁₆ coco quaternary ammonium	471 ppm	110 ppm
K3	Generic Inhibitor	Sodium thiosulfate	Non-surfactant	
K4	Inhibitor Blend	TOFA/DETA imidazolium and sodium thiosulfate (K1 + K3)	753 ppm	215 ppm
K5	Inhibitor Blend	Coco quaternary ammonium and sodium thiosulfate (K2+K3)	543 ppm	290 ppm

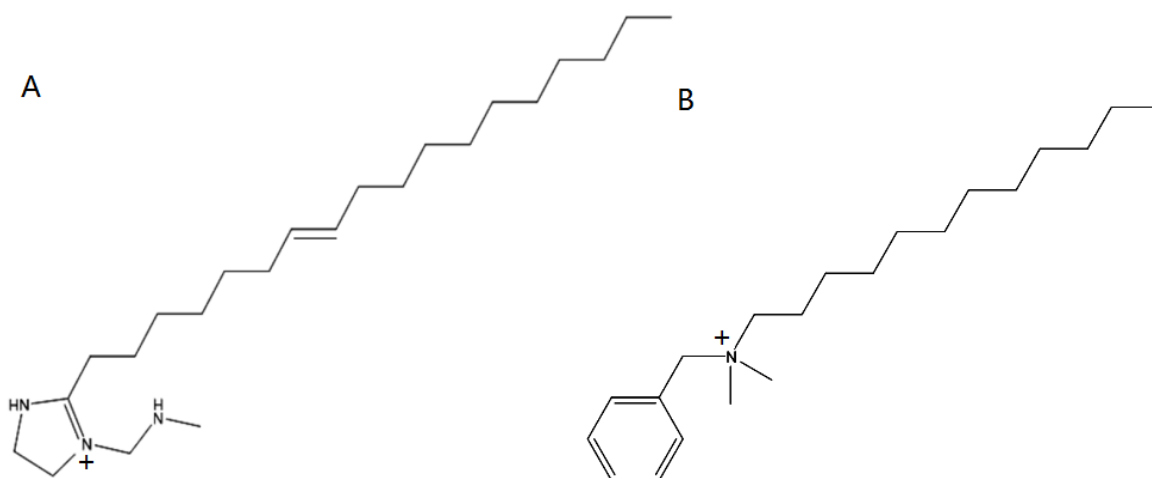


Figure 4.1 Molecular structures of (A) TOFA/DETA imidazolium and (B) C₁₆ coco quaternary ammonium salts.

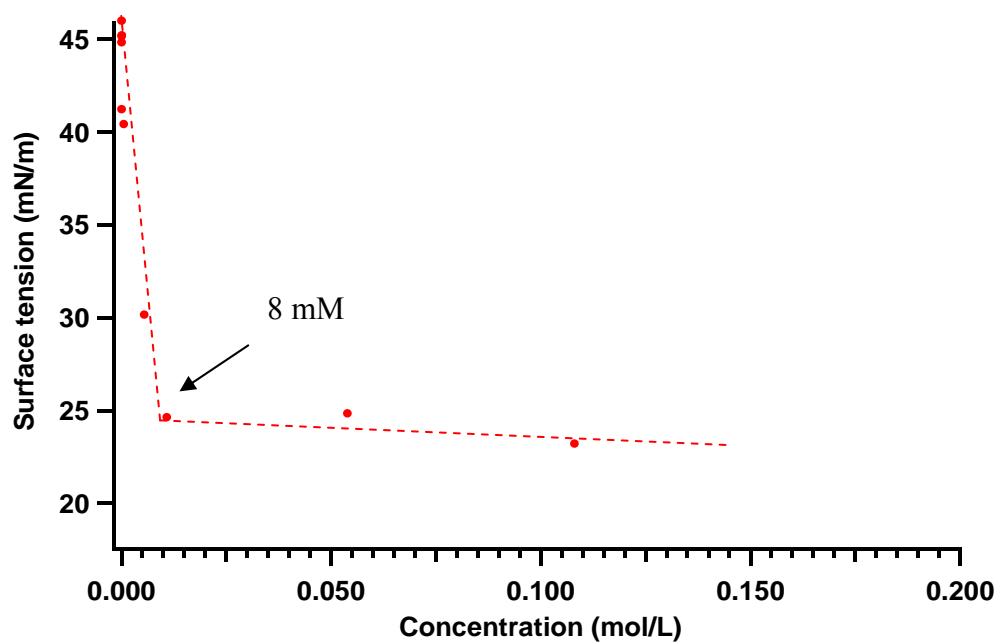


Figure 4.2 Critical micelle concentration (CMC) of corrosion inhibitor K1 TOFA imidazolium, 8 mM, determined by drop weight surface tension measurements.

Freshly cleaved mica, vapor deposited Au, vapor deposited Fe and polished X65 steel were used as the supporting substrates for inhibitor adsorption. For mica, Au and Fe substrates, no extra surface treatment was required because they can provide relative flat surfaces. For X65 steel surface, a fine polishing procedure was used for polishing the steel surface down to a surface roughness of less than 20 nm. An X65 specimen was polished on 400 grit, 600 grit, 1500 grit sand papers respectively, and then continued to be polished on silk cloth with 9 μm diamond suspension, and on napped cloth with 3 μm diamond suspension. Absolute ethanol (99.9%) was used in washing and rinsing the specimen during the polishing, to remove excessive heat and prevent the corrosion from moisture. A mirror finish was obtained after the polishing and the specimen was stored in absolute ethanol.

4.2.2 Methods

Two types of AFM were used to study the adsorption of corrosion inhibitors. AFM images shown in grey color were generated using a MFP-3D SA AFM (Asylum research), and AFM images shown in golden color were collected with a Picoscan 2000 AFM. Two types of AFM probes were used. SNL-10 probes ($k_n \sim 0.4$ N/m, Veeco probe. Inc) were used in MFP-3D SA AFM, while DP-19 probes ($k_n \sim 0.6$ N/m, MikroMasch) were applied in Picoscan 2000. The diameter of the “head” of a tip is ~ 30 nm (Figure 4.3a) for both two types, as measured by high resolution SEM.

A droplet of inhibitor solution was deposited onto a mica or metal substrate, and inhibitor film was allowed to evolve over a period of 3 hours prior to AFM analysis.

AFM scanning and force measurements were carried out inside the inhibitor solution. For mica, Au substrates, AFM analyses were carried out in ambient conditions as they are chemically stable. All analyses for inhibitor K1 on mica and Au surface were repeated in Laboratoire Interfaces et Systemes Electrochimiques, Université Pierre et Marie CURIE, France and same results were obtained. For Fe and steel substrates, anaerobic environments were provided by assembling the AFM instrument inside a closed box. Figure 4.4 shows the set-up of the closed box anaerobic environment. By pre-purging N_2 or CO_2 into this box, O_2 is eliminated and the corrosion on Fe or steel can be controlled.

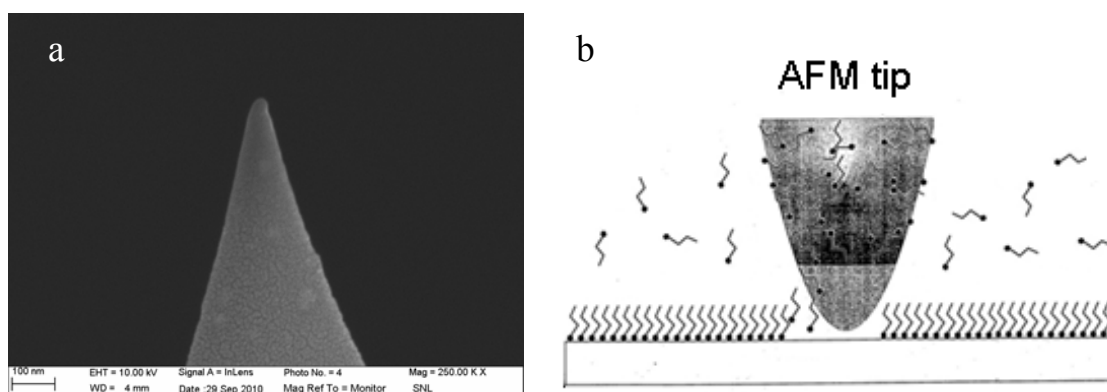


Figure 4.3 (a) The diameter of the “head” of the tip was determined to be ~ 30 nm. (b) Schematic drawing of AFM analysis with the tip fully immersed inside inhibitor solution.

To study adsorbed molecular structures, the scan was conducted over the top of the adsorbed layer. A low normal force (< 2 nN) was applied to the AFM cantilever to provide a necessary load for imaging and avoid damaging the film structure by scraping away inhibitor molecules. On a surface covered by inhibitor molecules, the method to measure film thickness was to remove a small section of the inhibitor film to the original

mica surface and then accurately measure the height difference. To remove the inhibitor molecules, the normal force applied to the cantilever was gradually increased until lateral movement of the cantilever was able to remove the adsorbed inhibitor molecules from the surface. Having determined the minimal normal force (~ 60 nN) to scratch inhibitor molecules from the surface, an xy lateral scan was performed on an area of $1 \times 1 \mu\text{m}$ while still maintaining this high normal force.

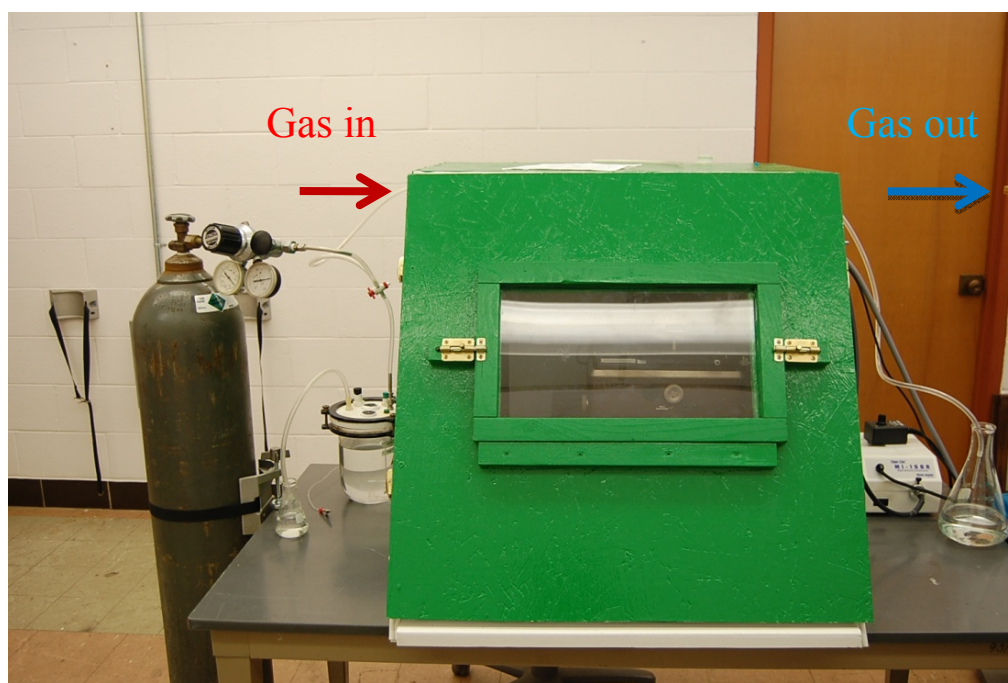


Figure 4.4 Set-up of AFM system in an anaerobic environment. By pre-purging N_2 or CO_2 into this box, O_2 is eliminated.

Besides surface morphology, AFM is able to quantitatively measure interactions between the AFM tip and inhibitor molecules²⁰²⁻²⁰⁴. The penetration forces shown in this study were obtained from force-distance curves which recorded the interaction during the

tip approaching process (Figure 4.5). On the other hand, the “lateral removal” force measurements were made using the friction loop technique which involved a forward and reverse scan parallel to the surface, under the identical and constant normal load of 60 nN used for the film thickness determinations (Figure 4.5). Using the same normal force in each friction loop allows direct comparison between measurements.

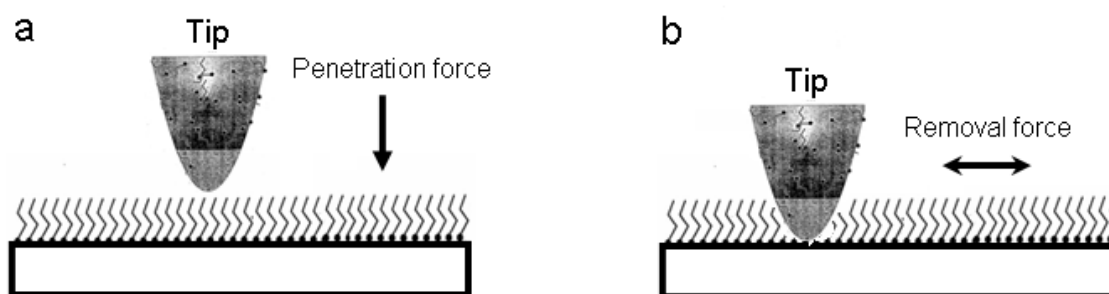


Figure 4.5 Schematic diagrams of (a) penetration force measurements and (b) lateral removal force measurements.

4.3 Results and Discussion

4.3.1 Surface morphology of corrosion inhibitors on mica

The adsorption of corrosion inhibitors was first studied on mica substrate. Mica is a silicate mineral with a sheet structure that has a high dielectric constant and excellent chemical stability. It has been reported that cationic surfactants have strong adsorption on mica which is negatively charged in aqueous solution^{119,205}. Figure 4.6 shows an atomically flat surface of a freshly cleaved mica substrate in deionized water. The surface roughness is only 0.1 nm, while the molecular length of inhibitors is ~2 nm. The surface

morphology and subsequent force measurements on a mica surface are used as blank values for analyzing the adsorption of inhibitor molecules.

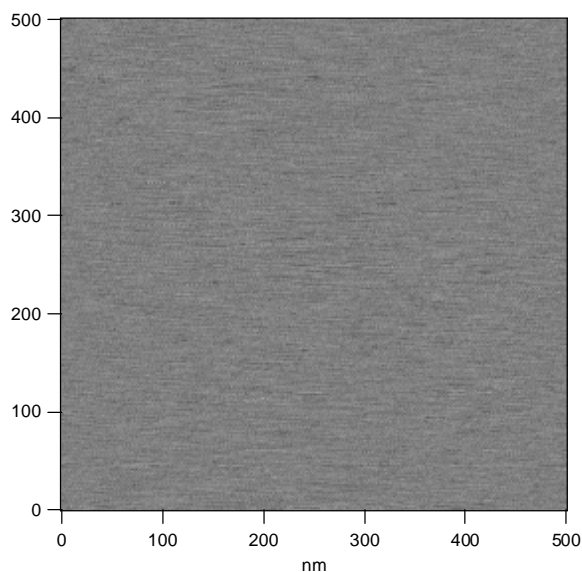


Figure 4.6 AFM image of blank mica substrate in deionized water. Mica provides an atomically flat surface with a roughness of 0.1 nm.

Figure 4.7 shows the surface morphologies and profiles of inhibitor K1 TOFA imidazolium on a mica surface at 0.5 CMC and 2 CMC. The uniform featureless surface indicates the inhibitor molecules adsorbed at the interface as a continuous flat film. This is regardless of the internal structure of the film which could vary due to the different concentration of inhibitor molecules relative to the CMC. No artifacts are shown in the images indicating that the adsorbed structure was not disrupted by the scanning process. Multiple images on different locations of the surface confirmed that the surfaces were fully covered with flat inhibitor films at concentrations of both 0.5 CMC and 2 CMC.

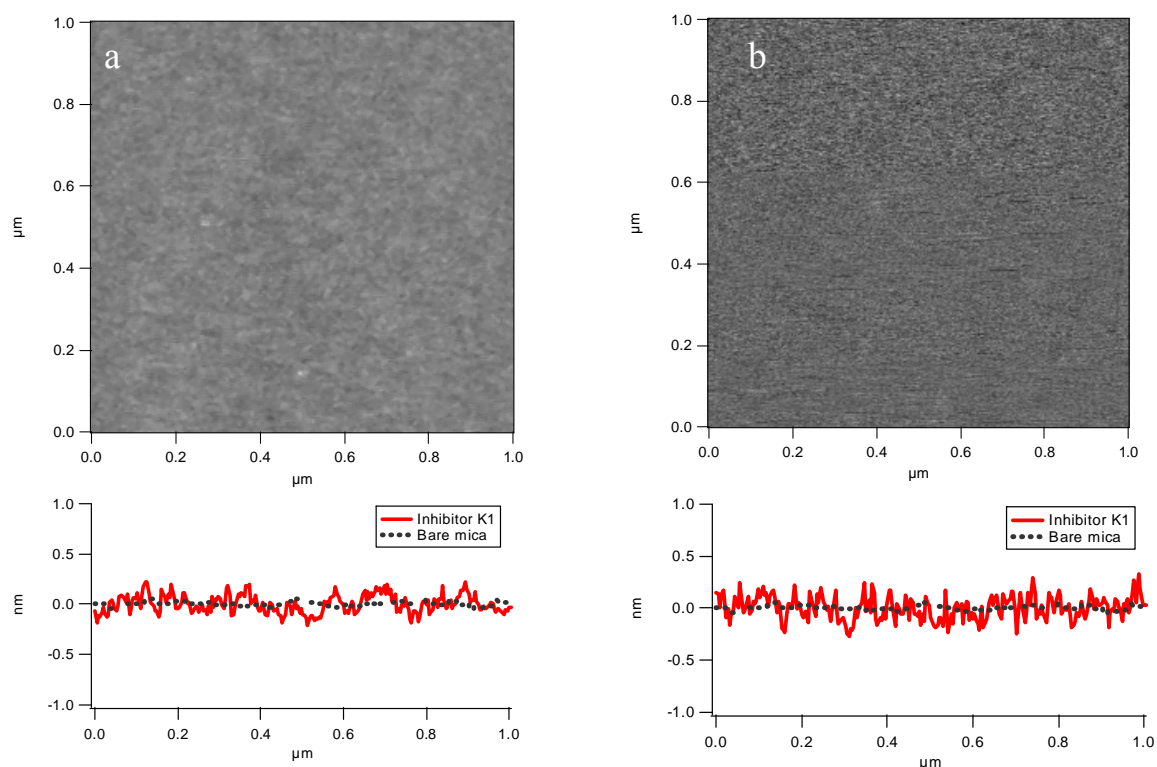


Figure 4.7 AFM images and corresponding profiles of inhibitor K1 at (a) 0.5 CMC and (b) 2 CMC on mica. In both condition, inhibitor molecules formed continuous flat films on surface, regardless of the internal film structure. All grey color images were collected from MFP-3D AFM using SNL-10 probes ($k_n \sim 0.4$ N/m)

The quality of images, however, is often affected by the scanning parameters and tip conditions. Artifacts and fake features can be created due to facts such as vibration noise, scanning at high velocity, excessive force on the cantilever, and tip contaminations. Figure 4.8 shows an AFM image of 2 CMC inhibitor K1 on mica surface. Comparing with previous flat surface morphology obtained from the same sample (Figure 4.7), this image shows additional periodic curves and horizontal lines. In order to verify whether these additional features are artifacts, several procedures can be applied. First, this image

can be repeated by scanning the same area multiple times. The positions of real surface features usually do not change in repeated images. Second, the scanning parameters can be further adjusted. In Figure 4.8, the horizontal lines disappeared after decreasing the applied force on the cantilever. Therefore, these horizontal lines were probably induced by the lateral interactions between inhibitor molecules and the scanning tip which was inside the inhibitor film. Decreasing the force applied on the cantilever can help to move the tip from inside the film to the top of the film. In our penetration force analysis (shown in section 4.3.3), we have determined the force to penetrate an inhibitor film is 1~2 nN. Therefore, the applied force for scanning surface morphology should not exceed this penetration force. For those periodic curves, they may still exist after repeated imaging or decreasing the applied force, because they were probably induced by vibration noise. One way to examine these curves is to change the scan rate. If they are artifacts, their periodicity, which is the distance between two parallel curves, will change after changing the scan rate. Otherwise, the scan rate can not affect the periodicity of real surface features. The other way to determine whether these periodic curves are artifacts is to change the scanning size. For example, the distance between two parallel curves should be consistent in a $5 \times 5 \mu\text{m}$ and a $1 \times 1 \mu\text{m}$ image, if they are real features. Otherwise they are artifacts. Based on these examination methods, we have found the periodic curves and horizontal lines shown in Figure 4.8 were artifacts.

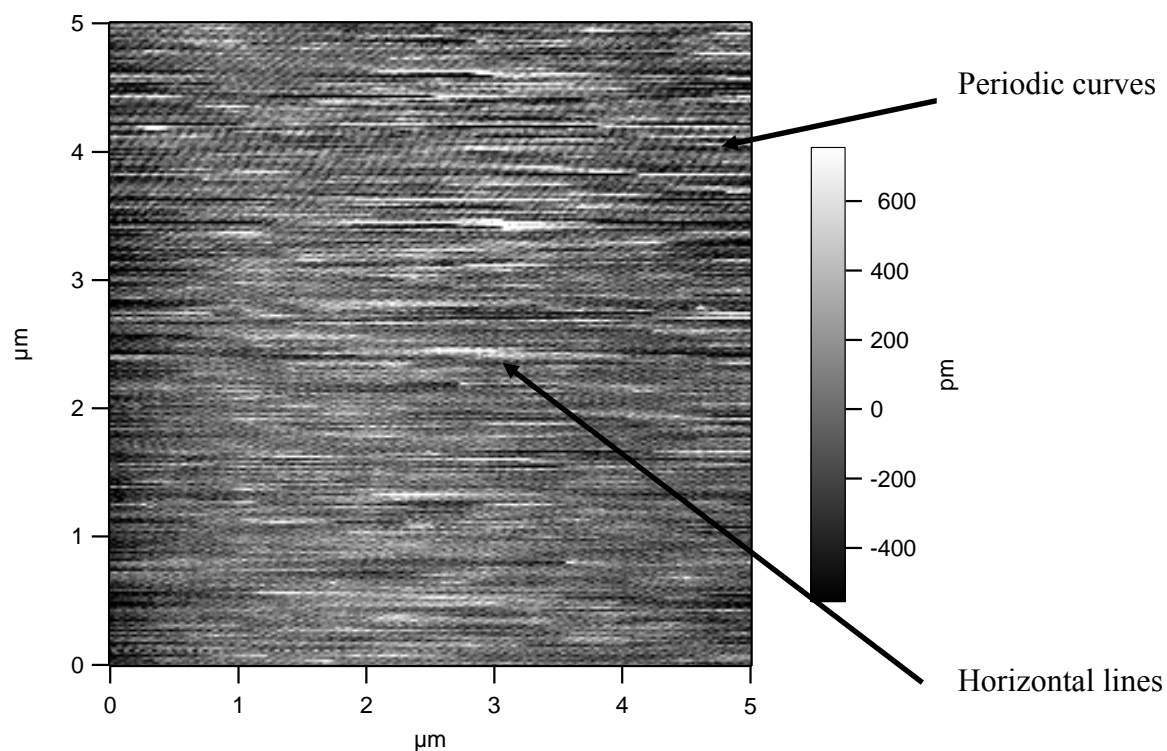


Figure 4.8. AFM image of 2 CMC inhibitor K1 on mica. Two types of artifacts, Periodic curves and horizontal lines, are shown in this image.

Figure 4.9 shows AFM images of inhibitor K1 on mica surface with other artifacts, including periodic curves, horizontal lines and random structures. By adjusting the scanning parameters or changing a new tip, these artifacts all disappeared. Therefore, one of the key issues in AFM analysis is to exclude the interference from artifacts. All images in this part of research have been repeated and verified using the discussed procedure.

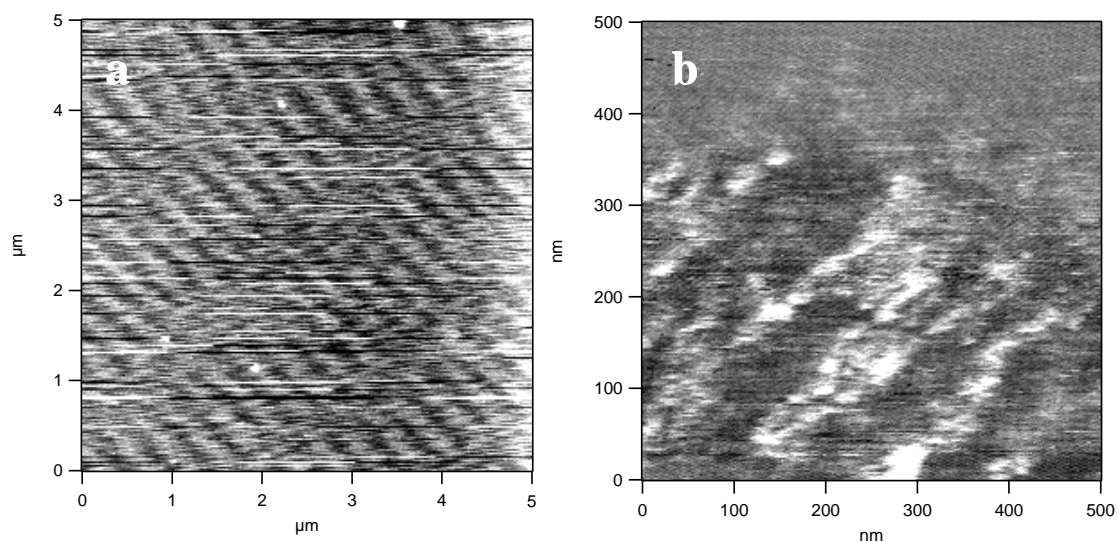


Figure 4.9. AFM images of inhibitor K1 on mica. Massive artifacts, including periodic curves, horizontal lines and random structures, were shown in images. By adjusting the scanning parameters or changing a new tip, these artifacts disappeared.

Besides the above procedures to diagnose artifacts, we further verified our results using different AFM systems and scanning probes. Figure 4.10 shows the AFM images of 0.5 CMC and 2 CMC inhibitor K1 on mica substrates. These gold color images were obtained from a Picoscan 2000 AFM using DP-19 probes ($k_n \sim 0.6$ N/m), while the previous grey images were obtained from a MFP-3D AFM using SNL-10 probes ($k_n \sim 0.4$ N/m). Same flat surface morphologies of inhibitor K1 on mica, shown in Figure 4.7 and Figure 4.10, were obtained from different instruments. This has confirmed the excellent repeatability of our AFM analysis on inhibitor films in aqueous solutions.

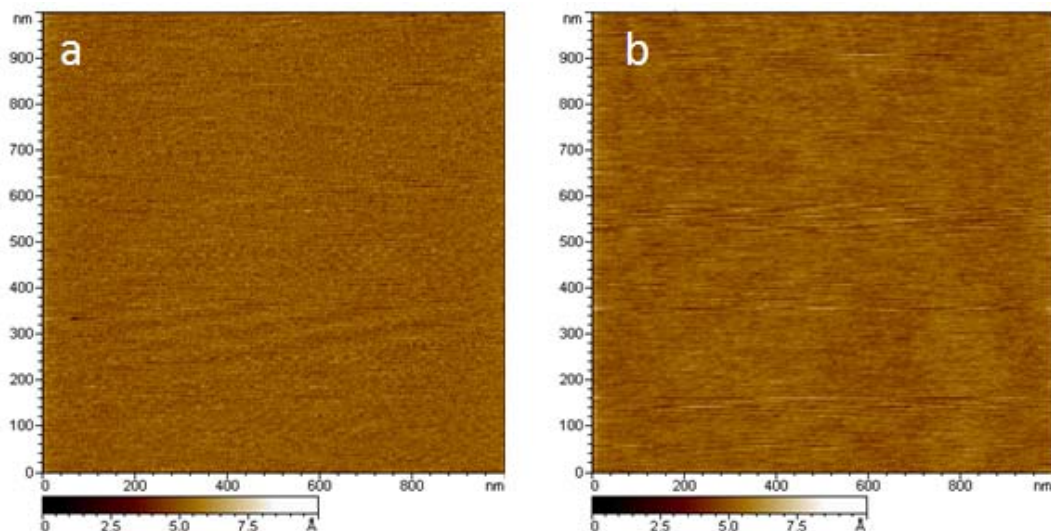


Figure 4.10. AFM images of inhibitor K1 at (a) 0.5 CMC and (b) 2 CMC on mica. All gold color images were collected from a Picoscan 2000 AFM using DP-19 probes ($k_n \sim 0.6$ N/m).

Figure 4.11 shows the surface morphologies and profiles of inhibitor K2 coco quaternary alkylammonium salts (quats) at 0.5 CMC and 2 CMC on mica. Different from the surface of inhibitor K1 TOFA imidozium, the surface is not uniformly flat at either 0.5 CMC or 2 CMC condition. At 0.5 CMC, the roughness of the surface shown from the profile curve is ~ 0.5 nm. Those curvy features can be due to the partial coverage of inhibitor film on the surface or the length difference among the C_{12} , C_{14} and C_{16} hydrocarbon chains of the adsorbed molecules. Considering the ~ 0.5 nm variation from the surface profile across the image, the surface features are more likely because of the length difference from the different hydrophobic chains. If the surface was partial covered by inhibitor molecules, the height variation should be the same as the molecular

length which is $\sim 2\text{nm}$. Interestingly, at the 2 CMC condition, the surface morphology of quats on mica is completely different from the morphology at 0.5 CMC. Cylindrical “worm-like”²⁰⁶ structures are shown in the AFM image (Figure 4.11b), indicating cylindrical micelles were formed on mica surface. These periodic cylindrical structures are real surface features, determined by using previous discussed procedures for artifacts.

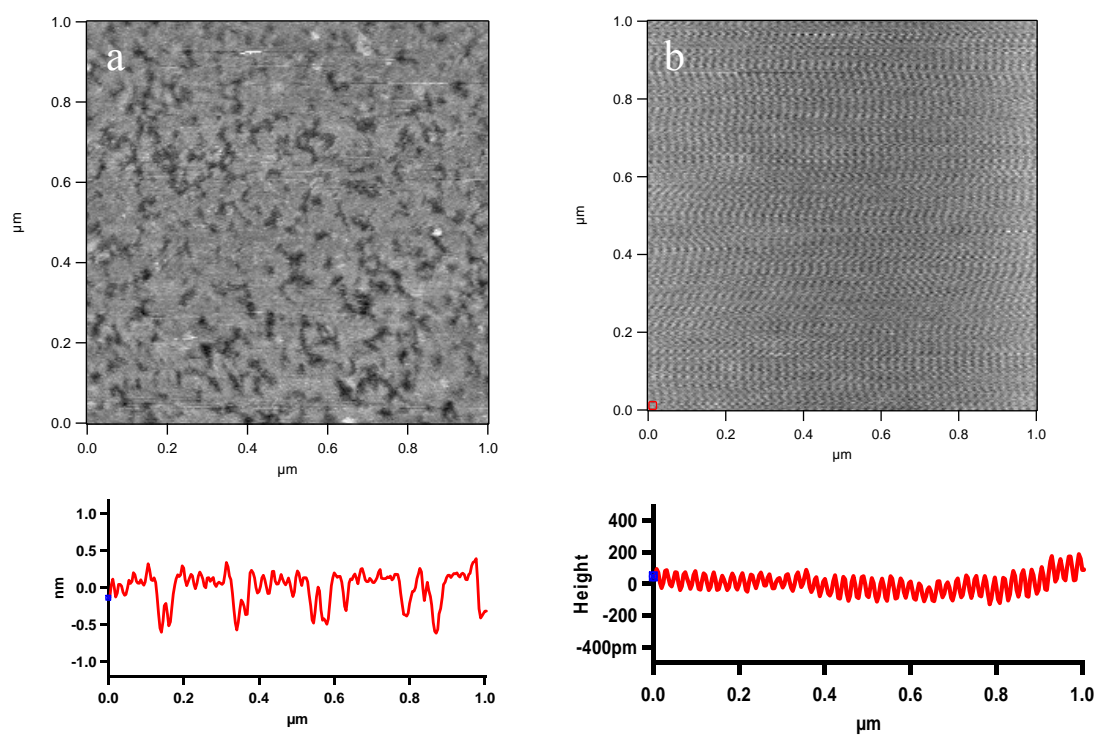


Figure 4.11 AFM images and corresponding profiles of inhibitor K2 coco quaternary alkyl ammonium salt (quat) at (a) 0.5 CMC and (b) 2 CMC on mica. At 0.5 CMC, the surface of adsorbed quats on mica is not uniformly flat. The surface features at 0.5 CMC is probably due to the different lengths of the alkyl chains of each of the three components in the inhibitor product. At 2 CMC, inhibitor molecules formed cylindrical micelles on the surface.

Inhibitor K3, sodium thiosulfate, has been widely used as an “inhibitor helper” to enhance the protection efficiency of surfactant type inhibitors. However, sodium thiosulfate is not a surfactant, and it does not have a hydrophobic chain and hydrophilic head. The mechanism of how sodium thiosulfate “helps” other surfactant inhibitors is still poorly understood. Figure 4.12 shows the surface morphology on mica in the presence of 24% sodium thiosulfate solution. The featureless surface shown in the image is actually the same as the surface in inhibitor K1 solution, indicating either sodium thiosulfate does not have any adsorption or it forms a uniform flat layer. It is hard to determine which one is the case only based on surface morphology. Further studies of the penetration force and film thickness measurements have confirmed that no surface film was formed on mica by sodium thiosulfate.

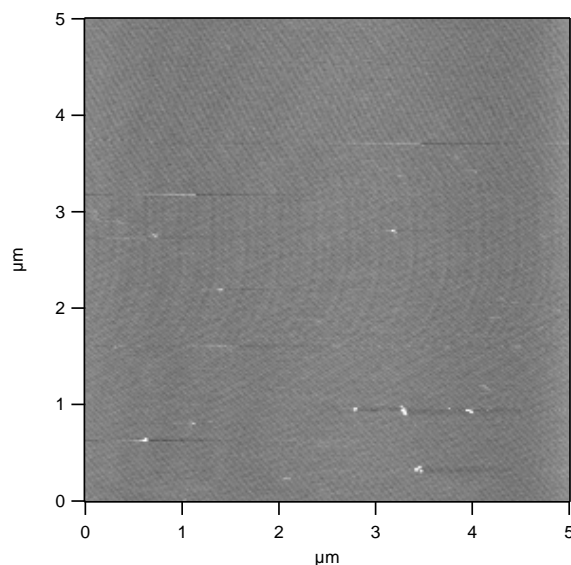


Figure 4.12 AFM images on mica surface in the presence of 24% sodium thiosulfate solution.

Whether or not sodium thiosulfate adsorbs on the surface, a goal was to determine if this compound can significantly change the adsorption structure of inhibitor molecules. Figure 4.13 shows the AFM images on mica in the presence of inhibitor K4, which is a mixture of 20% TOFA imidazolium (K1) and 4% sodium thiosulfate. Compared with the surface morphologies of K1 shown in Figure 4.7, the surface morphologies of inhibitor K4 are the same as those of K1 at both 0.5 CMC and 2 CMC. This indicates that the addition of sodium thiosulfate does not change the adsorption of surfactant type inhibitors. The same analyses on inhibitor K5, which is a mixture of 20% coco quaternary alkylammonium salt and 4% sodium thiosulfate, has led to the same conclusion that sodium thiosulfate does not change the structure of adsorbed inhibitor molecules, because no obvious change was found between the surface morphologies (Figure 4.14) of K5 and the surface morphologies (Figure 4.11) of K2 at both 0.5 and 2 CMC.

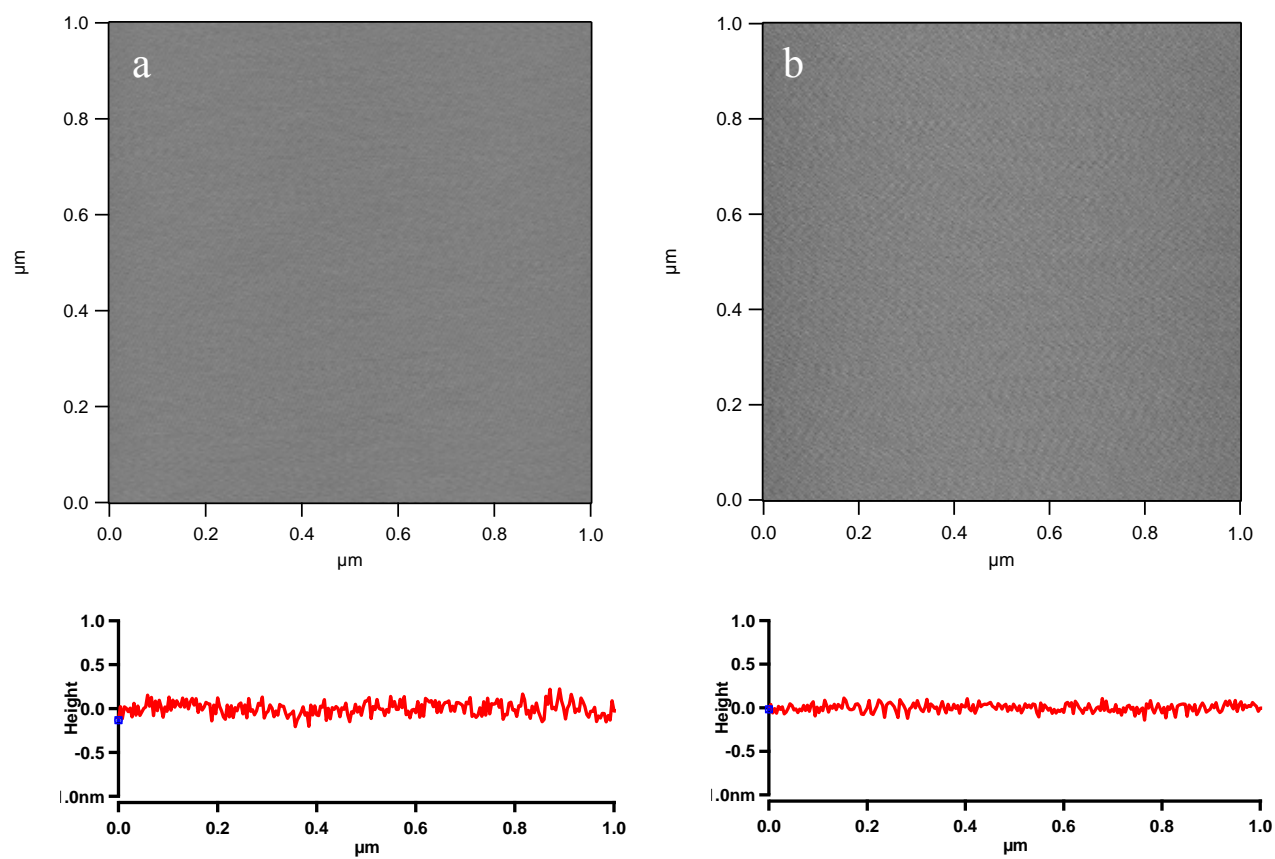


Figure 4.13 AFM images and corresponding profiles of inhibitor K4, a mixture of 20% TOFA imidazolium and 4% sodium thiosulfate at 0.5 CMC (a) and 2 CMC (b) on mica.

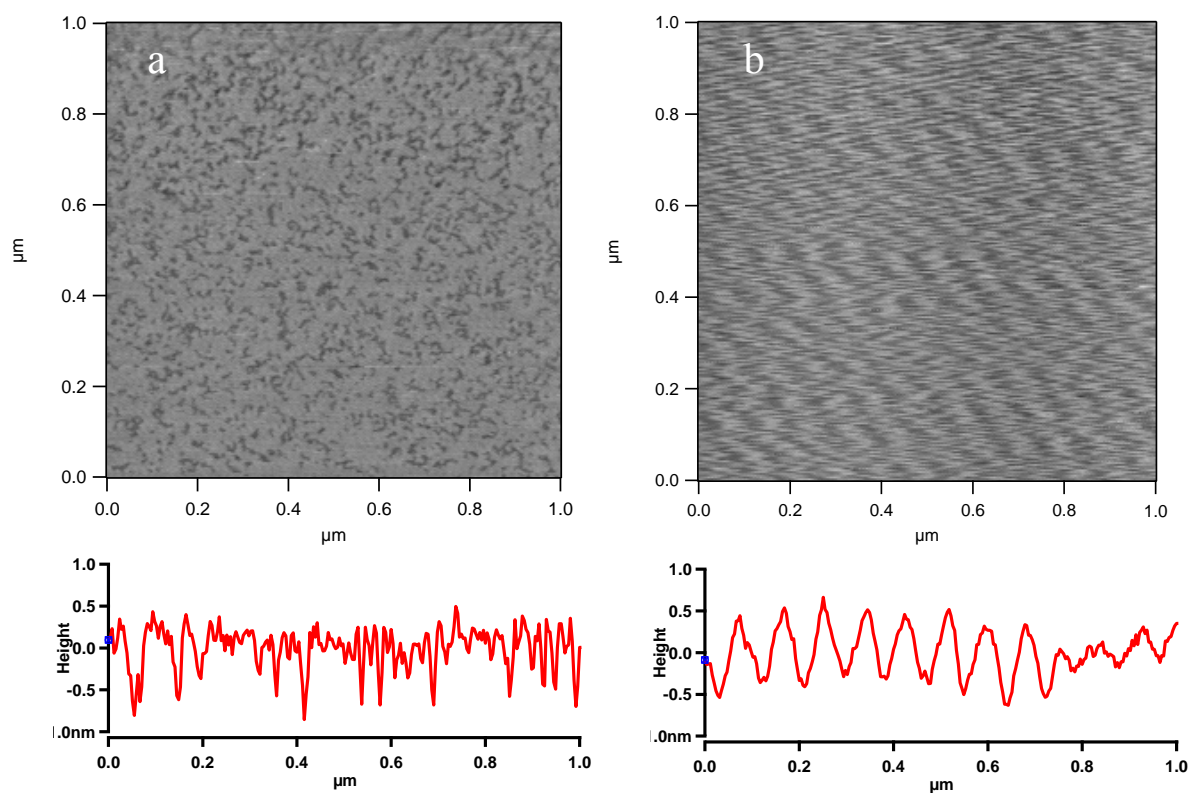


Figure 4.14 AFM images and corresponding profiles of inhibitor K5, a mixture of 20% coco quaternary amine salts (Quats) and 4% sodium thiosulfate at 0.5 CMC (a) and 2 CMC (b) on mica.

4.3.2 Film thickness measurement

To investigate the internal structure of inhibitor films and to accurately measure their thicknesses, the inhibitor molecules were removed by scratching from the surface over an area of $1 \times 1 \mu\text{m}$. Figure 4.15 shows the AFM images with the center area ($1 \times 1 \mu\text{m}$) where the inhibitor molecules were removed by the AFM tip at different applied normal forces. The same tip was used in these three experiments to maintain consistent conditions. When the applied normal force was 2 nN, *i.e.*, less than the critical force for the tip to penetrate the inhibitor film, the scan revealed the surface morphology of the

adsorbed inhibitor. When the normal force was 40 nN, the tip penetrated the inhibitor film and created artifacts in the image. However, because the force was insufficient to remove molecules from the surface, the inhibitor film stayed essentially intact after the lateral scratching procedure. At an applied normal force of 60 nN the inhibitor molecules were removed in the scratched area, shown in the center of the image. Increasing the normal force beyond 60 nN did not change the depth in the scratched area and the underneath hard mica surface was not scratched by the tip. Figure 4.16 shows the AFM images of scratched and unscratched areas and the corresponding depth measurements at 0.5 CMC and 2 CMC. These profiles show depths of approximately 2 and 4 nm in the scratched areas at 0.5 CMC and 2 CMC. This corresponds to film thicknesses of one and two molecular lengths (Figure 4.17), *i.e.*, a monolayer is formed at 0.5 CMC and a bimolecular layer at 2 CMC. This is consistent with the models proposed in previous publications^{126,207}. The film thickness measurements of 2 and 4 nm for the respective concentrations were repeatable at different areas on the mica surface, indicating that a continuous uniform adsorbed film had formed over the surface. To confirm the film thickness was due to adsorbed surfactant molecules, similar experiments were repeated in pure water without inhibitor molecules present. The experiments revealed a uniform surface with none of the mica removed in the area scratched by the AFM tip using a normal load of 60 nN.

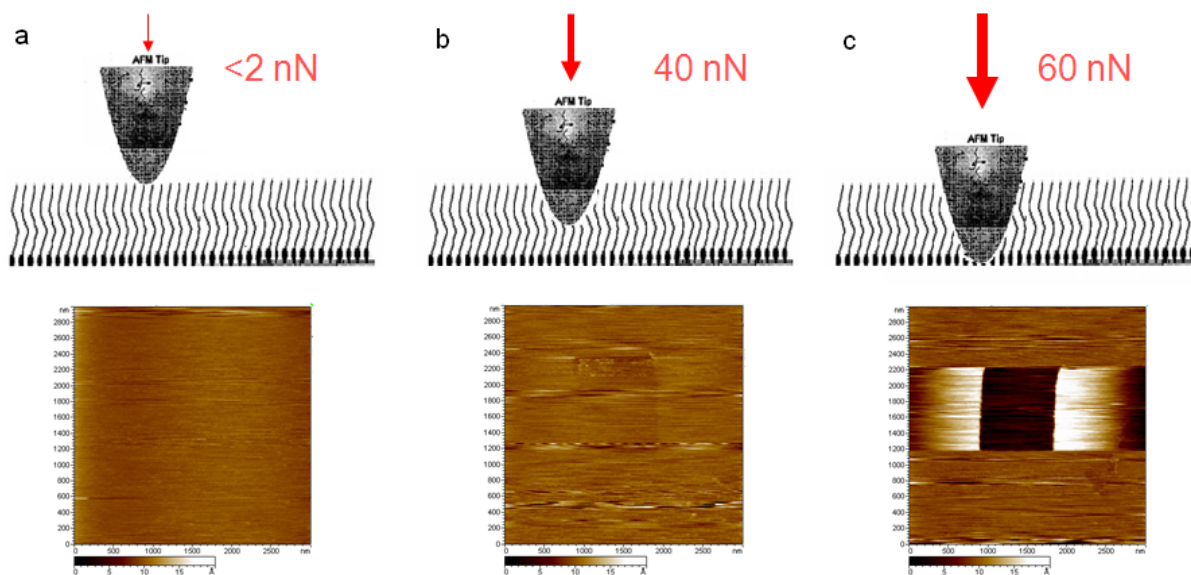


Figure 4.15 Inhibitor films formed at $2 \times \text{CMC}$ and scratched using different normal forces applied to the cantilever. When the normal force was $< 2\text{ nN}$ the tip did not penetrate the inhibitor film and the scan was able to show the topography of the inhibitor film. When the normal force was larger than 2 nN but less than 60 nN , the tip could penetrate the film and created artifacts in the image. However, the force was insufficient to remove inhibitor molecules from the surface and the film stayed intact. When the applied normal force was larger than the threshold value of 60 nN , inhibitor molecules were removed from the scanned or scratched area.

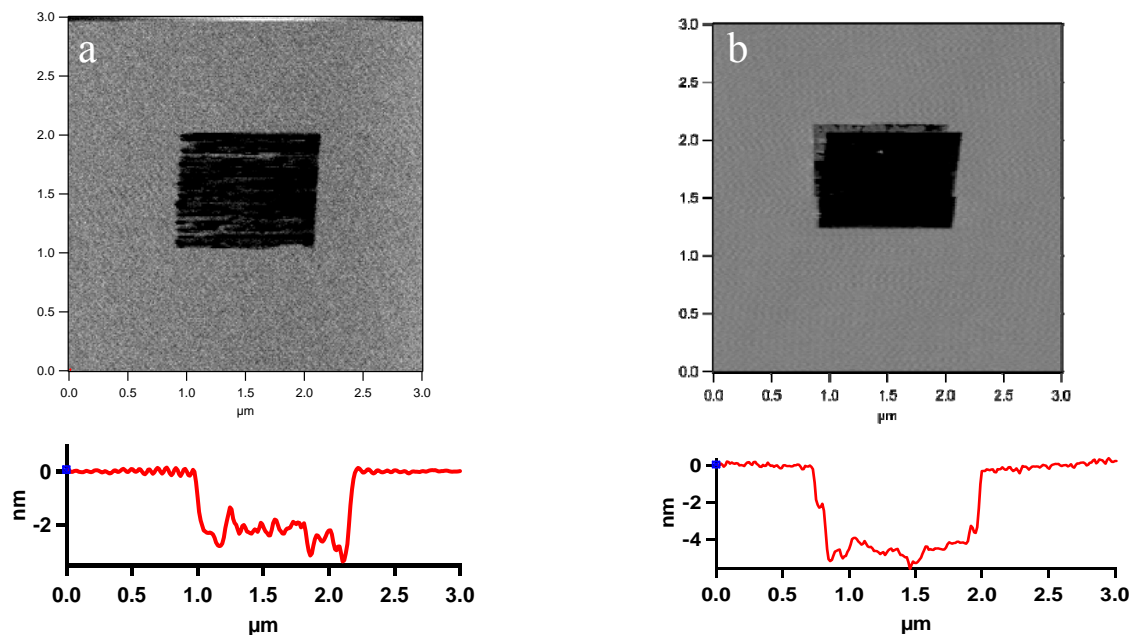


Figure 4.16 Film thickness measurement of TOFA imidazolium inhibitor K1 after scratching away an area ($\sim 1 \times 1 \mu\text{m}$) of the inhibitor film with a normal load of 60 nN applied to the cantilever, (a) film formed at 0.5 CMC and (b) at 2 CMC. The film thickness was determined by measuring the height difference between scratched and unscratched areas in contact mode. Results show the measured film thicknesses are ~ 2 nm at 0.5 CMC and ~ 4 nm at 2 CMC. Results obtained from MFP-3D AFM.

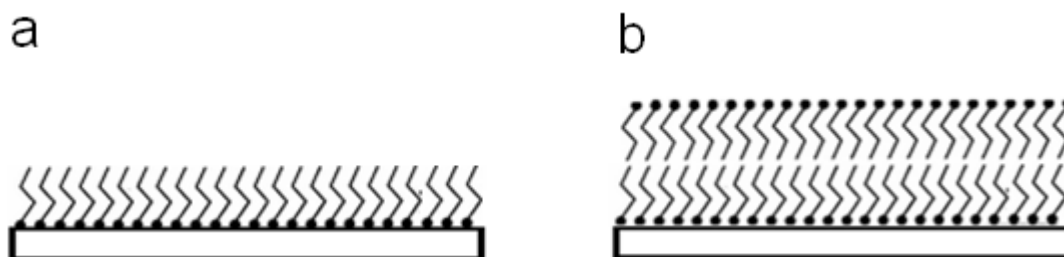


Figure 4.17 Schematic drawings of the monolayer and the bi-layer structures for inhibitor K1 TOFA imidazolium at 0.5 CMC (a) and 2 CMC (b).

The film thickness measurements of inhibitor K1 on mica were verified using a different AFM system and different scanning probes. Figure 4.18 shows the AFM images with scratched areas and corresponding surface profiles for inhibitor K1 at 0.5 CMC and 2 CMC conditions, obtained from Picoscan AFM using DP-19 probes ($k_n \sim 0.6$ N/m). Comparing with Figure 4.16 obtained from MFP-3D AFM using SNL-10 probes ($k_n \sim 0.4$ N/m), same surface morphologies and thicknesses were measured at both 0.5 CMC and 2 CMC conditions again. The only difference shown in gold color images are those “white areas” next to the scratched areas. These areas were automatically produced by converting the raw data to flattened images in the software of Picoscan 2000 AFM, and they do not affect the measurement of film thickness.

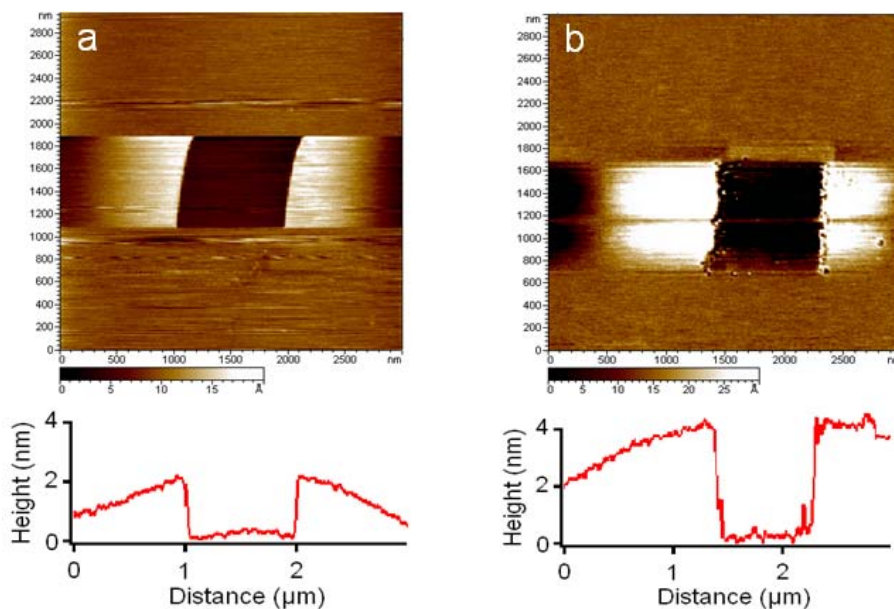


Figure 4.18 Film thickness measurement of TOFA imidazolium inhibitor K1 at (a) 0.5 CMC and (b) 2 CMC, using Picoscan AFM and DP-19 probes.

The same film thickness measurements were done on inhibitor K2 $C_{12} \sim C_{16}$ coco quaternary alkylammonium salts on mica at 0.5 CMC and 2 CMC conditions. Figure 4.19 shows AFM images of scratched and unscratched areas and the corresponding depth measurements at 0.5 and 2 CMC inhibitor concentrations, respectively. At 0.5 CMC, the film thickness is about 2 nm which is the same as the molecular length, indicating inhibitor K2 forms a monolayer. Because of the length difference among C_{12} , C_{14} and C_{16} hydrophobic chains, the monolayer formed by inhibitor K2 at 0.5 CMC is not as flat as the uniform monolayer formed by inhibitor K1 at 0.5 CMC. Figure 4.20a shows the schematic drawing of the monolayer for inhibitor K2 at 0.5 CMC. Even though their molecular lengths are different, $C_{12} \sim C_{16}$ coco quaternary alkylammonium molecules were all in the “standing-up” orientation and formed a monolayer film. At 2 CMC, different from the 4 nm bi-layer film for inhibitor K1, the measured film thickness for inhibitor K2 was only ~ 2 nm, indicating the formation of hemi-micelles (Figure 4.20b) on the mica surface.

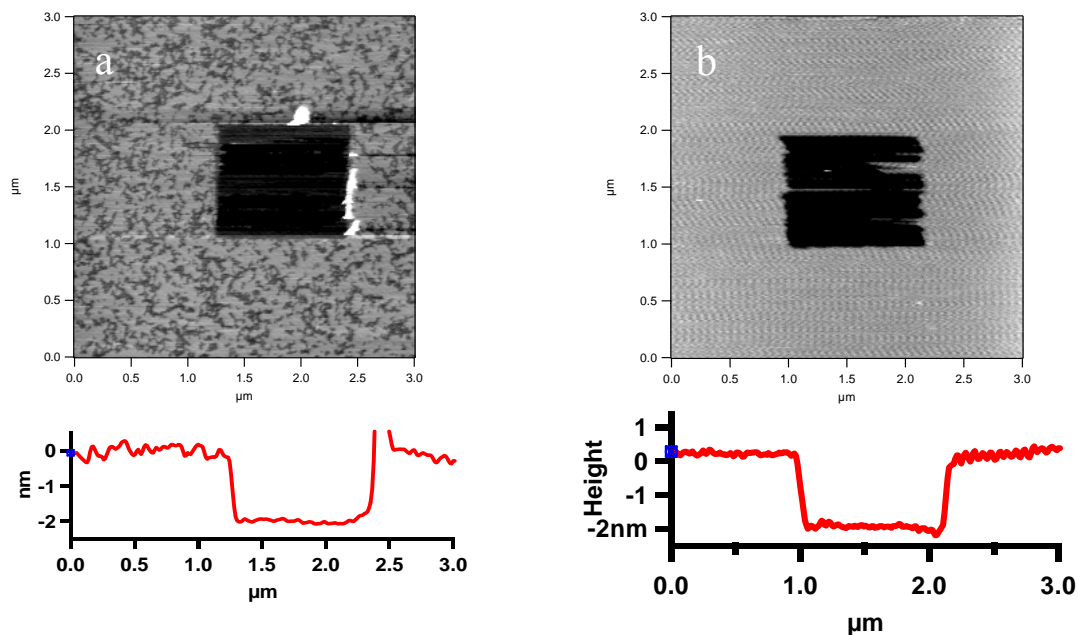


Figure 4.19 Film thickness measurement of $C_{12} \sim C_{16}$ coco quaternary alkylammonium (inhibitor K2) after scratching away an area ($\sim 1 \times 1 \mu\text{m}$) of the inhibitor film with a normal load of 60 nN applied to the cantilever tip, (a) film formed at $0.5 \times \text{CMC}$ and (b) at $2 \times \text{CMC}$. The film thickness was determined by measuring the height difference between scratched and unscratched areas in soft contact mode.



Figure 4.20 Schematic drawings of the monolayer and the hemi-micelle structures for inhibitor K2 $\sim C_{16}$ coco quaternary alkylammonium at (a) 0.5 CMC and (b) 2 CMC .

In order to verify our previous hypothesis that sodium thiosulfate does not adsorb on the mica surface, the film thickness measurements were carried out on mica surface in

the presence of a 24% sodium thiosulfate solution. After the scratching, the surface morphology on the scratched area is exactly the same as the surface before scratching. Therefore, the film thickness measurements for inhibitor K3 have confirmed that no surface layer was formed on mica surface in the presence of sodium thiosulfate. We further analyzed the film thicknesses of inhibitor blends K4 and K5, which are mixtures of sodium thiosulfate and inhibitor K1 and K2, respectively. Figure 4.21 shows AFM images of scratched and unscratched areas and the corresponding depth measurements for inhibitor K4 and K5 at 2 CMC. Their film thicknesses are the same as the thicknesses of K1 and K2 at 2 CMC respectively, indicating the additive sodium thiosulfate does not increase the film thickness and change the adsorption structure of inhibitor molecules. This is again a strong evidence that sodium thiosulfate does not adsorb on mica surface or form adsorption layer. Given that the silicate sheets of the mica structure are themselves anionic and thiosulfate is anionic, no electrostatic interactions between them would be expected to occur. Figure 4.22 shows a summary of film thickness of different inhibitor formulations at 0.5 CMC and 2 CMC conditions. These inhibitor film thicknesses are very important for understanding the internal structures of different inhibitor molecules at various conditions.

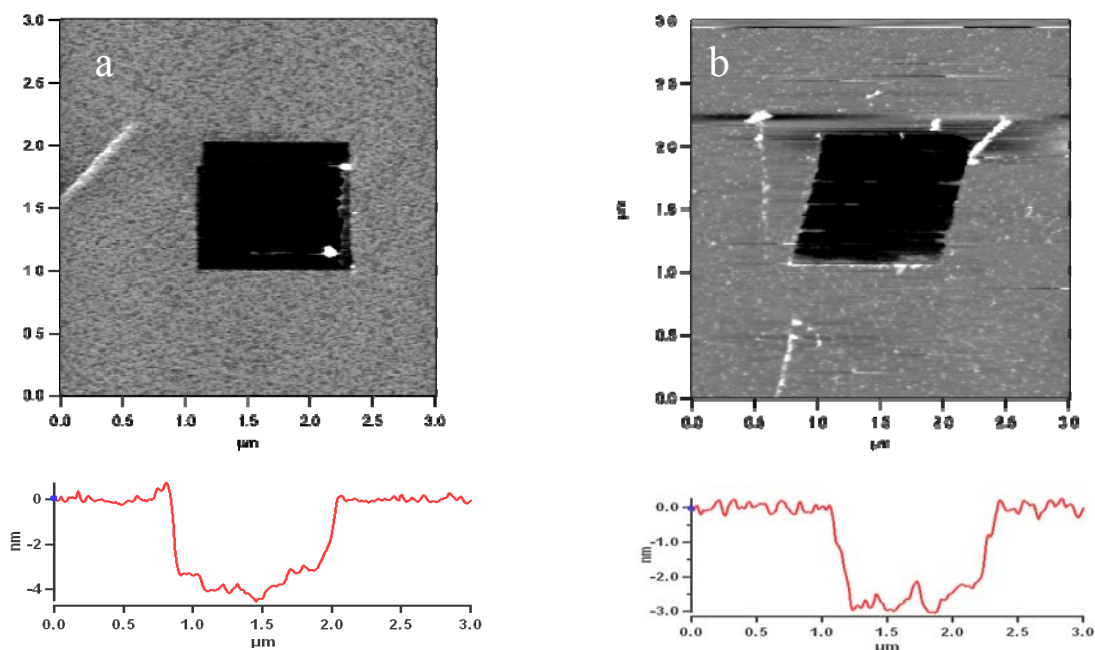


Figure 4.21 Film thickness measurement of corrosion inhibitor K4 and K5 after scratching away an area ($\sim 1 \times 1 \mu\text{m}$) of the inhibitor film with a normal load of 60 nN applied to the cantilever, (a) film formed by inhibitor K4 and (b) film formed by inhibitor K5. The film thickness was determined by measuring the height difference between scratched and unscratched areas in soft contact mode.

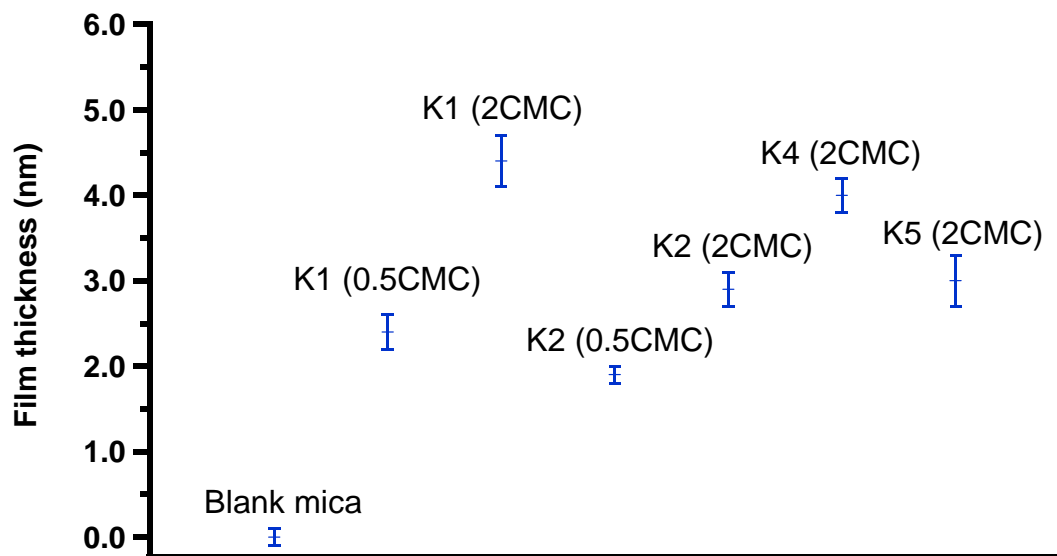


Figure 4.22 Summary of the film thickness for different inhibitors at 0.5 CMC and 2 CMC conditions.

4.3.3 Penetration force/force distance curves

Although it is not fully understood how the protective barrier, formed by inhibitor molecules, decreases corrosion on metal surfaces, the efficiency of an inhibitor film to reduce corrosion is related to the length of the hydrophobic chain^{178,208-209}, functional group^{178,210}, packing density of the inhibitor molecules¹²⁶, and the thickness of the inhibitor film²¹¹. It can be assumed that the protectiveness and integrity of these films could be related to their mechanical resistance. In this work, the mechanical resistance of the inhibitor film was determined using AFM force measurements.

Figure 4.23 shows the force-distance curve on blank mica in deionized water. On the mica surface, which is free of adsorbed surfactant molecules, the force between the tip and surface is zero when the distance is larger than 5 nm, indicating that there is no

interaction of the AFM tip and the surface. When the distance of the tip is approximately 5 nm, the tip is attracted to the surface due to short-range attractive forces, which shows as a negative force. At this point, the tip is in contact with the surface, and the interaction between the tip and surface becomes repulsive. Further downward movement of the AFM tip forces it against the mica surface and the force increases dramatically, because the tip is not able to penetrate the hard surface. This force curve is used as a blank force for further study on inhibitors.

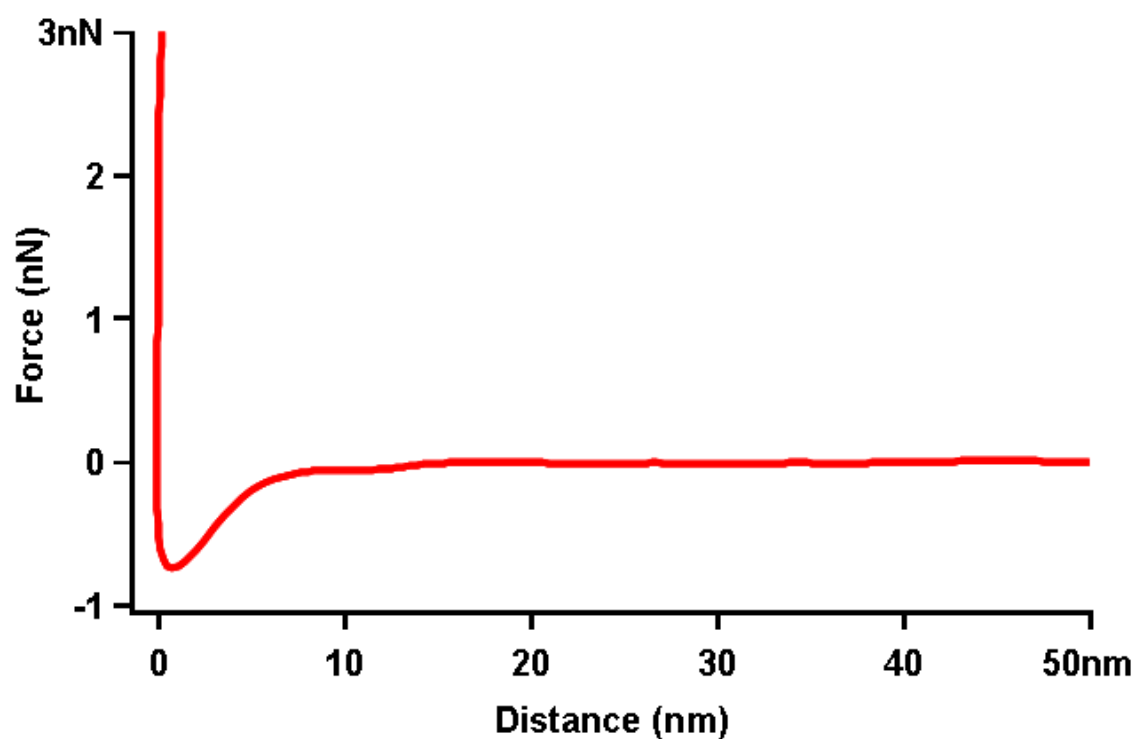


Figure 4.23 Force curve on blank mica on deionized water, used as the blank curve.

Figure 4.24 shows the force curves of inhibitor K1 adsorbed on mica surface at 0.5 CMC and 2 CMC. The presence of adsorbed inhibitor film produces repulsive

intermolecular force against the AFM tip. These repulsive forces start to be seen at a distance of about a 10 nm tip-surface separation. The repulsive force increases linearly as the tip is moved closer to the surface. In the case of the film formed at 0.5 CMC, the repulsive force reaches a maximum at about 1 nN before the tip “suddenly” penetrates the inhibitor film as shown by an abrupt decrease in repulsive force. Further movement of the AFM tip towards the surface causes the force to increase as the tip is pressed against the mica surface. The maximum force before the tip suddenly penetrates the film is the threshold value for penetrating the inhibitor layer, and in this research it is called the “penetration force”. In the case of the surfactant film formed at 2 CMC, the profile of the force/distance curve is very similar. However, the force required to penetrate the film is appreciably higher, about 2 nN. This is not unexpected, because a thicker film consisting of two molecular layers is formed at the higher inhibitor concentration as opposed to a monolayer film below the CMC (0.5 CMC).

It is worth to emphasize that the force-distance curve is not an accurate way to measure the film thickness, because of the following reasons: first, the tip-to-inhibitor interaction happens before the tip is in contact with the inhibitor film; second, inhibitor molecules can also adsorb on the tip surface and increase the tip-to-sample distance; third, the measured distance in a force-distance curve includes the bending of AFM cantilever when the repulsive tip-to-inhibitor interaction occurs. All these facts make the force-distance curve showing an overestimation of the film thickness. Therefore, the scratching technique described above, which physically removed inhibitor molecules, provides a more accurate and precise measurement of film thickness.

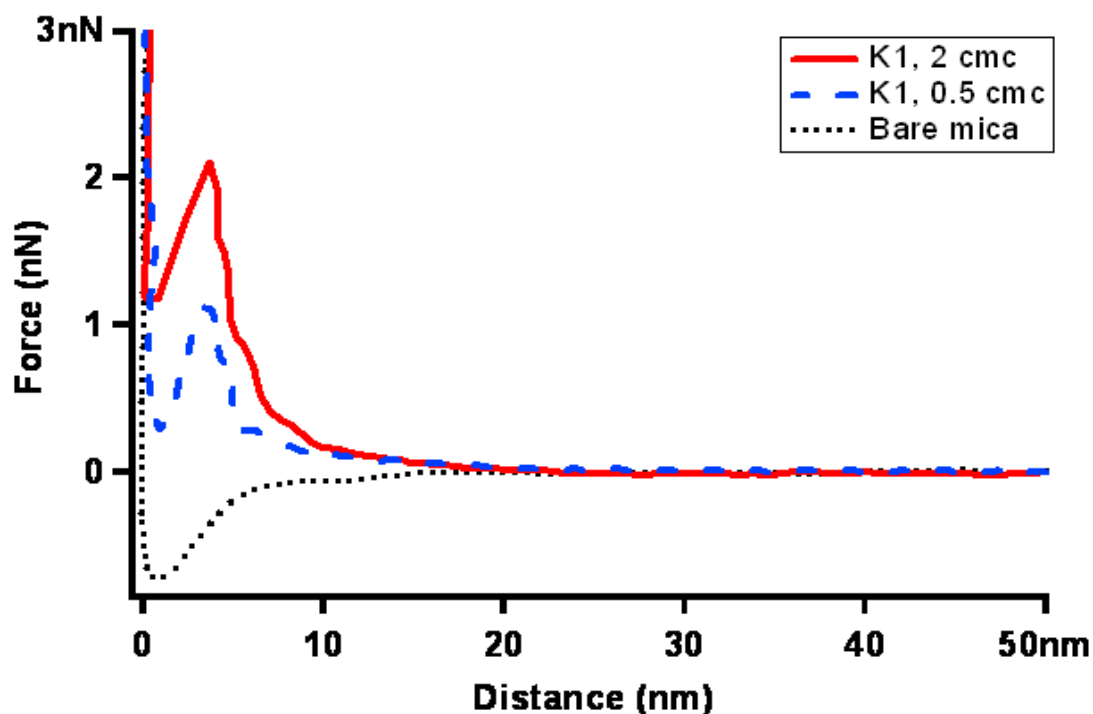


Figure 4.24 Force distance curves for inhibitor films on mica and a bare mica surface. The curves were recorded in aqueous solutions of TOFA imidazolium at 0.5, 2 times the CMC and in pure water. Results obtained from MFP-3D AFM using SNL-10 probes.

The penetration force measurements of inhibitor K1 on mica were verified using a different AFM system and different scanning probes. Figure 4.25 shows the force curves for inhibitor K1 at 0.5 CMC and 2 CMC conditions, obtained from Picoscan AFM using DP-19 probes ($k_n \sim 0.6$ N/m). Comparing with Figure 4.24 obtained from MFP-3D AFM using SNL-10 probes ($k_n \sim 0.4$ N/m), same penetration force values were measured at both 0.5 CMC and 2 CMC conditions, respectively. The only difference between Figure 4.24 and Figure 4.25 in the force curves is the slopes in the contact region. This is because the

X axis in Figure 4.24 is the tip-sample distance while the X axis in Figure 4.25 is the distance of Z scanner movement. This difference is caused by the different software used in two types of instruments, and it does not affect the measurement of penetration forces. Therefore, consistent results, again, were obtained confirming a good repeatability in our AFM analysis.

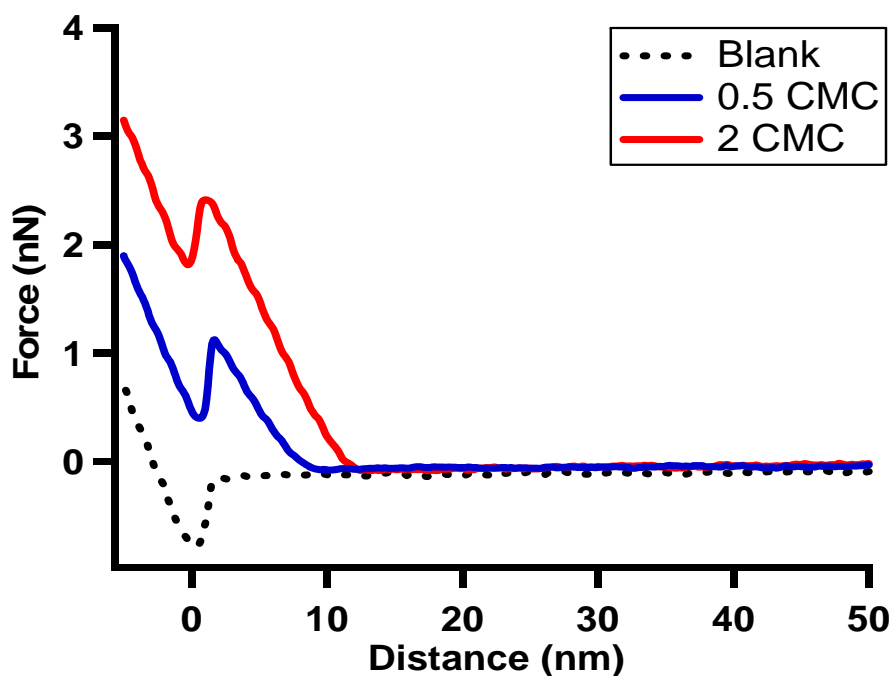


Figure 4.25 Force distance curves for 0.5 CMC and 2 CMC inhibitor films on mica and a bare mica surface. Results obtained from Picoscan 2000 AFM using DP-19 probes.

Figure 4.26 shows the force curves of inhibitor K2 adsorbed on mica surface at 0.5 CMC and 2 CMC. In the case of the film formed at 0.5 CMC, the repulsive force reaches a maximum at about 1 nN before the tip “suddenly” penetrates the inhibitor film, which is similar to the force measured on K1 at 0.5 CMC. This is not a surprise because both K1

and K2 molecules have similar structures and each forms a uniform monolayer at 0.5 CMC. In the case of the hemi-micelles formed at 2 CMC by K2 molecules, the force required to penetrate the hemi-micelle is also about 1 nN, similar to the force value measured at 0.5 CMC for a monolayer. This is probably because the film thickness of hemi-micelle structure is the same as the film thickness of monolayer, even though the hemi-micelle structure exhibits extra surface features.

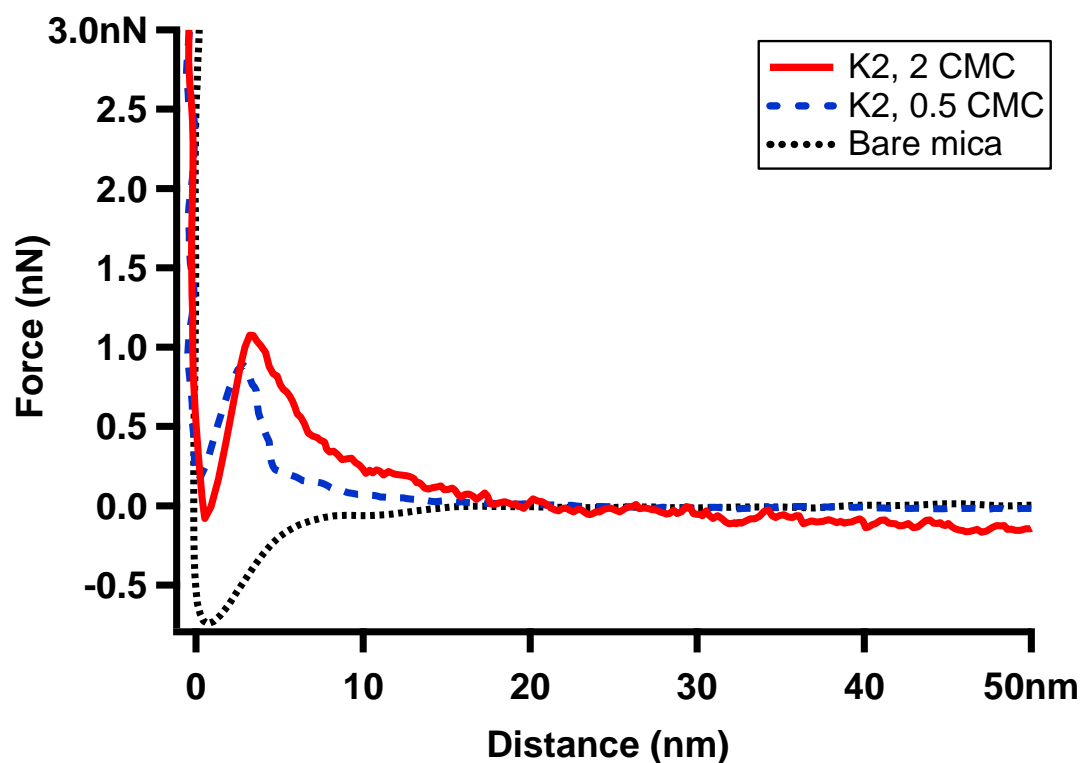


Figure 4.26 Force distance curves for inhibitor films on mica and a bare mica surface. The curves were recorded in aqueous solutions of inhibitor K2 quat at 0.5 and 2 times the CMC as well as in pure water.

As discussed, sodium thiosulfate does not adsorb on a mica surface. Force distance curves can also show whether there is a layer of sodium thiosulfate on a mica surface. Figure 4.27 shows the force curve on a mica surface in the presence of 24% sodium thiosulfate. The force curve measured in the solution of inhibitor K3 is the same as the curve on blank mica in deionized water (Figure 4.23). This result again has confirmed that sodium thiosulfate has insignificant adsorption on the mica surface.

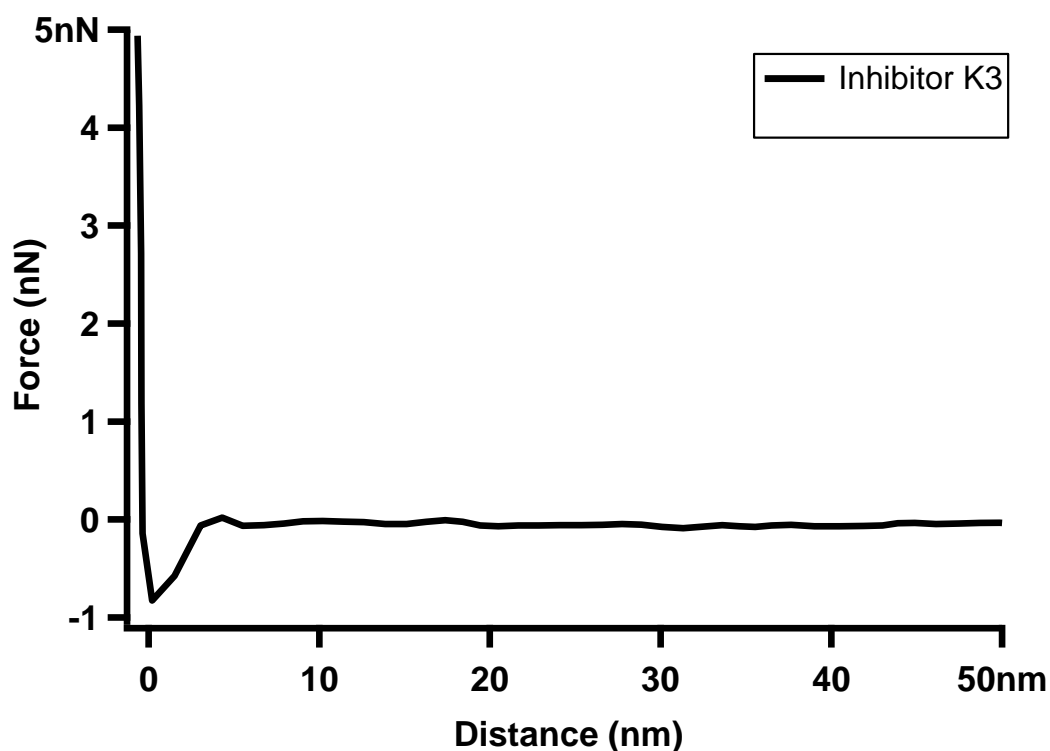


Figure 4.27 Force distance curves on mica in the presence of 24% K3 solution. The curve is the same as the curve on bare mica in water.

Since the sodium thiosulfate does not adsorb on mica and does not change the adsorption structure of inhibitor molecules, we expect the measured force curves for

inhibitor K4 and K5 to be the same as the curves for inhibitor K1 and K2, respectively. Figure 4.28 shows the force curves on mica in the presence of inhibitor K1, 2 CMC and K4, 2 CMC. Both curves almost overlap, indicating the sodium thiosulfate does not change the adsorption of inhibitor molecules. The same observation was found from the force curves for inhibitor K5 at 2 CMC, shown in Figure 4.29, which is the same as the curve for inhibitor K2 at 2 CMC. Therefore, this penetration force measurement not only exhibits a force value for the AFM tip to break through the inhibitor film, but can be subjectively used to tell if the internal structure of the film is changed by additives.

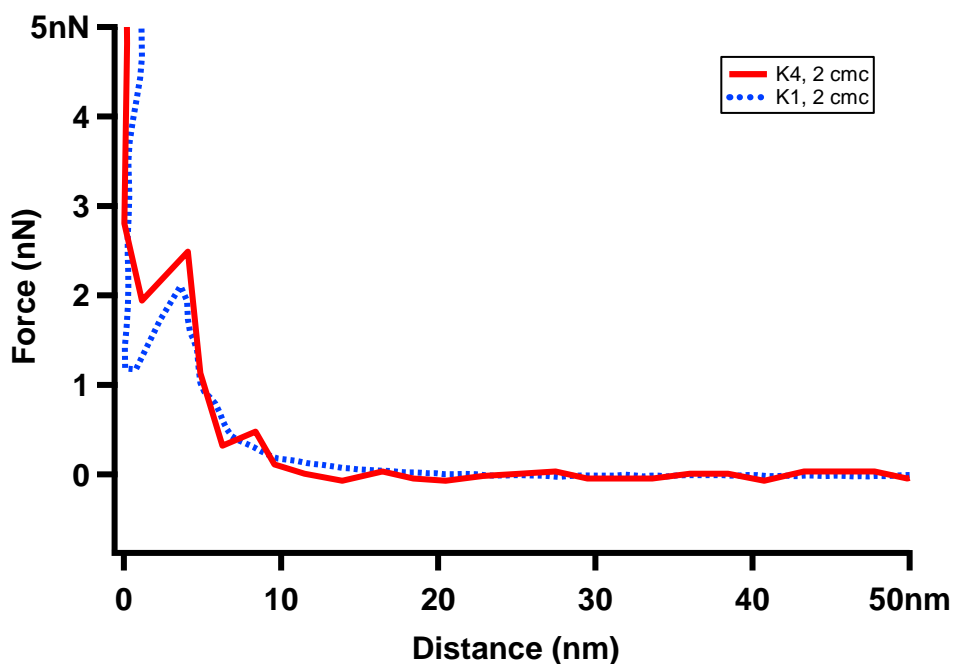


Figure 4.28 Force distance curves on mica in the presence of K1, 2 CMC (dotted line) and K4, 2 CMC (solid line), respectively. The same penetration force was obtained in the inhibitor solution with sodium thiosulfate.

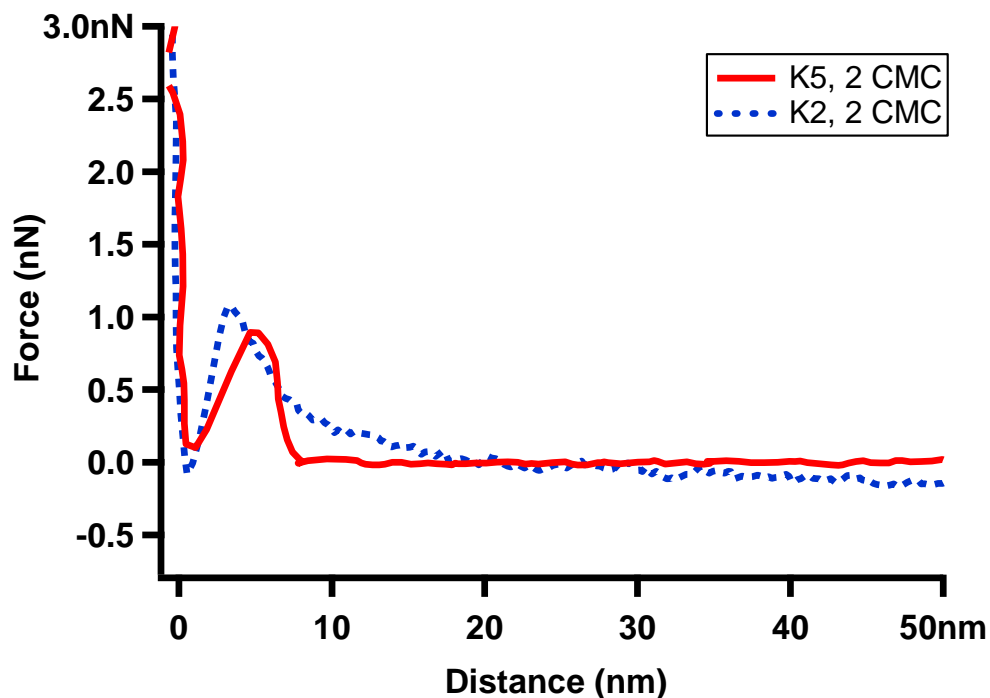


Figure 4.29 Force distance curves on mica in the presence of K2, 2 CMC (dotted line) and K5, 2 CMC (solid line), respectively. The same penetration force was obtained in the inhibitor solution with sodium thiosulfate.

The penetration force measurements described above may provide valuable information about the force required to penetrate an inhibitor film and this was the subject of further research. For a better appreciation of the mechanical resistance offered by the inhibitor film in the normal direction, the penetration force was converted into a stress by using an area based on the diameter of the head of the AFM tip, which was measured to be 30 nm by using the high-resolution SEM image of the tip. In this order of magnitude analysis, it can be assumed that the head of the tip is spherical, and the cross-sectional area was calculated as $\sim 700 \text{ nm}^2$ (within this order of magnitude)

Using the area of 700 nm^2 , the force to penetrate the inhibitor films of $\sim 1 \text{ nN}$ and $\sim 2 \text{ nN}$ were converted to a pressure (force/area) or shear stress. Shear stresses of $\sim 1 \text{ MPa}$ and $\sim 3 \text{ MPa}$ were determined for the 2 and 4 nm films formed at 0.5 CMC and 2 CMC, respectively. Although these numbers are approximate (only accurate to within an order of magnitude), they are meaningful in the context of engineering applications of inhibitors.

One mechanism for inhibitor failure has been repeatedly attributed to fluid flow removing inhibitor films by shear^{198,212}. A typical wall-shear stress due to the flow in an oil and gas line would not normally exceed 1 kPa, even in the case of violent multiphase slug flow. More typical values are in the range of 1 -10 Pa. Using the most extreme flow condition, the maximum hydrodynamic shear stress which has been blamed for inhibitor removal (order of 1 kPa), is still 2-3 orders of magnitude below the stress measured here which is required to penetrate the inhibitor film (order of 0.1 – 1 MPa). Due to this large discrepancy, it seems unlikely that the shear forces of fluid flow alone can be blamed for removal and failure of an inhibitor film. Another point need to be emphasized here is the claim of removing inhibitor films by fluid flow was often based on corrosion rate measurements²¹³. However, the corrosion process is actually a complicated process and often related to a lot of facts, such as pH, ionic strength, temperature, and flow conditions. When the flow rate is increased in a inhibitor solution, the increase of corrosion rate may not simply related to the removal of inhibitor film, because the flow rate may also change the mass transfer and surface pH, and can even change a single phase flow to a multi-

phase flow. Therefore, the increase of corrosion rate may not directly related to the desorption of corrosion inhibitors.

4.3.4 Lateral removal force

As discussed in previous sections, inhibitor molecules can be removed using a high-loaded scanning tip and the film thickness can be measured. In this section, we quantitatively study how much force is required to remove inhibitor molecules, which is related to the adhesion of inhibitor molecules. The force is created between the scanning tip and the molecules in a lateral direction, and thus the force is defined herein as the lateral force.

The lateral force was measured by applying a high load of 60 nN to the cantilever, as described above for the film thickness measurements. At this force, it was found that the inhibitor molecules could be removed from the surface by the scanning tip. To perform a lateral force measurement a “cyclic line scan”, also called a “friction loop”, was used. The AFM tip pushed against the substrate surface was firstly moved in one direction and then traversed back to the starting point by scanning in the reverse direction. Slightly different flexing of the cantilever in the forward and reverse scan ensures that the forward and reverse traces do not fully overlap. The instrument records the cantilever torque induced by the lateral interaction between the AFM tip and the sample surface. The lateral spring constant and AFM photodiode sensitivity were used to convert the raw data to quantitative force values. Therefore, the lateral force is calculated

with the following equation, where F_{trace} is the averaged force value in trace direction and F_{retrace} is the averaged force value in retrace direction.

$$F_{\text{lateral}} = (\bar{F}_{\text{trace}} - \bar{F}_{\text{retrace}})/2 \quad \text{Equation 4.1}$$

As the lateral forces measured in trace and retrace directions are in opposite directions, the F_{lateral} is actually the average value from trace force and retrace force.

Figures 4.30 and 4.31 show lateral force measurements for a monomolecular layer and a bimolecular layer film formed at 0.5 and 2 CMC, respectively. In each of these figures, there are two sets of lateral force curves recorded on two different surfaces, one for a mica surface in water (blank) and the other is for a filmed mica surface in an aqueous solution of the inhibitor. The curves were recorded using the same tip and with the same applied normal force of 60 nN to the cantilever. Positive and negative force curves shown in the graphs correspond to the force recorded during the forward and reverse scan, respectively. The measured lateral force is an average of a large number of force magnitude measurements (F_{trace} and F_{retrace}), recorded during the forward and reverse scans. In Figure 4.31, the average lateral force on inhibitor free mica was 163 nN while the average lateral force in the presence of the inhibitor film was 207 nN. The significant increase in the lateral force of 44 nN is attributed to a change in surface properties and the force to remove adsorbed inhibitor molecules from the mica surface.

In Figure 4.30, the magnitude of the lateral force measurements recorded on a monomolecular layer inhibitor film in a solution at 0.5 times the CMC are very similar to

the bimolecular layer film in Figure 4.31. For the monolayer film, the difference in average force between the two curves in the presence and absence of inhibitor was 40 nN. That is, there was no significant difference measured between the force to remove a bilayer or a monolayer film. These results provide further evidence that these lateral force measurements are determining the adhesive force acting between the hydrophilic moiety of the molecule and the mica surface.

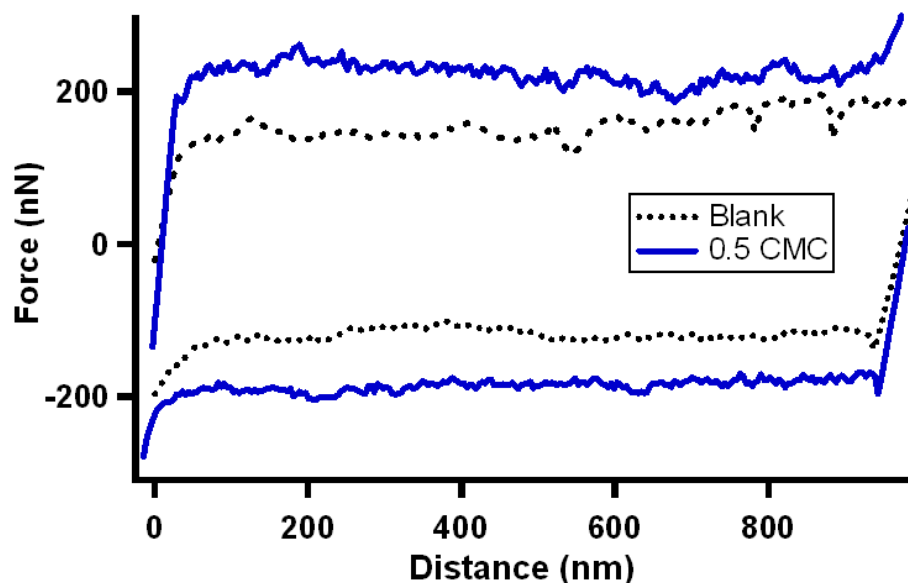


Figure 4.30 Lateral force curves performed under a normal load of 60 nN. The solid lines represent the force for TOFA imidazolium film at 0.5 CMC and the dotted lines show the force measured blank mica in pure water. The force to remove the inhibitor molecules was determined by subtracting the average force measured in pure water from the average force measured in the presence of inhibitor. The average force was determined from the forces measured in both the forward and reverse scans, ignoring the negative sign in the reverse scan.

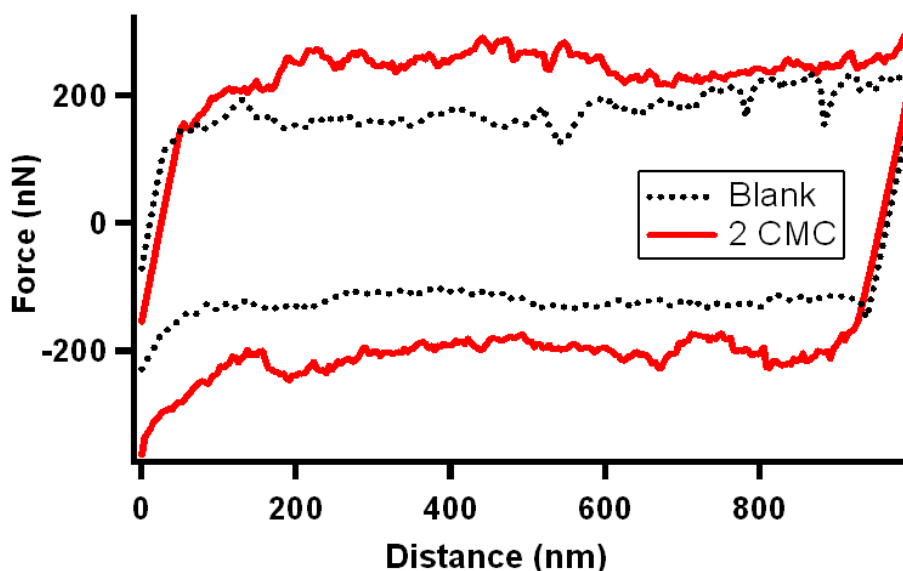


Figure 4.31 Lateral force curves performed under a normal load of 60 nN, solid lines, TOFA imidazolium at 2 CMC and dotted lines in pure water.

Figure 4.32 shows the measured lateral forces of four types of inhibitors on mica. Interestingly, considering the 10% variation in each measurement, the forces to remove different inhibitors on mica were all at a similar level. As the adhesive force acting between the hydrophilic moiety of the molecule and the surface is independent of film thickness, there is no significant difference between the force to remove a bilayer at 2 CMC or a monolayer film at 0.5 CMC. Inhibitor K2 shows similar removal force as K1 because structurally K1 molecules and K2 molecules are very similar and they are all adsorbed on the mica surface through electrostatic interactions between the positively charged hydrophilic groups and negatively charged mica surface. For inhibitor blends K4 and K5, they also exhibit similar removal forces as K1 and K2 as the additive sodium thiosulfate does not interact with mica surface. This result again indicates the lateral

removal force measurements can be used to determine the adhesion force between inhibitor molecules and the surface.

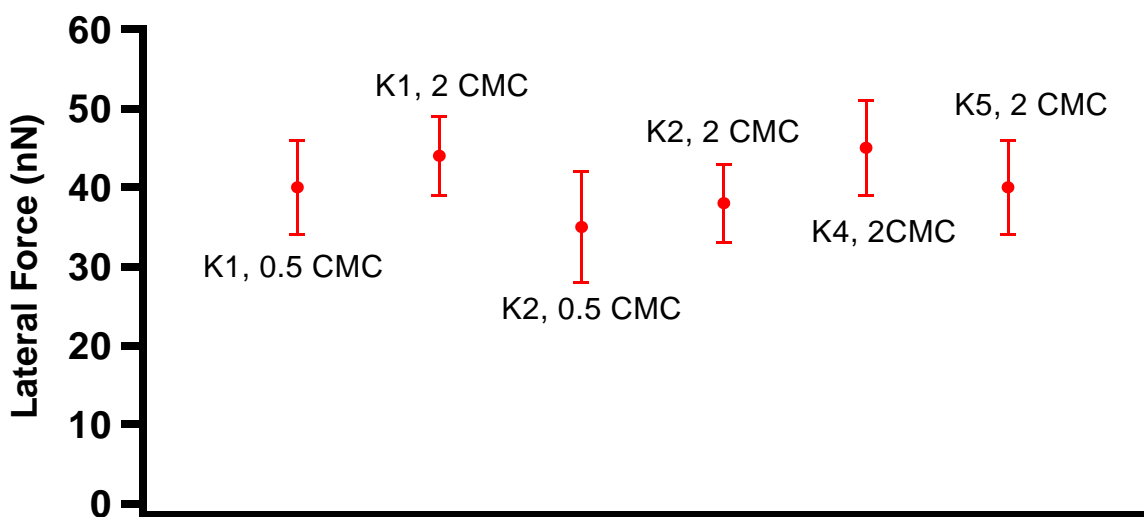


Figure 4.32 Measured lateral removal forces for different corrosion inhibitors.

4.3.5 Environmental effects

As corrosion happens in various conditions, the application of corrosion inhibitors can be affected by pH, temperature, ionic strength and other environmental conditions^{118,130,142,214}. Here, we study the adsorption of corrosion inhibitor K1, TOFA imidazolium, on a mica surface at various conditions.

4.3.5.1 Effect of $[NaCl]$ on inhibitor adsorption

Figure 4.33 shows the surface morphologies on mica in the presence of inhibitor K1 (2 CMC) at different NaCl concentrations of 3 wt.%, 5 wt.% and 10 wt.%, respectively. As the NaCl concentration increased from 3 wt.% to 10 wt.%, the apparent surface

roughness also significantly increased, indicating that dissolved NaCl can also adsorb on the surface. However, even though the surface roughness was different at these three NaCl concentrations, the thicknesses of inhibitor layers were similar (Figure 4.33 d, e and f), indicating the addition of NaCl did not change the bilayer structure of the adsorbed inhibitor molecules.

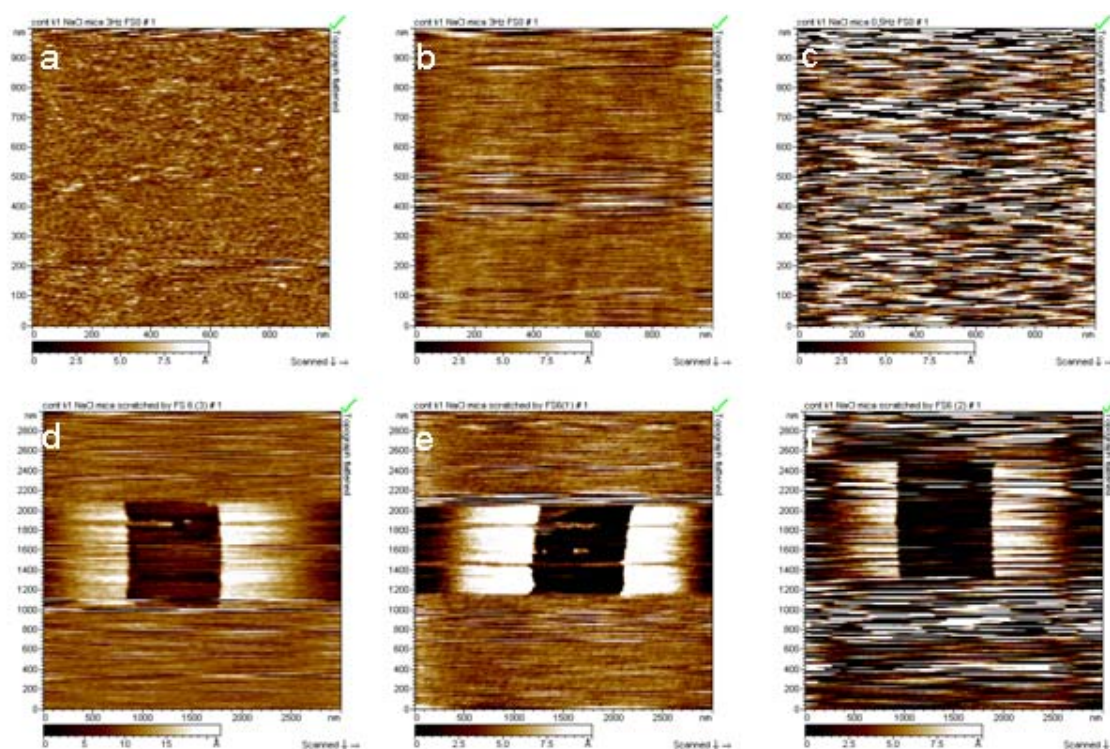


Figure 4.33 AFM images on mica surface in the presence of inhibitor K1 (2 CMC) solution with (a) 3 wt.%, (b) 5 wt.%, (c) 10 wt.% NaCl, respectively, and corresponding film thickness measurements at (d) 3 wt.%, (e) 5 wt.%, (f) 10 wt.% NaCl conditions, respectively.

The penetration force increased as the concentration of NaCl increased (Figure 4.34a) and since the film thickness stayed the same, the rise in penetration force is

probably attributed to the closer packing of the inhibitor molecules. It has been reported that the NaCl can lower the ionic repulsion between adsorbed surfactants and make surfactant molecules pack more closely²¹⁵. Therefore, the AFM tip met a higher resistance from a more compact inhibitor film in higher NaCl concentration, and the measured penetration force is higher. The presence of NaCl can help inhibitor molecules form denser structures and may provide higher mechanical resistance. Here, the force curves show negative distance values after the tip was in contact with the surface, because the Pico scan 2000 AFM recorded the moving distance of the z-piezo as the x axis. The z-piezo can keep moving even when the tip is in contact with the mica surface, in which case the tip cannot go deeper into the mica. Therefore, a negative distance is further shown as we set the “0 nm” as the contact point.

Figure 4.34b shows the lateral force measurements on mica in the presence of inhibitor K1 with different NaCl concentrations. Only a very small increase in lateral force is due to the increase of NaCl concentration. This is probably because NaCl does not change the adhesion of inhibitor molecules on the sample surface, and the slight increase may be due to the weak adsorption of NaCl molecules on the surface.

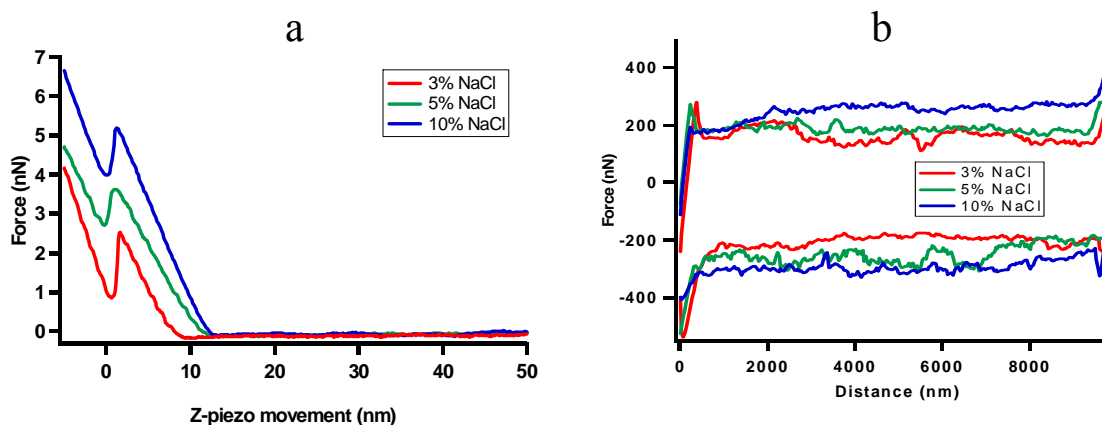


Figure 4.34 (a) Penetration force measurements for inhibitor K1 (2 CMC) at different NaCl concentrations; (b) Lateral force measurements for inhibitor K1 (2 CMC) at different NaCl concentrations.

4.3.5.2 Effect of pH on inhibitor adsorption

In reality, the pH of corrosive environments can be quite different and requires further study in terms of how pH affects the adsorption of inhibitor molecules. In order to observe this, the pH values of inhibitor K1 solution at 2 CMC were adjusted to 2 and 8, respectively, in comparison to the original test at pH 5. The same surface morphologies were found for these three conditions, indicating the adsorption of inhibitor on mica stayed the same over a wide pH range. However, further film thicknesses measurements show that the internal packing structure of inhibitor films were different at different pH values (Figure 4.35). Under acidic condition, no matter whether the pH was 2 or 5, the inhibitor film thickness remained at about 4 nm which was consistent with the bilayer structure. At pH 8, the measured film thickness was only 2 nm, corresponding to the monolayer structure of inhibitor film. The reason for the change from a bilayer to a monolayer structure is unclear and more research is required. One possible contribution

could be a change in CMC at pH 8, but this was not measured. By further considering the penetration force and lateral removal force, inhibitor molecules were easier to be penetrated and removed in a more basic solution than in a more acidic solution (Figure 4.36). Therefore, AFM measurements have confirmed that inhibitor K1 provides better protection and stability in acidic conditions than under basic conditions in agreement with the manufacturer's suggested use that this type of inhibitor is for acidic conditions.

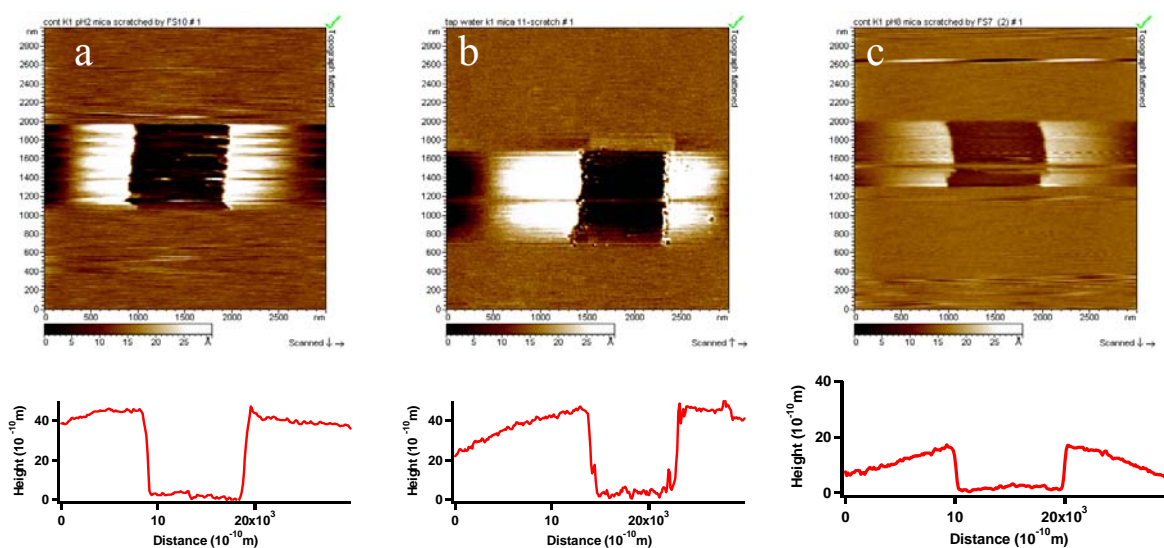


Figure 4.35 (a.) Film thickness measurement for inhibitor K1 at pH 2; (b.) Film thickness measurement for inhibitor K1 at pH 5; (c.) Film thickness measurement for inhibitor K1 at pH 8.

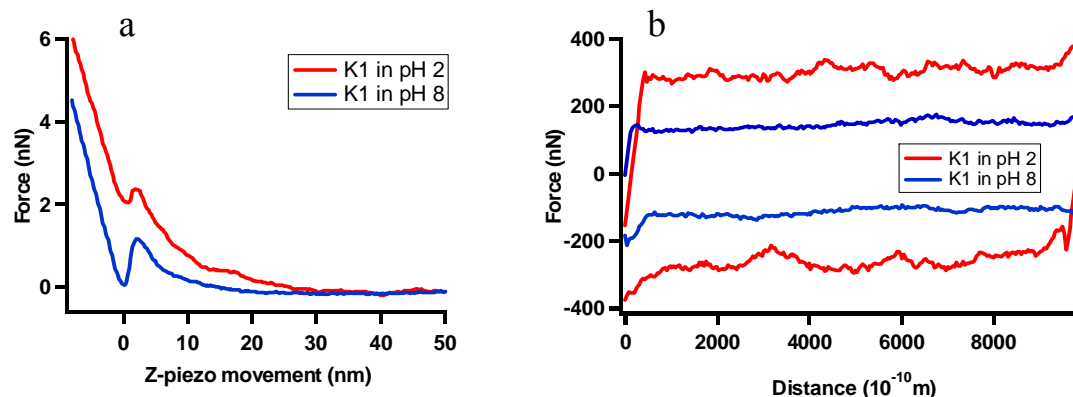


Figure 4.36 (a) Penetration forces for inhibitor K1 at different pH values; (b) Lateral forces for inhibitor K1 at different pH values.

4.3.5.3 Effect of ethanol on inhibitor adsorption

In the field and in transmission pipelines, inhibitors are often used in oil and water mixtures, and thus the fundamental study of the effect of organic molecules on inhibitor adsorption is very important. In this section, we applied AFM analysis on inhibitor K1 (2 CMC) solutions which were pre-mixed with organic solvents such as hexane, heptane and ethanol. However, hexane and heptane have very low solubility in aqueous inhibitor solution and can create two phases in inhibitor-organic mixtures. Having two immiscible phases strongly interfered with subsequent AFM scanning and no convincing results were obtained. Therefore, AFM analysis was only carried out in a homogeneous water-ethanol mixture. A water-ethanol inhibitor solution (1:1 water-ethanol ratio) was prepared and added into the fluid cell with freshly cleaved mica. Figure 4.37a shows the surface morphology of inhibitor K1 in a water-ethanol mixture. In the mixture solution, inhibitor molecules no longer formed a uniform layer on the surface. Inhibitor molecules aggregated together and randomly covered the surface. Further measurement of film

thickness (Figure 4.37b) also confirmed that inhibitor molecules did not form a flat layer in this water-ethanol condition. The measured film thickness was only 0.5 nm indicating the molecules were not standing-up and forming a compact protective layer. Force curve measurement shows no penetration force peak in the inhibitor-ethanol mixture and the curve is the same as the curve on bare mica. Again, in this force curve, the negative distance value is from the relative distance of z-piezo movement, as described above. All these results confirmed that inhibitor molecules did not form a protective layer in the water-ethanol mixture, and ethanol can strongly hinder the adsorption of inhibitor molecules.

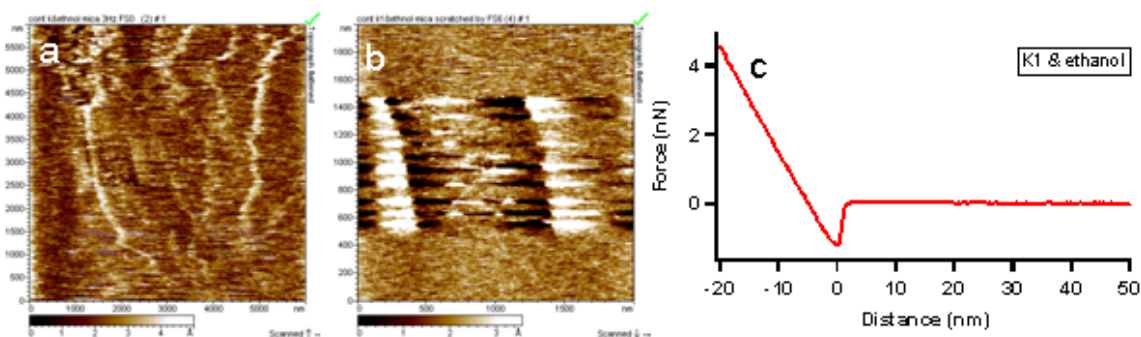


Figure 4.37 (a) Surface morphology of inhibitor K1 in water-ethanol mixture; (b) film thickness measurement for inhibitor K1 in water-ethanol mixture; (c) penetration force for inhibitor K1 in water-ethanol mixture.

4.3.6 Desorption of inhibitor molecules

It was unclear whether the inhibitor molecules were removed away in the vertical penetration process. Therefore, multiple penetration force measurements were carried out on the same position and the force curves stayed almost the same each time, as shown in

Figure 4.38a. This result indicates that the penetration of inhibitor film by the AFM tip did not destroy the inhibitor structure, and inhibitor molecules returned to their original positions after the AFM tip left the surface. Therefore, the only possible way to remove inhibitor away by the AFM tip is to laterally scratch the molecules away. Further film thickness measurements show that this inhibitor-removal process was unaffected by the scan rate of the tip. Figure 4.38b shows the AFM images of the surface where inhibitor molecules were removed away in three areas with three different scan rates of 1Hz, 2Hz and 3Hz, respectively. The surface profiles across these three areas show the same film thicknesses measured at different scan rates. This has confirmed that the removal of inhibitor molecules is not related to the scan rate of the AFM tip.

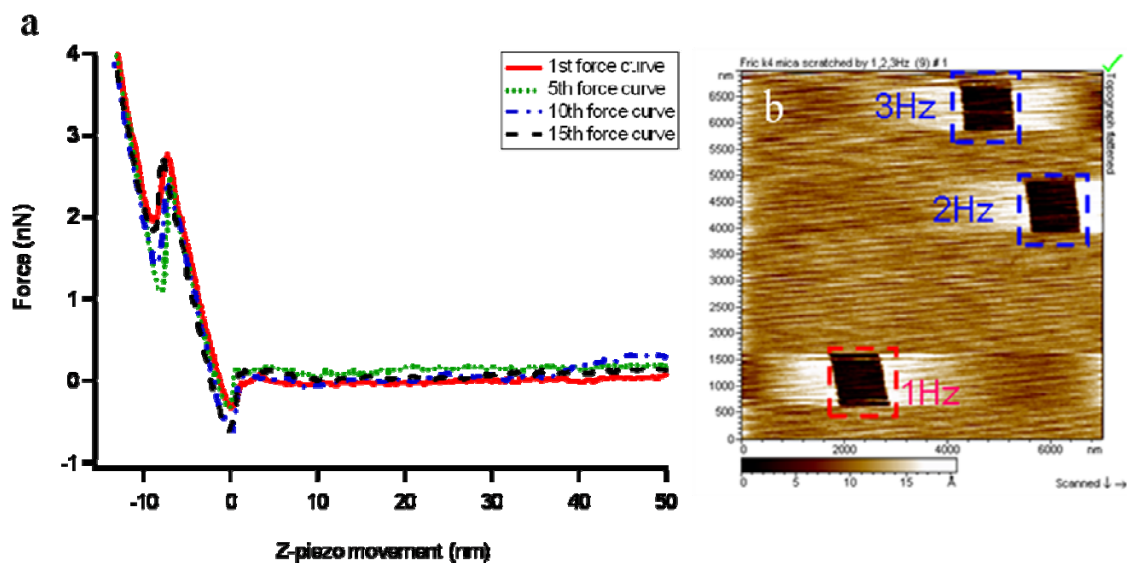


Figure 4.38 (a) Multiple force curves on the same position showing the penetration process did not destroy the inhibitor film; (b) inhibitor molecules were removed away under different scan rates of the tip.

4.3.7 Re-adsorption of inhibitor molecules

After inhibitor molecules were removed, the film thickness can be measured because inhibitor molecules did not immediately re-adsorb back on the surface. Further study was carried out on the kinetics of inhibitor re-adsorption by monitoring the change of the depth in the scratched area. Firstly, inhibitor molecules were removed with a high-load scanning tip using the previous procedure, and then the surface was rescanned every hour to observe the change of the scratched area. Figure 4.39 shows the film thickness measurements and surface profiles 6 hours after inhibitor molecules were removed. The immediate rescan of the scratched area, at 0 hour, shows the film thickness in the area was 0 nm. After 1 hour, the thickness was only 0.5 nm indicating only a few inhibitor molecules re-adsorbed and those molecules had random orientations instead of a compact film structure. After 3 hours the thickness recovered to 2.3 nm, which is equal to the molecular length of K1, indicating one layer of inhibitor molecules re-adsorbed. After 6 hours the scratched area had reestablished complete surface coverage by inhibitor molecules, the film structure having recovered.

These results indicate that it may take several hours for the re-adsorption of inhibitor molecules. The kinetics of initial adsorption is probably different from that of re-adsorption, and thus it is not fully understood how long it takes for the full adsorption of inhibitor molecules on a bare surface. However, the study of re-adsorption process gives us a clue that inhibitor molecules do not immediately form the protective film on the surface.

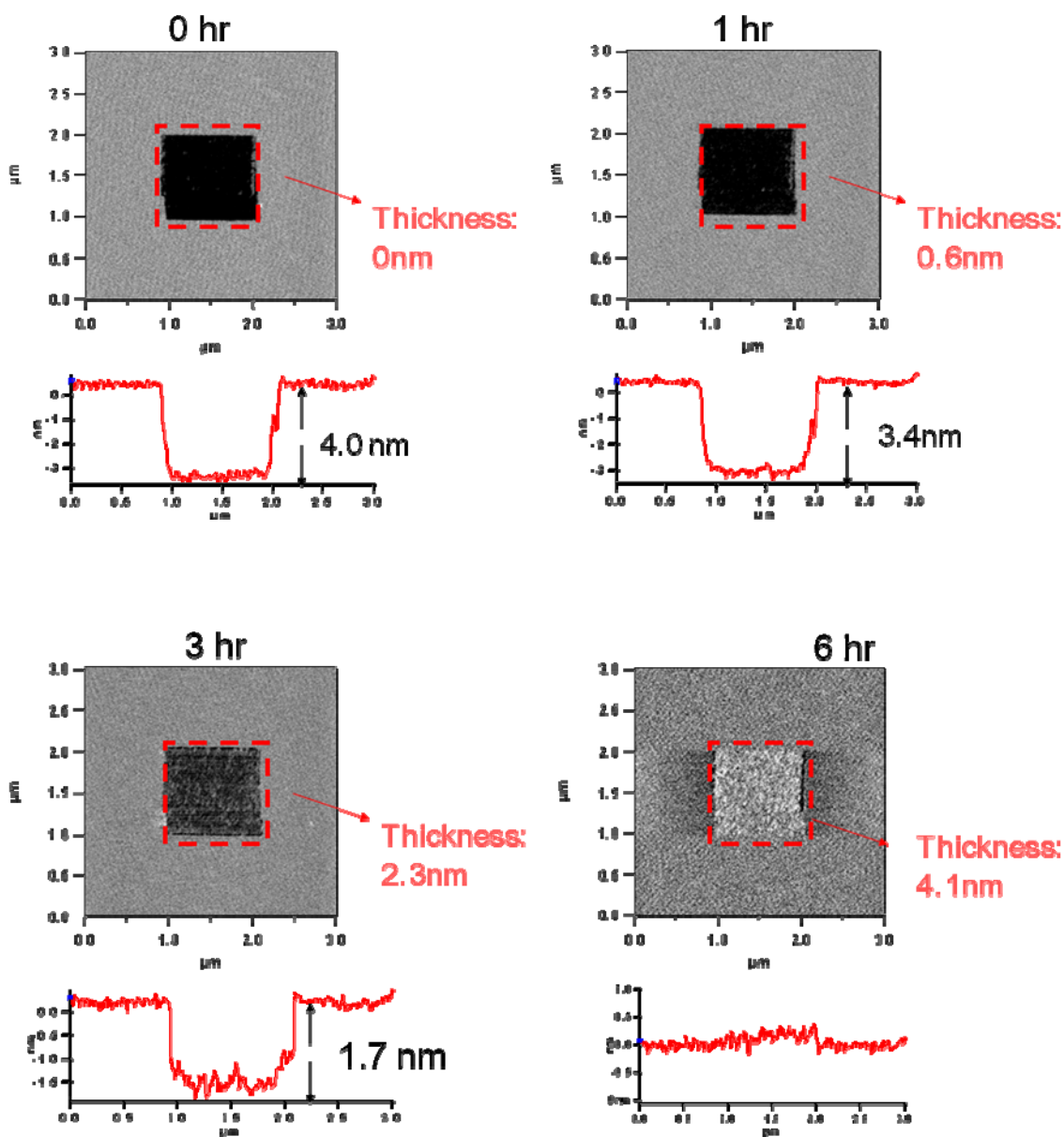


Figure 4.39 The re-adsorption of inhibitor molecules *versus* time. At 0 hour, the film thickness was 0 nm in the scratched area. At 1 hour, the thickness started to recover, and the first layer of inhibitor re-adsorbed back onto the surface after 3 hours. At 6 hours, the inhibitor molecules fully re-adsorbed back to the scratched area.

4.3.8 Adsorption of corrosion inhibitors on metal surfaces

The purpose of studying inhibitor adsorption is to provide a better understanding of the protection mechanisms of inhibitors. In a realistic scenario, corrosion inhibitors are applied to decrease the corrosion rate on metal materials²¹⁶. In previous reports, we studied the adsorption of inhibitor on mica because mica is chemically stable and provides an atomic-level flat surface. Here, we continue to study the adsorption of inhibitors on metal surfaces, including Au, Fe and X65 steel.

One problem while studying inhibitor adsorption on Fe or steel is the corrosion happening on the metal surface. For the previously studied mica surface, oxygen was present because mica is chemically stable and does not corrode. However, if the same oxygen environment is applied to study Fe or steel, all AFM analysis of inhibitor adsorption would be compromised by the morphology change due to the corrosion reactions. Therefore, the analysis of corrosion inhibitors on a metal surface in aqueous solution requires the elimination of oxygen. Another problem for scanning on metal is the surface roughness. Mica provides an atomically flat surface, while metals, especially commercial metal materials, usually have much higher roughness. For example, the roughness of a 600-grit polished steel surface is ~1000 nm. Since the film thickness of corrosion inhibitors is expected to be less than 10 nm, the change of surface morphology due to the adsorption of inhibitors will be overwhelmed by the original metal surface roughness. Therefore, the vapor deposited Au and Fe substrates were selected for inhibitor adsorption because the vapor deposition methods usually provide a relatively smooth surface (roughness < 50nm). Also Au is chemically stable and thus the analysis

of inhibitor molecules on Au can give a first hint of how these molecules adsorb on metal surface.

Figure 4.40 shows the AFM images of blank Au in deionized water, and Au in the presence of 2 CMC inhibitor K1 solution. Both AFM images, in the absence and presence of inhibitors, exhibit similar surface morphologies. The similar surface morphologies in both conditions indicate that inhibitor molecules adsorbed on the surface mimicking the original surface morphology of Au.

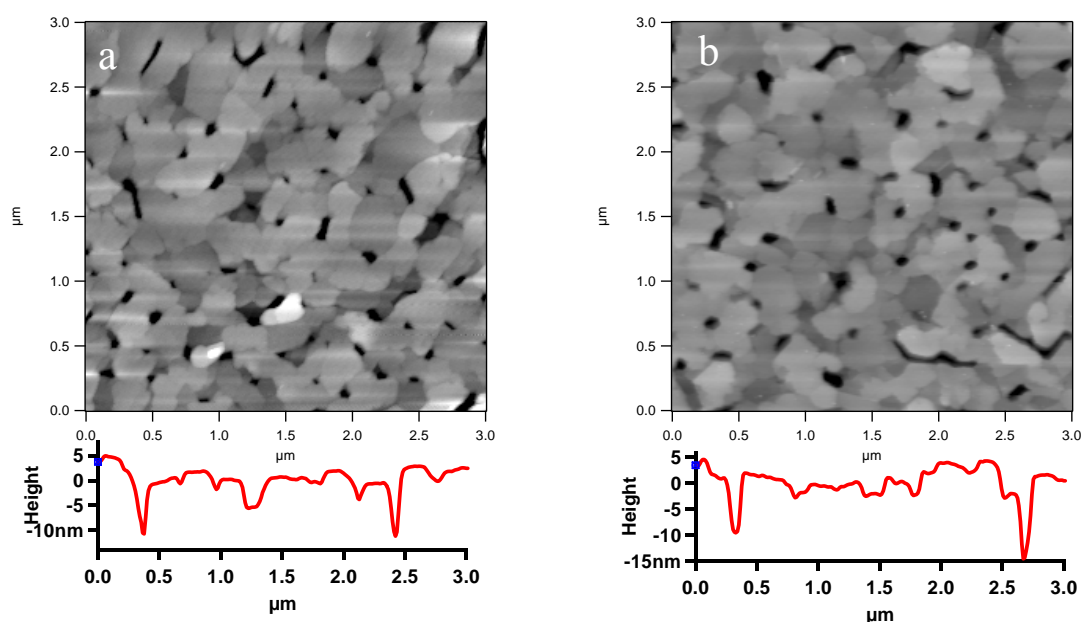


Figure 4.40 (a) Surface morphology of blank Au in DI water and (b) Au in the presence of 2 CMC inhibitor K1 solution.

Figure 4.41 shows the penetration force measurements on Au substrates in the presence of 2 CMC inhibitor K1. The force peak shown at ~ 5 nm in the plot indicates that

inhibitor molecules formed a protective film on the Au surface, similar to what was observed for the mica surface (see Figure 4.24).

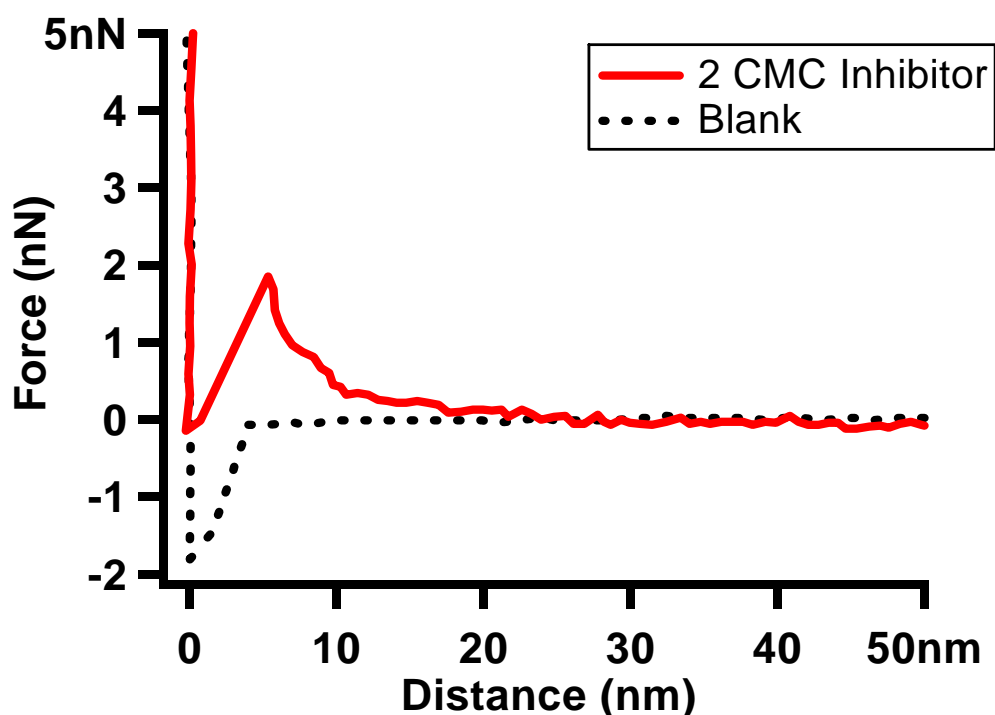


Figure 4.41 Penetration force measurement on blank Au in deionized water (blank) and on Au in the presence of 2 CMC inhibitor K1. A 2 nN penetration force was measured on the inhibitor film.

By applying a high load on the AFM tip, inhibitor molecules were removed from the Au surface and the film thickness was measured. Figure 4.42 shows the AFM image with the center area ($1 \times 1 \mu\text{m}$) where the inhibitor molecules were removed and the surface profile across the image. Different from on the mica surface, it is difficult to accurately measure the film thickness on Au because of the original surface morphology

and roughness. However, from the profile across the image, we can still estimate that the film thickness is ~ 4 nm, which is similar to the thickness of a bilayer structure.

At the same high load for film thickness measurements, the lateral force to remove inhibitor molecules was measured through friction loops. Figure 4.43 shows the lateral removal force of a blank Au surface in deionized water and Au in the presence of 2 CMC inhibitor K1 solution. The average lateral force for blank Au surface in DI water is ~ 20 nN and the average lateral force to remove inhibitor K1 molecules on Au is ~ 55 nN. The significant increase of 35 nN in lateral force is attributed to the adsorption of the inhibitor film. However, the force measurements at different locations exhibit huge variations because of the grain boundaries among Au crystals. The lateral force induced by these boundaries is at least one order of magnitude higher than the force created by the adsorbed inhibitor molecules. Therefore, the lateral force measurements were carried out inside one single Au crystal, avoiding across any grain boundaries. This ~ 35 nN lateral force can be further calculated to a stress value of ~ 50 MPa, based on the ~ 700 nm² area of tip.

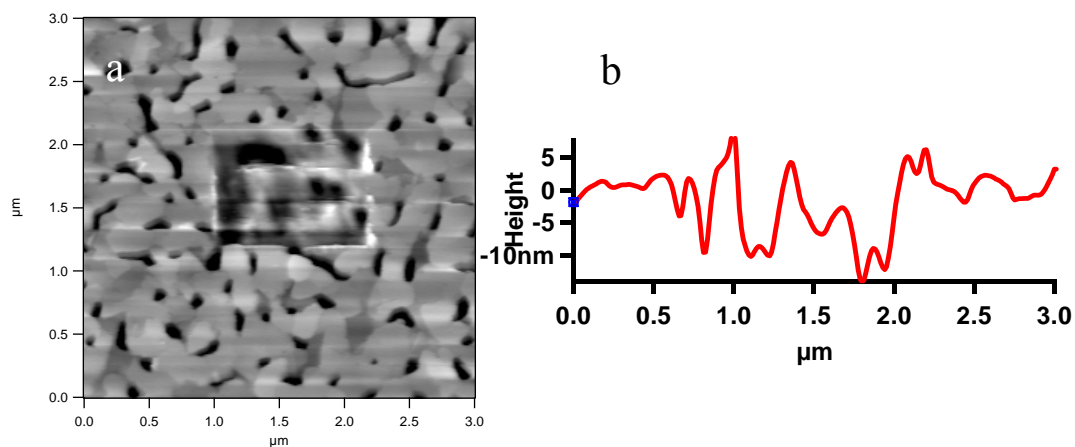


Figure 4.42 AFM image of Au surface with the center area where inhibitor molecules were removed and the surface profile across the image. The depth in the scratched area is estimated to be ~ 4 nm.

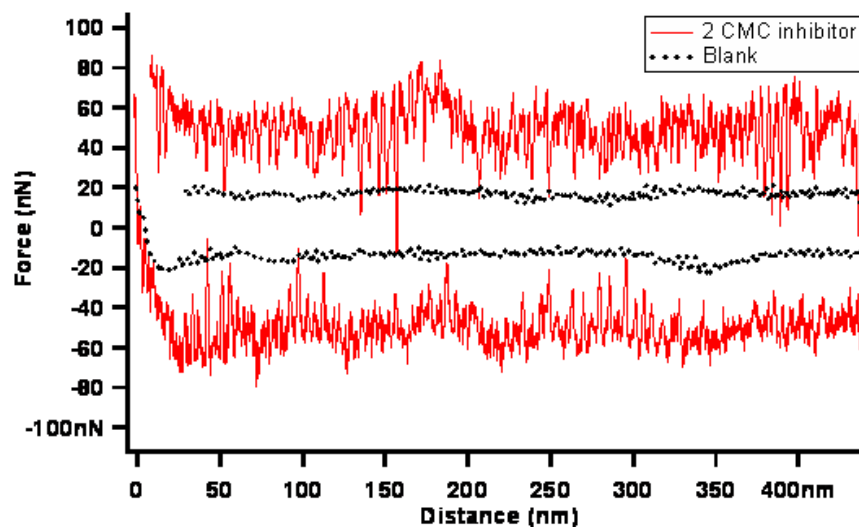


Figure 4.43 Lateral force curves measured on blank Au in DI water (black curve) and on Au in the presence of 2 CMC inhibitor K1 (red curve). The significant increase in force values of red curves was contributed by the adhesion of inhibitor molecules on the Au surface.

In general, the adsorption of TOFA imidazolium (inhibitor K1) on Au, including the film thickness and force measurements, is similar to its adsorption on mica. This has confirmed that our analysis of inhibitor adsorption can be done on rougher metal surfaces.

We continue to study the inhibitor adsorption on vapor deposited Fe surface. As in ambient condition, Fe can be oxidized if oxygen is present in an aqueous solution. Therefore the analysis of corrosion inhibitors was performed under the protection gas. The study of inhibitor adsorption on Fe substrates was first carried out inside a N₂ saturated environment. Both the inhibitor solution and closed box were pre-purged with N₂ for 3 hrs, and a continuous N₂ flow was kept on during the analysis. In a N₂ saturated system, the corrosion rate of Fe is negligible. Figure 4.44 shows the AFM images of blank Fe in deionized water and the Fe surface in the presence of inhibitor K1 (2 CMC). After the adsorption of inhibitor molecules, the surface morphology is almost the same as blank Fe, indicating inhibitor molecules formed a uniform layer following the original Fe morphology.

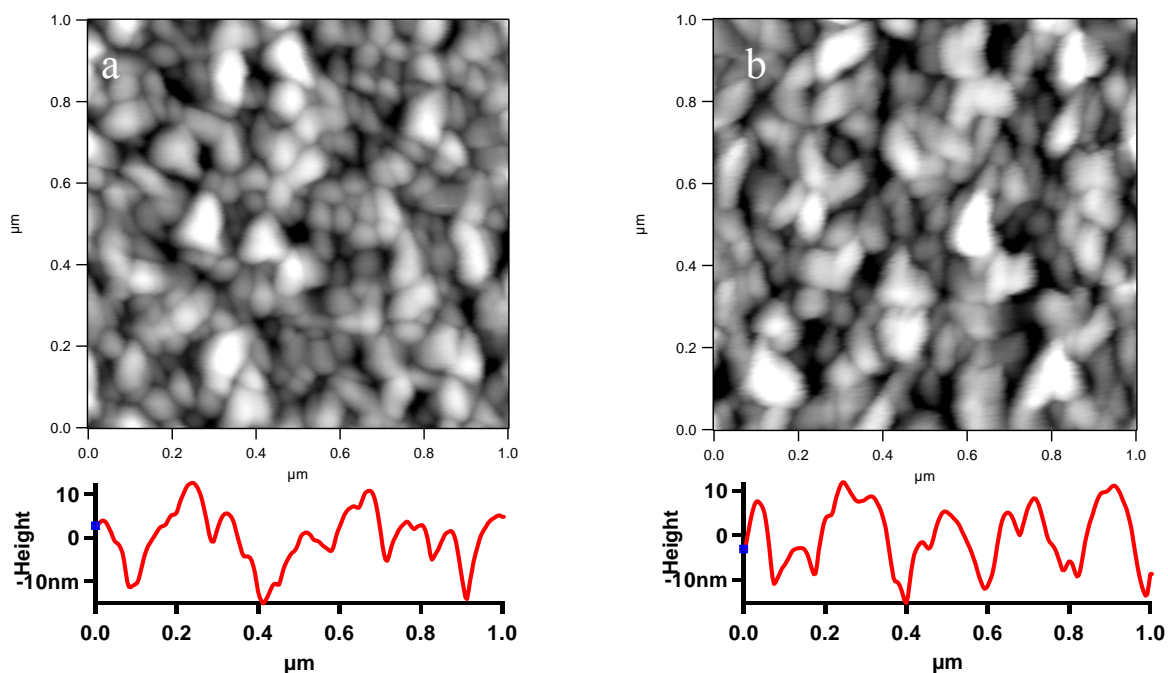


Figure 4.44 (a) The surface morphology and surface profile of blank Fe in DI water and (b) Fe in the presence of 2 CMC inhibitor K1, both in N_2 saturated environment. After adding inhibitor K1, no obvious surface morphology change was observed.

Figure 4.45 shows the penetration force measurement on blank Fe in deionized water and Fe in the presence of 2 CMC inhibitor K1. The blank force is a typical force curve on clean hard surface, and a 0.2 nN penetration force was measured from the force curve on inhibitor film. The same penetration force values were obtained in different locations of this sample. This is an evidence that inhibitor molecules formed a uniform protective layer on a Fe surface. This 0.2 nN penetration force can be calculated to a stress of ~ 0.3 MPa, based on the 700 nm^2 area of the tip.

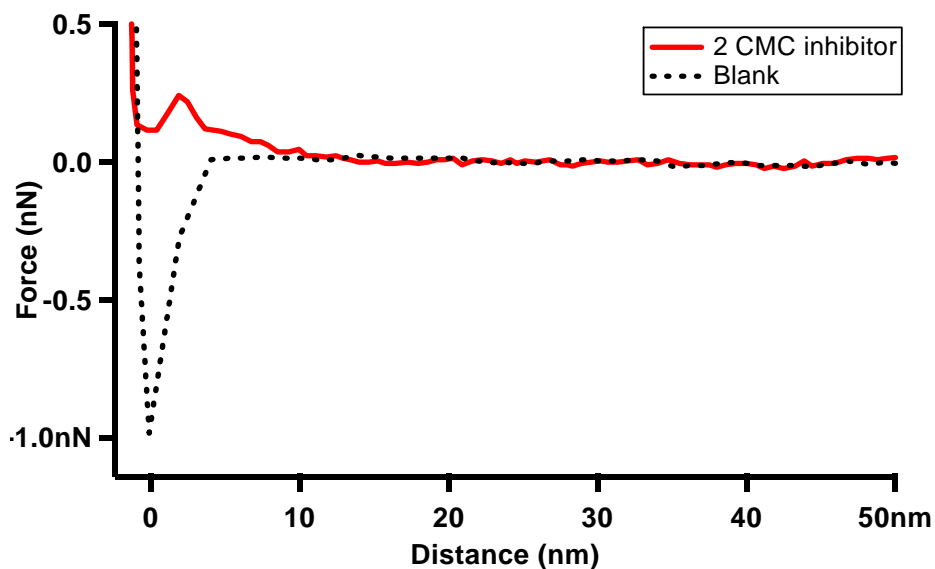


Figure 4.45 Force curve of blank Fe in deionized water and Fe in the presence of inhibitor K1, 2 CMC. A 0.2 nN penetration force was measured from the inhibitor film.

The film thickness of inhibitor K1 at 2 CMC concentration was measured on Fe surface by removing part of the inhibitor film in a $1 \times 1 \mu\text{m}$ area. Figure 4.46 shows the AFM image with center area where inhibitor molecules were removed and the surface profile across the image. The measured depth in the scratched area, which is the thickness of the inhibitor film, is approximately 4 nm. This, again, corresponds to a bi-layer structure of inhibitor film on Fe, similar to what was observed on Au and mica.

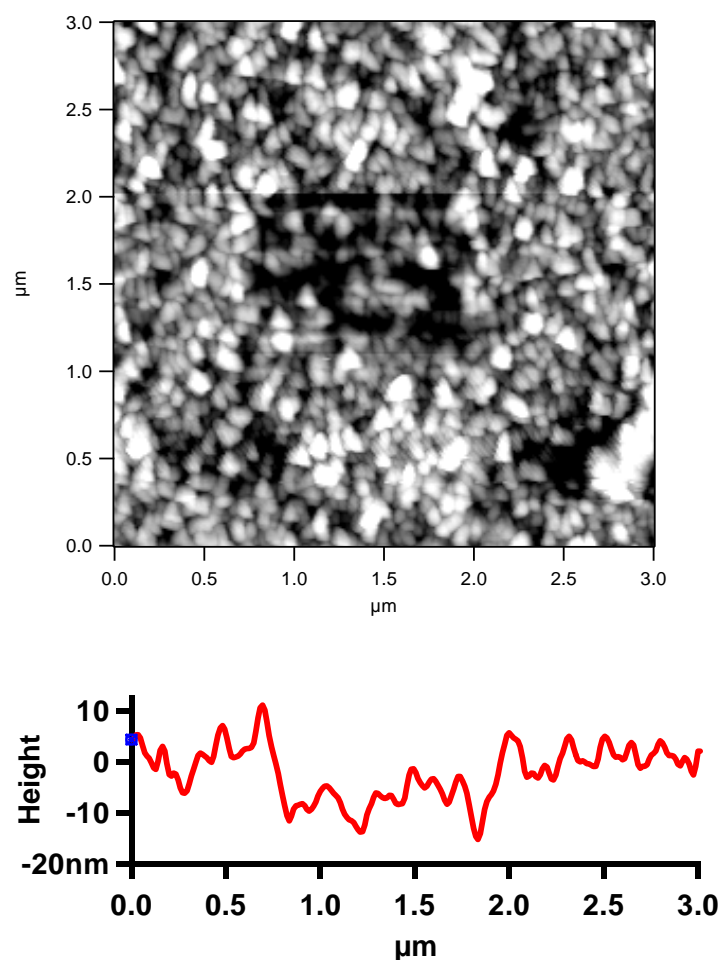


Figure 4.46 AFM images with the center area where inhibitor molecules were removed and the surface profile across the image. The depth in the scratched area is estimated to be ~ 4 nm.

Lateral force measurements were carried out on Fe surface by applying the same high-load on the cantilever to remove inhibitor molecules for measuring film thickness. Figure 4.47 shows the lateral force on blank Fe in DI water and Fe in the presence of inhibitor film. Since the original surface morphology and roughness of Fe surface causes large variations in the measured force curves, it is not obvious to directly measure the influence from the adsorbed inhibitor film on lateral force. The average lateral force on

blank Fe is 55 nN and the average lateral force on Fe in the presence of inhibitor K1 film is 85 nN. An increase of 30 nN is due to the adsorption of inhibitor film. However, this 30 nN value is very subjective because the measurements are highly dependent on the surface roughness, and thus it is hard to conclude if this 30 nN increase is due to inhibitor adsorption or surface roughness. The 30 nN can be calculated to a stress value of ~ 40 MPa, based on the 700 nm^2 area of the tip. Therefore, the force measurements on Fe surface also indicate a stress value of the order of MPa to remove inhibitor films.

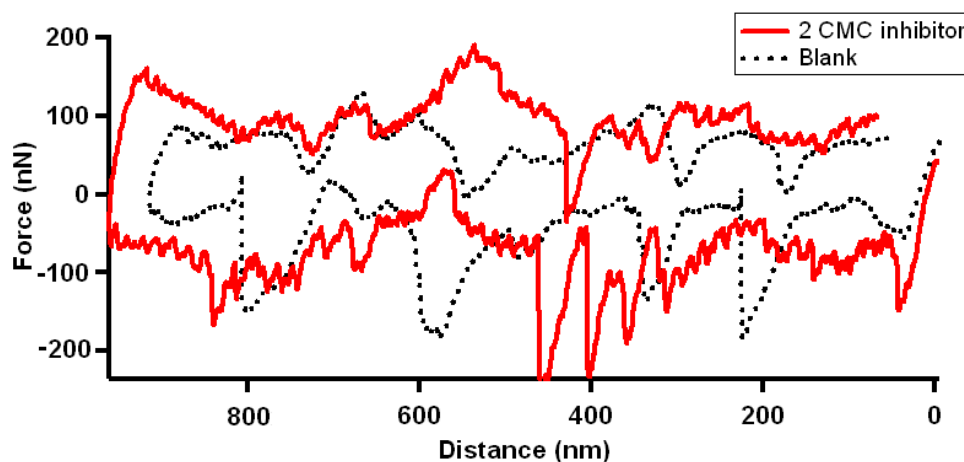


Figure 4.47 Lateral force curves measured on blank Fe in deionized water (black curve) and on Fe in the presence of 2 CMC inhibitor K1 (red curve).

Previously, it was discussed that sodium thiosulfate does not change the adsorption of inhibitors on mica. Here we applied AFM analysis on inhibitor K4, which is a mixture of TOFA imidazolium (K1) and 4% sodium thiosulfate (K3), to study whether sodium thiosulfate can change the adsorption of inhibitor molecules on the Fe surface. Figure 4.48 shows the surface morphology, the film thickness measurement,

penetration force measurement and lateral removal force measurement on an Fe surface in the presence of inhibitor K4 (2 CMC) solution. Compared with the above results for K1 at 2 CMC (Figure 4.44-47), no obvious change in surface morphology, film thickness and force measurements were found on the inhibitor film of K4, indicating the additive sodium thiosulfate does not change the adsorption structure of inhibitor molecules or increase the film thickness. Since no adsorption change of inhibitor molecules was induced by sodium thiosulfate, the effect of sodium thiosulfate to improve inhibitor efficiency may be due to the changes of surface properties. This needs to be studied by other surface analysis methods in future work.

The adsorption of inhibitor on X65 was further studied as X65 steel is one of the most widely used materials in oil pipeline. However, for a normal X65 steel specimen, the surface roughness is usually larger than 1000 nm after 600 grit polishing. It is impossible to study the adsorption of 2 nm long inhibitor molecules on a surface in which the roughness is two orders of magnitude larger than the molecular length of inhibitors. Therefore, a fine polishing procedure was used for polishing the X65 steel surface down to a surface roughness of less than 20 nm. An X65 specimen was polished on 400 grit, 600 grit, 1500 grit sand papers respectively, and then continued to be polished on silk cloth with 9 μm diamond suspension, and on napped cloth with 3 μm diamond suspension. A mirror finish was obtained after this polishing procedure. Figure 4.49 shows the AFM images on the polished X65 steel surface. Even with small polishing scratches shown in the image, the surface roughness is less than 15 nm in a $3 \times 3 \mu\text{m}$ area

and less than 5 nm in a $1 \times 1 \mu\text{m}$ area. The polished X65 steel surface is therefore considered to be smooth enough for AFM scanning.

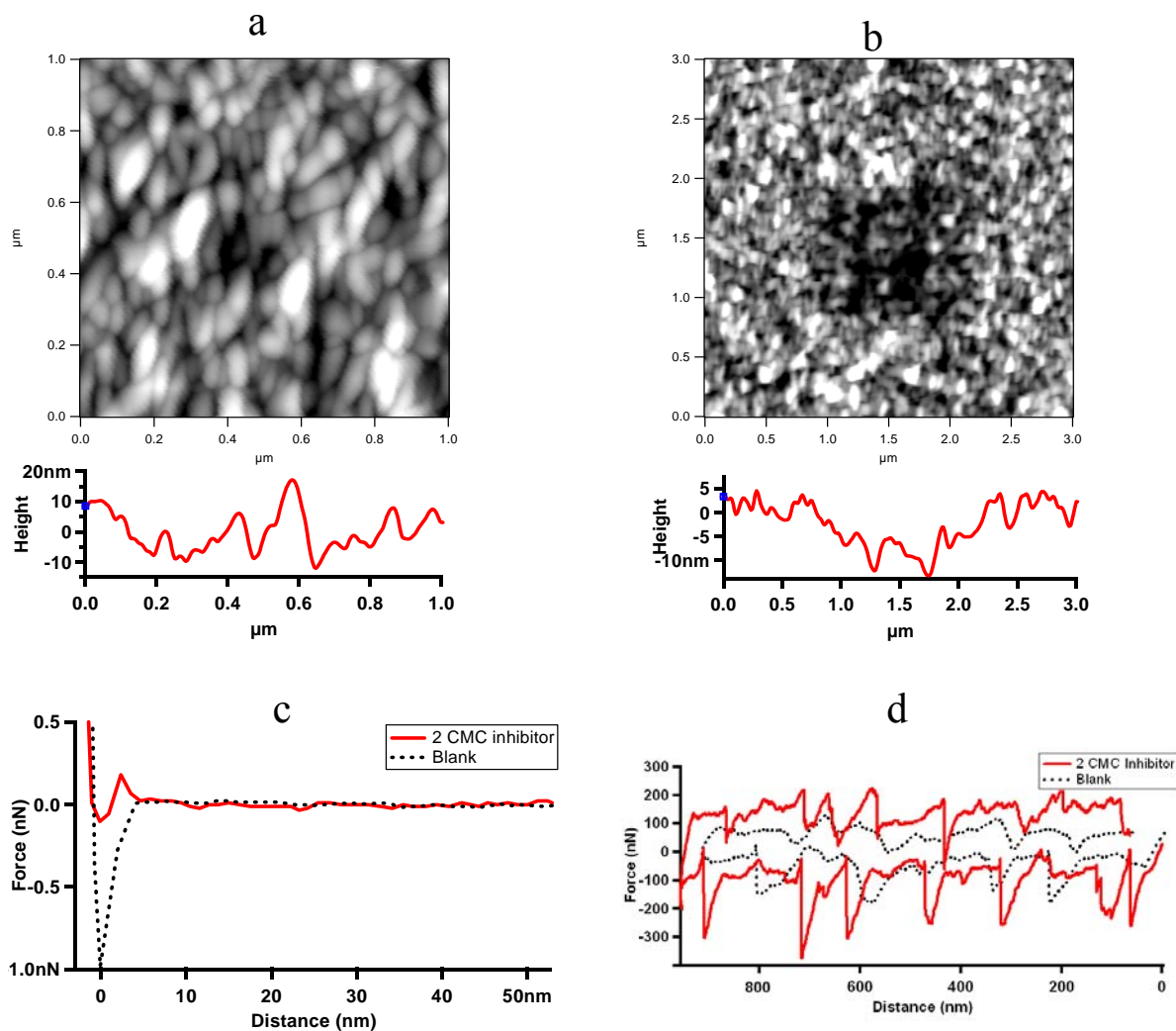


Figure 4.48 (a) surface morphology, (b) film thickness, (c) penetration force, and (d) lateral removal force on Fe in the presence of 2 CMC inhibitor K4 solution. Comparing with results for K1, no obvious change was found due to the addition of sodium thiosulfate.

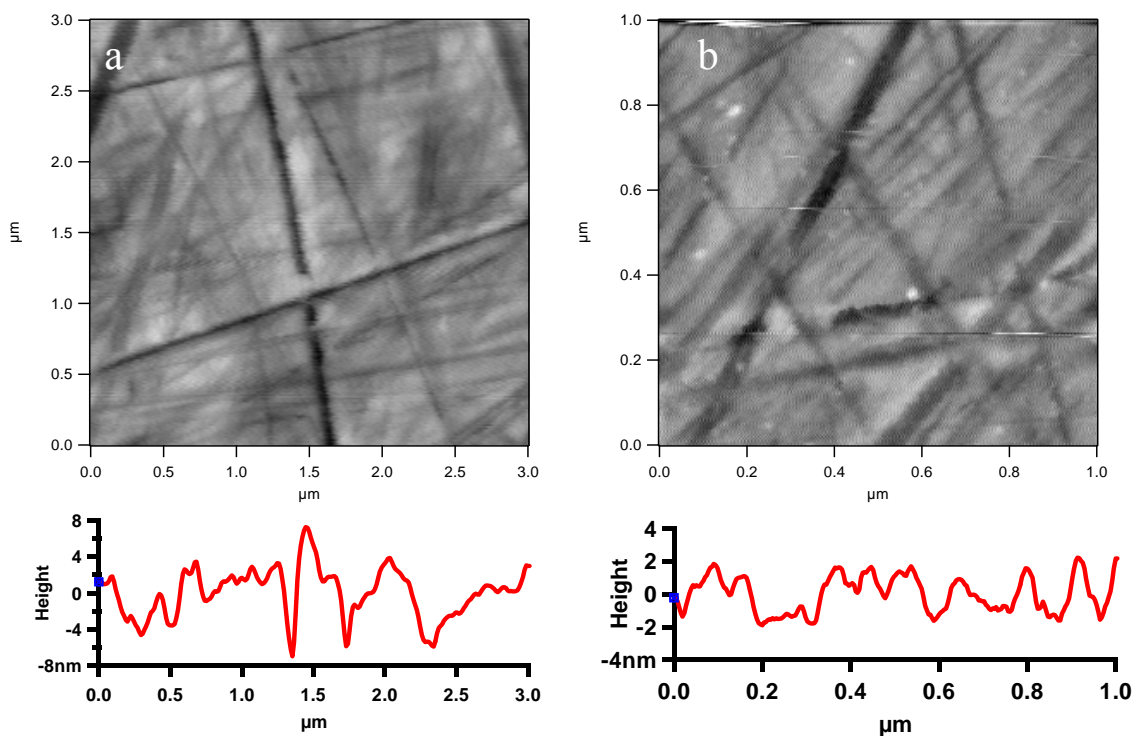


Figure 4.49 AFM images of polished X65 steel surface, (a) $3 \times 3 \mu\text{m}$ area and (b) $1 \times 1 \mu\text{m}$ area, in deionized water, in N_2 saturated environment. The surface roughness after polishing was less than 15 nm.

The adsorption of inhibitor K1 was studied on the X65 steel surface at 0.5 CMC and 2 CMC in N_2 saturated condition. Figure 4.50 shows the surface morphology of the X65 surface in the presence of the inhibitor solution. Comparison with the blank X65 surface shown in Figure 4.49, no surface morphology change was found for either 0.5 CMC or 2 CMC conditions, indicating uniform flat films were formed on the X65 surface, which could be similar to the mica surface.

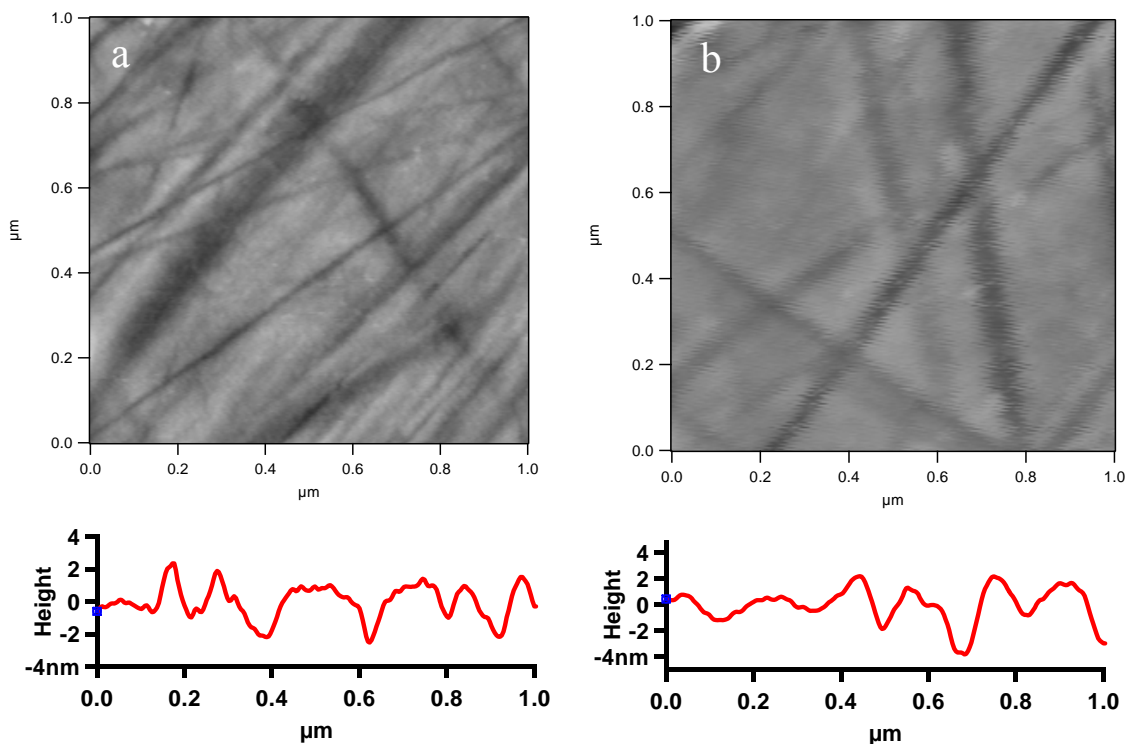


Figure 4.50 AFM images of X65 steel in the presence of 0.5 CMC (a) and 2 CMC (b) inhibitor K1 solutions in N_2 saturated condition.

Figure 4.51 shows AFM images of scratched and unscratched areas and the corresponding depth measurements on the X65 surface at 0.5 and 2 CMC conditions. The profiles across the images show depths of approximately 2 and 4 nm in the scratched areas at 0.5 and 2 times the CMC, respectively. This corresponds to film thicknesses of one and two molecular lengths, *i.e.*, a monolayer is formed at 0.5 CMC and a bimolecular layer at 2 CMC. These monolayer and bilayer adsorption structures on Fe are consistent with the previous studies on mica surface (see Figure 4.14).

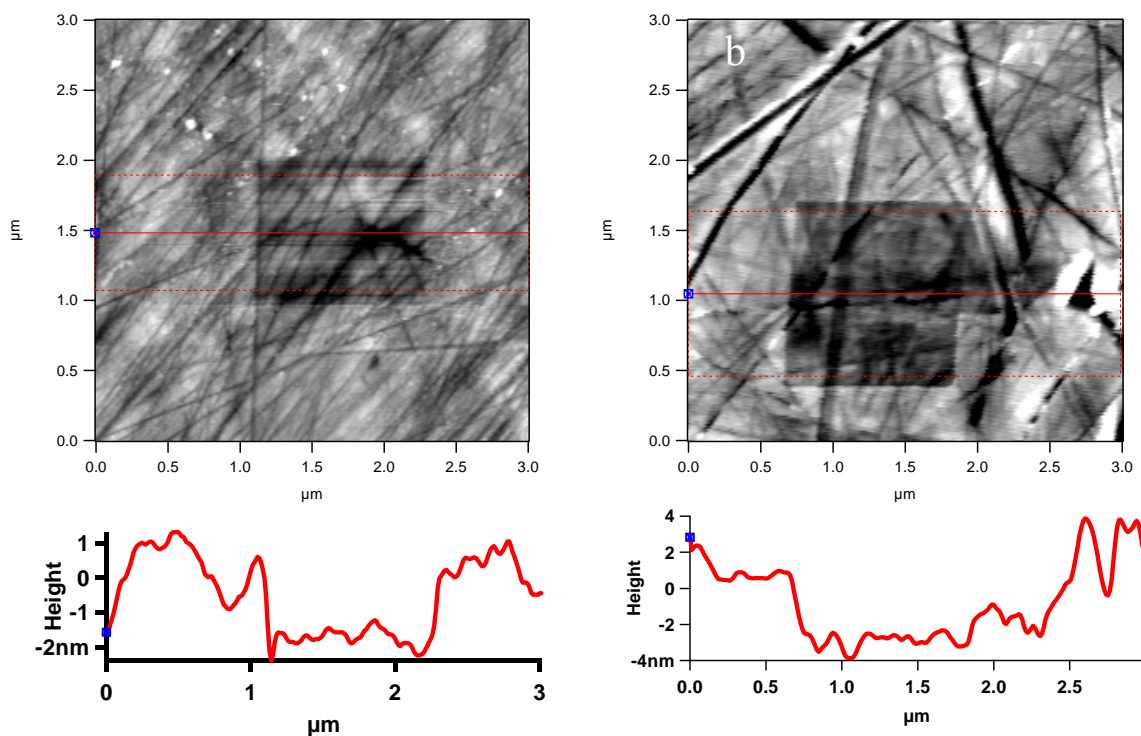


Figure 4.51 AFM images of X65 steel surface with the center area where inhibitor K1 molecules were removed and the surface profile across the image. The depth in the scratched area is ~ 2 nm for 0.5 CMC condition (a) and ~ 4 nm for 2 CMC (b).

Penetration and lateral removal forces were also measured on X65 steel in the presence of inhibitor K1 at 0.5 CMC and 2 CMC. The penetration forces shown in Figure 4.52 indicate a 2 nN force for bilayer inhibitor film at 2 CMC and 1 nN force for monolayer inhibitor film at 0.5 CMC. These nN level penetration force can be converted to MPa level stress to penetration inhibitor films, based on the 700 nm^2 area of the tip. This is again the same as for the previous study of inhibitors on a mica surface where penetration force is related to the film thickness.

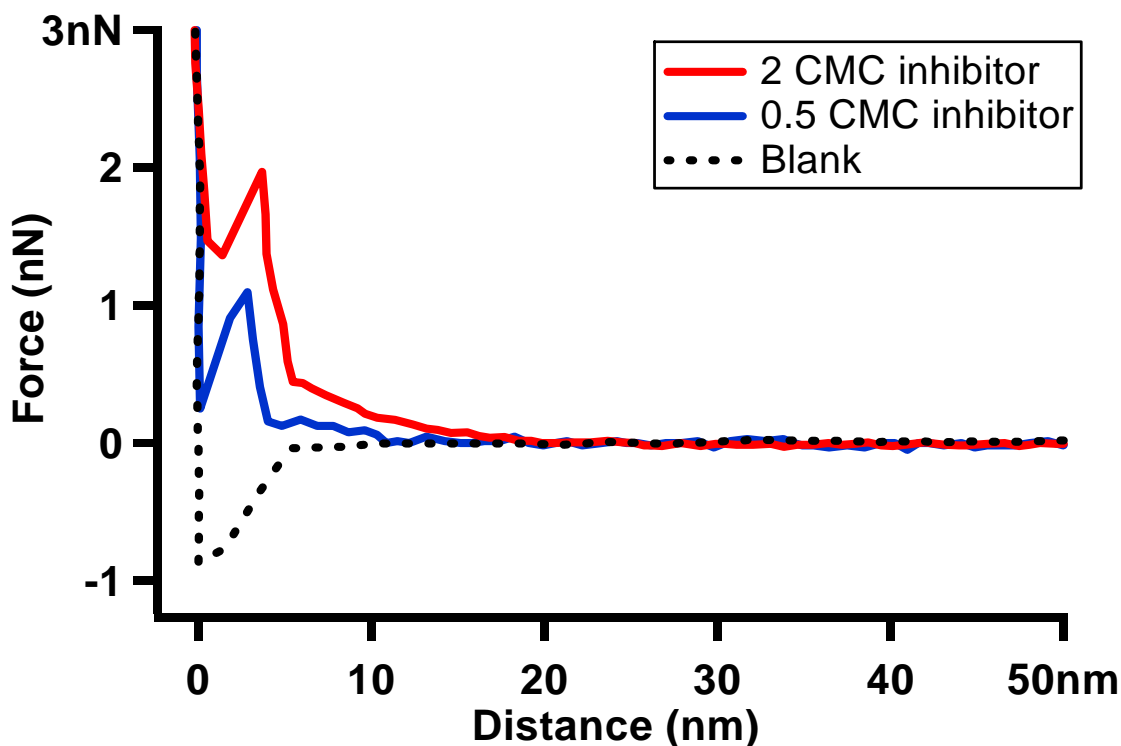


Figure 4.52 Force distance curves for inhibitor films on X65 surface in the presence and absence of inhibitor films. The curves were recorded in aqueous solutions of TOFA imidazolium at 0.5, 2 times the CMC and in pure water.

Figure 4.53 shows the lateral removal force measurements on X65 in the presence of 0.5 CMC and 2 CMC inhibitor K1 solutions, respectively. Due to the polishing, the measured force curves on blank X65 in deionized water show significant variations in the measurements. The lateral force curves measured on X65 in the presence of 0.5 CMC and 2 CMC all show significant increase in force values, indicating the adsorbed inhibitor film provided extra resistance to the scanning tip on the surface. A quantitative 75 nN and 70 nN lateral removal force were determined by subtracting the average force measured in pure water for the average force measured in the presence of inhibitor K1 at 0.5 CMC

and 2 CMC, respectively. These 70~75 nN level lateral forces can be converted to stress values of the order of 100 MPa for removing inhibitor molecules from X65 steel surface.

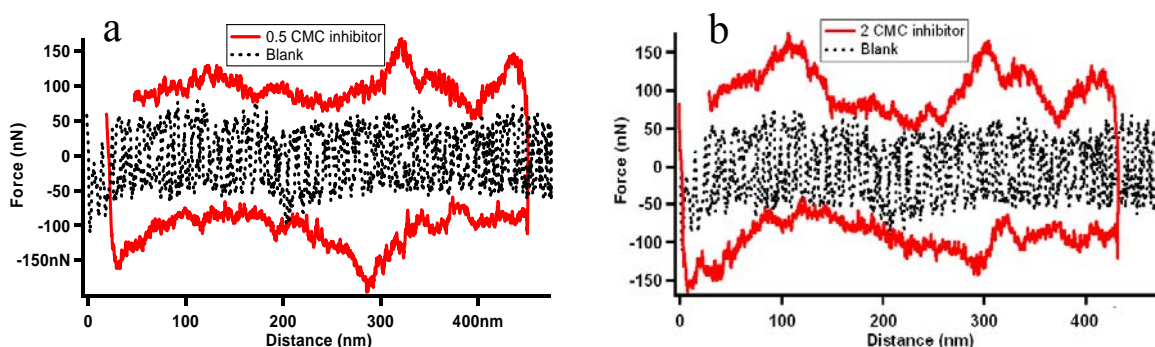


Figure 4.53 Lateral removal force measured on X65 steel in the presence of 0.5 CMC (a) and 2 CMC (b) inhibitor K1 solutions. The force to remove the inhibitor molecules was determined by subtracting the average force measured in pure water from the average force measured in the presence of inhibitor. The average force was determined from the forces measured in both the forward and reverse scans, ignoring the negative sign in the reverse scan.

The AFM analysis of TOFA imidazolium (K1) on the steel surface in this section has shown consistent results as on mica. Inhibitor molecules formed monolayer and bi-layer structures at below and above CMC conditions. Stresses to penetrate and remove inhibitor films are of the order of MPa value. The consistent results on steel and mica are not unexpected, because both steel and mica surfaces are negatively charged at the experimental conditions and the adsorption of cationic inhibitors on negatively charged surfaces should be similar. This is the first time adsorption of inhibitor molecules on X65 steel surface in aqueous solution has been directly studied with an AFM. Further

investigation of other types of inhibitor molecules can be done on different surfaces in various conditions using this AFM technique.

4.4 Conclusions

AFM is a powerful technique for imaging and studying of the properties of surfactant inhibitor films adsorbed on solid surfaces. The surface morphologies, film thicknesses, penetration forces and lateral forces of five corrosion inhibitors were studied on mica, Au, Fe and X65 steel surfaces.

The adsorption structure of corrosion inhibitors depends on their molecular structures, surface properties and environmental conditions. For example, inhibitor K1, TOFA imidazolium, formed a continuous and uniform film on the surface as it did not change the original surface morphology after adsorption. The thickness measurements indicated that a monolayer formed below the critical micelle concentration (CMC) at 0.5 times CMC, while a bi-layer formed above the CMC (2 times CMC). Tests with a quat-type inhibitor K2, have shown it can form a monolayer at 0.5 CMC but hemi-micelles at 2 CMC.

The mechanical resistance of corrosion inhibitors was studied by measuring the penetration force in the normal direction and the removal force in the lateral direction. Normal force measurements were used to penetrate the inhibitor films appeared to be related to film structure. A significantly greater force was required to penetrate bilayer films than monolayer films. Lateral removal force measurements appeared to be directly related to the strength of adhesion between the molecules hydrophilic groups and the

surface. The removal force measurements were independent of film thickness. These penetration and removal forces can be divided by the contact area to calculate the stresses in normal and lateral directions. The shear stresses required to remove inhibitor molecules from the surface were found to be of the order of MPa. This is at least three orders of magnitude above the maximum shear stress obtained by fluid flow in pipelines. Therefore, it appears unlikely that inhibitor films can be removed from steel pipe walls due to fluid flow shear forces alone.

Environmental conditions, such as pH, ionic strength and organic solvent have significant impacts on inhibitor adsorption. For example, inhibitor K1, TOFA imidazolium, has larger film thickness, larger penetration force and larger removal force in acidic condition than in basic condition, indicating this type of inhibitor performs better in acidic conditions. By adding organic solvents, such as ethanol or methanol, the adsorption of TOFA imidazolium significantly decreased, which is consistent with the reported inhibition failure by additive methanol components in industry.

Chapter 5. Future work

This dissertation describes studies undertaken in two main topics: the electronic properties of carbon nanotubes and the adsorption of corrosion inhibitors on various substrates. Most of the initial objectives have been achieved, but other areas for further investigation have become apparent, including the following:

1. Irradiation can preferentially affect metallic nanotubes and their breakdown. This implies that, mechanistic processes at work can lead to the selective etching of metallic content. Future work can focus on enhancement of irradiation efficiency, by changing the irradiation strength, frequency and duration, to achieve tuned or complete breakdown of metallic nanotubes.
2. Although the adsorption of corrosion inhibitors has been investigated in this research, the relationship between molecular adsorption and realistic corrosion inhibition remains poorly understood. Future work can focus on the combination of AFM technique with other techniques, such as corrosion rate measurements by linear polarization resistance, and adsorbed mass measurements by electrochemical quartz crystal microbalance, to reveal how the inhibition is associated with the adsorption.
3. It has been reported in industry that corrosion inhibitors sometimes can accelerate the corrosion rate. This phenomenon is commonly believed to be caused by the galvanic effect between inhibited and uninhibited areas. To study whether the electric properties of a whole inhibitor film is uniform, electrostatic force

microscopy or scanning Kelvin probe microscopy, which are based on AFM, can be applied to map the surface potential. Conductive AFM may also be applied to detect whether the conductivity of a surface covered by an inhibitor film is uniform.

4. Application of AFM is still very limited in corrosion science. Most of AFM work published in corrosion studies focus on corrosion inhibitors. In comparison to scanning electron microscopy (SEM), which is widely used in studying corrosion mechanism, AFM provides higher resolution images but requires a relative flat surface. Future usage of AFM can be applied to study the initial stage of protective film formation, such as for FeCO_3 and FeS .

References

- 1 Binnig, G. and Rohrer, H. Scanning Tunneling Microscopy. *Physica B & C* **127**, 37 (1984).
- 2 Binnig, G. and Rohrer, H. The Scanning Tunneling Microscope. *Sci Am* **253**, 50 (1985).
- 3 Binnig, G. and Rohrer, H. Scanning Tunneling Microscopy. *Surf Sci* **152**, 17 (1985).
- 4 Baro, A. M., Miranda, R., Alaman, J., Garcia, N., Binnig, G., Rohrer, H., Gerber, C. and Carrascosa, J. L. Determination of Surface-Topography of Biological Specimens at High-Resolution by Scanning Tunneling Microscopy. *Nature* **315**, 253 (1985).
- 5 Binnig, G., Rohrer, H., Salvan, F., Gerber, C. and Baro, A. Revisiting the 7x7 Reconstruction of Si(111). *Surf Sci* **157**, 373 (1985).
- 6 Hamers, R. J., Koch, R. H. and Demuth, J. E. Scanning Tunneling Microscopy - an Atomic-Scale Probe of Surface Geometry and Electronic-Structure. *J Electrochem Soc* **135**, 136 (1988).
- 7 Binnig, G., Gerber, C., Stoll, E., Albrecht, T. R. and Quate, C. F. Atomic Resolution with Atomic Force Microscope. *Surf Sci* **189**, 1 (1987).
- 8 Binnig, G., Gerber, C., Stoll, E., Albrecht, T. R. and Quate, C. F. Atomic Resolution with Atomic Force Microscope. *Europhys Lett* **3**, 1281 (1987).
- 9 Binnig, G., Quate, C. F. and Gerber, C. Atomic Force Microscope. *Phys Rev Lett* **56**, 930 (1986).
- 10 Albrecht, T. R. and Quate, C. F. Atomic Resolution with the Atomic Force Microscope on Conductors and Nonconductors. *J Vac Sci Technol A* **6**, 271 (1988).
- 11 Abraham, F. F., Batra, I. P. and Ciraci, S. Effect of Tip Profile on Atomic-Force Microscope Images - a Model Study. *Phys Rev Lett* **60**, 1314 (1988).
- 12 Gould, S., Marti, O., Drake, B., Hellemans, L., Bracker, C. E., Hansma, P. K., Keder, N. L., Eddy, M. M. and Stucky, G. D. Molecular Resolution Images of Amino-Acid Crystals with the Atomic Force Microscope. *Nature* **332**, 332 (1988).
- 13 Meyer, E., Grutter, P., Heinzelmann, H., Rosenthaler, L., Hidber, H. R. and Guntherodt, H. J. Applications of the Atomic Force Microscope. *Helv Phys Acta* **61**, 179 (1988).
- 14 Persson, B. N. J. The Atomic Force Microscope - Can It Be Used to Study Biological Molecules. *Chem Phys Lett* **141**, 366 (1987).
- 15 Vezenov, D. V., Noy, A. and Lieber, C. M. Probing intermolecular interactions in contact and tapping mode with chemical force microscopy. *Abstr Pap Am Chem S* **216**, 100 (1998).
- 16 Lieber, C. M., Noy, A., Vezenov, D. V., Wong, S. S., Woolley, A. T. and Joselevich, E. Chemical force microscopy. *Abstr Pap Am Chem S* **216**, 200 (1998).

- 17 Lu, W., Xiong, Y., Hassanien, A., Zhao, W., Zheng, M. and Chen, L. W. A Scanning Probe Microscopy Based Assay for Single-Walled Carbon Nanotube Metallicity. *Nano Lett* **9**, 1668 (2009).
- 18 Joshi, N. R., Ozer, S., Ashworth, T. V., Stickar, P. G., Romer, S., Marioni, M. A. and Hug, H. J. Engineering the ferromagnetic domain size for optimized imaging of the pinned uncompensated spins in exchange-biased samples by magnetic force microscopy. *Appl Phys Lett* **98**, 1 (2011).
- 19 Ma, T. Y., Zhang, C. S., Zhang, J. J., Tao, S. and Yan, M. Magnetic force microscopy study of magnetically annealed Tb_{0.36}Dy_{0.64}(Fe_{0.85}Co_{0.15})(2) polycrystals. *J Appl Phys* **107**, 1 (2010).
- 20 Bhushan, B. *Springer handbook of nanotechnology*. (Springer-Verlag, 2004).
- 21 S.S. Sheiko, M. M., E.M.C.M. Reuvekamp, H.W. Zandbergen. Evaluation of the probing profile of scanning force microscopy tips. *Ultramicroscopy* **53**, 10 (1994).
- 22 Michael J. Allen, N. V. H., Mehdi Balooch, Robert J. Tench, Wigbert J. Siekhaus and Rod Balhorn. Tip-radius-induced artifacts in AFM images of protamine-complexed DNA fibers. *Ultramicroscopy* **44**, 6 (1992).
- 23 Westra, K. L. M., A. W.; Thomson, D. J.; . Tip artifacts in atomic force microscope imaging of thin film surfaces. *Journal of Applied Physics* **74**, 3 (1993).
- 24 Martin, Y., Williams, C. C. and Wickramasinghe, H. K. Atomic Force Microscope Force Mapping and Profiling on a Sub 100-Å Scale. *J Appl Phys* **61**, 4723 (1987).
- 25 Hansma, P. K., Cleveland, J. P., Radmacher, M., Walters, D. A., Hillner, P. E., Bezanilla, M., Fritz, M., Vie, D., Hansma, H. G., Prater, C. B., Massie, J., Fukunaga, L., Gurley, J. and Elings, V. Tapping Mode Atomic-Force Microscopy in Liquids. *Appl Phys Lett* **64**, 1738 (1994).
- 26 Noy, A., Vezenov, D. V. and Lieber, C. M. Chemical force microscopy. *Annu Rev Mater Sci* **27**, 381 (1997).
- 27 Wei Lu, Y. X., Abdou Hassanien, Wei Zhao, Ming Zheng and Liwei Chen. A Scanning Probe Microscopy Based Assay for Single-Walled Carbon Nanotube Metallicity. *Nano Lett* **9**, 1668 (2009).
- 28 Degao Xu, G. D. W., John N. Harb, and Robert C. Davis. Electrical Conductivity of Ferritin Proteins by Conductive AFM. *Nano Lett* **5**, 571 (2005).
- 29 Sarid, D. *Scanning force microscopy : with applications to electric, magnetic, and atomic forces*. Rev. edn, (Oxford University Press, 1994).
- 30 Saenz, J. J., Garcia, N., Grutter, P., Meyer, E., Heinzelmann, H., Wiesendanger, R., Rosenthaler, L., Hidber, H. R. and Gunterodt, H. J. Observation of Magnetic Forces by the Atomic Force Microscope. *J Appl Phys* **62**, 4293 (1987).
- 31 Nonnenmacher, M., OBoyle, M. P., Wickramasinghe, H. K., . Kelvin probe force microscopy. *Appl Phys Lett* **58**, 2921 (1991).
- 32 R. W. Carpick, D. F. O., and M. Salmeron. Lateral stiffness: A new nanomechanical measurement for the determination of shear strengths with friction force microscopy. *Appl. Phys. Lett.* **70**, 3 (1996).

- 33 Bowen, W. R., Hilal, N., Lovitt, R. W. and Williams, P. M. Visualisation of an ultrafiltration membrane by non-contact atomic force microscopy at single pore resolution. *J Membrane Sci* **110**, 229 (1996).
- 34 Morita, S., Fujisawa, S., Kishi, E., Ohta, M., Ueyama, H. and Sugawara, Y. Contact and non-contact mode imaging by atomic force microscopy. *Thin Solid Films* **273**, 138 (1996).
- 35 Schmitz, I., Schreiner, M., Friedbacher, G. and Grasserbauer, M. Tapping-mode AFM in comparison to contact-mode AFM as a tool for in situ investigations of surface reactions with reference to glass corrosion. *Anal Chem* **69**, 1012 (1997).
- 36 Cherniavskaya, O., Chen, L. W., Weng, V., Yuditsky, L. and Brus, L. E. Quantitative noncontact electrostatic force Imaging of nanocrystal polarizability. *J Phys Chem B* **107**, 1525 (2003).
- 37 Wendel, M., Kuhn, S., Lorenz, H., Kotthaus, J. P. and Holland, M. Nanolithography with an Atomic-Force Microscope for Integrated Fabrication of Quantum Electronic Devices. *Appl Phys Lett* **65**, 1775 (1994).
- 38 Boisen, A., Hansen, O. and Bouwstra, S. AFM probes with directly fabricated tips. *J Micromech Microeng* **6**, 58 (1996).
- 39 Luo, K., Shi, Z., Lai, J. and Majumdar, A. Nanofabrication of sensors on cantilever probe tips for scanning multiprobe microscopy. *Appl Phys Lett* **68**, 325 (1996).
- 40 Rief, M., Oesterhelt, F., Heymann, B. and Gaub, H. E. Single molecule force spectroscopy on polysaccharides by atomic force microscopy. *Science* **275**, 1295 (1997).
- 41 Quate, C. F. The Afm as a Tool for Surface Imaging. *Surf Sci* **300**, 980 (1994).
- 42 Rugar, D. and Hansma, P. Atomic Force Microscopy. *Phys Today* **43**, 23 (1990).
- 43 Iijima, S. Helical Microtubules of Graphitic Carbon. *Nature* **354**, 56 (1991).
- 44 Dai, H. J. Carbon nanotubes: opportunities and challenges. *Surf Sci* **500**, 218 (2002).
- 45 Thess, A., Lee, R., Nikolaev, P., Dai, H. J., Petit, P., Robert, J., Xu, C. H., Lee, Y. H., Kim, S. G., Rinzler, A. G., Colbert, D. T., Scuseria, G. E., Tomanek, D., Fischer, J. E. and Smalley, R. E. Crystalline ropes of metallic carbon nanotubes. *Science* **273**, 483 (1996).
- 46 Odom, T. W., Huang, J. L., Kim, P. and Lieber, C. M. Structure and electronic properties of carbon nanotubes. *J Phys Chem B* **104**, 2794 (2000).
- 47 Yu, M. F., Files, B. S., Arepalli, S. and Ruoff, R. S. Tensile loading of ropes of single wall carbon nanotubes and their mechanical properties. *Phys Rev Lett* **84**, 5552 (2000).
- 48 Hone, J., Llaguno, M. C., Biercuk, M. J., Johnson, A. T., Batlogg, B., Benes, Z. and Fischer, J. E. Thermal properties of carbon nanotubes and nanotube-based materials. *Appl Phys a-Mater* **74**, 339 (2002).
- 49 Peng, B., Locascio, M., Zapol, P., Li, S. Y., Mielke, S. L., Schatz, G. C. and Espinosa, H. D. Measurements of near-ultimate strength for multiwalled carbon nanotubes and irradiation-induced crosslinking improvements. *Nat Nanotechnol* **3**, 626 (2008).

- 50 Futaba, D. N., Hata, K., Yamada, T., Hiraoka, T., Hayamizu, Y., Kakudate, Y., Tanaike, O., Hatori, H., Yumura, M. and Iijima, S. Shape-engineerable and highly densely packed single-walled carbon nanotubes and their application as super-capacitor electrodes. *Nat Mater* **5**, 987 (2006).
- 51 Moriguchi, I., Hidaka, R., Yamada, H., Kudo, T., Murakami, H. and Nakashima, N. A mesoporous nanocomposite of TiO₂ and carbon nanotubes as a high-rate Li-intercalation electrode material. *Adv Mater* **18**, 69 (2006).
- 52 Kam, N. W. S., O'Connell, M., Wisdom, J. A. and Dai, H. J. Carbon nanotubes as multifunctional biological transporters and near-infrared agents for selective cancer cell destruction. *P Natl Acad Sci USA* **102**, 11600 (2005).
- 53 Li, S. S., He, H., Jiao, Q. C. and Chuong, P. H. Applications of Carbon Nanotubes in Drug and Gene Delivery. *Prog Chem* **20**, 1798 (2008).
- 54 Bianco, A., Kostarelos, K. and Prato, M. Applications of carbon nanotubes in drug delivery. *Curr Opin Chem Biol* **9**, 674 (2005).
- 55 Che, G. L., Lakshmi, B. B., Fisher, E. R. and Martin, C. R. Carbon nanotubule membranes for electrochemical energy storage and production. *Nature* **393**, 346 (1998).
- 56 Chesnokov, S. A., Nalimova, V. A., Rinzler, A. G., Smalley, R. E. and Fischer, J. E. Mechanical energy storage in carbon nanotube springs. *Phys Rev Lett* **82**, 343 (1999).
- 57 Saito, R., Dresselhaus, G. and Dresselhaus, M. S. *Physical properties of carbon nanotubes*. (Imperial College Press, 1999).
- 58 Dresselhaus, M. S., Dresselhaus, G. and Avouris, P. *Carbon nanotubes : synthesis, structure, properties, and applications*. (Springer, 2001).
- 59 Wildoer, J. W. G., Venema, L. C., Rinzler, A. G., Smalley, R. E. and Dekker, C. Electronic structure of atomically resolved carbon nanotubes. *Nature* **391**, 59 (1998).
- 60 Terranova, M. L., Sessa, V. and Rossi, M. The world of carbon nanotubes: An overview of CVD growth methodologies. *Chem Vapor Depos* **12**, 315 (2006).
- 61 Liu, J., Fan, S. S. and Dai, H. J. Recent advances in methods of forming carbon nanotubes. *Mrs Bull* **29**, 244 (2004).
- 62 Dai, H. J. Carbon nanotubes: Synthesis, integration, and properties. *Accounts Chem Res* **35**, 1035 (2002).
- 63 See, C. H. and Harris, A. T. A review of carbon nanotube synthesis via fluidized-bed chemical vapor deposition. *Ind Eng Chem Res* **46**, 997 (2007).
- 64 Nikolaev, P., Bronikowski, M. J., Bradley, R. K., Rohmund, F., Colbert, D. T., Smith, K. A. and Smalley, R. E. Gas-phase catalytic growth of single-walled carbon nanotubes from carbon monoxide. *Chem Phys Lett* **313**, 91 (1999).
- 65 Daniel E. Resasco, B. K., Walter Alvarez, Leandro Balzano,. Method and apparatus for producing carbon nanotubes. *U. S. Patent 7,585,482* (2009).
- 66 Bachilo, S. M., Strano, M. S., Kittrell, C., Hauge, R. H., Smalley, R. E. and Weisman, R. B. Structure-assigned optical spectra of single-walled carbon nanotubes. *Science* **298**, 2361 (2002).

- 67 Niyogi, S., Hamon, M. A., Hu, H., Zhao, B., Bhowmik, P., Sen, R., Itkis, M. E. and Haddon, R. C. Chemistry of single-walled carbon nanotubes. *Accounts Chem Res* **35**, 1105 (2002).
- 68 Minami, N., Kazaoui, S., Jacquemin, R., Yamawaki, H., Aoki, K., Kataura, H. and Achiba, Y. Optical properties of semiconducting and metallic single wall carbon nanotubes: effects of doping and high pressure. *Synthetic Met* **116**, 405 (2001).
- 69 Miyata, Y., Yanagi, K., Maniwa, Y. and Kataura, H. Optical properties of metallic and semiconducting single-wall carbon nanotubes. *Phys Status Solidi B* **245**, 2233 (2008).
- 70 O'Connell, M. J., Bachilo, S. M., Huffman, C. B., Moore, V. C., Strano, M. S., Haroz, E. H., Rialon, K. L., Boul, P. J., Noon, W. H., Kittrell, C., Ma, J. P., Hauge, R. H., Weisman, R. B. and Smalley, R. E. Band gap fluorescence from individual single-walled carbon nanotubes. *Science* **297**, 593 (2002).
- 71 Dyke, C. A. and Tour, J. M. Overcoming the insolubility of carbon nanotubes through high degrees of sidewall functionalization. *Chem-Eur J* **10**, 813 (2004).
- 72 Yeung, C. S., Tian, W. Q., Liu, L. V. and Wang, Y. A. Chemistry of Single-Walled Carbon Nanotubes. *J Comput Theor Nanos* **6**, 1213 (2009).
- 73 Bahr, J. L. and Tour, J. M. Covalent chemistry of single-wall carbon nanotubes. *J Mater Chem* **12**, 1952 (2002).
- 74 Bahr, J. L., Yang, J. P., Kosynkin, D. V., Bronikowski, M. J., Smalley, R. E. and Tour, J. M. Functionalization of carbon nanotubes by electrochemical reduction of aryl diazonium salts: A bucky paper electrode. *J Am Chem Soc* **123**, 6536 (2001).
- 75 Britz, D. A. and Khlobystov, A. N. Noncovalent interactions of molecules with single walled carbon nanotubes. *Chem Soc Rev* **35**, 637 (2006).
- 76 Karajanagi, S. S., Yang, H. C., Asuri, P., Sellitto, E., Dordick, J. S. and Kane, R. S. Protein-assisted solubilization of single-walled carbon nanotubes. *Langmuir* **22**, 1392 (2006).
- 77 Chatterjee, T., Yurekli, K., Hadjiev, V. G. and Krishnamoorti, R. Single-walled carbon nanotube dispersions in poly(ethylene oxide). *Adv Funct Mater* **15**, 1832 (2005).
- 78 Zheng, M., Jagota, A., Strano, M. S., Santos, A. P., Barone, P., Chou, S. G., Diner, B. A., Dresselhaus, M. S., McLean, R. S., Onoa, G. B., Samsonidze, G. G., Semke, E. D., Usrey, M. and Walls, D. J. Structure-based carbon nanotube sorting by sequence-dependent DNA assembly. *Science* **302**, 1545 (2003).
- 79 Tasis, D., Tagmatarchis, N., Bianco, A. and Prato, M. Chemistry of carbon nanotubes. *Chem Rev* **106**, 1105 (2006).
- 80 Wang, D., Ji, W. X., Li, Z. C. and Chen, L. W. A biomimetic "polysoap" for single-walled carbon nanotube dispersion. *J Am Chem Soc* **128**, 6556 (2006).
- 81 Ausman, K. D., Piner, R., Lourie, O., Ruoff, R. S. and Korobov, M. Organic solvent dispersions of single-walled carbon nanotubes: Toward solutions of pristine nanotubes. *J Phys Chem B* **104**, 8911 (2000).

- 82 Strano, M. S., Dyke, C. A., Usrey, M. L., Barone, P. W., Allen, M. J., Shan, H. W., Kittrell, C., Hauge, R. H., Tour, J. M. and Smalley, R. E. Electronic structure control of single-walled carbon nanotube functionalization. *Science* **301**, 1519 (2003).
- 83 Krupke, R., Hennrich, F., von Lohneysen, H. and Kappes, M. M. Separation of metallic from semiconducting single-walled carbon nanotubes. *Science* **301**, 344 (2003).
- 84 Zheng, M., Jagota, A., Semke, E. D., Diner, B. A., Mclean, R. S., Lustig, S. R., Richardson, R. E. and Tassi, N. G. DNA-assisted dispersion and separation of carbon nanotubes. *Nat Mater* **2**, 338 (2003).
- 85 Zheng, M. and Semke, E. D. Enrichment of single chirality carbon nanotubes. *J Am Chem Soc* **129**, 6084 (2007).
- 86 Tu, X. M., Manohar, S., Jagota, A. and Zheng, M. DNA sequence motifs for structure-specific recognition and separation of carbon nanotubes. *Nature* **460**, 250 (2009).
- 87 Arnold, M. S., Green, A. A., Hulvat, J. F., Stupp, S. I. and Hersam, M. C. Sorting carbon nanotubes by electronic structure using density differentiation. *Nat Nanotechnol* **1**, 60 (2006).
- 88 Martel, R., Schmidt, T., Shea, H. R., Hertel, T. and Avouris, P. Single- and multi-wall carbon nanotube field-effect transistors. *Appl Phys Lett* **73**, 2447 (1998).
- 89 Tans, S. J., Devoret, M. H., Dai, H. J., Thess, A., Smalley, R. E., Geerligs, L. J. and Dekker, C. Individual single-wall carbon nanotubes as quantum wires. *Nature* **386**, 474 (1997).
- 90 Dresselhaus, M. S., Dresselhaus, G., Jorio, A., Souza, A. G., Pimenta, M. A. and Saito, R. Single nanotube Raman spectroscopy. *Accounts Chem Res* **35**, 1070 (2002).
- 91 Dresselhaus, M. S., Dresselhaus, G., Jorio, A., Souza Filho, A.G., Saito, R. Raman spectroscopy on isolated single wall carbon nanotubes. *Carbon* **40**, 2043 (2002).
- 92 Dresselhaus, M. S., Dresselhaus, G., Saito, R. and Jorio, A. Raman spectroscopy of carbon nanotubes. *Phys Rep* **409**, 47 (2005).
- 93 Dresselhaus, M. S., Dresselhaus, G. and Jorio, A. Raman spectroscopy of carbon nanotubes in 1997 and 2007. *J Phys Chem C* **111**, 17887 (2007).
- 94 Kataura, H., Kumazawa, Y., Maniwa, Y., Umez, I., Suzuki, S., Ohtsuka, Y. and Achiba, Y. Optical properties of single-wall carbon nanotubes. *Synthetic Met* **103**, 2555 (1999).
- 95 Bahr, J. L., Mickelson, E. T., Bronikowski, M. J., Smalley, R. E. and Tour, J. M. Dissolution of small diameter single-wall carbon nanotubes in organic solvents? *Chem Commun*, 193 (2001).
- 96 Weisman, R. B. and Bachilo, S. M. Dependence of optical transition energies on structure for single-walled carbon nanotubes in aqueous suspension: An empirical Kataura plot. *Nano Lett* **3**, 1235 (2003).
- 97 Maeda, Y., Kimura, S., Kanda, M., Hirashima, Y., Hasegawa, T., Wakahara, T., Lian, Y. F., Nakahodo, T., Tsuchiya, T., Akasaka, T., Lu, J., Zhang, X. W., Gao,

- Z. X., Yu, Y. P., Nagase, S., Kazaoui, S., Minami, N., Shimizu, T., Tokumoto, H. and Saito, R. Large-scale separation of metallic and semiconducting single-walled carbon nanotubes. *J Am Chem Soc* **127**, 10287 (2005).
- 98 Hartschuh, A., Pedrosa, H. N., Peterson, J., Huang, L., Anger, P., Qian, H., Meixner, A. J., Steiner, M., Novotny, L. and Krauss, T. D. Single carbon nanotube optical spectroscopy. *Chemphyschem* **6**, 577 (2005).
- 99 Hartschuh, A., Pedrosa, H. N., Novotny, L. and Krauss, T. D. Simultaneous fluorescence and Raman scattering from single carbon nanotubes. *Science* **301**, 1354 (2003).
- 100 Raja, P. B. and Sethuraman, M. G. Natural products as corrosion inhibitor for metals in corrosive media - A review. *Mater Lett* **62**, 113 (2008).
- 101 Ismail, K. A. Evaluation of cysteine as environmentally friendly corrosion inhibitor for copper in neutral and acidic chloride solutions. *Electrochim Acta* **52**, 7811 (2007).
- 102 Zheludkevich, M. L., Shchukin, D. G., Yasakau, K. A., Mohwald, H. and Ferreira, M. G. S. Anticorrosion coatings with self-healing effect based on nanocontainers impregnated with corrosion inhibitor. *Chem Mater* **19**, 402 (2007).
- 103 Bouklah, M., Hammouti, B., Lagrenee, M. and Bentiss, F. Thermodynamic properties of 2,5-bis(4-methoxyphenyl)-1,3,4-oxadiazole as a corrosion inhibitor for mild steel in normal sulfuric acid medium. *Corros Sci* **48**, 2831 (2006).
- 104 Moretti, G., Guidi, F. and Grion, G. Tryptamine as a green iron corrosion inhibitor in 0.5 M deaerated sulphuric acid. *Corros Sci* **46**, 387 (2004).
- 105 Antonijevic, M. M. and Petrovic, M. B. Copper corrosion inhibitors. A review. *Int J Electrochem Sc* **3**, 1 (2008).
- 106 Tan, Y. J., Bailey, S. and Kinsella, B. The monitoring of the formation and destruction of corrosion inhibitor films using electrochemical noise analysis (ENA). *Corros Sci* **38**, 1681 (1996).
- 107 Zhang, D. Q., An, Z. X., Pan, Q. Y., Gao, L. X. and Zhou, G. D. Volatile corrosion inhibitor film formation on carbon steel surface and its inhibition effect on the atmospheric corrosion of carbon steel. *Appl Surf Sci* **253**, 1343 (2006).
- 108 Bommersbach, P., Alemany-Dumont, C., Millet, J. P. and Normand, B. Hydrodynamic effect on the behaviour of a corrosion inhibitor film: Characterization by electrochemical impedance spectroscopy. *Electrochim Acta* **51**, 4011 (2006).
- 109 Bethencourt, M., Botana, F. J., Calvino, J. J., Marcos, M. and Rodriguez-Chacon, M. A. Lanthanide compounds as environmentally-friendly corrosion inhibitors of aluminium alloys: A review. *Corros Sci* **40**, 1803 (1998).
- 110 Armstrong, R. D., Peggs, L., Walsh, A. Behaviour of sodium silicate and sodium phosphate (tribasic) as corrosion inhibitors for iron. *Journal of Applied Electrochemistry* **24**, 1244 (1994).
- 111 Osman, M. M., El-Ghazawy, R. A. and Al-Sabagh, A. M. Corrosion inhibitor of some surfactants derived from maleic-oleic acid adduct on mild steel in 1 M H₂SO₄. *Mater Chem Phys* **80**, 55 (2003).

- 112 Alsabagh, A. M., Migahed, M. A. and Awad, H. S. Reactivity of polyester aliphatic amine surfactants as corrosion inhibitors for carbon steel in formation water (deep well water). *Corros Sci* **48**, 813 (2006).
- 113 Popova, A., Christov, M., Raicheva, S. and Sokolova, E. Adsorption and inhibitive properties of benzimidazole derivatives in acid mild steel corrosion. *Corros Sci* **46**, 1333 (2004).
- 114 Migahed, M. A., Mohamed, H. M. and Al-Sabagh, A. M. Corrosion inhibition of H-11 type carbon steel in 1 M hydrochloric acid solution by N-propyl amino lauryl amide and its ethoxylated derivatives. *Mater Chem Phys* **80**, 169 (2003).
- 115 Soror, T. Y. and El-Ziady, M. A. Effect of cetyl trimethyl ammonium bromide on the corrosion of carbon steel in acids. *Mater Chem Phys* **77**, 697 (2003).
- 116 Rosen, M. J. *Surfactants and interfacial phenomena*. 3rd edn, Wiley-Interscience, (2004).
- 117 Myers, D. *Surfactant science and technology*. 3rd edn, Wiley-Interscience, (2006).
- 118 Goloub, T. P., Koopal, L. K., Bijsterbosch, B. H. and Sidorova, M. P. Adsorption of cationic surfactants on silica. Surface charge effects. *Langmuir* **12**, 3188 (1996).
- 119 Sharma, B. G., Basu, S. and Sharma, M. M. Characterization of adsorbed ionic surfactants on a mica substrate. *Langmuir* **12**, 6506 (1996).
- 120 Fan, A. X., Somasundaran, P. and Turro, N. J. Adsorption of alkyltrimethylammonium bromides on negatively charged alumina. *Langmuir* **13**, 506 (1997).
- 121 Rupprecht, H. and Gu, T. Structure of Adsorption Layers of Ionic Surfactants at the Solid Liquid Interface. *Colloid Polym Sci* **269**, 506 (1991).
- 122 Elewady, G. Y., El-Said, I. A. and Fouda, A. S. Anion surfactants as corrosion inhibitors for aluminum dissolution in HCl solutions. *Int J Electrochem Sc* **3**, 177 (2008).
- 123 Zhao, T. P. and Mu, G. N. The adsorption and corrosion inhibition of anion surfactants on aluminium surface in hydrochloric acid. *Corros Sci* **41**, 1937 (1999).
- 124 Nikoobakht, B. and El-Sayed, M. A. Evidence for bilayer assembly of cationic surfactants on the surface of gold nanorods. *Langmuir* **17**, 6368 (2001).
- 125 Somasundaran, P. and Huang, L. Adsorption/aggregation of surfactants and their mixtures at solid-liquid interfaces. *Adv Colloid Interfac* **88**, 179 (2000).
- 126 Atkin, R., Craig, V. S. J., Wanless, E. J. and Biggs, S. Mechanism of cationic surfactant adsorption at the solid-aqueous interface. *Adv Colloid Interfac* **103**, 219 (2003).
- 127 Somasundaran, P. and Huang, L. Adsorption behavior of surfactant mixtures at solid-liquid interface. *Pol J Chem* **71**, 568 (1997).
- 128 Somasund.P and Fuersten.Dw. Mechanisms of Alkyl Sulfonate Adsorption at Alumina-Water Interface. *J Phys Chem-Us* **70**, 90 (1966).
- 129 Abe, M. and Scamehorn, J. F. *Mixed surfactant systems*. 2nd edn, (Marcel Dekker, 2005).

- 130 Paria, S. and Khilar, K. C. A review on experimental studies of surfactant adsorption at the hydrophilic solid-water interface. *Adv Colloid Interfac* **110**, 75 (2004).
- 131 Parfitt, G. D. and Rochester, C. H. *Adsorption from solution at the solid/liquid interface*. (Academic Press, 1983).
- 132 Scamehorn, J. F., Schechter, R. S. and Wade, W. H. Adsorption of Surfactants on Mineral Oxide Surfaces from Aqueous-Solutions .1. Isomerically Pure Anionic Surfactants. *J Colloid Interf Sci* **85**, 463 (1982).
- 133 Fuerstenau, D. W. Equilibrium and nonequilibrium phenomena associated with the adsorption of ionic surfactants at solid-water interfaces. *J Colloid Interf Sci* **256**, 79 (2002).
- 134 Golub, T. P., Koopal, L. K. and Sidorova, M. P. Adsorption of cationic surfactants on silica surface: 1. Adsorption isotherms and surface charge. *Colloid J+* **66**, 38 (2004).
- 135 Manne, S., Cleveland, J. P., Gaub, H. E., Stucky, G. D. and Hansma, P. K. Direct Visualization of Surfactant Hemimicelles by Force Microscopy of the Electrical Double-Layer. *Langmuir* **10**, 4409 (1994).
- 136 Manne, S. and Gaub, H. E. Molecular-Organization of Surfactants at Solid-Liquid Interfaces. *Science* **270**, 1480 (1995).
- 137 Liu, J. F., Min, G. and Ducker, W. A. AFM study of adsorption of cationic surfactants and cationic polyelectrolytes at the silica-water interface. *Langmuir* **17**, 4895 (2001).
- 138 Patrick, H. N., Warr, G. G., Manne, S. and Aksay, I. A. Surface micellization patterns of quaternary ammonium surfactants on mica. *Langmuir* **15**, 1685 (1999).
- 139 Ducker, W. A. and Wanless, E. J. Surface-aggregate shape transformation. *Langmuir* **12**, 5915 (1996).
- 140 Jaschke, M., Butt, H. J., Gaub, H. E. and Manne, S. Surfactant aggregates at a metal surface. *Langmuir* **13**, 1381 (1997).
- 141 Koopal, L. K., Lee, E. M. and Bohmer, M. R. Adsorption of Cationic and Anionic Surfactants on Charged Metal-Oxide Surfaces. *J Colloid Interf Sci* **170**, 85 (1995).
- 142 Pavan, P. C., Crepaldi, E. L., Gomes, G. D. and Valim, J. B. Adsorption of sodium dodecylsulfate on a hydrotalcite-like compound. Effect of temperature, pH and ionic strength. *Colloid Surface A* **154**, 399 (1999).
- 143 Russel, W. B., Saville, D. A. and Schowalter, W. R. *Colloidal dispersions*. (Cambridge University Press, 1989).
- 144 Lyklema, J. *Fundamentals of interface and colloid science*, Academic Press, San Diego, (2000).
- 145 Lewis, J. A. Colloidal processing of ceramics. *J Am Ceram Soc* **83**, 2341 (2000).
- 146 Pagac, E. S., Prieve, D. C. and Tilton, R. D. Kinetics and mechanism of cationic surfactant adsorption and coadsorption with cationic polyelectrolytes at the silica-water interface. *Langmuir* **14**, 2333 (1998).
- 147 Frank, S., Poncharal, P., Wang, Z. L. and de Heer, W. A. Carbon nanotube quantum resistors. *Science* **280**, 1744 (1998).

- 148 Park, J. Y., Rosenblatt, S., Yaish, Y., Sazonova, V., Ustunel, H., Braig, S., Arias, T. A., Brouwer, P. W. and McEuen, P. L. Electron-phonon scattering in metallic single-walled carbon nanotubes. *Nano Lett* **4**, 517 (2004).
- 149 Kong, J., Franklin, N. R., Zhou, C. W., Chapline, M. G., Peng, S., Cho, K. J. and Dai, H. J. Nanotube molecular wires as chemical sensors. *Science* **287**, 622 (2000).
- 150 Durkop, T., Getty, S. A., Cobas, E. and Fuhrer, M. S. Extraordinary mobility in semiconducting carbon nanotubes. *Nano Lett* **4**, 35 (2004).
- 151 Fuhrer, M. S., Kim, B. M., Durkop, T. and Brintlinger, T. High-mobility nanotube transistor memory. *Nano Lett* **2**, 755 (2002).
- 152 Islam, M. F., Rojas, E., Bergey, D. M., Johnson, A. T. and Yodh, A. G. High weight fraction surfactant solubilization of single-wall carbon nanotubes in water. *Nano Lett* **3**, 269 (2003).
- 153 Shaffer, M. S. P., Fan, X. and Windle, A. H. Dispersion and packing of carbon nanotubes. *Carbon* **36**, 1603 (1998).
- 154 Winey, K. I. and Moniruzzaman, M. Polymer nanocomposites containing carbon nanotubes. *Macromolecules* **39**, 5194 (2006).
- 155 Choi, Y. C., Shin, Y. M., Lee, Y. H., Lee, B. S., Park, G. S., Choi, W. B., Lee, N. S. and Kim, J. M. Controlling the diameter, growth rate, and density of vertically aligned carbon nanotubes synthesized by microwave plasma-enhanced chemical vapor deposition. *Appl Phys Lett* **76**, 2367 (2000).
- 156 Kim, W., Choi, H. C., Shim, M., Li, Y. M., Wang, D. W. and Dai, H. J. Synthesis of ultralong and high percentage of semiconducting single-walled carbon nanotubes. *Nano Lett* **2**, 703 (2002).
- 157 Chen, L. W., Lu, W. and Wang, D. Near-static dielectric polarization of individual carbon nanotubes. *Nano Lett* **7**, 2729 (2007).
- 158 Schonberger, C. and Alvarado, S. F. Observation of Single Charge-Carriers by Force Microscopy. *Phys Rev Lett* **65**, 3162 (1990).
- 159 Belaidi, S., Girard, P. and Leveque, G. Electrostatic forces acting on the tip in atomic force microscopy: Modelization and comparison with analytic expressions. *J Appl Phys* **81**, 1023 (1997).
- 160 Girard, P. Electrostatic force microscopy: principles and some applications to semiconductors. *Nanotechnology* **12**, 485 (2001).
- 161 Gomez-Monivas, S., Froufe-Perez, L. S., Caamano, A. J. and Saenz, J. J. Electrostatic forces between sharp tips and metallic and dielectric samples. *Appl Phys Lett* **79**, 4048 (2001).
- 162 Benedict, L. X., Louie, S. G. and Cohen, M. L. Static Polarizabilities of Single-Wall Carbon Nanotubes. *Phys Rev B* **52**, 8541 (1995).
- 163 Kozinsky, B. and Marzari, N. Static dielectric properties of carbon nanotubes from first principles. *Phys Rev Lett* **96** (2006).
- 164 Lu, W., Xiong, Y. and Chen, L. W. Length-Dependent Dielectric Polarization in Metallic Single-Walled Carbon Nanotubes. *J Phys Chem C* **113**, 10337 (2009).
- 165 Lourtioz, J. M. *Photonic crystals : towards nanoscale photonic devices*. Springer, (2005).

- 166 Gomez-Navarro, C., De Pablo, P. J., Gomez-Herrero, J., Biel, B., Garcia-Vidal, F. J., Rubio, A. and Flores, F. Tuning the conductance of single-walled carbon nanotubes by ion irradiation in the Anderson localization regime. *Nat Mater* **4**, 534 (2005).
- 167 Chen, R. J., Zhang, Y. G., Wang, D. W. and Dai, H. J. Noncovalent sidewall functionalization of single-walled carbon nanotubes for protein immobilization. *J Am Chem Soc* **123**, 3838 (2001).
- 168 Dresselhaus, M. S., Dresselhaus, G., Jorio, A., Souza, A. G. and Saito, R. Raman spectroscopy on isolated single wall carbon nanotubes. *Carbon* **40**, 2043 (2002).
- 169 Jorio, A., Saito, R., Hafner, J. H., Lieber, C. M., Hunter, M., McClure, T., Dresselhaus, G. and Dresselhaus, M. S. Structural (n, m) determination of isolated single-wall carbon nanotubes by resonant Raman scattering. *Phys Rev Lett* **86**, 1118 (2001).
- 170 Raghuvver, M. S., Agrawal, S., Bishop, N. and Ramanath, G. Microwave-assisted single-step functionalization and in situ derivatization of carbon nanotubes with gold nanoparticles. *Chem Mater* **18**, 1390 (2006).
- 171 Wang, Y. B., Iqbal, Z. and Mitra, S. Microwave-induced rapid chemical functionalization of single-walled carbon nanotubes. *Carbon* **43**, 1015 (2005).
- 172 Harutyunyan, A. R., Pradhan, B. K., Chang, J. P., Chen, G. G. and Eklund, P. C. Purification of single-wall carbon nanotubes by selective microwave heating of catalyst particles. *J Phys Chem B* **106**, 8671 (2002).
- 173 Chen, C. M., Chen, M., Leu, F. C., Hsu, S. Y., Wang, S. C., Shi, S. C. and Chen, C. F. Purification of multi-walled carbon nanotubes by microwave digestion method. *Diam Relat Mater* **13**, 1182 (2004).
- 174 Imholt, T. J., Dyke, C. A., Hasslacher, B., Perez, J. M., Price, D. W., Roberts, J. A., Scott, J. B., Wadhawan, A., Ye, Z. and Tour, J. M. Nanotubes in microwave fields: Light emission, intense heat, outgassing, and reconstruction. *Chem Mater* **15**, 3969 (2003).
- 175 Electrodynamics of carbon nanotubes: Dynamic conductivity, impedance boundary conditions, and surface wave propagation. *Phys Rev B* **60**, 17136 (1999).
- 176 Collins, P. C., Arnold, M. S. and Avouris, P. Engineering carbon nanotubes and nanotube circuits using electrical breakdown. *Science* **292**, 706 (2001).
- 177 Wang, L., Xiong, Y., Wu, Z. R., Duong, B., Seraphin, S., Xin, H. and Chen, L. W. Demetalization of single-walled carbon nanotube thin films with microwave irradiation. *Appl Phys a-Mater* **102**, 401 (2011).
- 178 Edwards, A., Osborne, C., Webster, S., Klenerman, D., Joseph, M., Ostovar, P. and Doyle, M. Mechanistic Studies of the Corrosion-Inhibitor Oleic Imidazoline. *Corros Sci* **36**, 315 (1994).
- 179 Zhang, X. Y., Wang, F. P., He, Y. F. and Du, Y. L. Study of the inhibition mechanism of imidazoline amide on CO₂ corrosion of Armco iron. *Corros Sci* **43**, 1417 (2001).

- 180 Wang, D. X., Li, S. Y., Ying, Y., Wang, M. J., Xiao, H. M. and Chen, Z. X. Theoretical and experimental studies of structure and inhibition efficiency of imidazoline derivatives. *Corros Sci* **41**, 1911 (1999).
- 181 Bereket, G., Hur, E. and Ogretir, C. Quantum chemical studies on some imidazole derivatives as corrosion inhibitors for iron in acidic medium. *J Mol Struct-Theochem* **578**, 79 (2002).
- 182 Gasparac, R., Martin, C. R. and Stupnisek-Lisac, E. In situ studies of imidazole and its derivatives as copper corrosion inhibitors - I. Activation energies and thermodynamics of adsorption. *J Electrochem Soc* **147**, 548 (2000).
- 183 Gasparac, R., Martin, C. R., Stupnisek-Lisac, E. and Mandic, Z. In situ and ex situ studies of imidazole and its derivatives as copper corrosion inhibitors II. AC impedance, XPS, and SIMS studies. *J Electrochem Soc* **147**, 991 (2000).
- 184 Zhu, B. Y. and Gu, T. R. General Isotherm Equation for Adsorption of Surfactants at Solid Liquid Interfaces. *J Chem Soc Farad T 1* **85**, 3813 (1989).
- 185 Zhu, B. Y., Gu, T. R. and Zhao, X. L. General Isotherm Equation for Adsorption of Surfactants at Solid Liquid Interfaces .2. Applications. *J Chem Soc Farad T 1* **85**, 3819 (1989).
- 186 Levitz, P. and Vandamme, H. Fluorescence Decay Study of the Adsorption of Nonionic Surfactants at the Solid-Liquid Interface .2. Influence of Polar Chain-Length. *J Phys Chem-Us* **90**, 1302 (1986).
- 187 Levitz, P., Vandamme, H. and Keravis, D. Fluorescence Decay Study of the Adsorption of Nonionic Surfactants at the Solid Liquid Interface .1. Structure of the Adsorption Layer on a Hydrophilic Solid. *J Phys Chem-Us* **88**, 2228 (1984).
- 188 Lu, J. R., Marrocco, A., Su, T. J., Thomas, R. K. and Penfold, J. Adsorption of Dodecyl-Sulfate Surfactants with Monovalent Metal Counterions at the Air-Water-Interface Studied by Neutron Reflection and Surface-Tension. *J Colloid Interf Sci* **158**, 303 (1993).
- 189 Lee, E. M., Thomas, R. K., Cummins, P. G., Staples, E. J., Penfold, J. and Rennie, A. R. Determination of the Structure of a Surfactant Layer Adsorbed at the Silica Water Interface by Neutron Reflection. *Chem Phys Lett* **162**, 196 (1989).
- 190 Physical characterization of non-ionic surfactant layers adsorbed at hydrophilic and hydrophobic solid surfaces by time-resolved ellipsometry. *J Chem Soc Faraday T* **92**, 531 (1996).
- 191 Manne, S., Schaffer, T. E., Huo, Q., Hansma, P. K., Morse, D. E., Stucky, G. D. and Aksay, I. A. Gemini surfactants at solid-liquid interfaces: Control of interfacial aggregate geometry. *Langmuir* **13**, 6382 (1997).
- 192 Velegol, S. B., Fleming, B. D., Biggs, S., Wanless, E. J. and Tilton, R. D. Counterion effects on hexadecyltrimethylammonium surfactant adsorption and self-assembly on silica. *Langmuir* **16**, 2548 (2000).
- 193 Atkin, R., Craig, V. S. J., Wanless, E. J. and Biggs, S. Adsorption of 12-s-12 gemini surfactants at the silica-aqueous solution interface. *J Phys Chem B* **107**, 2978 (2003).
- 194 Grant, L. M., Ederth, T. and Tiberg, F. Influence of surface hydrophobicity on the layer properties of adsorbed nonionic surfactants. *Langmuir* **16**, 2285 (2000).

- 195 Becker, T., Kinsella, B. The Use of Atomic Force Microscopy in Corrosion Research. *Corrosion & Materials* **34**, 31 (2009).
- 196 Fang, J. and Li, J. Quantum chemistry study on the relationship between molecular structure and corrosion inhibition efficiency of amides. *J Mol Struct-Theochem* **593**, 179 (2002).
- 197 Schmitt, G. A., Bucken, W. and Fanebust, R. Modeling Microturbulences at Surface Imperfections as Related to Flow-Induced Localized Corrosion. *Corrosion* **48**, 431 (1992).
- 198 Tan, Y. J., Bailey, S. and Kinsella, B. An investigation of the formation and destruction of corrosion inhibitor films using electrochemical impedance spectroscopy (EIS). *Corros Sci* **38**, 1545 (1996).
- 199 Jiang, X., Zheng, Y. G. and Ke, W. Effect of flow velocity and entrained sand on inhibition performances of two inhibitors for CO₂ corrosion of N80 steel in 3% NaCl solution. *Corros Sci* **47**, 2636 (2005).
- 200 Gulbrandsen, E. and Grana, A. Testing of carbon dioxide corrosion inhibitor performance at high flow velocities in jet impingement geometry. Effects of mass transfer and flow forces. *Corrosion* **63**, 1009 (2007).
- 201 Yildirim, O. E., Xu, Q. and Basaran, O. A. Analysis of the drop weight method. *Phys Fluids* **17** (2005).
- 202 Weisenhorn, A. L., Hansma, P. K., Albrecht, T. R. and Quate, C. F. Forces in Atomic Force Microscopy in Air and Water. *Appl Phys Lett* **54**, 2651 (1989).
- 203 Liu, Y. H., Evans, D. F., Song, Q. and Grainger, D. W. Structure and frictional properties of self-assembled surfactant monolayers. *Langmuir* **12**, 1235 (1996).
- 204 Cappella, B. and Dietler, G. Force-distance curves by atomic force microscopy. *Surf Sci Rep* **34**, 1 (1999).
- 205 Shubin, V. Adsorption of Cationic Polymer onto Negatively Charged Surfaces in the Presence of Anionic Surfactant. *Langmuir* **10**, 1093 (1994).
- 206 Manne, S. Visualizing self-assembly: force microscopy of ionic surfactant aggregates at solid-liquid interfaces. *Progr Colloid Polym Sci* **103**, 226 (1997).
- 207 Bellmann, C., Synytska, A., Caspari, A., Drechsler, A. and Grundke, K. Electrokinetic investigation of surfactant adsorption. *J Colloid Interf Sci* **309**, 225 (2007).
- 208 Ersoy, B. and Celik, M. S. Effect of hydrocarbon chain length on adsorption of cationic surfactants onto clinoptilolite. *Clay Clay Miner* **51**, 172 (2003).
- 209 Taylor, D. J. F., Thomas, R. K. and Li, P. X. Adsorption of oppositely charged polyelectrolyte/surfactant mixtures. Neutron reflection from alkyl trimethylammonium bromides and sodium poly(styrenesulfonate) at the air/water interface: The effect of surfactant chain length. *Langmuir* **19**, 3712 (2003).
- 210 Fouda, A. S., Moussa, M. N., Taha, F. I. and Elneanaa, A. I. The Role of Some Thiosemicarbazide Derivatives in the Corrosion Inhibition of Aluminum in Hydrochloric-Acid. *Corros Sci* **26**, 719 (1986).
- 211 Trachli, B., Keddami, M., Takenouti, H. and Srhiri, A. Protective effect of electropolymerized 3-amino 1,2,4-triazole towards corrosion of copper in 0.5 M NaCl. *Corros Sci* **44**, 997 (2002).

- 212 Chen, Y., Hong, T., Gopal, M. and Jepson, W. P. EIS studies of a corrosion inhibitor behavior under multiphase flow conditions. *Corros Sci* **42**, 979 (2000).
- 213 Schmitt, G., Bosch, C., Bauer, H., Mueller, M. Modelling the drag reducing effect of CO₂ corrosion inhibitors. *Corrosion, NACE, Houston, TX, Paper 0002* (2000).
- 214 dos Reis, M. J., Silverio, F., Tronto, J. and Valim, J. B. Effects of pH, temperature, and ionic strength on adsorption of sodium dodecylbenzenesulfonate into Mg-Al-CO₃ layered double hydroxides. *J Phys Chem Solids* **65**, 487 (2004).
- 215 Berthod, A., Girard, I. and Gonnet, C. Additive Effects on Surfactant Adsorption and Ionic Solute Retention in Micellar Liquid-Chromatography. *Anal Chem* **58**, 1362 (1986).
- 216 Bentiss, F., Lagrenee, M., Traisnel, M. and Hornez, J. C. The corrosion inhibition of mild steel in acidic media by a new triazole derivative. *Corros Sci* **41**, 789 (1999).